



ÉCOLE
POLYTECHNIQUE
DE BRUXELLES



UNIVERSITÉ LIBRE DE BRUXELLES

Active seismic isolation using interferometric inertial sensors

Thesis presented by Jennifer WATCHI

in fulfillment of the requirements of the PhD Degree in Engineering Sciences and Technology ("Docteur en Sciences de l'Ingénieur et Technologie")

Academic year 2021-2022

Supervisor : Professor Christophe COLLETTE
[BEAMS Department]

Thesis jury :

Prof. Christophe COLLETTE (Université libre de Bruxelles and Université de Liège, Supervisor)

Prof. Michel Kinnaert (Université libre de Bruxelles, Chair)

Prof. Simon-Pierre GORZA (Université libre de Bruxelles, Secretary)

Prof. Conor MOW-LOWRY (Vrije Universiteit Amsterdam)

Prof. Krishna VENKATESWARA (R&D Director at Paroscientific, Inc.)

beams

Precision
Mechatronics
Laboratory

fnrs
FREEDOM TO RESEARCH

You can only make as well as you can measure.

Joseph Whitworth
(1803-1887)

Abstract

The transmission of ground motion to sensitive equipment can affect their performance or their duty cycle. To overcome this limitation, passive and active isolation solutions have been developed. When it is supported by springs, a system is isolated passively in a frequency range above its resonance frequency. On the other hand, active isolation consists in sensing the motion of the payload to isolate and canceling this motion by injecting a force that opposes this motion. To increase the performance, passive and active solutions can be combined [1]. The goal of this research is to isolate a six degree-of-freedom (d.o.f.) platform from ground motion in the low-frequency range, i.e. between 10 mHz and 10 Hz. At low frequency, the performance of the active isolation stage is limited by the sensor resolution. To overcome this limitation, one can use inertial sensors whose inertial mass' motion is measured by an interferometric readout.

In this thesis, the characterization of a horizontal inertial sensor (HINS) and a vertical inertial sensor (VINS) developed is presented. The Michelson interferometer used to sense the inertial mass is studied with a numerical model; the current resolution is limited by the optics too sensitive to their mounting's motion and by the signal drift at low frequency. The mechanical system is made of a pendulum. By deriving the equations of motion of the system, the sensor's dynamics can be studied; Inertial sensors sense a coupled signal between rotation and translation. Because of this coupling, the dynamics include a pair of complex or real zeroes at low frequency, below the resonance frequency of the inertial system.

To subtract the spurious tilt motion from the sensor's signal, a liquid sensor is under development. The inclination is measured by comparison to the horizontal surface of liquid Mercury sealed inside a container. It has been characterized experimentally to study its sensitivity, 306.75 V/rad, and its resolution on the order of $5 \cdot 10^{-5}$ rad/ $\sqrt{\text{Hz}}$. The current version is too noisy principally because the viscosity of the reflective liquid is not large enough and hence, the reference surface moves too much with ground motion.

The effect of the tilt-translation coupling on inertial control is studied on a 2 d.o.f. model; when applying inertial control, the motion of the payload becomes coupled with the ground inclination at low frequency due to the sensor's dynamics. Solutions to cope with coupling have been investigated: projecting the system in a decoupled frame (centralized projection and singular value decomposition (SVD)), closing a first loop to control the rotation of the payload or sensing the inclination and subtracting it from the inertial sensor signal. The last two methods gave the most promising results.

Finally, a 6 d.o.f. platform has been assembled. It consists of a hexagonal table with three pairs of vertical and horizontal inertial sensors. The table lays on three isolators containing voice coil actuators. The effect of inertial control on a multiple input/multiple output (MIMO)

system is studied experimentally and the solutions tested numerically on the 2 d.o.f. model are extended to the full isolation stage. The platform could reduce of one order of magnitude the amplitude of the payload's motion between 0.1 Hz and 10 Hz in the vertical direction and between 0.1 Hz and 1 Hz in the horizontal direction.

Keywords: Inertial control – MIMO system – Tilt-translation coupling – Tiltmeter

Résumé

Beaucoup d'instruments sensibles ne peuvent opérer correctement quand ils sont déposés directement sur la terre ferme à cause de l'amplitude des mouvements du sol qui leur est transmise. L'amplitude transmise peut être réduite grâce à des systèmes d'isolation passive ou active. Par ailleurs, certains instruments comme les gravimètres atomiques [2] ou les détecteurs d'ondes gravitationnelles [3] doivent être isolés dans plusieurs directions en parallèle pour assurer leur bon fonctionnement.

Dans cette thèse, un système d'isolation active est présenté qui permet d'isoler une charge des mouvements du sol et ce, dans les six degrés de libertés. Le but est de réduire la transmission des mouvements du sol entre 10 mHz et 10 Hz. Deux limitations liées à l'isolation à basses fréquences dans plusieurs directions sont étudiées. Premièrement, la résolution des capteurs limitent les performances à basse fréquence. Deuxièmement, des phénomènes de couplages entre directions peuvent apparaître ce qui risque de déstabiliser le système.

Les capteurs inertiels qui utilisent un système de lecture interférométrique permettent d'obtenir une bonne résolution à basse fréquence. Un modèle optique a permis d'étudier la résolution de l'interferomètre de Michelson utilisé; les éléments optiques doivent être mieux fixés et la lente dérive du signal doit être supprimée par exemple au moyen d'un filtre passe-haut pour améliorer les performances. La partie mécanique du capteur, composée d'un pendule avec la masse inertielle suspendue au bout, a été étudiée au moyen d'un modèle analytique pour comprendre la dynamique du capteur. Le capteur mesure un signal couplé entre translation et rotation et ce couplage est également responsable de l'apparition d'une paire de zéros complexes conjugués ou réels à basse fréquence dans la dynamique du capteur.

Un capteur liquide a été développé pour étudier l'inclinaison du système. Le capteur permet de mesurer la rotation par rapport à la surface d'un liquide, du mercure, qui sert de référence. La sensibilité du capteur, 306.75 V/rad, ainsi que sa résolution, de l'ordre de $5 \cdot 10^{-5}$ rad/ $\sqrt{\text{Hz}}$, ont été évaluées expérimentalement. Le capteur est trop bruité parce que le mercure bouge trop avec les mouvements du sol. Pour remédier à ce problème, il faudra trouver un liquide plus visqueux mais avec des bonnes propriétés de réflectivité.

L'effet du couplage translation-rotation des capteurs inertiels sur le contrôle inertiel est étudié sur un modèle à deux degrés de libertés; lorsqu'il est contrôlé, tout le système devient couplé avec la rotation à basse fréquence. Pour remédier à ce couplage, différentes solutions ont été étudiées: projection dans un référentiel où le système est découplé (coordonnées centralisées ou valeurs singulières), contrôle en cascade avec une boucle interne qui isole le mouvement de rotation et suppression du signal de rotation du signal mesuré par le capteur inertiel. Cette étude a permis de montrer que les deux dernières propositions permettent de réduire le couplage rotation-translation quand on applique du contrôle inertiel.

Finalement, une table d'isolation hexagonale a été assemblée. Elle est supportée par trois

isolateurs et trois paires de capteurs inertiels verticaux et horizontaux sont placés dessus pour permettre le contrôle inertiel. Le système complet doit être isolé dans les six degrés de liberté. Le contrôle inertiel est appliqué au système, en tenant compte des conclusions de l'étude sur le modèle à deux degrés de liberté. La transmission des mouvements du sol a pu être réduite d'un ordre de grandeur entre 0.1 Hz et 10 Hz dans la direction verticale et entre 0.1 Hz et 1 Hz dans la direction horizontale.

Mots-clés: Contrôle inertiel – Système MIMO – Couplage rotation-translation – Capteur de rotation

Acknowledgements

First, I would like to thank Christophe Collette, my supervisor, for introducing me to the incredible world of gravitational wave detectors and this community of researchers that push the science of detection forward. I would like to thank him for proving me that we can combine experiments and models to understand how things work and improve them and for all the seismic isolation things I've learned. I would like to thank him for the amazing opportunities I had, whether for conferences or to spend three months at the LIGO Livingston Observatory.

I would also like to thank Michel Kinnaert and Simon-Pierre Gorza for patiently following my evolution and giving me advice through years. I would also like to thank the members of the jury Krishna Venkateswara and Conor Mow-Lowry for their valuable suggestions and comments on the revision of this thesis.

In addition, I would like to thank Pierre Lambert and Arnaud Deraemaeker for the discussion and time they spent to help me.

I am also grateful to the members of the LIGO Scientific Collaboration and more specifically to the people attending the seismic working group calls for their thoughtful comments and suggestions. This thesis has been assigned the LIGO document number LIGO-P2100451.

The life in the lab wouldn't have been the same without the help, support and good times we shared. For these moments spent in UC2, thanks to Vicente Lafarga, Mohit Verma, Loïc Blanc, Jean-Charles Larrieu, Binlei Ding, Guoying Zhao, Thomas Dehaeze, Ahmad Paknejad, Dimitri Piron, Sophie Gernay, Youness Tourtit, Adam Chafaï, Franco Pina, Loïc Amez-Droz, Matéo Tunon de Lara Ramos, Haidar Lakkis, Anthony Amorosi, Clément Rigaut, Cédric Dumoulin, Shashank Pathak.

I would like to thank the members of the technical staff that helped me manufacturing parts and solve all the technical issues met: Geoffrey Vanbienne, Michel Osee, Axel Dero, Jean Salvatore Mele, Patrizio Madau. In addition, I have a special thought for the administrative staff that helped me navigate through the ocean of administrative procedures that you meet when working in a university: Ariane Ducornez, Anne-Cécile Muffat, Natascha Vander Heyden, Laure Bodenghien.

I also have to thank the interns and master students I had the chance to supervise: Christophe Becel, Eloise Lintanf and Ignacio Sanchez Casanova.

I would like to mention the amazing people I had the chance to work with when I was a teaching assistant: Robin De Garnier, Matthieu Arnhem, Virginie Lecocq and Robin Wilmart, it was a pleasure working with you. I also think about the teaching assistants with whom we

shared our personal teaching experience: Quentin Delhayé and Adrien Debelle. In addition, thanks to Nicolas Englebert for the phase noise discussions.

Moreover, I would like to thank Sam Cooper and Christopher Collins for the discussions and collaboration regarding interferometric readouts.

Thanks to the amazing people I had the chance to spend three months with at the LIGO Livingston Observatory: Arnaud Pelé, Huyen Pham, TJ O'Hanlon, Marie Kasprzack, Karla Ramirez, Joe Hanson, Adam Mullavey and Matthew Heinze.

To my family and friends, thanks for the support and the joy you bring me everyday. Finally, I would like to thank all the construction work in the building that starts at the beginning of my last year of PhD and helped me to prove the robustness of the isolation system when a jack hammer is working 3 floors above my experiment. Thank you so much for making me start again several long time measurements. A special thank to the bump in the street right next to the lab that allows me to sense every delivery and construction truck that was passing by.

The research presented in this manuscript has been possible thanks to the Fonds de la recherche scientifique (FRS-FNRS) through a FRIA grant given to Jennifer Watchi.

Acronyms

ADC analog to digital conversion.

ASD amplitude spectral density.

BRS beam-rotation-sensor.

CLIC Compact Linear Collider.

COK center of stiffness.

COM center of mass.

CPS cumulative power spectrum.

d.o.f. degree-of-freedom.

DAC digital to analog conversion.

DAQ data acquisition system.

FBG fiber Bragg grating.

FEM finite element model.

FRF frequency response function.

GAS geometric anti-spring.

HINS horizontal inertial sensor.

KAGRA Kamioka Gravitational Wave Detector.

LHC large hadron collider.

LIGO laser interferometer gravitational-wave observatory.

LQG linear-quadratic gaussian regulator.

LQR linear-quadratic regulator.

MIMO multiple input/multiple output.

NLNM new low noise model.

PSD power spectral density.

PZT piezoelectric transducer.

RGA relative gain array.

RIN relative intensity noise.

RMS root mean square.

SISO single input/single output.

SVD singular value decomposition.

TF transfer function.

ULB Université libre de Bruxelles.

VINS vertical inertial sensor.

Contents

Introduction	1
1 Seismic Isolation Review	9
1.1 Ground motion	9
1.2 Passive isolation	11
1.2.1 Suspensions	13
1.2.2 Ways to reduce the resonance frequency	14
1.2.3 Limitations	19
1.3 Active isolation	20
1.3.1 Working principle	20
1.3.2 Sensors in feedback loop	21
1.3.3 Controllers	25
1.3.4 Platforms from the literature and commercial products	28
2 Interferometric readout	31
2.1 Working principle	32
2.2 Review of compact interferometers	33
2.2.1 Small range interferometers	34
2.2.2 Large range interferometers	35
2.2.3 Quadrature signals carried by the polarization states	36
2.2.4 Linearity of Phasemeters	41
2.2.5 Summary	47
2.3 Readout model	49
2.3.1 Description of the readout	49
2.3.2 Identification of the sources of noise	50
2.3.3 Description of the readout model	57
2.3.4 Comparison with experimental data	59
2.3.5 Noise budgeting	61
2.4 Resolution of the inertial sensor	62
2.5 Summary	64
3 Inertial and liquid sensors	66
3.1 Gravity coupling in inertial sensors	67
3.1.1 Limitations for vertical control	67

CONTENTS

3.1.2	Limitations for horizontal control	71
3.2	Decoupling strategies	74
3.3	Review of tiltmeters	77
3.4	The liquid sensor	79
3.4.1	Sensitivity	80
3.4.2	Noise budgeting	82
3.4.3	Coupling study	86
3.5	Summary	90
4	Inertial control	92
4.1	Translation control	93
4.2	Translation-rotation control	95
4.2.1	Control with an ideal sensor	95
4.2.2	Inertial control	98
4.3	MIMO control	102
4.3.1	Centralized frame	103
4.3.2	Singular value decomposition	106
4.4	Coupling mitigation techniques	111
4.4.1	Cascade control	111
4.4.2	Sensor correction	118
4.4.3	Tilt subtraction	121
4.4.4	Control performance comparison	122
4.5	Summary	123
5	Experimental inertial control	125
5.1	Description of the platform	125
5.1.1	Yuanda isolators	126
5.1.2	Current amplifier	129
5.2	Identification of the system	130
5.3	Isolation	134
5.3.1	Vertical decentralized control	135
5.3.2	Horizontal decentralized control	135
5.3.3	Performance	138
5.3.4	Liquid sensor on the platform	141
5.4	Summary	142
	Conclusions and Perspectives	143
	References	149
	Appendices	167
A	Frequency content of stationary random processes	169

A.1	Power Spectral Density	169
A.1.1	The amplitude spectral density	170
A.1.2	The integrated root mean square	170
A.1.3	The transfer function	170
A.1.4	The coherence	171
B	Sensor readout	172
B.1	Optical readout	172
B.2	Electrostatic and electromagnetism readout	173
B.3	Strain readout	175
C	MIMO active isolation tables from the literature and commercial products	177
D	Singular value decomposition	181
E	Phase noise measurement methods	182
E.1	Delayed self-heterodyne measurement	182
E.2	Delayed self-homodyne measurement	183
E.3	Beat-note method	183
E.4	Comparison between the measurements methods	184
F	Plant identification of the platform: the diagonal elements	186

Thesis motivation

Over the years, the performance of commercial products and scientific instruments has been drastically improved. The most famous law characterizing this improvement is the Moore's law. This empirical law, imagined by Moore, predicts that the amount of transistor on a printed circuit will double every two years. To respect this law, several challenges and issues have been tackled. Among others, the size of the transistor had to be reduced, as a consequence, the tools used to pick and place them were redesigned. Nowadays transistors measure a few nanometers. Printing properly the thin layers to manufacture transistors is another challenge. If printed in a noisy environment, the layers are not correctly overlaid.

Similarly, many instruments have been improved over the last decades such as lithography machines (used to produce transistors) [4], atomic force microscopes [5], atomic gravimeters [6], medical imaging, and large instruments dedicated to experimental physics [7]. As most of these devices are working on Earth, the transmission of ground motion limits their performance; the resolution and accuracy can be degraded if they are not isolated properly. In addition, some devices not connected to the ground can be disturbed by their driving motor. For example, the resolution of drone cameras is limited by the transmission of the motor to the camera [8]. Space telescopes and satellites are also hindered by the space launchers when sent to space and by the driving device aligning the device during operation [1, 9, 10].

In this thesis, the isolation of science instruments from external disturbance and more specifically from ground motion is studied. In order to understand how ground motion affects the performance of scientific experiments, three examples of sensitive instruments are described: particle colliders, atomic gravimeters and gravitational wave detectors. The limitations of these equipments and the largest amplitude of motion tolerated for their proper operation are quantified.

Example 1: Particle accelerators

Nowadays, physicists struggle to unify the four fundamental laws of physics. In theory, it has been proven that some of the interactions due to these forces or between these forces can be explained by the existence of yet unidentified particles. To validate these theories, these unknown particles have to be measured and identified experimentally. This is the reason behind the development of particle colliders.

A particle collider is a modified version of a particle accelerator where two counter-propagating beams of particles are accelerated and collide against each other, see Fig. 1. The particles are accelerated because collisions at high energy, on the order of the TeV, should allow to

produce more particles. The acceleration is induced by injecting a beam of moving charged particles in an increasing electromagnetic field [11]. The deflection of the beam is controlled by a transverse magnetic field (up to 8 T in some cases [11]). The magnets used to generate the magnetic field locally are made of pairs of coils, alternating north and south magnetic poles. A magnet with one pair of poles is called a dipole and with two pairs, a quadrupole, etc.

Particle colliders can be linear or circular. For circular colliders, the deflection is imposed by quadrupoles. For example, at CERN, the large hadron collider (LHC) has a circumference of 27 km to accelerate protons to an energy of 7 TeV [11].

Note that it is not the collision itself that is measured but the particles produced by the interactions between the two beams when these products propagate through layers of sensitive detection materials.

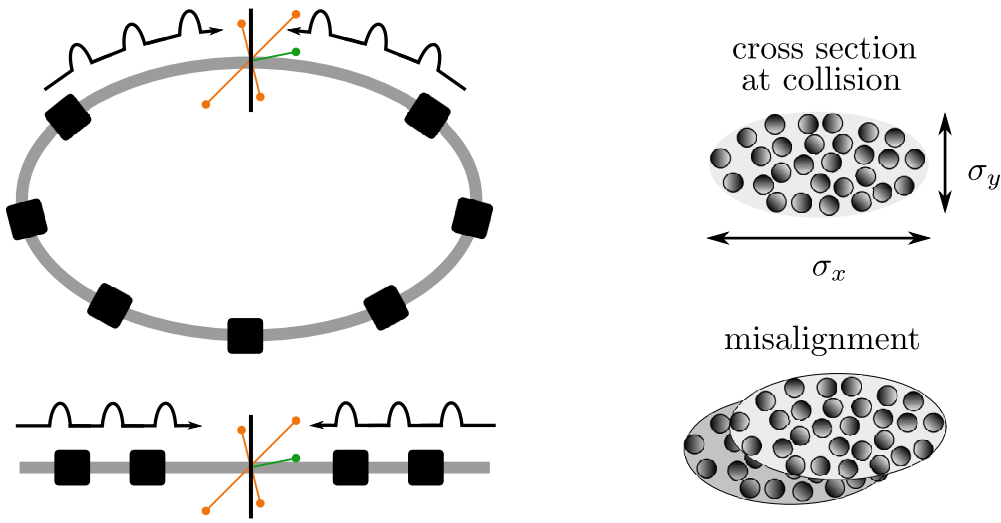


Figure 1: Illustration of a circular (top left) and linear (bottom left) particle collider. The black boxes represent the quadrupoles and dipoles used to deflect the beam. The impact point is located at the vertical line. Two counter-propagating beams made of bunches of particles are also represented. On the right the cross section of the beam is represented (top). At the bottom right, two misaligned beams are superimposed; the misalignment reduces the amount of possible collisions.

To increase the number of collisions, the beam is not a continuous beam but it is made of bunches of particles [12]. The efficiency of the collision is characterized by the luminosity L defined by [11]

$$L = \frac{fNn_xn_y}{4\pi\sigma_x\sigma_y}, \quad (1)$$

where f is the frequency of collisions of the particle bunches;
 N is the number of bunches per beam;
 n_x and n_y is the number of particles per bunch of the two beams;
 σ_x and σ_y are the transverse cross sections of the beams.

For example, at the LHC, the beam cross sections, σ_x and σ_y , at the collision sites are approximately 16 μm , N is 2808, n_x and n_y are $1.1 \cdot 10^{11}$ [13], which leads to a nominal

luminosity of $10^{34} \text{ cm}^{-2}\text{s}^{-1}$.

The next generation of particle colliders, currently in development, aims at increasing the luminosity by reducing the cross section. For example the Compact Linear Collider (CLIC) is a linear collider made of two 20 km long linear particle accelerators where the beam cross section will be 1 nm x 39 nm [14]. The motion of the quadrupoles should not exceed 1.5 nm vertically and 5 nm laterally to maintain the alignment of the two counter-propagating beams [15, 16], illustrated in Fig. 1. At the collision point, the energy of the two beams will be 1.5 TeV [11].

Due to these impressive features, particle colliders are extremely sensitive to external disturbances. For example, the moon attraction is responsible of variation of the total length of the LHC of 1 mm between full moon and half moon [13]. Such variation needs to be taken into account in the measurements made on site to avoid a distortion of the results. In addition, if the magnets are subjected to external disturbances, the beams are deflected and there is a loss of collisions. Solutions to stabilize the quadrupoles will have to stabilize several directions and to operate in harsh environment due to the strong magnetic fields of the quadrupoles.

Example 2: Absolute gravimeters

An absolute gravimeter is an instrument which measures the local fluctuations of gravity. This local measurement is of interest for applications like inertial navigation [6] or for fundamental physics. In fact, the definition of the attractive force F_g between two bodies of mass m_1 and m_2 separated from a distance r is given by

$$F_g = -G \frac{m_1 m_2}{r^2}, \quad (2)$$

where G is the gravity constant.

The gravity constant G is set to $6.674 \cdot 10^{-11} \text{ m}^3 \text{ kg}^{-1} \text{ s}^{-2}$ but this value has an uncertainty of 100 ppm which is much higher than any other physical constant [6].

On Earth, the gravitational field is defined by $g = GM_{\oplus}/R_{\oplus}^2$ and is approximately 9.85 m/s^2 , where $M_{\oplus} = 5.9 \times 10^{24} \text{ kg}$ is the Earth mass and $R_{\oplus} = 6.37 \text{ km}$ is the Earth radius.

The gravitational field can be measured on Earth by dropping a mass and measuring its time of flight on a known distance.

In some absolute gravimeters, the falling mass is not an object but a cloud of neutral atoms forming a matter-wave bunch. In this case, the device is called an atomic gravimeter. The atoms used are often Cesium [17] or Rubidium [18, 19].

The atoms are split in two groups and propagate on two different paths before they recombine thanks to a series of Raman transitions [6], similarly to an optical Michelson interferometer. A Raman transition changes the internal state of the matter-wave and its direction of propagation thanks to a momentum transfer from a standing wave to the atoms. The distance traveled by each state of matter-wave is modulated by gravity. Therefore, the interference between the two clouds of matter-wave allows to measure the gravity.

Current absolute atomic gravimeters have a resolution between 50 nm/s^2 and $1 \mu\text{m/s}^2$ when measured in laboratories [20]. However, when used for gravity surveys, their resolution is limited by the transmission of ground motion [20] and is between $1 \mu\text{m/s}^2$ and $10 \mu\text{m/s}^2$ [21]. Some gravimeters are isolated from the ground motion in the vertical direction which is the most critical direction [19, 22, 23]. However, most of the devices are not isolated from the horizontal motion and the tilt that can be coupled to the vertical direction. It has been demonstrated in Ref. [2] that the vertical motion of the gravimeter has a sensitivity to horizontal ground motion of 0.01. The coupling can increase by a factor of ten between 0.5 Hz and 1 Hz.

The effect of tilt on the gravimeter is illustrated in Fig. 2. A mass is dropped from a known height h . If the gravimeter is perfectly aligned with gravity, the time of flight measured allows to measure accurately the gravity. However, if the gravimeter is tilted, the distance traveled by the mass h' is reduced which will lead to an overestimation of the gravity constant. The spurious inclination is due to the transmission of seismic motion to the gravimeter. Similarly to particle accelerator, the performance of gravimeters is limited by the transmission of ground motion.

Note that the only atomic gravimeter that is isolated in the three directions has reached the best resolution so far which is $7.5 \cdot 10^{-10} \text{ g}/\sqrt{\text{Hz}}$ at 1 Hz [2] which corresponds to a resolution below 10 nm/s^2 .

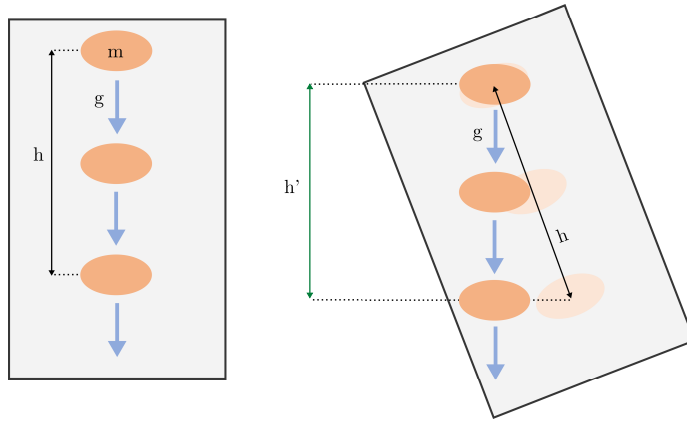


Figure 2: Exaggerated effect of the rotation of the absolute gravimeter from the gravity direction on the distance of flight traveled by the falling mass. The distance h' is reduced in comparison to the designed distance h which leads to an overestimation of the gravity constant.

Example 3: Gravitational waves detectors

In the beginning of the 20th century, Albert Einstein predicted that when two massive bodies interact at high speed, in order to not violate causality, gravitational waves are emitted. These waves travel at the speed of light. The propagation of such a gravitational wave through space induces a periodic dilatation and contraction transverse to the direction of propagation [24].

The Minkowsky metrics were introduced to give a description of the time and space where the Maxwell equations are independent of the inertial frame reference and are invariant by any inertial transformation [25].

In the Minkowsky space, the propagation of a gravitational wave along the z direction can be seen as a perturbation $h_{\mu,\nu}(z, t)$ of the Minkowsky metrics $\eta_{\mu,\nu}$ [26]

$$g_{\mu,\nu} = \eta_{\mu,\nu} + h_{\mu,\nu}(z, t) = \begin{bmatrix} -c^2 & 0 & 0 & 0 \\ 0 & 1 & 0 & 0 \\ 0 & 0 & 1 & 0 \\ 0 & 0 & 0 & 1 \end{bmatrix} + \begin{bmatrix} 0 & 0 & 0 & 0 \\ 0 & -h_+ & h_\times & 0 \\ 0 & h_\times & h_+ & 0 \\ 0 & 0 & 0 & 0 \end{bmatrix} \cos(\omega(t - \frac{z}{c})) , \quad (3)$$

where h_+ and h_\times corresponds to the two polarization states of the gravitational wave and ω its pulsation.

In other words, when a gravitational wave travels through a body, it distorts the body in the transverse plane to the direction of propagation; the body is periodically dilated in one direction and contracted in the other direction of the plane, as illustrated in Fig. 3.

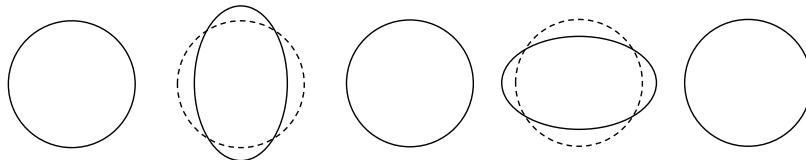


Figure 3: *Effect of the gravitational wave polarization h_+ on a body over one period inspired from [24, 26]. The wave propagates in the direction perpendicular to this page. The polarization h_\times has a similar effect but tilted of an angle 45° .*

The amplitude of the gravitational wave is proportional to the mass of the emitting body and inversely proportional to the distance between the origin of the wave and the deformed body [27]. For earthly macroscopic bodies, the amplitude of these strains is too small to be detected. Therefore, gravitational waves emitted by astrophysical events are more likely to be detected if they involve large body masses, e.g. the merger of compact binary objects like neutron stars and black holes [26].

For example, the merger of two neutron stars with a mass of $1.4 M_\odot$ in the Virgo cluster, the nearest large galaxy cluster, will generate gravitational waves with strains on the order of 10^{-21} when it arrives on Earth [28].

According to the shape of the deformation induced by a gravitation wave, the detector should be ideally sensitive to the two directions transverse to the direction of propagation. Michelson interferometers are therefore good detector candidates.

In a Michelson interferometer, a laser beam is split in two parts; each part propagates in a different arm, of length L_x and L_y . After reflection, they recombine at the beamsplitter, as illustrated in Fig. 4.a. The power measured at the photodiode P_{out} is

$$P_{out} = \frac{P_{in}}{2} (1 + \cos \phi_d) , \quad (4)$$

where P_{in} is the input power and the differential phase $\phi_d = 2k\Delta L$ is due to the difference of path length $\Delta L = L_x - L_y$ traveled by the two beams in each arm. Note that k is the wave

number.

When a gravitational wave distorts the arms of a Michelson interferometer, the power measured at the photodiode changes due to the variation of the arm length difference ΔL .

The variation of the interferometer's arm length due to a gravitational wave is extremely small as it induces a strain on the order of 10^{-21} . To increase the sensitivity to the deformation, the arms of the interferometer are long (4 km for the laser interferometer gravitational-wave observatory (LIGO) detector, 3 km for the VIRGO detector). The arm length is then artificially extended [26] by adding a second mirror in each arm of the interferometer, creating a Fabry-Pérot cavity. For the LIGO detectors, the artificial length is 1200 km [29]. To avoid that too much power from the interferometer returns to the source, a mirror is placed between the source and the beamsplitter forming a new cavity to recycle the power [28].

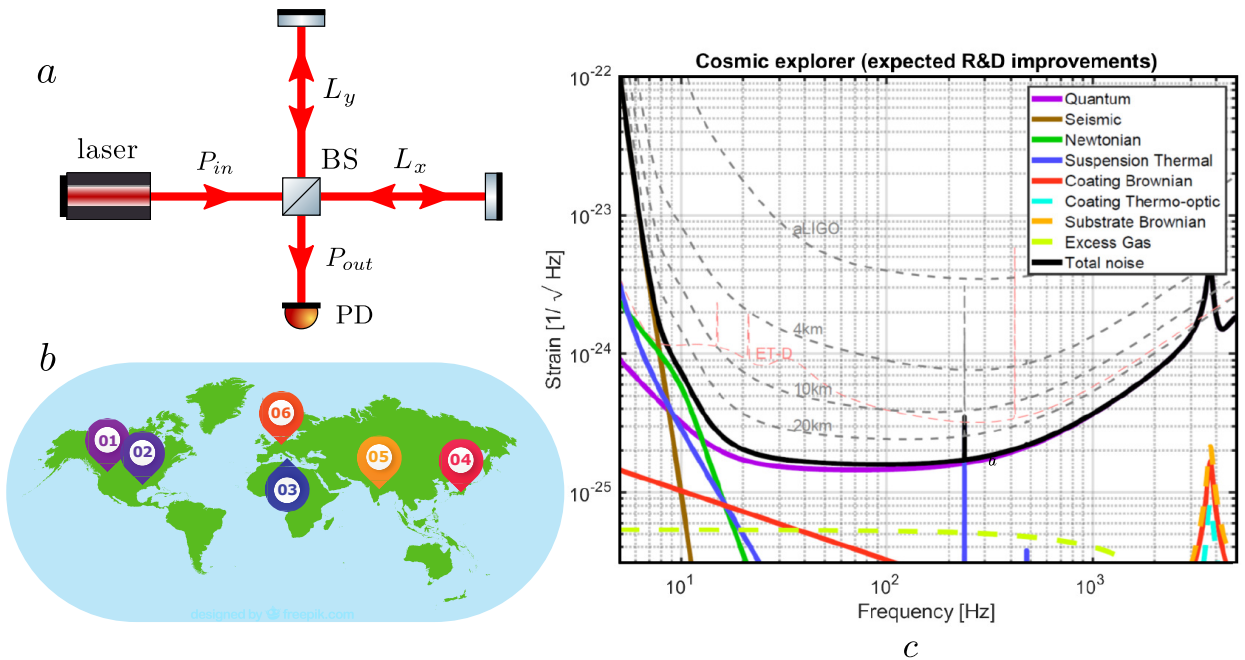


Figure 4: (a) Working principle of the Michelson interferometer [30]: the input power P_{in} is split in two parts at the beamsplitter (BS). Each part propagates in a different arm, respectively of length L_x and L_y , and is reflected by the end mirrors. The two beams recombine at the beamsplitter and the combined power is measured at the photodiode (PD). (b) Current and future gravitational wave detectors location on Earth: 1. and 2. LIGO (USA), 3. VIRGO (Italy), 4. KAGRA (Japan), 5. IndIGO (India) and 6. Einstein Telescope (Europe). (c) Sensitivity of the current LIGO detector (higher grey dashed curve), designed sensitivity of the Einstein Telescope (red dashed curve) and sensitivity of the next generation of detectors with different arm length (other grey dashed curves) [31]. The solid black curve corresponds to the designed sensitivity of a 40 km arm length interferometer.

Gravitational wave detectors based on the Michelson interferometer principle have been developed during the last decades, see Fig. 4.b. The continuous improvement of the instruments' resolution has led to the first detection recently. In 2015, the two interferometers of the LIGO detector, located in two different places in the USA, detected a gravitational wave emitted by the merger of two black holes for the first time [32]. In 2017, the VIRGO detector, located in Italy, joined the observation runs of LIGO and they measured for the first time the gravitational wave emitted by the merger of two neutron stars the same year [33].

New detectors are currently developed. The Kamioka Gravitational Wave Detector (KAGRA), located in Japan, will soon join the three other detectors during the observation runs. In addition, the IndIGO in India and the Einstein Telescope in Europe plan to have a working gravitational wave detector for the next decade.

The Einstein telescope consists in three nested pairs of gravitational wave detectors built about 200 m underground [34]. To improve by a factor 10 the detection performance of the current instruments, one pair of detector is made of one detector dedicated to measure low-frequency information between 2 Hz and 40 Hz, the ET-LF, and one for high frequency observation, the ET-HF. To cope with thermal fluctuations limiting the resolution in the low frequency domain, the ET-LF is operating at cryogenic temperature. At high frequency, to reduce the effect of fluctuation of the laser intensity, high power laser source is injected in the ET-HF detector.

The sensitivity of the future instruments is shown in Fig. 4.c. This figure illustrates the frequency bandwidth where the disturbances are sufficiently rejected or have a sufficiently low amplitude. Below 10 Hz, the transmission of ground motion is clearly the limiting contribution.

The reduction of the transmission of ground motion at low frequency is of critical importance for the future of gravitational wave astronomy [35]. Among other benefits, a good sensitivity at low frequency allows to detect events earlier, and send warnings to point electromagnetic telescopes in specific directions for multi-messenger astronomy. Another advantage is that the detector will detect more events and events involving heavier masses, up to a few thousand solar masses [36].

From the three examples provided, the effect of the transmission of ground motion to scientific instruments can be summarized as follows: Ground motion indeed limits the resolution of the detectors. This transmission is usually larger in the sub-Hz frequency band. Ground motion is transmitted to all degrees of freedom (d.o.f.) of the instrument and hence, all directions have to be isolated to reduce coupling between directions.

Thesis outline

In this thesis, an active isolation platform is developed to reduce the transmission of ground motion by a factor 100 in the 6 d.o.f. between 10 mHz and 10 Hz. This corresponds to the bandwidth where ground motion limits the performance of gravitational wave detectors. The system has to address several challenges. For example, there exists no commercial sensor that offers a sufficient resolution in the sub-Hz domain. Therefore, to reach the requirements, there is a need to develop new sensors.

To present the different steps that lead to the development of the isolation platform, this thesis is organized as follows. First, the working principle of isolation systems is described in chapter 1. A review of existing platforms is included which highlights the lack of performance in the low-frequency domain. The sensors developed to meet the requirements are characterized in the next chapters: vertical and horizontal inertial sensors in chapter 2 and a liquid sensor in chapter 3. The effect of inertial sensors on the control of MIMO systems and on decoupling methods is then studied on a 2 d.o.f. model in chapter 4. Solutions to cope with this limitation

are studied. Finally, the 6 d.o.f. experimental platform is presented and an experimental validation of inertial control is conducted in chapter 5.

Original contributions

This thesis presents the first 6 d.o.f. active isolation platform controlled using inertial sensors with an interferometric readout. It provides the tools to understand and test numerically and experimentally this 6 d.o.f. inertial control. This includes:

- The numerical model, based on Jones matrices and the different sources of noise of the interferometer, to study and understand the resolution of interferometers.
- The model made with the *Simscape* library from Matlab to study the dynamics of inertial sensors in the gravity field.
- The analytical model to study the impact of gravity coupling on inertial control and solutions to mitigate this coupling.
- The development and characterization of a liquid sensor and the identification of the maximum sensitivity to translation of a tiltmeter that can be integrated in a solution to deal with the tilt-translation coupling of inertial sensors.
- The description and control of a 6 d.o.f. active isolation platform and the prediction of the performance with a *Simscape* model.
- The experimental validation of active seismic isolation using six interferometric inertial sensors.

Chapter 1

Seismic Isolation Review

Contents

1.1	Ground motion	9
1.2	Passive isolation	11
1.2.1	Suspensions	13
1.2.2	Ways to reduce the resonance frequency	14
1.2.3	Limitations	19
1.3	Active isolation	20
1.3.1	Working principle	20
1.3.2	Sensors in feedback loop	21
1.3.3	Controllers	25
1.3.4	Platforms from the literature and commercial products	28

The transmission of ground motion and other disturbances limits the performance of sensitive equipments. Therefore, solutions to mitigate this transmission have been developed for decades. The working principle of these solutions is presented here.

Ground motion and many others disturbances, such as environmental perturbations, are random processes. To study the frequency content of this type of signals, one can use the power spectral density (PSD). Reader non familiar with this unit can go to appendix A for a detailed definition of the quantities used in this thesis. As explained, instruments on Earth are affected by ground motion. Therefore, this chapter will start by a description of ground motion and the order of magnitude of this disturbance. By comparison with the allowed motion of the sensitive instruments, one will understand why ground motion limits performance.

1.1 Ground motion

The exact frequency content of the ground motion depends on the site where it is measured. However, despite some differences, the ground motion amplitude spectral density (ASD) has a general shape that can be explained thanks to the phenomenons that dominate the following frequency bands [28, 37]:

1.1. Ground motion

- Below 0.1 Hz: earthquakes and tide strains caused by Earth-Moon-Sun interactions, atmospheric pressure fluctuations
- Between 0.1 Hz and 1 Hz: microseismic activity
- Above 1 Hz: human activity

Microseismic activity: The motion of water waves in large bodies of water such as seas and oceans is responsible for two peaks in the ASD of ground motion. The primary peak, around 75 mHz, is smaller than the secondary peak at 0.15 Hz, except in case of earthquake [38, 39]. The secondary peak corresponds to the beat frequency resulting from the interaction of two counter-propagating waves in the ocean. Microseismic peak has an amplitude on the order of $10^{-6} \text{ m}/\sqrt{\text{Hz}}$, hence its name, micro-seismic.

Human activity: Transportation, construction site or farming among others are human activities responsible for the ground motion above 1 Hz. As these motion are anthropogenic, the motion above 1 Hz varies a lot from one place on Earth to another.

Wind: In addition to these sources of motion, the wind plays also an important role. At high frequency, gusting winds can move buildings and trees. In the low frequency region, the wind tilts the sensors which affects their performance as discussed later.

To illustrate these features, the ASD of ground motion is measured in the lab at the Université libre de Bruxelles (ULB) campus in December 2016 using a seismometer, the Guralp CMG-6T, see Fig. 1.1. On this figure, the microseismic peak is visible. In addition, the human activity is clearly dominant above 1 Hz.

For comparison, the ground motion measured in the LHC tunnel at CERN is shown on the same figure. The LHC tunnel is located 100 m underground and far from human activity. Therefore, the microseismic peak is similar to the one observed at ULB but the amplitude of the motion due to human activity is drastically smaller.

Depending on the location on Earth, it is thus possible to reduce the amplitude of the ground motion of one order of magnitude above 1 Hz. However, some of the applications presented in the introduction require a rejection of the ground motion of several orders of magnitude which is not feasible by moving the equipment on a quieter location. In addition, the working frequency range can be in the sub-Hz domain where ground motion can not be reduced.

To reach these requirements, the solution consists in placing the sensitive equipment on an isolation platform. An isolation system can be basically seen as a table that reduces the transmission of any external disturbance coming from the attachment point of the legs of the table to the equipment placed on the table.

Isolation systems can be of two types: passive and active. Their working principle are detailed hereafter.

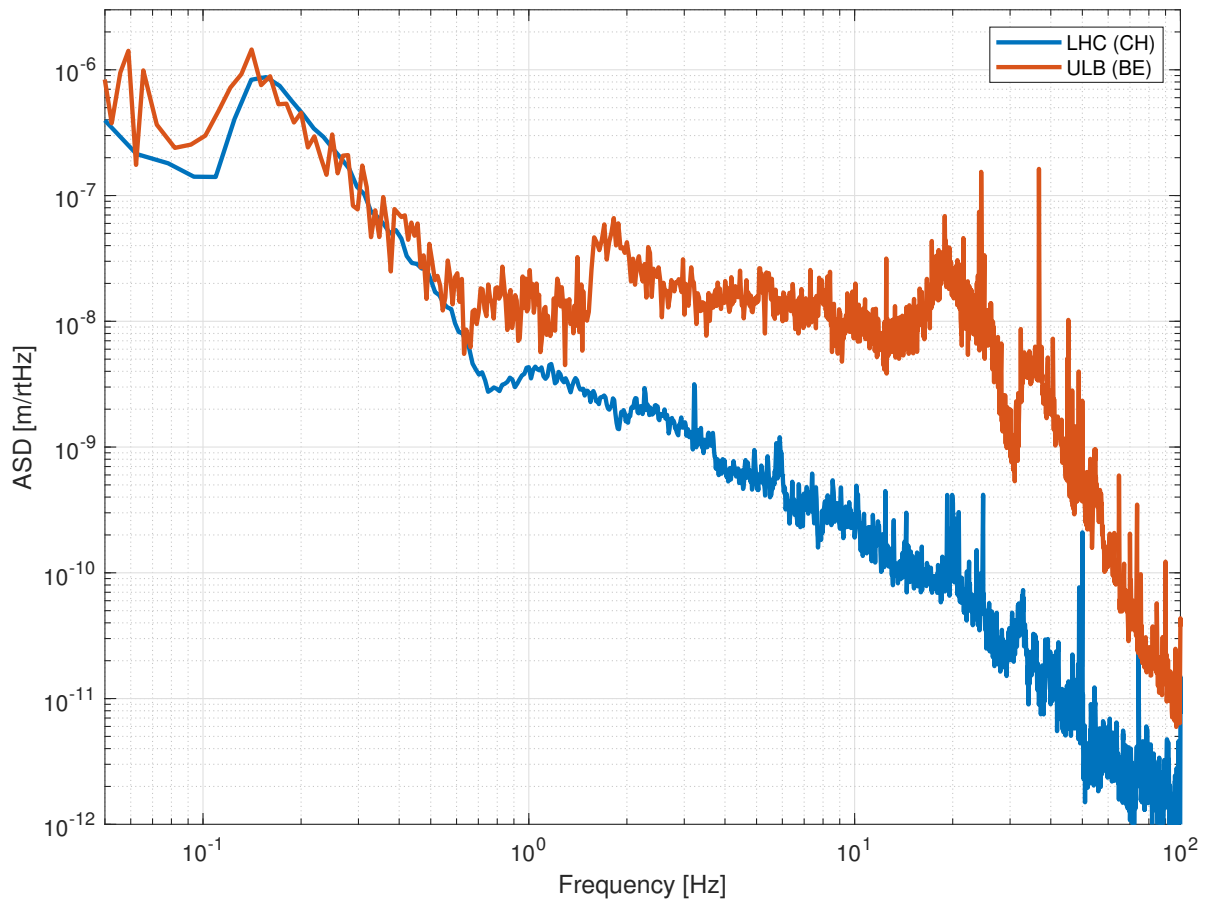


Figure 1.1: ASD of the ground motion measured in the lab on the ULB campus (red) and in the LHC tunnel at CERN (blue). The microseismic peak at 150mHz and human activity above 1Hz are visible in the spectra.

1.2 Passive isolation

To understand the working principle of passive isolation, a 1 degree-of-freedom (d.o.f.) system is represented in Fig. 1.2. The ground motion w is transmitted to the body of mass m through the spring of stiffness k . The motion of the body is given by the variable x . In addition, an external disturbance f_d is applied to the body.

For sake of simplicity, the only form of damping c considered in the rest of this document is a damping force proportional to velocity, similarly to viscous damping. In fact, damping represents the energy loss or energy dissipation in the stage. For each different form of damping, it is thus possible to find an equivalent velocity dependent term that dissipates the same amount of energy [40].

In the time domain, the equation of motion of the system can be derived using Newton's second law

$$m\ddot{x} = k(w - x) + c(\dot{w} - \dot{x}) + f_d . \quad (1.1)$$

Using the Laplace transform, the equation of motion becomes

$$ms^2X = k(W - X) + cs(W - X) + F_d . \quad (1.2)$$

1.2. Passive isolation

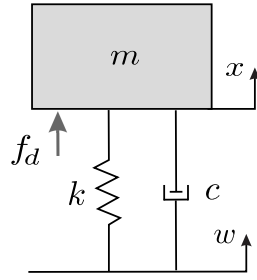


Figure 1.2: Illustration of a 1 d.o.f. passive isolation system. The motion of the ground w is transmitted to the motion x of the body of mass m through the spring k and the energy loss of the system is characterized by the damper c . An external force f_d applied to the body is also represented.

From Eq. (1.2), the transfer function between the motion of the mass m and the external disturbance F , called the compliance, is obtained

$$\frac{X}{F_d} = \frac{1}{ms^2 + cs + k}. \quad (1.3)$$

In addition, the transfer function between the motion of the mass m and the ground w , called the transmissibility, can be deduced

$$\frac{X}{W} = \frac{cs + k}{ms^2 + cs + k}. \quad (1.4)$$

The frequency response function (FRF) can be deduced from Eq. (1.2) by substituting s by $i\omega = i2\pi f$.

At low frequency, the transfer function tends to the frequency-independent term. This constant is called the static gain. In the case of the transmissibility, the static gain is 1 which means that the DC ground motion is fully transmitted to the body.

The frequency corresponding to a minimum of the denominator term is called a resonance frequency. In an undamped system, the resonance frequency is simply $\sqrt{k/m}$. At the resonance frequency, the system amplifies the amplitude of the transfer function, i.e. the motion of the table is amplified. This amplification is limited in practice because part of the energy corresponding to the resonance is dissipated by the damping.

Finally, at high frequency, the higher order term of the numerator and denominator dominates the transfer function. In the case of the transmissibility, the ms^2 term at the denominator is responsible for a $1/s^2$ slope that is generally called the roll-off. Regarding the compliance, a first order term dominates the numerator at high frequency and the roll-off has a $1/s$ slope.

The transmission of disturbance is reduced in the roll-off frequency-band above the resonance frequency. Above the resonance frequency, we can say that the payload is isolated. To have more isolation and increase the roll-off, passive systems can be put in series [41–43].

Passive isolation stages are of interest for applications where the payload has to be isolated at frequencies above a few hertz. In fact, it becomes difficult to reduce the resonance frequency to the sub-Hz domain as presented in the next sections.

In addition, passive isolation is a solution for applications where the weight carried is limited or when there is no power supply available. The isolation of satellites from the space launcher

is a good example of a sensitive instrument that needs to be isolated in such conditions [44,45]; During the launch, the instrument can be damaged and its lifetime reduced if the transmission of the launcher disturbances is not reduced sufficiently. However, the isolation system cannot weight too much as any extra weight launched to space is at a high cost. One solution consists in supporting the satellite with several lightweight flexures or springs [44].

The next sections present the suspensions used in passive systems, ways to reduce their resonance frequency and their limitations. The damping mechanisms are not described here. Damping can be achieved by elastomers and fluid dampers among others [46].

1.2.1 Suspensions

The suspensions used in a passive isolation stage can be of different types: coil springs, air springs or pads [37,47].

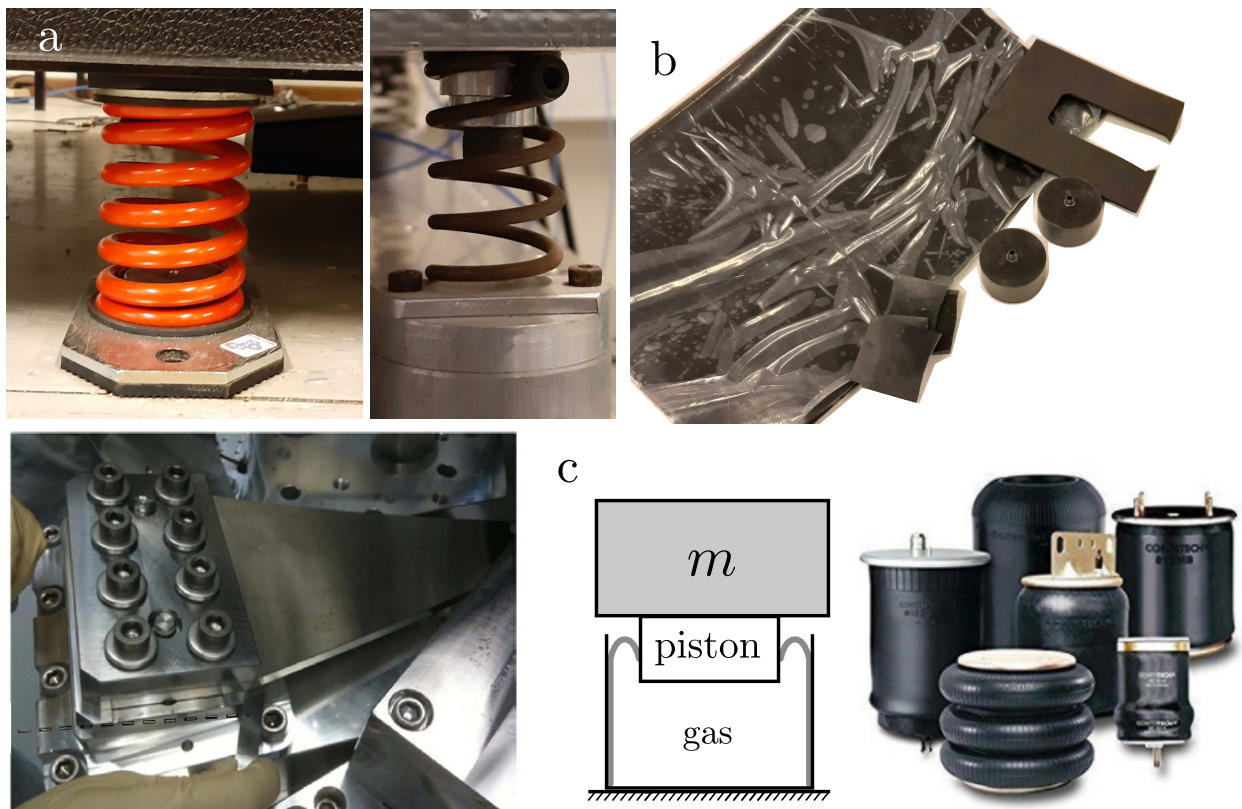


Figure 1.3: Picture of the different types of suspensions. (a) Different sizes of coil springs and the blade spring used in the LIGO suspensions [48]. (b) Pads can be found in layers that can be cut to fit the shape of the payload or as small cylindrical feet to place under a table. (c) Air springs consists in a gas enclosure whose upper side is made of a piston supporting the payload.

- Elastic springs

Elastic spring such as coil springs, see Fig. 1.3.a, is a widely used type of spring. The mechanism is generally made of metal but it can be made in other materials such as fused silica to

1.2. Passive isolation

reduce the damping coefficient [49].

The shape of the springs can be designed by taking into account the free and the constrained d.o.f. of the system [50]. During the design, one should also pay attention to the extension or compression of the spring's length due to the static load supported by the spring. These springs have a high Q-factor hence some damping mechanisms, such as rubber pads, can be added in parallel to increase the damping of the resonances. In addition, they have a linear stiffness over their working range. The resonance frequency of such platforms is usually between 1 Hz and 8 Hz.

- Air springs

An air spring is made of a gas enclosure with its upper side made of a piston on which the payload is placed, see Fig. 1.3.c. Inside the air spring, the air is compressed to the required pressure to support the load. A membrane connects the piston to the rest of the enclosure to permit the mobility of the piston while avoiding gas leakage.

The resonance frequency is between 1 Hz and 5 Hz. The damping in air springs is due to the frictions between the piston and the enclosure and to the motion of the gas molecules.

Due to the fluctuation of environmental conditions and leakage of the fluid, a self-leveling system is often required to maintain the height of the stage.

Air springs are commonly used to lift optical tables; the experiment is then floating on air. These springs are suited for long term experiments that do not evolve fast with time. Due to the size of the enclosure and piston systems, air springs are not convenient to support small masses of a few grams.

- Pads

In addition to their stiffness, pads have higher damping properties than coil and air springs. Pads are made of elastomeric material such as rubber or neoprene. They can be stacked and used as legs to support a payload or can be used as layers, as shown in Fig. 1.3.b. They are mostly used under compression and have a resonance frequency between 5 Hz and 30 Hz. However, pads exhibits creep with time which increases the resonance frequency. Therefore, pads are not recommended for precision alignment applications [47].

Table 1.1: *Properties of the different types of suspensions.*

	Resonance frequency	Q-factor	Load
Elastic springs	1-8 Hz	> 100	From a few grams to several tons
Air springs	1-5 Hz	~ 10	from 25 kg to 50 10^3 kg
Pads	5-30 Hz	~ 1	From a few grams to several tons

1.2.2 Ways to reduce the resonance frequency

A passive isolation stage reduces the transmission of external disturbance at frequencies larger than its resonance frequency. Therefore, the lower the resonance frequency, the larger the isolation bandwidth can be.

In a spring-mass system, the resonance frequency can be reduced by increasing the mass or

reducing the stiffness. However, the mass cannot be increased arbitrarily. Moreover, if the stiffness is reduced too much, it will not be able to support the mass of the payload and it will sag.

To reduce the resonance frequency and increase the isolation bandwidth, negative stiffness mechanisms or sag compensation methods can be implemented. However, sag compensation methods such as using a leaf-spring to compensate gravitational force cannot be applied to large massive bodies like isolation platforms. Different methods developed to reduce the stiffness for the horizontal and the vertical directions are presented hereafter.

Mechanisms for the horizontal direction

Pendulums are often used as passive systems in the horizontal direction. The resonance frequency can be evaluated using the equation of motion and considering small motion [51]

$$m\ddot{x} = -mg \sin \theta \approx -mg\theta \quad (1.5)$$

$$ml\ddot{\theta} = -mg\theta, \quad (1.6)$$

where m is the mass of the pendulum, l its length;

x the motion of the pendulum w.r.t. the horizontal axis;

θ is the angle between the pendulum and the vertical axis, see Fig. 1.4.

Taking the Laplace transform of Eq. (1.6) we can see that the resonance frequency of the pendulum is

$$\omega_0 = \sqrt{\frac{g}{l}}. \quad (1.7)$$

The resonance frequency is thus independent of the mass supported by the pendulum. In comparison to the resonance frequency of a mass spring system where the larger the mass, the smaller the resonance frequency, here, a small resonance frequency can be obtained when supporting a light payload.

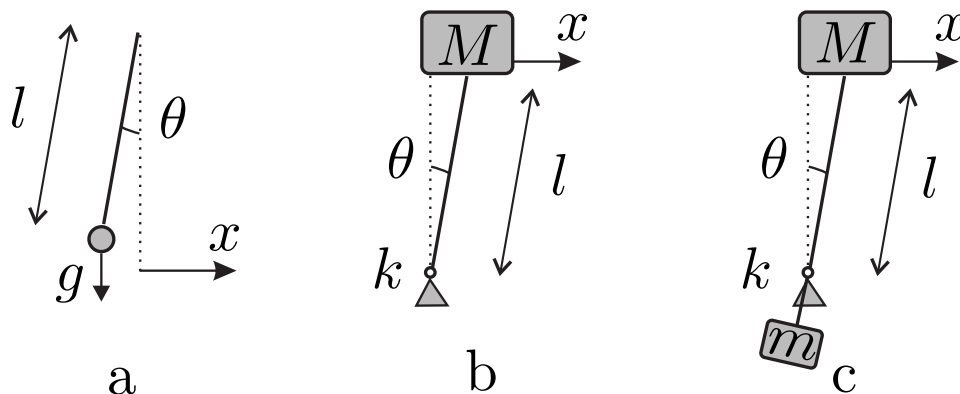


Figure 1.4: (a) Pendulum of mass m and length l whose motion is characterized by the angle θ and the horizontal displacement x . (b) Inverted pendulum of length l supporting a payload of mass M . The stiffness of the elastic joint is k . (c) Counterweight of mass m used to adjust the position of the center of percussion of the inverted pendulum.

As explained in the applications section, gravitational wave detectors need to be isolated below 1 Hz. If we want to isolate the horizontal direction with a pendulum and have some

1.2. Passive isolation

performance at 0.5 Hz, we need a passive system with a resonance frequency smaller than 0.5 Hz. However, to have a resonance frequency at 0.1 Hz, the pendulum has to be 24 m long. In practice, the pendulum should be even longer if we want to have a good isolation level at 0.5 Hz.

To overcome this limitation, one can replace a pendulum by an inverted pendulum.

- Inverted pendulum

As illustrated in Fig. 1.4.b, a payload of mass M and inertia I can be supported by an inverted pendulum of length l connected to the ground by an elastic joint represented by the stiffness k . The equation of motion of the system for small displacements ($\sin \theta \simeq \theta$) is [52]

$$I\ddot{\theta} = -k\theta + Mgl\theta . \quad (1.8)$$

By rearranging the terms, we can see that the effective stiffness is reduced

$$k_{eff} = k - Mgl . \quad (1.9)$$

In an inverted pendulum, the gravitational force acts as an anti-spring. Hence, for small displacements, the resonance frequency is reduced assuming that $x = l\theta$ and $k_x = l^2k_{eff}$ in $m\ddot{x} = -k_x x$.

The center of percussion of a body is a point that doesn't undergo any acceleration (rotation nor translation) when the body is excited [53]. If the center of percussion of the inverted pendulum is located at the height of the joint, when exciting the beam at high frequency at the joint, the other end of the inverted pendulum does not move. On the contrary, if the height of the center of percussion does not corresponds to the height of the joint, the beam will rotate around de center of percussion and the upper end of the inverted pendulum moves at high frequency and Eq. (1.9) is not valid anymore [52]. In order to place the center of percussion at the height of the joint, a counterweight is placed with a mass equivalent to the mass of the pendulum's leg [53], as illustrated in Fig. 1.4. The counterweight is equivalent to a pendulum. This results in having an inverted pendulum combined with a pendulum.

Inverted pendulums are used in different ways to support a payload. Either several inverted pendulums are placed in parallel, or they are combined with a pendulum, or both.

Three inverted pendulums are placed in parallel in [54, 55] to serve as the horizontal pre-isolator of the VIRGO detector with a resonance frequency of 30 mHz. To support a mass of 1 ton, the three inverted pendulums have a length of 6.18 m and a base stiffness of 566 N/m each [].

A combination of a pendulum and an inverted pendulum has been validated experimentally to isolate both horizontal directions [57]. The resonance frequency of the system developed can be below 1 Hz. In addition, this combination has been used in a horizontal inertial sensor to support the proof mass and have a sensor with a sub-Hz resonance frequency [58]. The configuration used in the sensor is known as the Watt's linkage which is one type of combination among others presented in [53].

Mechanisms for the vertical direction

- Anti-springs

By fixing two bars free to move horizontally to the tip of a vertical spring and loading them in compression, an additional negative stiffness k_N is added, as illustrated in Fig. 1.5. The stiffness k_N is obtained by first evaluating the contribution to the vertical force of the two compression forces

$$F_N = -2F \tan \theta , \tag{1.10}$$

where θ is the angle between the horizontal axis and the bar.

Using the definition of the stiffness, knowing the force F_N and the vertical displacement $L \sin \theta$, the negative stiffness added for small displacements is [59]

$$k_N = -\frac{2F}{L} . \tag{1.11}$$

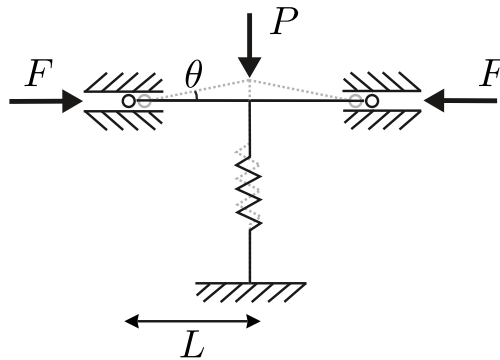


Figure 1.5: Negative stiffness mechanism for the vertical direction: two opposite forces F are compressing two bars of length L attached to the tip of a vertical spring that supports a load P . When the payload is not at equilibrium (dashed grey) and when the payload is at equilibrium (solid black).

With this mechanism, the stiffness is reduced without degrading the static load capability of the spring. Note that the two opposite forces have to be applied at the tip of the spring at the height corresponding to the equilibrium position. This position varies depending on the payload supported. Hence, the level is adjusted for a given payload.

Commercial products using the negative stiffness mechanism, like Minus K and Yuanda isolators, have a vertical and horizontal resonance frequency of 0.5 Hz.

Anti-springs mechanisms in the vertical directions can be based on different mechanical configurations [53]. For example, geometric anti-spring (GAS) filters are commonly used in gravitational wave detectors to isolate in the vertical direction. They reduce the coupling with other directions as these filters constrains the motion to a pure vertical translation [60]. GAS filters are made of an ensemble of flat triangular metallic cantilevered blades which are arranged in a circle. The payload is supported by the tip of the blades and bend them. The appropriate radial and horizontal compression of the blades are ensured by a proper

1.2. Passive isolation

clamping mechanism. The compression is important because when the platform moves vertically, the release of the radial stress in the blades is responsible for the anti-spring effect [61]. The resulting stiffness at the tip can be deduced from the mechanical properties of the blades [48, 55]. In Ref. [48], a vertical suspension made of three blades has a resonance frequency of 1.8 Hz, when supporting a table with a dummy mass of 1100 kg.

Finally, anti-springs can also be implemented using repulsive magnets [62]. One magnet is attached to the spring and the other one is connected to the ground and positioned to impose the largest repulsive force when the payload is at its equilibrium position.

- Euler buckling springs

When a load is placed on top of a vertical beam, the beam does not deflect below a critical load P_{crit} at which buckling occurs. This critical load is defined by $P_{crit} = 4\pi^2 EI/l^2$ [53], where I is the moment of inertia, E the Young modulus and l the length of the bar. In comparison to a classical coil spring, below the critical load, the spring does not store the static energy $\frac{1}{2}k\Delta x^2$ corresponding to the initial extension or compression under load Δx [63], see Fig. 1.6.a.

Fig. 1.6.b illustrates the buckling phenomenon. When subjected to a critical load P_{crit} , the beam of length l starts to deflect. It has been shown that the equivalent stiffness can be approximated when the spring is in the buckling regime by [53]

$$k = \frac{P_{crit}}{2l} . \quad (1.12)$$

Here, the critical load corresponds to the weight of the mass supported mg and hence, the resonance frequency of the system is

$$\omega_0 = \sqrt{\frac{k}{m}} = \sqrt{\frac{g}{2l}} . \quad (1.13)$$

Similarly to a horizontal pendulum, the resonance frequency is independent of the mass supported. In addition, as the static energy is not stored, the mass of the supporting beam can be reduced which allow to have internal modes with a higher resonance frequency [63, 64].

Euler springs use the buckling mechanism explained above to have a spring with a low resonance frequency. A combination of Euler springs used to support a payload in the vertical direction is shown in Fig. 1.5. The design of Euler springs is currently studied to improve the distribution of stress in the material [65].

To reduce the resonance frequency of Euler springs, they can be combined with an anti-spring mechanism [64]; the distance h between the attachment point of the Euler spring and the attachment point of the rod supporting the payload is increased, see Fig. 1.6.c. Therefore, the payload is suspended by a Euler spring and an inverted pendulum in series. Sub-Hz resonance frequencies can be obtained experimentally with this technique [64].

Note that there exist other types of springs that use buckling mechanism. Among others, the Belleville spring which is a washer with a conic profile [47].

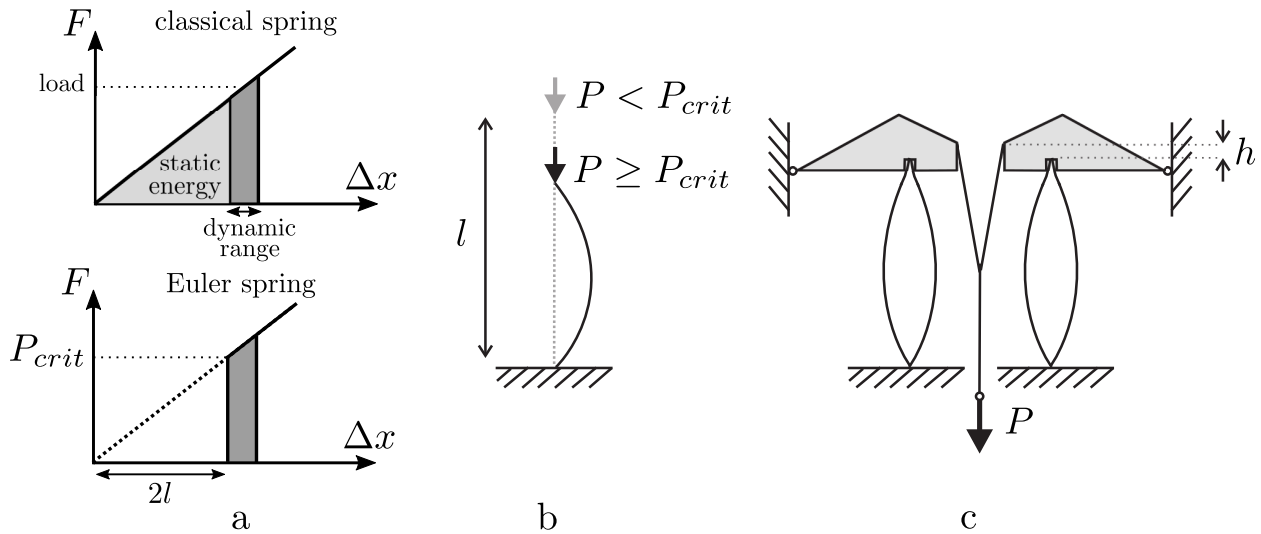


Figure 1.6: Euler springs working principle (a) Top: force-deflection graph of a classical spring. The static energy corresponding to the static deflection is stored and added to the dynamic energy of the operating range. Bottom: the Euler spring does not store static energy as the beam deflects only above the critical load P_{crit} . (b) Buckling of a beam: below a critical load, the beam does not bend (dashed grey). When the load is equal or above the critical load, the beam deflects. (c) Combination of two Euler springs used to support a load P in the vertical direction.

1.2.3 Limitations

The passive systems presented above and the solutions presented to reduce the resonance frequency are not ideal systems. Some of their disadvantages are summarized here. They demonstrate the need to develop active isolation stages if we want to reach the level of isolation required by some applications at low frequency.

First, some applications require a transportable solution. Massive air springs with pumping systems to ensure the self-leveling are thus not an option.

Second, for space applications, most of the payloads sent to space are isolated at high frequency by passive suspensions. At low frequency, the suspensions modes are amplified which can be harmful for the satellite [66].

The systems developed to reduce the resonance frequency are also limited. To reduce the resonance frequency of an inverted pendulum, the length of the pendulum or the mass of the payload can be increased. However, the length of the instrument can not be arbitrary large and one should take into account the space available. In addition, the mass of the payload can sometimes be constrained by the specification set for the platform. Indeed, if the mass is too large, the flexible modes appears at lower frequencies and can be in the performance bandwidth.

Similarly to the horizontal pendulum, to have a resonance frequency at 0.1 Hz using a Euler spring, the beam should be 12 m long. Depending on the application, a platform with such large dimensions can not be implemented in practice.

Regarding the pre-stressed anti-spring, if the force applied is too high, it becomes difficult in practice to keep the payload at its equilibrium position as the springs will not be able to

1.3. Active isolation

remain horizontal.

Note that most of the anti-springs systems are based on non-linear stiffness mechanisms which limit their linear working range.

Finally, in this section, the passive system considered is made of rigid bodies. However, real bodies are flexible and hence have some high frequency internal modes. To avoid that these spurious resonances amplify the motion, the isolation stage has to be designed in order to have these internal modes at frequencies higher than the isolation bandwidth.

1.3 Active isolation

To reduce the transmission of external disturbances to sensitive payload, one can apply a force that suppresses the motion of the payload. The isolation system is then said to be active.

The working principle of active isolation systems is introduced here. The performance on the controlled payload is studied depending on the type of sensor used to control the motion. From this comparison, the best candidate to reject external disturbances is identified. The limitations related to sensor resolution are then introduced.

The control laws and their characteristics to achieve a proper isolation are then briefly reviewed. Finally, the properties of commercial products are summarized.

1.3.1 Working principle

A 1 d.o.f. active system is represented in Fig. 1.7. By comparison with the passive system shown in Fig. 1.2, a sensor measuring the payload motion x and an actuator are added. The force injected corresponds to the signal x multiplied by a controller, represented here by the operator H .

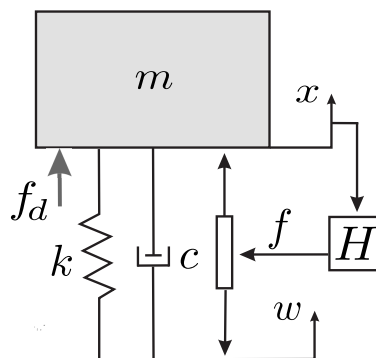


Figure 1.7: Illustration of a 1 d.o.f. active system. The motion of the ground w is transmitted to the motion x of the body of mass m through the spring k and the energy loss of the system is characterized by the damper c . A sensor measures the motion x of the body and this motion is multiplied by the controller H to inject a signal f to the actuator. An external disturbance characterized by the force f_d is also shown.

Similarly to Eq. (1.2), the equation of motion of the system can be expressed in the Laplace domain

$$(ms^2 + cs + k)X = (cs + k)W + F_d + F , \quad (1.14)$$

where F is the force injected by the actuator.

In closed loop, the interactions between the different signals can be represented with the block diagram shown in Fig. 1.8. The output y of the system G is compared to the reference to track r and the resulting error signal is used to process the signal f injected to the actuator using the controller H .

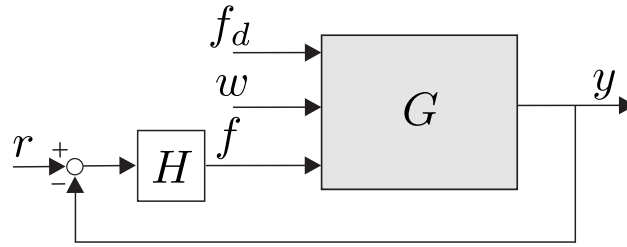


Figure 1.8: Block diagrams representing the system G whose output motion y is compared to the reference signal r . The control signal f injected to the actuator is multiplied by the controller H . The variables w and f_d are the ground motion and the external disturbance.

In order to isolate a payload from an external disturbance, the reference r of the feedback loop is set to zero. Consequently, the error tends to zero when the motion of the payload is canceled. The signal f fed to the actuator depends on the signal measured y and the operator $H(s)$. In the Laplace domain, it gives

$$F = -H(s)Y . \quad (1.15)$$

1.3.2 Sensors in feedback loop

Depending on the type of signal measured y used in the feedback loop, the performance of the active isolation stage varies. Three types of signals measured can be used: relative motion sensor, force sensor and absolute motion sensor, see Fig. 1.9. The three cases are studied hereafter to identify the best candidate to reject disturbances.

Relative motion control

When a relative motion sensor is used in an active isolation loop, see Fig. 1.9.a, the feedback force F in Eq. (1.14) becomes $F = -H(s)(X - W)$. Rearranging the terms of Eq. (1.14), we have

$$(ms^2 + cs + k + H(s))X = (cs + k + H(s))W + F_d , \quad (1.16)$$

$$X = \frac{cs + k + H(s)}{ms^2 + cs + k + H(s)}W + \frac{1}{ms^2 + cs + k + H(s)}F_d . \quad (1.17)$$

We can estimate the limits of the control loop by studying the effect of an infinite controller gain on the transmissibility (X/W) and on the compliance (X/F_d)

$$\lim_{H \rightarrow \infty} X = W \quad \lim_{H \rightarrow \infty} \frac{X}{F_d} = 0 . \quad (1.18)$$

1.3. Active isolation

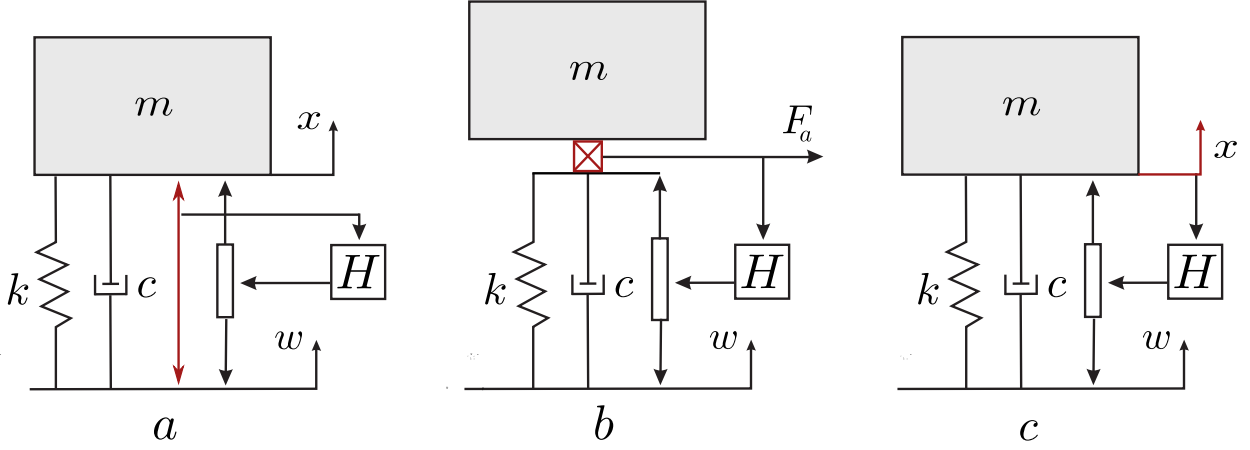


Figure 1.9: Active isolation of a 1 d.o.f. system using (a) a relative motion sensor, (b) a force sensor and (c) an absolute motion sensor in the feedback loop.

In other words, when we isolate actively with a relative motion sensor, the motion of the mass m is completely driven by the ground motion. Indeed, the feedback loop reduces the relative motion between the payload and the ground. When this quantity is canceled $x - w = 0$, it means that the motion of the payload corresponds to the ground motion $x = w$.

Force control

The force sensor measures the forces $F_a = F - (k + cs)(X - W)$ when collocated with the leg suspending and actuating the platform, see Fig. 1.9.b. The force injected to control the payload becomes

$$F = -H(s)F_a = -H(s)(F - (k + cs)(X - W)) , \quad (1.19)$$

$$F = \frac{H(s)(k + cs)}{1 + H(s)}(X - W) . \quad (1.20)$$

When injecting this feedback force in Eq. (1.14), the effect of force control can be evaluated

$$((1 + H(s))ms^2 + cs + k)X = (cs + k)W + (1 + H(s))F_d , \quad (1.21)$$

$$X = \frac{cs + k}{(1 + H(s))ms^2 + cs + k}W + \frac{1 + H(s)}{(1 + H(s))ms^2 + cs + k}F_d . \quad (1.22)$$

By setting the controller gain to infinity, the limits of the performance of force control on the transmissibility and the compliance are evaluated

$$\lim_{H \rightarrow \infty} \frac{X}{W} = 0 \quad \lim_{H \rightarrow \infty} \frac{X}{F_d} = \frac{1}{ms^2} . \quad (1.23)$$

Force control can effectively reduce the transmission of the forces measured by the force sensor. Here, the force sensor is collocated with the leg supporting the payload and hence, the spring force injected due to ground motion can be reduced. On the contrary, the force sensor cannot measure the external disturbance and hence, the compliance is not improved.

Inertial control

When measuring the absolute motion of the payload x , see Fig. 1.9.c, the feedback force f becomes $F = -H(s)X$. When rearranging the terms of Eq. (1.14), we have

$$(ms^2 + cs + k + H(s))X = (cs + k)W + F_d , \quad (1.24)$$

$$X = \frac{cs + k}{ms^2 + cs + k + H(s)}W + \frac{1}{ms^2 + cs + k + H(s)}F_d . \quad (1.25)$$

Again, the limits of the control loop are evaluated with an infinite controller gain applied on the transmissibility and the compliance

$$\lim_{H \rightarrow \infty} \frac{X}{W} = 0 \quad \lim_{H \rightarrow \infty} \frac{X}{F_d} = 0 . \quad (1.26)$$

With inertial control, the absolute motion of the payload m is reduced; The control loop achieves to reduce the transmission of ground motion and other external disturbances. To effectively reduce the motion of sensitive instruments, inertial control is thus used here. In practice, absolute motion of the payload is measured with an inertial sensor. These sensors are described in chapter 2.

Sensor limitations

Each sensor is characterized by its resolution, i.e. the smallest quantity it can measure. Below this value, the sensor signal is dominated by its noise. In a control loop, the sensor noise is injected in the system as the signal from the sensor is used to compute the actuation force.

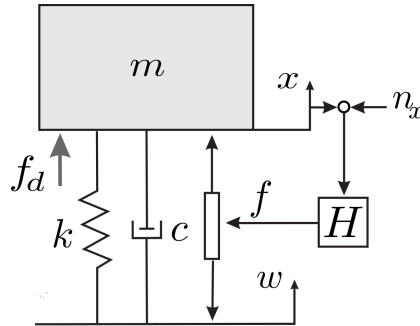


Figure 1.10: Illustration of the 1 d.o.f. active system of Fig. 1.7 when adding the sensor noise.

Let's consider the 1 d.o.f. active isolation stage shown in Fig. 1.10, the force injected when including the sensor noise n_x is

$$F = -H(x + n_x) . \quad (1.27)$$

Injecting the definition of the force and considering that the only external disturbance is ground motion, the Laplace transform of the equation of motion becomes

$$(ms^2 + cs + k)X = kW - H(s)(X + N_x) . \quad (1.28)$$

1.3. Active isolation

And rearranging the terms

$$X = \frac{k}{ms^2 + cs + k + H(s)}W - \frac{H(s)}{ms^2 + cs + k + H(s)}N_x . \quad (1.29)$$

The limitation of the control system can be estimated by considering an infinite gain of the controller

$$\lim_{H \rightarrow \infty} X = -N_x . \quad (1.30)$$

When isolating a 1 d.o.f. payload using inertial control, the payload will ultimately moves as the sensor noise. Therefore, in order to reduce the motion of the payload as low as possible, the sensor noise has to be the lowest possible.

Noise budgeting

In practice, the gain of the controller is not infinite and the sensor noise is not the only source of limitation. Each noise and perturbation source contributes differently to the total noise of the system. To identify which source dominates which frequency domain, the sources of noise are combined in a noise budgeting [67].

The noise sources taken into account come from:

- The sensor n_1 : Analog to Digital Conversion (ADC), sensor resolution;
- The amplification/actuation stage n_2 : digital to analog conversion (DAC), power amplification system;
- The ground motion itself w .

The combination of these sources of noise is illustrated here on a 1 d.o.f. model, see the block diagram in Fig. 1.11.

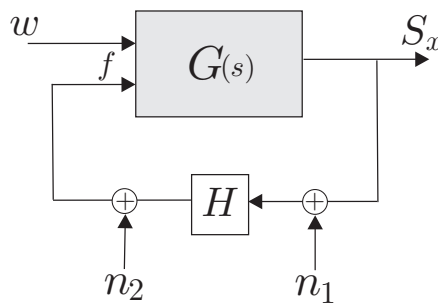


Figure 1.11: Block diagram to control the 1 d.o.f. system G . The different sources of noise are included: n_1 corresponds to the resolution of the sensor, n_2 to the amplification noise and w to the ground motion.

The sources of noise are added by summing them to the term f representing the force applied to the active isolation stage in Eq. (1.14), taking the Laplace transform

$$F = N_2 - H(s)(X + N_1) , \quad (1.31)$$

where $H(s)$ is the controller used.

The equation of motion becomes

$$(H(s) + ms^2 + cs + k)X = KW + N_2 - H(s)N_1 \quad (1.32)$$

which can be expressed as

$$X = \frac{k}{H(s) + ms^2 + cs + k}W + \frac{H(s)}{H(s) + ms^2 + cs + k}N_1 + \frac{1}{H(s) + ms^2 + cs + k}N_2 . \quad (1.33)$$

Assuming that the three sources are uncorrelated, the corresponding Power Spectral Density (PSD) of the residual motion is given by

$$\Phi_x = \left| \frac{k}{H - m\omega^2 + j\omega c + k} \right|^2 \Phi_w + \left| \frac{H}{H - m\omega^2 + j\omega c + k} \right|^2 \Phi_{n_1} + \left| \frac{1}{H - m\omega^2 + j\omega c + k} \right|^2 \Phi_{n_2} , \quad (1.34)$$

where Φ_{n_1} , Φ_{n_2} and Φ_w are respectively the PSD of the sensor resolution, the amplification stage and the ground motion. Knowing these PSD, the noise budgeting will be studied for the platforms presented here. Thanks to this study, the elements of the platform limiting the performance at each frequency will be identified.

1.3.3 Controllers

As explained in section 1.3.1, the signal measured by the sensor is used to actuate the stage and reduce its motion. There exists a large variety of control laws that can be applied to the signal measured but they can be divided into two main categories: classical control such as PID controller [50] and optimal control such as \mathcal{H}_∞ synthesis [68, 69] and linear-quadratic gaussian regulator (LQG) [70]. Depending on the requirements and the application, the control law used to process the signal will vary. However, the control law applied will always have to ensure stability and robustness of the closed loop system. These two notions are briefly introduced before explaining how to extend the control performance and how to control several directions.

Stability A stable system is a system whose motion converges to an equilibrium position [71]. Such systems are characterized by having all their poles with a negative real part. In fact, for a pole with a real part a in the system transfer function, a term of the form e^{at} appears in the impulse response of the system. If a is positive, for a bounded input, the amplitude of the output of the system diverges with time, which characterizes an unstable system. The closed loop needs to respect the same criterion. For some control laws, when increasing the gain, the poles move to the positive real axis part. For these systems, the maximum gain applicable before instability has to be determined.

Robustness Robustness is related to the capability of the system to work and to remain stable even if the platform changes (e.g. mass added to the platform) [72]. In fact, the system can be perturbed by a variation of the operating conditions or an additional payload, for example. Moreover, the model on which the control law is designed can consider a perfect alignment of the structure and of the sensors and actuators which cannot be achieved in practice. Therefore, it is needed to define a tolerance range in which the system works properly.

1.3. Active isolation

Extending the control To improve the performance, the control laws can be combined. For example, in a high authority/low authority control (HAC/LAC), a first loop is closed with a controller that simplifies the system, for example by damping some modes. A second loop is closed on the resulting system with more aggressive isolation [73]. In other systems, feedback and feedforward controls are combined to increase the performance [1, 10]. Feedforward is another type of classical controller where a sensor measures the motion of the disturbance, e.g. it is placed on the ground. This signal is then used with a plant inversion to reduce the motion of the structure to isolate.

Note that the flexible modes of the structure are often limiting the isolation performance of the isolation stage. If the gain applied to control is too high, these modes can be excited. In addition, the frequency of these flexibilities can vary which makes it difficult to control the platform.

A good practice is to design a structure with the frequency of the flexible modes at one or two orders of magnitude higher than the frequency of the suspension modes [3, 74]. The suspensions modes can then be controlled without being disrupted by the unwanted flexibilities.

With this type of system (suspension modes at lower frequency than flexible modes), sensor fusion can be used to improve the performance [75]: a low pass filter is applied to the signal of the sensor used to control the suspension modes and a high pass filter to a sensor which is robust at high frequency. Consequently, the bandwidth is increased and the gain used for the controller can be high as robustness is guaranteed by the sensor used at high frequency. A robust sensor can be for example a force sensor. Note that the high pass and low pass filter used in sensor fusion are complementary [76].

Architecture of MIMO systems

When controlling several d.o.f. in a multiple input/multiple output (MIMO) system, there is a risk that while trying to control one direction, some spurious signal is injected into another direction, see Fig. 1.12. When the signal in one direction is influenced by the signal from another direction, we say that these directions are coupled. This coupling between directions can be mitigated thanks to a careful design of the controller; the controller has to be diagonal (consider independent single input/single output (SISO) systems) and it has to be applied to a diagonal plant. In practice, this corresponds to a system with non-diagonal elements as small as possible compared to the diagonal ones.

Among others, the coupling in a system $G(\omega)$ can be evaluated by the two following indicators: the relative gain array (RGA) and the Gershgorin radius [72]. The RGA estimates for each frequency the product $G(\omega)x(G^{-1})^T(\omega)$ [68]. If the system is decoupled, all the diagonal elements λ_{ii} are equal to 1 for all frequencies [72] i.e. the RGA corresponds to an identity matrix. The Gershgorin radius evaluates for each frequency and each output, the ratio between the sum of all non-diagonal terms and the diagonal term of the system. In a decoupled plant, also said to be diagonal dominant, all Gershgorin radii are smaller than 1 [77].

If the system is not decoupled, it can sometimes be projected in a frame where it becomes decoupled, see Fig. 1.13. This implies that the matrix used to project the sensors coordinates

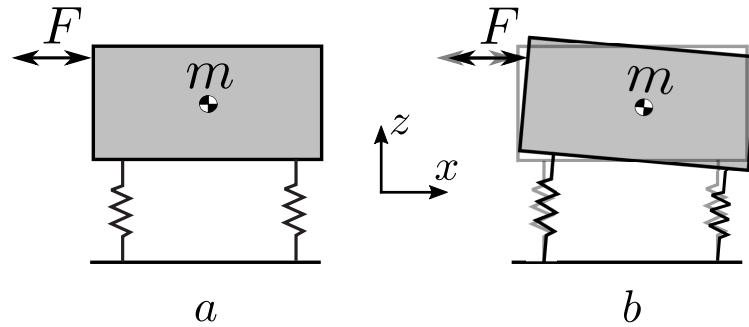


Figure 1.12: Illustration of coupling on a 2 d.o.f. system. The body (at rest in (a)) of mass m lies on a pair of springs and a horizontal force F is applied, not aligned with the center of mass. (b) When the force is applied, the body translates and rotates due to the coupling.

to the new coordinates system, called the post-compensator, and the other one used to project these new coordinates to the actuators one, the pre-compensator, have to be identified properly. The frames can be the centralized coordinates, the modal coordinates and the singular values of the system for example.

Note that the location of the sensors and actuators influences the coupling between directions and has to be carefully studied.

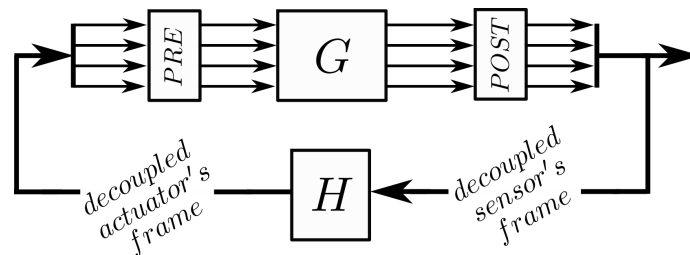


Figure 1.13: Block scheme illustrating the decoupling of the system G . A post-compensator $POST$ is applied to the outputs sensed to project the system in a decoupled frame. The controller H is applied in this frame. The signal is then projected in the actuators leg direction with the pre-compensator PRE .

Data acquisition system

If the controller is implemented digitally, the signals involved in the control loop are not continuous, they are said to be discrete-time signals. The discretization, i.e. the conversion from analog to digital signals, and vice versa has to be considered during the design of the control system, see Fig. 1.14.

First, the analog signal measured is converted into digits. The smallest quantity measurable is determined by the number of bits of the data acquisition system (DAQ). Note that in the frequency domain, the PSD of the analog to digital conversion (ADC) signal is limited by this quantity and by the sampling frequency [78]. defining the resolution of the system. Similarly, the signal injected to the actuators is converted from digital to analog using methods like the zero-order hold [71, 79]. This method holds the last sampled value during one sampling period to avoid that the signal injected in the actuator is zero between each discrete-time

1.3. Active isolation

signal injected.

Second, in a system with a digital DAQ, the controller is a digital controller. One can design an analog controller using the Laplace transform and discretizes it using different numerical approximations such as the Tustin method [79].

When designing a digital controller, a good practice is to have the control bandwidth two orders of magnitude smaller than the sampling frequency [46]. This is due to the phase delay added to the response due to the sampling period [80], i.e. the system does not respond instantly to the perturbation. The phase delay at a frequency f due to the sampling frequency f_s can be computed by

$$\theta = \frac{2\pi f}{f_s} \frac{180}{\pi} \text{ [deg]}. \quad (1.35)$$

Therefore, if the control bandwidth is small enough compared to the sampling frequency, the phase delay is not too large. Note that in practice, the phase delay is larger than Eq. (1.35) as the sensor and actuator phase delays have not been considered here.

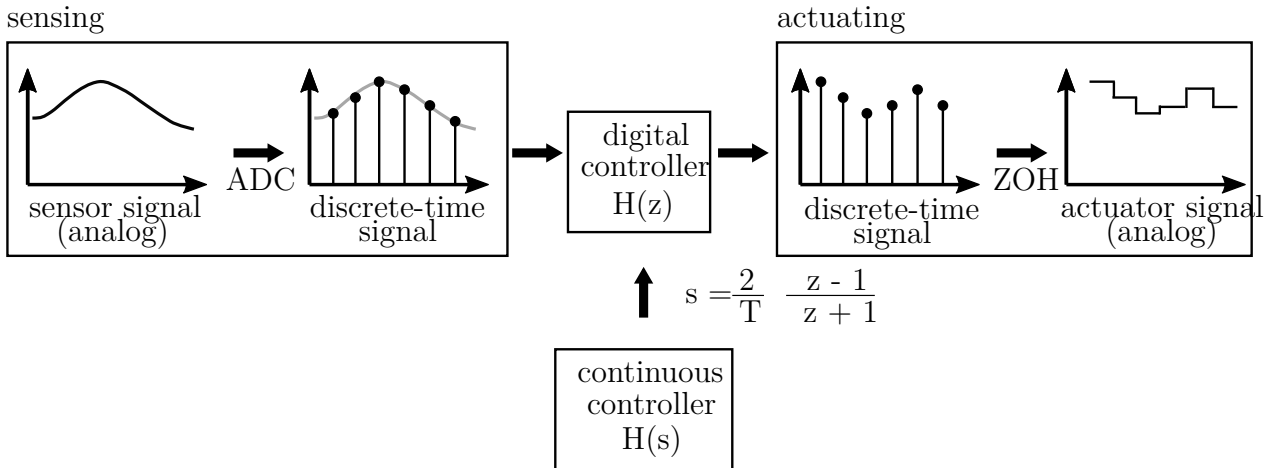


Figure 1.14: Illustration of a digital DAQ system: the analog signal measured by the sensor is discretized. A digital controller is implemented by approximating the continuous controller with the Tustin method. The actuation signal is then fed to the actuators after using the zero-order hold (ZOH) to keep the sampled value during one sampling period.

1.3.4 Platforms from the literature and commercial products

A review of the existing isolation tables has been conducted to identify 6 d.o.f. active isolation platforms from the literature and commercial products. The goal of this review is to study the architecture and performance of the current active systems. In addition, we will see what type of controller is used for MIMO systems. The tables containing this study are included in appendix C.

Note that even though these platforms are MIMO platforms, the performance was not always given for the vertical and the horizontal directions.

Platforms from the literature : All the isolation tables that reduce the transmission of ground motion around 1 Hz are using voice coils actuators. Indeed, pneumatic actuators act by changing the pressure inside their enclosure which is a slow process. Therefore, pneumatic actuators are not suited for fast process. In addition, piezoelectric transducer (PZT) actuators have a high stiffness and consequently a high resonance frequency. If the payload is supported and isolated by PZT, the benefit of the roll-off appears at frequencies above 10 Hz which is not convenient for low frequency isolation systems.

If the voice coils are used as the suspension and the actuation system, a large DC current needs to be injected to support the payload. To avoid the generation of large DC currents, a solution is to mount the payload on suspensions and use the voice coils only to isolate the system. A combination of passive and active systems is called a hybrid system [37].

Moreover, the platforms with performance around 1 Hz have their suspension modes on the order of 1 Hz. In some cases, this is achieved thanks to a negative stiffness mechanism; some tables use the Minus K suspensions. The suspensions used in parallel to the actuation system are given in table C.1 and table C.2.

The control laws mostly used are the classical PI, PD and PID controllers. For example, isolation systems with geophones use only classical control laws. Six isolation platforms use sensor fusion to increase the bandwidth while three structures are increasing the performance with a feedforward control.

Regarding the general architecture, all these isolation tables rely on three, four or six feet, the last configuration corresponding to the Stewart platform.

With years more platforms could have acceptable performance at 1 Hz. The best performance is obtained when using geophones and a classical control law.

The performance of the platforms presented here can be understood based on the resolution of the sensors used as shown in Fig. 1.15. For indication, the new low noise model (NLNM) [81] is also plotted. The NLNM represents the lowest amplitude of ground motion recorded on Earth. Hence, if the sensor has a resolution higher than the NLNM, it means that an isolation system with this sensor cannot measure the ground motion and hence, cannot reduce the transmission of ground motion to the sensitive payload. For example, in Ref. [82], the sensor has a resolution higher than the NLNM above 10 Hz and hence the system can not isolate at high frequency. The platform developed to isolate the sensitive equipments of the laser interferometer gravitational-wave observatory (LIGO) achieves the highest level of isolation as the sensors used (GS13 and T240) in the control loop surpass the resolution of the sensors used in other isolation stages. The GS13 from Geotech and the Trillium T240 are commercial sensors with one of the best resolution at low frequency.

Commercial products : The products found are often black box systems that can in average support a payload up to 200 kg. Most of them use pneumatic actuators, PZT or force transducers. They are not using voice coil actuators nor inertial sensors. Therefore, it is not surprising that none of them offer satisfactory performance at 1 Hz.

The architecture of the prototypes found in the literature are similar to the commercial products. For example, the AVIS table from Ref. [84] is supported by four legs in a similar way to the AIMS design from Philips [85].

1.3. Active isolation

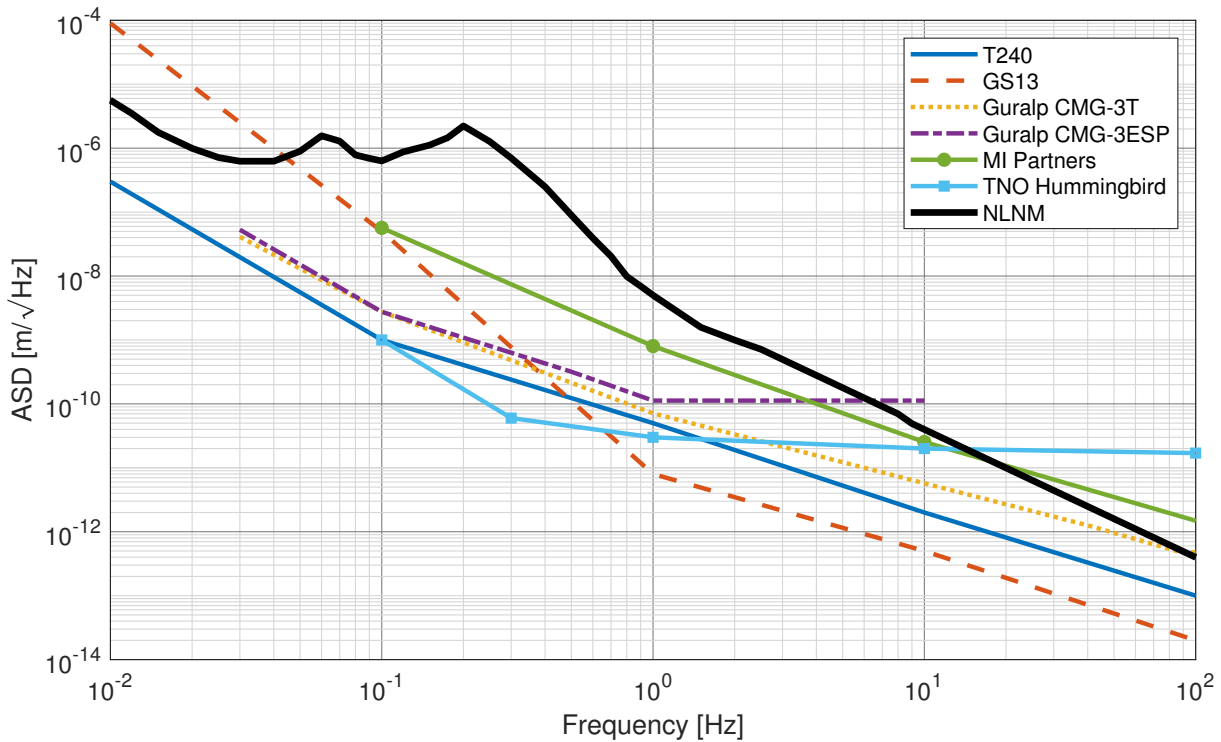


Figure 1.15: *Sensor resolution of the devices used in the following isolation tables: GS13 and T240 in Ref. [3, 48], Guralp CMG-3T in Ref. [1, 18, 22], Guralp CMG-3ESP in Ref. [2], homemade MI partners sensor in Ref. [82] and homemade TNO sensor in Ref. [83]. For indication, the NLNM is also shown [81].*

Effect of the environment : Fluctuations of temperature and pressure are responsible for signal variations of the readout. For example, they modify the refractive index of air which affects the optical path [86] in an optical readout.

In order to reduce the influence of temperature, the sensor can be placed inside a vacuum chamber. Another option is to use a weather station and correct the signal based on the pressure, temperature and humidity measurements [87–89]. In addition, the sensor can be made of a material with a low thermal expansion coefficient e.g. Zerodur, fused silica [90]. Electronics are responsible for acoustic noise. To avoid their influence, electronics have been placed in another room in Ref. [88, 91].

Varying magnetic field can also disturb the signal of electromagnetic readouts [85]. The sensor can be isolated from environmental magnetic field by placing it inside a shield made of μ -metal for example [92].

From this review, we can see that hybrid systems and classical control laws are a good combination to develop the desired isolation stage. To obtain low resonance frequencies for the suspension modes, negative stiffness mechanisms can be used.

In addition, we have seen that indeed, inertial sensors are needed to achieve performance. In the next chapter, the working principle and the development of inertial sensors with an improved resolution by comparison to commercial products are described.

Chapter 2

Interferometric readout

Contents

2.1	Working principle	32
2.2	Review of compact interferometers	33
2.2.1	Small range interferometers	34
2.2.2	Large range interferometers	35
2.2.3	Quadrature signals carried by the polarization states	36
2.2.4	Linearity of Phasemeters	41
2.2.5	Summary	47
2.3	Readout model	49
2.3.1	Description of the readout	49
2.3.2	Identification of the sources of noise	50
2.3.3	Description of the readout model	57
2.3.4	Comparison with experimental data	59
2.3.5	Noise budgeting	61
2.4	Resolution of the inertial sensor	62
2.5	Summary	64

In section 1.3.2, it has been demonstrated that inertial control can effectively isolate a payload from ground motion and other external disturbances. The demonstration assumed that one can sense the absolute motion of the payload. In practice, this is not the case and instead, inertial sensors are used to perform inertial control.

A sensor is made of a mechanical part and a readout system that aims to measure a physical quantity. The quantity measured can be a displacement, a velocity, an acceleration or a force. Sensors are characterized by many parameters: sensitivity, contactless or not, repeatability, bandwidth, measuring range, linearity, resolution and environmental conditions [50].

Here, we are mostly interested by a sensor with a large working range allowing to measure in the sub-Hz domain and the highest resolution possible, hence, with the smallest noise.

2.1. Working principle

In this chapter, the working principle of inertial sensor is presented. As explained, the sensors used for low frequency seismic isolation should have a good resolution at low frequency. Currently, interferometric readouts offer the best resolution for a large dynamic range. After a review of the interferometric readouts, this chapter presents the Michelson interferometer selected to sense the motion of the inertial sensors developed in this thesis. A numerical model of the readout is presented to study its resolution.

The review presented in section 2.2 is the result of a collaborative work published in Ref. [30].

2.1 Working principle

An inertial sensor is made of an inertial mass m_i connected to the moving payload by a spring, see Fig. 2.1. The readout actually measures the relative motion between the inertial mass and the payload m . The dynamics of inertial sensors can be deduced from Eq. (1.2) assuming that the motion of the payload is x , the motion of the proof mass is x_s and by subtracting ms^2X to both members of the equations, we have

$$m_i s^2 (X_s - X) = k(X - X_s) + cs(X - X_s) - m_i s^2 X . \quad (2.1)$$

Defining the relative motion $Y = X_s - X$,

$$\frac{Y}{X} = -\frac{-m_i s^2}{m_i s^2 + cs + k} . \quad (2.2)$$

The sensitivity of inertial sensor is shown in Fig. 2.2 for an inertial system with a resonance frequency at 1 Hz. Above the resonance frequency of the inertial sensor, the signal y is a good estimator of the motion of the payload x .

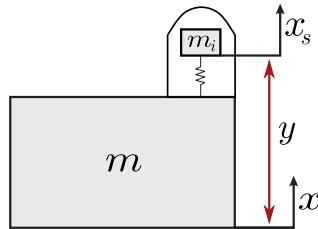


Figure 2.1: Inertial sensor measuring the motion of the payload of mass m . The inertial sensor is made of a spring-mass system connected to the payload and the signal measured is the relative displacement y between the payload x and the inertial mass x_s .

Note that the spring-mass system is responsible for additional sources of limitations for the sensor. First, the operating region is not only limited by the linearity range of the readout but also by that of the spring [85]. Second, to have an inertial sensor sensitive at low frequency, the spring is soft and hence, the frequencies of the internal modes of the spring will also be low and might be in the control bandwidth.

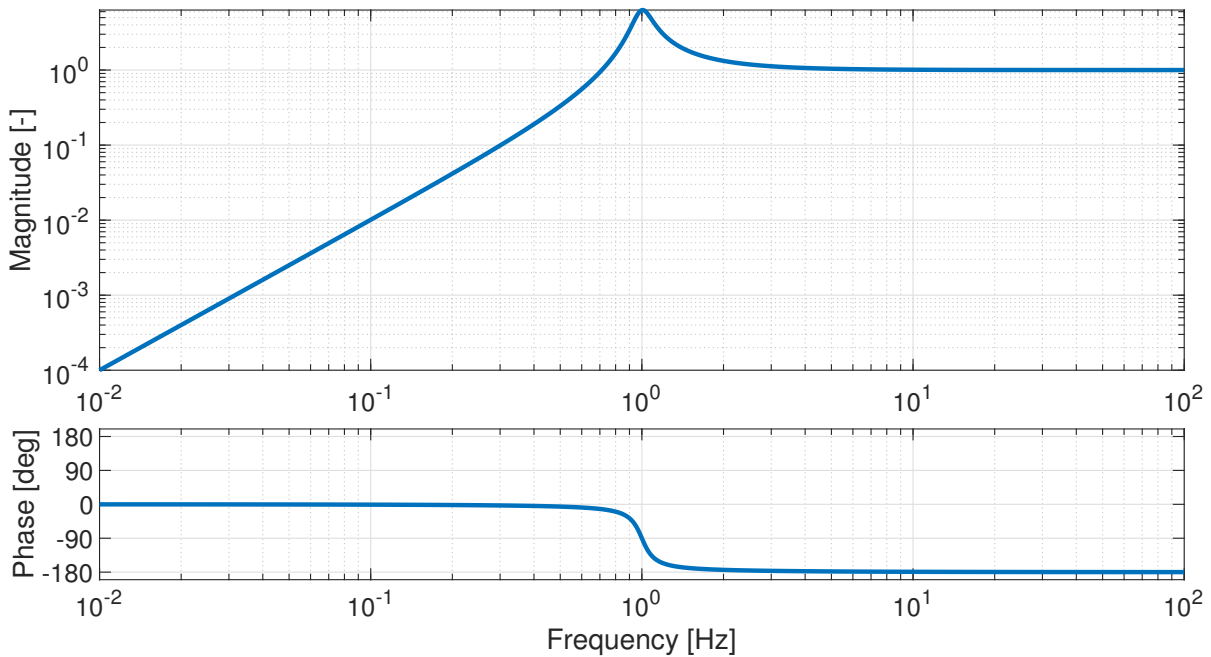


Figure 2.2: *Transfer function between the signal measured by the inertial sensor y and the motion of the payload x for a system with a resonance frequency at 1 Hz.*

2.2 Review of compact interferometers

In appendix B, the different types of readout commonly used are briefly described. Relative motion between two points can be measured by a number of transducers, converting the variation of a physical quantity into some useful voltage. Some examples of commonly used sensors are capacitive sensors, linear variable differential transformers (LVDT) and eddy current sensors. For each application, the adequate choice depends on many criteria, including resolution, dynamic range, space available, price, and compatibility with operating environment. While based on very different working principles, all of these sensors are fundamentally limited by a trade-off between resolution and dynamic range. In other words, none of them can process both small and large quantities. Moreover, even the most sensitive of these techniques have limited resolution and are not reliable in operating environments with stray magnetic fields.

These two aforementioned limitations prevent them from being used in some applications like high precision machine tools or production chains.

Interferometers are an excellent alternative due to their high sensitivity, non-contact measurement, and immunity to magnetic field. Conventional interferometers have a small working range, but when the optical phase is measured in two quadratures, the output can be unwrapped creating a large working range optical-phaserometer.

In this section, a range of devices that can be called ‘compact’ is reviewed, which implies that either the complete system or an optical head can be deployed onto an apparatus. While not all reviewed works clearly specify the size and form of the interferometer, these two criteria are investigated to determine their relevance.

The objective here is to provide a comparison of compact interferometers in terms of resolution,

2.2. Review of compact interferometers

dynamic range, and linearity. The focus is on devices with a working range of more than one fringe. The first section explains the working principle and limitations of conventional two-beam interferometers. Section 2.2.2 explains how to extend the range of small range interferometers. It is followed by section 2.2.3 dedicated to homodyne phasometers. Their working principle is presented and several examples from relevant literature are described.

Section 2.2.4 discusses problems related to the limited accuracy due to the non-linearities in the phase measurement. These problems are common to all types of phasometers. Counter measures that mitigate this problem are also introduced.

2.2.1 Small range interferometers

The focus of this review is on large range interferometers, capable of tracking the position of a target mirror with resolution much smaller than a wavelength over a working range of (much) more than a wavelength. In this section the key interferometry concepts and nomenclature are introduced. We consider two-beam interferometers, such as Michelson, Mach-Zender, and Sagnac interferometers, separately from resonant (or multi-bounce) interferometers.

For the Michelson interferometer shown in Fig. 2.3, the output field E_{out} can be calculated knowing the input field E_{in}

$$E_{\text{out}} = irtE_{\text{in}}(e^{i\phi_x} + e^{i\phi_y}), \quad (2.3)$$

where $\phi_{x,y}$ are the round-trip phase acquired in the respective arm, r is the reflection of the beamsplitter and t its transmission ($|r|^2 + |t|^2 = R + T \leq 1$). It is useful to express this in terms of the sum (ϕ_s) and difference (ϕ_d) of the phases, such that

$$\phi_s = \phi_x + \phi_y, \quad \phi_d = \phi_x - \phi_y. \quad (2.4)$$

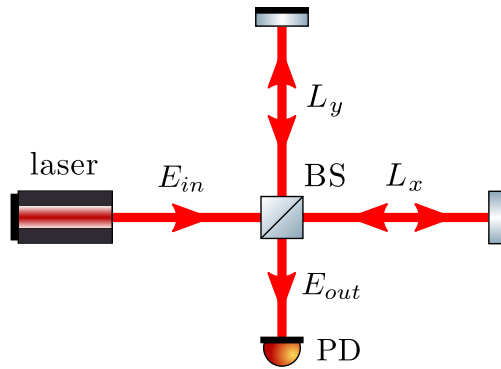


Figure 2.3: Optical setup of the Michelson interferometer. The incoming field E_{in} is split by the beamsplitter BS . One part of the beam propagates in the arm of length L_x and the other one in the arm of length L_y . The power of the output field E_{out} is recorded by the photodiode PD . Figure used from [30] with permission.

Assuming the beam splitter is lossless and has $r^2 = t^2 = 0.5$, the output power, $P_{\text{out}} = |E_{\text{out}}|^2$, as a function of the input power, P_{in} , is

$$P_{\text{out}} = \frac{P_{\text{in}}}{2}(1 + \cos(\phi_d)), \quad (2.5)$$

With Eq. (2.5) we see that the output power is independent of the common arm length. For a monochromatic light source with wavelength λ , and wavenumber $k = 2\pi/\lambda$, the optical phase difference is simply

$$\phi_d = 2k\Delta L, \tag{2.6}$$

proportional to the arm length difference, $\Delta L = L_x - L_y$, where L_x and L_y are the length of each arm of the interferometer.

The relative displacement is recovered from the signal measured given in Eq. (2.5) by inverting the equation

$$\Delta L = \frac{\lambda}{4\pi} \arccos\left(2\frac{P_{out}}{P_{in}} - 1\right). \tag{2.7}$$

The range ΔL of the Michelson interferometer is limited to the distance corresponding to a phase difference of π . In fact, by definition of the *arccos*, this function is not capable of making the distinction between the *cos* corresponding to 90° and -90° . From Eq. (2.6), a phase difference of π corresponds to a displacement of $\lambda/4$. Hence, the range of a classical Michelson interferometer corresponds to one quarter of the wavelength of the laser beam.

2.2.2 Large range interferometers

To increase the working range of a two-beam interferometer, the phase must be unambiguously extracted over more than one cycle, which is not possible by using Eq. (2.5). The general idea consists of creating two signals in quadrature, P_1 and P_2 , given by

$$P_1 = P_0(1 + \cos(\phi_d)), \tag{2.8}$$

$$P_2 = P_0(1 + \sin(\phi_d)), \tag{2.9}$$

where P_0 is the optical power. Then, an arbitrarily large phase can be calculated using

$$\phi_d = \text{atan2}((P_1 - P_0), (P_2 - P_0)). \tag{2.10}$$

Since the unwrapping occurs in signal processing, the fringe-counting is noiseless as long as the direction of the wrapping is known. The *atan2* function provides the unwrapped phase assuming that it is evaluated on a circle. For the rest of the section, we will consider the ideal case that corresponds to two perfect quadrature signals. Phase shift issues and any other causes of circle distortion are discussed in the section 2.2.4.

In this section, different methods to generate quadrature signals are presented. The quadrature signals can be carried by the two polarizations states of the beam or by two transverse modes of the intensity beam profile or by using two different lasers with different wavelength, each one carrying a different quadrature signal. When the quadrature signals are carried by different laser sources with different wavelength, the optical scheme is called a heterodyne interferometer. Otherwise, it is called a homodyne interferometer. The advantages and drawbacks of these methods are mainly related to the resolution of the interferometer, which is the smallest physical quantity that a sensor can measure [93].

2.2. Review of compact interferometers

For the sake of simplicity, the homodyne interferometer is preferred. Indeed, a good resolution with the heterodyne interferometer requires to use two laser sources with similar low noise properties which is difficult to find.

Therefore, only homodyne interferometers are studied here. The working principle of heterodyne interferometers can be found in Ref. [30].

2.2.3 Quadrature signals carried by the polarization states

Two quadrature signals can be generated by imposing a delay of $\pi/2$ of one polarization state of the beam with respect to the other one thanks to a waveplate. The phase shift of $\pi/2$ can be obtained either by passing once through a $\lambda/4$ waveplate or twice through a $\lambda/8$ waveplate. The implementation of these two options to obtain quadrature signals is detailed below.

- **$\lambda/8$ wave plate**

A $\lambda/8$ wave plate is placed in one of the interferometer's arms to provide a differential (round-trip) phase shift of $\pi/2$ between the linear polarization entering one arm and the other [94–96]. In fact, this creates two co-located Michelson interferometers that measure the position of the target mirror, each one carrying one of the two orthogonal polarizations. The output of these interferometers are then separated by using a polarizing beam splitter.

A schematic representation is shown in Fig. 2.4 where the dot on the beam indicates the s-polarized axis and the perpendicular line, the p-polarized axis. The beam is split by a non-polarizing beam splitter and the transmitted part is delayed in the x-arm of length L_x . After recombination at the beam splitter, the two polarizations are measured independently at the photodiodes 1 and 2.

An interferometer of this kind has been mounted in a seismometer [16, 95–97]. In Ref. [96], the interferometer has a resolution of around $1 \text{ pm}/\sqrt{\text{Hz}}$ at 1 Hz. Several modifications of the optical path have been introduced to reduce the noise and hence improve the interferometer resolution. These structure modifications are discussed hereafter.

Extra photodiodes to delete the DC component

When the sinusoidal signals are not oscillating around zero, the phase and hence the displacement cannot be accurately extracted from the signal measured by the photodiode. This variation of the mean signal can be due to intensity fluctuations of the laser source. In Ref. [94], three signals are measured by using two polarizing beam splitters instead of one: two out of phase signals carried by the same polarization state and one signal carried by the orthogonal polarization are measured. If we don't consider a gain mismatch between sensors, the three signals can be written as

$$P_{PD1} = P_0(1 + \sin(\phi_d)) , \quad (2.11)$$

$$P_{PD2} = P_0(1 + \cos(\phi_d)) , \quad (2.12)$$

$$P_{PD3} = P_0(1 - \cos(\phi_d)) . \quad (2.13)$$

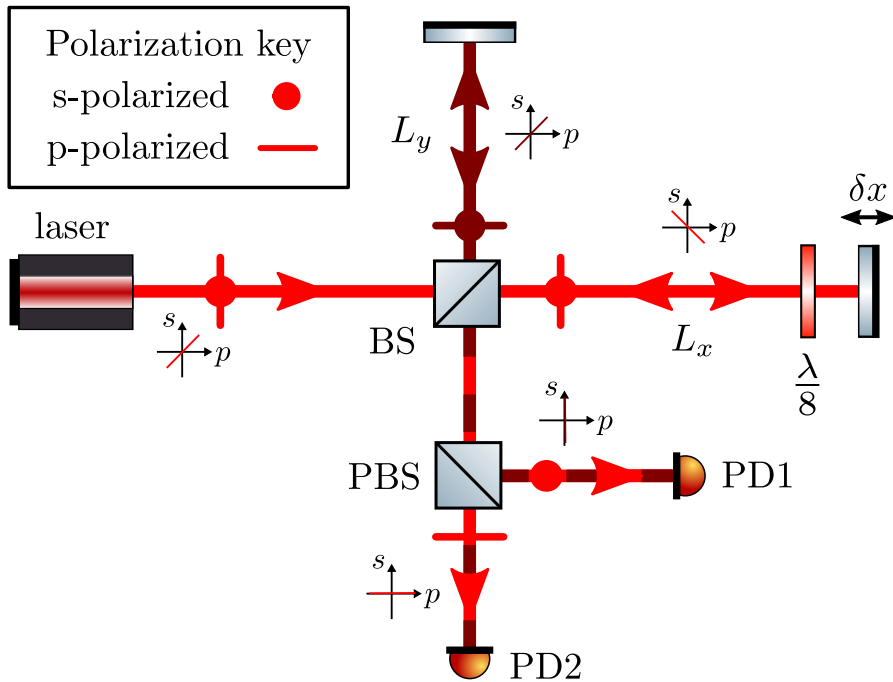


Figure 2.4: A homodyne phasemeter. The $\lambda/8$ wave plate in the x -arm has its fast axis aligned with the s - (or p -) polarisation, effectively creating two co-incident Michelson interferometers with one polarization delayed by $\pi/2$ in the x -arm. The polarising beamsplitter (PBS) splits the two outputs into the photodiodes PD1 and PD2. The orientation of the beam in the polarization plane is given by the small graphs for each part of the optical setup. The incoming beam has a linear polarization. Figure used from [30] with permission.

Thanks to a correct subtraction of the sine signal to the two others, the two resulting signals are in quadrature and the DC component is removed:

$$P_1 = P_{PD1} - P_{PD2} = \sqrt{2}P_0 \sin(\phi_d - \frac{\pi}{4}), \quad (2.14)$$

$$P_2 = P_{PD1} - P_{PD3} = \sqrt{2}P_0 \sin(\phi_d + \frac{\pi}{4}). \quad (2.15)$$

As the phase is obtained from the atan2 of the ratio between these two signals, the results become insensitive to the input power fluctuations. Consequently, the resolution is not deteriorated by intensity fluctuations even when the laser intensity drops down to 10 % [94].

The use of additional photodiodes also has certain advantages for the reduction of non-linearities which is discussed in Section 2.2.4.

Multiple-reflections in the measurement arm

One way to improve the resolution is to increase the number of reflections on the target mirror by slightly tilting the mirror and placing a fixed mirror in front of it, see Fig. 2.5. If the measurement mirror moves along its normal axis, represented by δx on the figure, the phase change increases at each reflection [98]. Consequently, the phase measured is proportional to $G\delta x$, where G corresponds to the number of reflections on the moving mirror, see Fig. 2.5.

Consequently, the smallest phase increment measurable is proportional to $\delta x/G$. It means that the resolution is improved by a factor G in comparison with a single-bounce interferometer. In Ref. [98], this assumption has been verified experimentally: a comparison between a simple Michelson interferometer and a 60 reflections version has been presented.

2.2. Review of compact interferometers

Around 2 Hz, the new configuration resolution is 20 times better than the classical version. At high frequencies, an improvement of the resolution by a factor 60 is reached. The resolution can still be improved because while using multiple-reflections in one arm, the phase noise related to unequal optical arm length increases.

To increase the resolution, the number of reflections must be as large as possible. However, the beam should not overshoot the size of the mirror. An optimum number of reflections can be adjusted as explained in Ref. [99]. In addition, the number of reflections cannot be too large to avoid being beyond the laser coherence. In order to maintain the coherence between the two paths, a Michelson interferometer with two multiple-reflections arms has been studied [100]. The two mirrors are rotated with the same angle as they are coupled thanks to a gear mechanism. Because the two beams are reflected the same number of times, the intensity loss due to the multiple bounces is also identical. In comparison, in the system with a single multiple-reflections arm, the intensity loss must be estimated because it reduces the fringe visibility [100].

Finally, for large number of reflections, air fluctuations can induce changes of the refractive index of air and hence phase jumps. Therefore, a compromise must be found between an increase in resolution and a loss of coherence between the signal measured and the motion of the mirror. All these aspects and their impact on the delay are discussed in Refs. [98, 100] describing multiple-reflection interferometers.

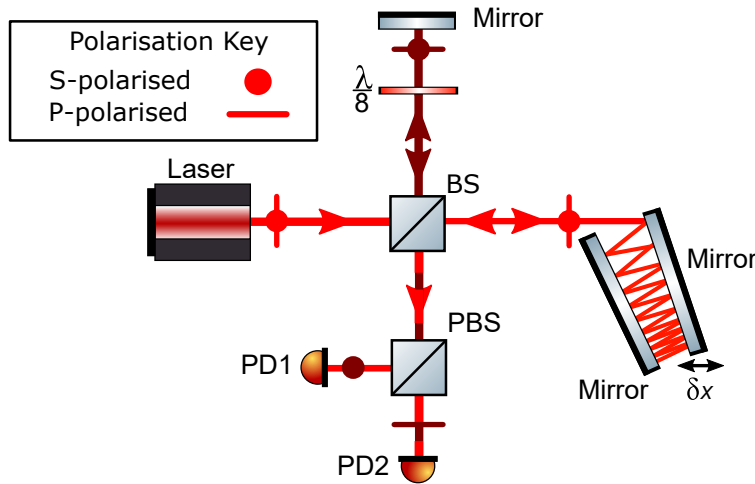


Figure 2.5: A homodyne phasemeter using a $\lambda/8$ wave plate and multiple reflections on the target mirror to enhance sensivity. Adapted from the experimental setup figure in Ref. [98].

Other configurations

Some additional modifications can be found in the literature. Their impact on the resolution is not clear or has not been verified experimentally. In Ref. [94], it is suggested that a lens can be used to reduce the beam motion across the active area of the photodiode. Moreover, in Ref. [101, 102], the polarizing beam splitter used to separate the two polarizations is replaced by a Wollaston prism. With this prism, the two polarization states are emitted in the same plane but their direction varies with a defined angle.

- $\lambda/4$ wave plate

Similarly, a $\lambda/4$ wave plate can also introduce the required phase shift in the system. The phase shift is generated either before entering the two arms [103–106] or just before the signals are measured [107,108]. In the first case, the beam polarization state is rotated before and after entering the interferometer so that both polarizations enter the two arms: one polarization will carry the phase shift $\pi/2$ through the whole optical path. In the second case, after splitting the beam in two thanks to a beam splitter, the phase of one part is delayed by $\pi/2$, see Fig. 2.6. Here, the first PBS ensures the beam to have a clean polarization state when entering the interferometer, and the $\lambda/2$ wave plate adjusts this state to ensure that PBS2 splits the beam into two orthogonal polarization states. Note that the configuration in Fig. 2.6 shows more than two photodiodes. The additional photodiode is used to delete the DC component as already explained above.

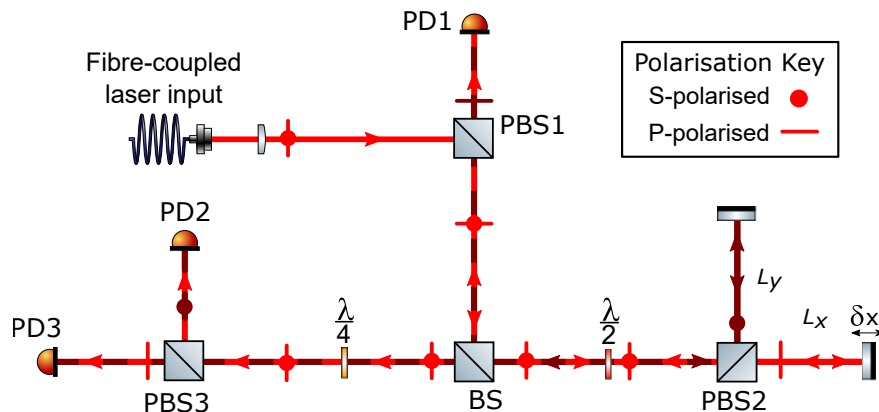


Figure 2.6: Diagram of the homodyne Michelson interferometer with $\lambda/4$ waveplate [108]. Figure used from [30] with permission.

Some examples of resolution obtained with the homodyne quadrature interferometers mentioned above are shown in table 2.1. Even though the use of $\lambda/8$ waveplate eases the optical path, this product is difficult to obtain on the market. However, the improvements developed for the $\lambda/8$ configuration can be easily implemented on the $\lambda/4$ one. For example, the use of additional photodiodes to remove a DC component has been used in Ref. [108] where the $\pi/2$ phase shift is induced by the mean of a $\lambda/4$ waveplate.

- Using a special beam splitter coating

In order to avoid the unwanted extra reflections that appear when adding wave plates, an interferometer that uses beam splitter plates and corner cubes has been developed [114], see Fig. 2.7.

In this setup, the BS is replaced by two slightly wedged plates coated with a three-layer metal film [114]. The beam phase is delayed differently when it is reflected or when it is transmitted through the plates [115]. With a careful choice of the plate coating, the phase shift between the two path is $\pi/2$ and the two signals are in quadrature. In Ref. [115], a method to produce the coating is explained. However, the authors can only guarantee that the phase difference between the two signals is included in the range $90^\circ \pm 10^\circ$ which corresponds to a relative uncertainty of more than 10 %. Consequently, such a beam splitter

2.2. Review of compact interferometers

Table 2.1: Chronological evolution of homodyne quadrature interferometers resolution and other properties. All devices cited uses a waveplate to generate a phase shift of $\pi/2$ between the two polarization states. The resolution is given in Amplitude Spectral Density (ASD) for the interferometers found in the literature and in Root Mean Square (RMS) for the commercial products. The area corresponds to the surface occupied by the interferometer, without the laser source and the data acquisition system.

Year	Device	Resolution (ASD) pm/ $\sqrt{\text{Hz}}$ @1Hz	Wavelength nm	Area cm ²
2008	Ponceau [103]	1	632.8	27x27
2009	Pisani [98]	5	632.8	20x20
2010	Zumberge [109]	0.3	632.8	12x17
2011	Aston [104]	5	850	8.7x4
2012	Acernese [110]	1	632.8	13.4x13.4
2015	Bradshaw [105]	420	1550	28x16
2016	Watchi [106]	1	1550	14x11
2017	Cooper [108]	0.1	1064	17x10
Year	Commercial Product	Resolution RMS (pm)	Wavelength nm	Area cm ²
2017	Renishaw [111] RLD10	38.6	632.8	9.8x5
2018	Zygo [112] DynaFiz	60	633	60x34
2018	Dayoptronics [113] AK-40	80	632.8	25x12.7

plate can not provide the phase shift with sufficient precision to ensure that this option can replace the use of wave plates.

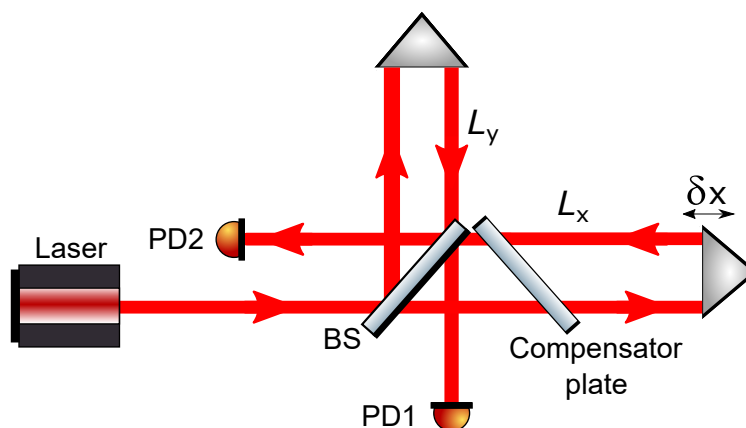


Figure 2.7: Diagram of the homodyne Michelson interferometer with a special beamsplitter coating. Figure used from [30] with permission.

Quadrature signals carried by transverse electromagnetic modes: tilted mirror

In order to have quadrature signals, the previous methods aim to induce a phase shift of $\pi/2$ between the two polarization states of the beam. A phase shift of $\pi/2$ can also be generated between two modes of the intensity beam profile [116]. In fact, the intensity profile can be seen as a superposition of Transverse Electromagnetic Modes (TEM) [117]. When all optics are well aligned with the cavity of the laser, the intensity distribution of the beam has a Gaussian profile, defined as the TEM_{00} mode [118]. By slightly tilting the mirror of the interferometer, the intensity distribution becomes the sum of a TEM_{00} mode and a TEM_{01} mode. When propagating, these modes accumulate different phase, called a Gouy phase [117, 119]. After traveling, the two modes Gouy phases have acquire a phase shift of $\pi/2$. Consequently, two quadrature signals are measured by placing one photodiode at the maximum intensity of each mode. A diagram of such a device is shown in Fig. 2.8. The beam expander plays two roles. First, it allows to be in the condition where the phase shift between the two modes is $\pi/2$ [117]. Second it eases the positioning of the two photodiodes.

No resolution using this method could be found in the literature. Consequently, its performance will not be discussed.

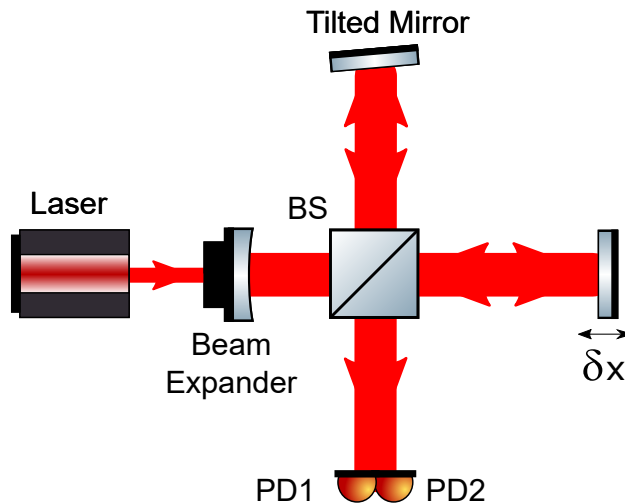


Figure 2.8: Diagram of the homodyne Michelson interferometer with a tilted mirror. Figure used from [30] with permission.

2.2.4 Linearity of Phasemeters

Phasemeters recover the optical phase by evaluating the four-quadrant arctangent of the ratio between two quadrature signals, as explained in section 2.2.2. The relation between the real phase and the phase measured should be linear but there are often distortions due to spurious effects in the optics or signal-processing of the phase. These distortions correspond to non-linearities and cause periodic errors of the relation between the real phase and the measured phase. Techniques to reduce and quantify non-linearities, are the scope of this section.

The ideal signal of a homodyne interferometer is a sinusoidal shape Eq. (2.5). For a quadrature homodyne interferometer, it is a circular Lissajous figure Eq. (2.9). These perfect

2.2. Review of compact interferometers

patterns are distorted by offset Fig. 2.9(a), quadrature imperfections Fig. 2.9(b), and gain imbalance of the signal due to an intensity difference between the two arms of the interferometer Fig. 2.9(c). The resulting Lissajous figure is an ellipse that can be rotated or off-centered depending on the type of non-linearity. The phase recovered from this figure is different from the real phase [120] and the signals measured for a homodyne interferometer have the following form [96]:

$$P_1 = P_0(1 + a \cos(\phi_d)) , \quad (2.16)$$

$$P_2 = b P_0(1 + a \sin(\phi_d + c)) + d . \quad (2.17)$$

where P_1 and P_2 are the measured signals as in Eq. (2.9), P_0 is proportional to the laser power, a is the fringe visibility, b is the gain mismatch between sensors, c is the quadrature imperfection, and d is the differential offset.

As seen in Fig. 2.9, distortions due to translation and dilatation of the Lissajous figure induce a periodic variation of overestimation and underestimation of the phase. In fact, over one period, the sine and/or cosine are alternatively smaller and bigger than the ideal case. On the contrary, the rotation of the figure corresponds to an additional constant phase applied to one of the two signals. Depending on the phase sign, this extra phase is responsible for either an overestimation or an underestimation of the relation between the real and measured phases.

Causes of non-linearities include:

- Elliptical polarization of the laser beam [86, 89]
- Misalignment between the laser beam and the polarizing beam splitter axis [121, 122]
- Imperfections in alignment or quality of optical components [121, 122]
- Non-orthogonality of the laser polarizations in heterodyne interferometers [121, 123, 124]
- Imperfect photodiode (responsivity, gain, etc.) [125]

This non-exhaustive list shows the complexity of the non-linear origins [122]. Moreover, one cause of non-linearity engenders combinations of offset, quadrature and gain imbalance distortions. For example, if the two polarization states are not perfectly orthogonal, the two polarizations measured will not have the same intensity and they will not be in quadrature.

In order to reduce the sources of non-linearities, several solutions have been implemented: ellipse fitting algorithms, phase-lock systems, temperature isolation, etc. The different techniques and the improvements brought are listed below. The corresponding residual non-linearities are gathered in table 2.2.

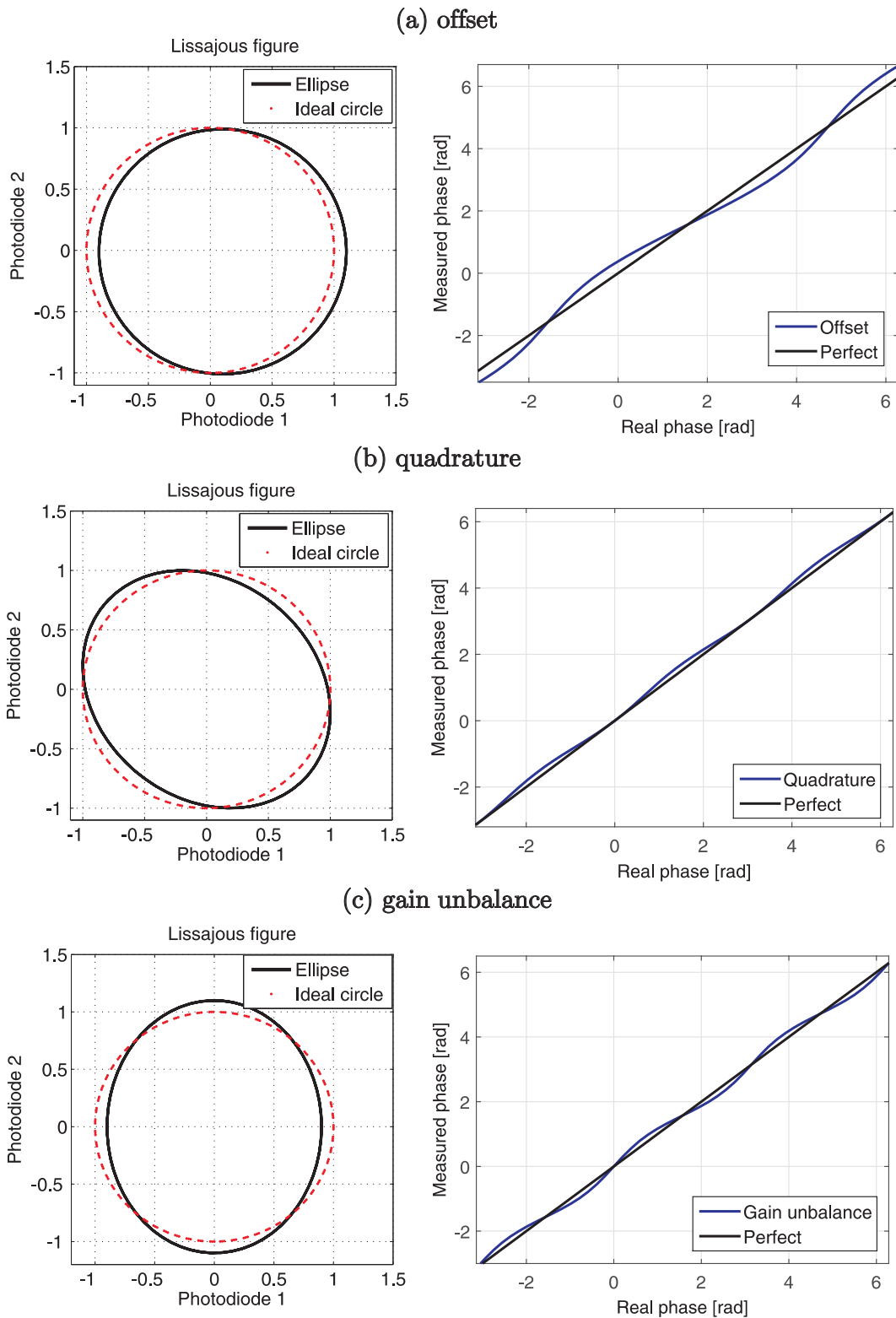


Figure 2.9: Plots of P_1 against P_2 (left) and the effect of the non-linearity on the relation between the real and the measured phases (right). The effect of offset (a), quadrature error (b), and gain imbalance (c) can be seen in the Lissajous figures when compared with an ideal circle. For simplification, the circles and ellipses are centered at the origin. The right figures allow to identify the order of the non-linearity in comparison to the period of the sinusoidal signals: the offset has an order 1 and the quadrature and the gain imbalance an order 2. Figure used from [30] with permission.

2.2. Review of compact interferometers

Ellipse fitting algorithms

In order to convert the ellipse into a unitary circle, the ellipse parameters in Eq. (2.16) and (2.17) need to be determined. This can be done by using ellipse fitting algorithms either in post-processing or real-time. Algorithms that employ the method of least squares have been used to reconstruct the ellipse parameters [126, 127] and then recover the parameters from Eqs. (2.16) and (2.17) [95, 96, 121, 124, 128–132]. In Ref. [133], the phase error is compensated in the Fourier domain by a least squares approximation of the first order errors. A clear explanation of this ellipse fitting technique is contained in Ref. [126].

In order to identify the ellipse parameters, a cost term, S , is minimized. Using the algebraic distance between data and fit points $Q(x, y)$

$$S = \sum_{i=1}^n Q(x_i, y_i)^2, \quad (2.18)$$

In Fig. 2.10, the reconstruction of circle thanks to ellipse fitting algorithm is illustrated on experimental data [106].

In these algorithms, some parameters need to be correctly chosen in order to reduce the non-linearities. First, the fit point on the ellipse closest to the data point has to be properly chosen [134]. Second, least squares method is very often used and the residual non-linearities with this fitting method are on average between 0.1 and 1 nm, see table 2.2. However, other fitting methods exist which reduce the non-linearities. In Ref. [135], the phase is fitted by a polynomial function and in Ref. [136], the parameters are dynamically re-evaluated by iterative refinement. An iterative evaluation is also presented in Ref. [137] where Kalman filters are used to estimate the ellipse parameters. Moreover, the size and shape of the window sampling function used is a crucial parameter for the algorithm performance. The influence of the window function on the phase error has already been studied theoretically and experimentally [138, 139]: rectangular windows are more sensitive to high-frequency phase errors than bell-shape windows like Von Hann [138] and Hanning [139] windows.

Non-linearities reduction methods

Correcting the signal measured is not the only mean to reduce non-linearities. Modifications of the optical path in the interferometer can also improve the signal. Some solutions and their performance are discussed in the next sections.

- **Multiple reflection in the measurement arm**

In section 2.2.3, it has been shown that the multiple reflection technique improves the resolution of homodyne interferometer by a factor G [98]. With this configuration, the distortions on the resulting signals are similar to the ones obtained with a simple homodyne interferometer. However, as the signal has traveled a longer distance, it has crossed more fringes. From Fig. 2.9, we can see that non-linearities are periodic and do not increase depending on the number of fringes crossed. Consequently, the ratio between the non-linearities and the whole signal is reduced by a factor G in a multiple reflection interferometer. Note that this assumption has not been verified experimentally.

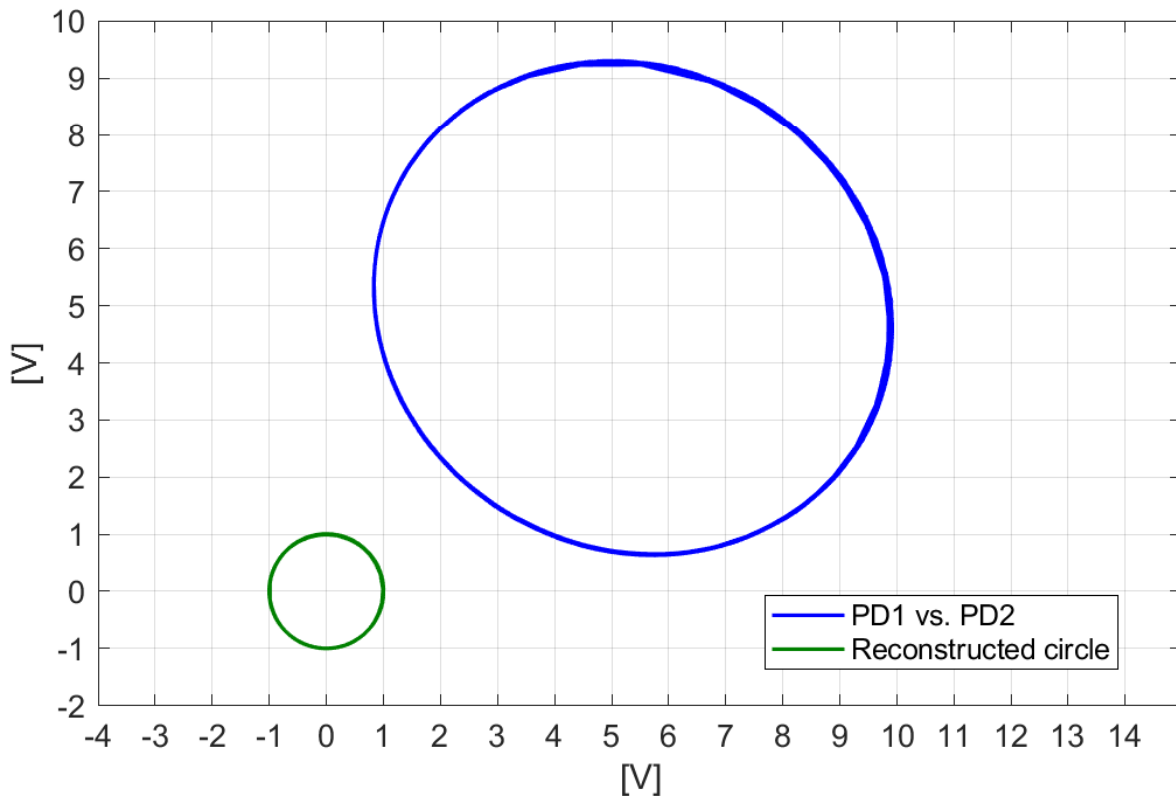


Figure 2.10: Transformation of the ellipse, the signal directly measured by the two photodiodes PD1 and PD2 (blue curve), into a unitary circle (green curve) using ellipse fitting algorithm [106]. Figure used from [30] with permission.

- **Additional sensors**

In section 2.2.3, it has been shown that additional photodiode reduces the sensitivity of the sensor to fluctuations of the laser intensity. In addition, the use of one [102, 103] or two [107, 140] additional signals to normalize the measurements reduces the gain imbalance, seen in Fig. 2.9(c). In term of accuracy, two additional photodiodes is more effective because it does not require additional modeling to reduce all types of non-linearities, as explained in Ref. [107].

The four photodiodes design can recover in real time all the ellipse parameters of Eq. (2.16) and Eq. (2.17) thanks to an electronic circuit. To obtain four signals, two for each polarization state, two PBS are used. This technique reduces all the major types of non-linearity, and the resulting signal has phase error reduced by a factor 10 [140].

One additional photodiode can be used in two different ways to cancel or reduce intensity fluctuation and offset. In Ref. [103], the additional signal is used to monitor the input power and normalize the outputs from the signal photodiodes. This makes the two signals independent of intensity fluctuations and in a secondary way this reduces gain imbalance. Moreover, the offset non-linearity is reduced as the signal is divided to make the normalization. In Ref. [94, 108], two signals measured are out of phase and one signal is in quadrature with the

2.2. Review of compact interferometers

two others as already explained in Section 2.2.3. If we don't consider a gain mismatch between sensors, see Eq. (2.16) and Eq. (2.17), quadrature imperfection and a differential offset (as they are not altered with this method), the signal measured is given by Eq. (2.14) and Eq. (2.15) and the result becomes insensitive to the fringe visibility, which is the parameter a in Eq. (2.16).

- **Reduction of the phase mixing**

In homodyne interferometers, one polarization is measured by one photodiode. When a fraction of one polarization state is measured by the other photodiode, we talk about phase mixing. In other interferometers [141], each polarization propagates in a different arm. If a part of the polarization propagates in the other arm, both polarizations states will carry information about the reference and measurement arm as they have propagated in both arms. Heterodyne interferometers are also subjected to phase mixing when one of the two frequencies is transmitted to the other path. This phase mixing is responsible for imperfect quadrature and gain imbalance as shown in Ref. [89]. Phase mixing can come from imperfect optical elements [123] such as PBS.

In order to avoid the injection of one polarization state (or wavelength for the heterodyne interferometer) into the other arm, one solution is to make the signals travel into two spatially separated paths and measure the signals with two independent photodiodes. One example of spatial separation can be found in Ref. [142]: the central part of the beam cross section is reflected by the measuring mirror and measured by one photodiode. The outer part of the beam is reflected by the reference mirror and recorded by a second photodiode. Note that with this configuration, some diffraction at the separating optics can cause injection of one phase into the other arm but this effect can be reduced thanks to a careful sizing of the setup [142].

Spatial separation is also implemented in Ref. [120, 143] where two lasers with different frequency propagate in two different interferometers: the only common element between the two interferometers is the moving mirror but the beams are not reflected at the same position on the mirror. With this configuration, interference occurs at the photodiodes where the two beams with different frequencies recombine.

- **Closing the loop to decrease the non-linearities**

Feedback loops can be designed to control the frequency of the laser or its polarization. The implementation of closed loops for these two purposes are summarized hereafter.

Frequency correction : It is well known that laser frequency oscillates around a fixed value. This fluctuation creates some phase shift that can be misinterpreted as being a displacement signal. To avoid these fluctuations, the frequency of some interferometers lasers is locked: a reference signal, measured before the beam enters the interferometer, is used to drive the laser cavity. This method is used for homodyne interferometers [144], heterodyne interferometers [89, 145–147] and resonators [88, 91, 148–151]. Some papers discuss the implementation of frequency lock techniques [144, 147, 149, 150].

The disadvantage of actuating the laser frequency is that the non-linearity of the measured signal is transmitted to the actuator which will then have a non-linear behavior.

Note that the undesired frequencies can be rejected without any control. In Ref. [130], an optical narrow band pass filter is placed before the photodiodes. This filter reduces beam signals which do not have the desired wavelength.

Polarization correction : Misalignment between the polarization states of the incoming beam and the polarizing beam splitter causes phase shift in the recorded signal Fig. 2.9(b) and gain imbalance Fig. 2.9(c). The incoming polarization state orientation can be controlled using a $\lambda/2$ wave plate; The wave plate orientation is permanently controlled [89, 95] to keep the beam aligned with the beam splitter. In Ref. [89], one wave plate adjustment technique is described. An extra beam with a known linear polarization at $\pi/4$ is injected into the interferometer. A feedback loop adjusts the angle of the wave plate to ensure that the polarization state of this reference signal is not modified by the interferometer. The interferometer made of the reference beam, the optical path and the polarimeter is called a polarimetric interferometer. In Ref. [89], the polarimetric interferometer has an accuracy of 9 pm.

Performance of the different interferometers

The performance of the different versions of interferometers are listed in table 2.2 and chronologically represented in Fig. 2.11. The RMS of the residual non-linearities has decreased by four order of magnitude since 1980. After 2010, several new non-linearity reduction techniques have emerged both for homodyne and heterodyne interferometers. From Fig. 2.11, the Fabry-Pérot interferometer including the phase-lock method shows better results than the Michelson interferometer version.

Several papers were agreeing that the primary origin of noise comes from the non-orthogonality of the two linear polarizations measured [121, 123, 124]. The use of an adjustable $\lambda/2$ wave plate can correct this issue as explained in the previous section. From Fig. 2.11, this method leads indeed to one of the lowest residual non-linearities.

2.2.5 Summary

The review of ‘compact’ interferometers shows setups that employ different methods to increase the dynamic range compared with that of a simple interferometer. All techniques are based on the same principle: create a phasemeter by generating two (or more) quadrature signals from which the phase, and as such the displacement, can be extracted over more than one fringe by unwrapping the outputs with a 4-quadrant arctangent.

The dimensions of the systems have been identified. From table 2.1, we see that in average the optical homodyne interferometer occupies an area of approximately $17 \times 17 \text{ cm}^2$, with some substantial variation in size. Heterodyne phasemeters are somewhat larger, typically $30 \times 30 \text{ cm}^2$, but in both cases the ‘size’ often neglects the input beam preparation optics and data acquisition system. Heterodyne devices typically require more space as either an additional laser source or an AOM is required.

The resolution of homodyne phasemeters has improved considerably since their inception, largely due to decreasing technical noises. Table 2.1 shows that several devices in the last 10 years have reached a sensitivity at or below $1 \text{ pm}/\sqrt{\text{Hz}}$ at 1 Hz. To improve sensitivity it is possible to increase the number of reflections in one or both arms of an interferometer. Several experiments have employed additional photodiodes to reduce intensity-noise coupling.

2.2. Review of compact interferometers

Table 2.2: *Residual non-linearities. Displacement error improvement by the mean of correction algorithms and other improvements are also listed. The "Real Time" column shows if the algorithm can be applied to correct in real time the error. The root mean square (RMS) values plotted are directly taken from the papers.*

Year	Ref.	Type	Method	Residual displacement error (RMS)	Real Time
1981	[128]	Hom.	Least square	10^4 pm	no
1987	[152]	Hom.		$1.32 \cdot 10^5$ pm	-
1996	[129]	Hom.	Least square	700 pm	no
1999	[124]	Hom.		<500 pm	no
2001	[140]	Hom.	Least square	400 pm	yes
2009	[130]	Hom.	Least square	$3 \cdot 10^3$ pm	yes
2010	[153]	Hom.	Phase-lock	10^4 pm	-
2010	[154]	Hom.	Capacitive reference sensor	200 pm	yes
2011	[155]	Hom.	Capacitive reference sensor + improved algorithm from [154]	10 pm	yes
2011	[131]	Hom.	Least square	10^3 pm	no
2012	[88]	Hom.	Common path	5 pm	-
2012	[88]	Hom.	Capacitive sensor corr.	14 pm	-
2014	[132]	Hom.	Least square	22 pm	no
1989	[156]	Het.		< 10^4 pm	no
1992	[121]	Het.	1st order phase error compensation	$1.2 \cdot 10^3$ pm	yes
2009	[157]	Het.	Phase-lock	5 pm	-
2012	[88, 143]	Het.	Spatial separation	<10 pm	-
2012	[88]	Het.	Phase-lock	150 pm	-
2012	[88, 148]	FPI	Phase-lock	2 pm	-
2013	[89]	Het.	Adjustable $\lambda/2$	9 pm	-

A significant advantage of all phasometers is that they are inherently calibrated to the wavelength of the laser. There are, however, several sources of non-linearity that affect their accuracy, and these have also been reviewed. Non-linearities can be reduced in several ways. Ellipse fitting algorithms, are widely used to transform the phasometers output into a unitary circle centered at the origin, removing both the leading order of non-linearity and the offsets inherent to measuring intensity with photodiodes. Additional sensors, can reduce the residual non-linearity by reducing the effect of power fluctuations or by subtracting large input phase-shifts. Polarization mixing (homodyne) and phase mixing (heterodyne) can be reduced thanks to spatially separating beams. From figure 2.11, it is clear that non-linearities have been improving consistently during the last decades and that modern interferometers can consistently achieve single-digit picometer accuracy.

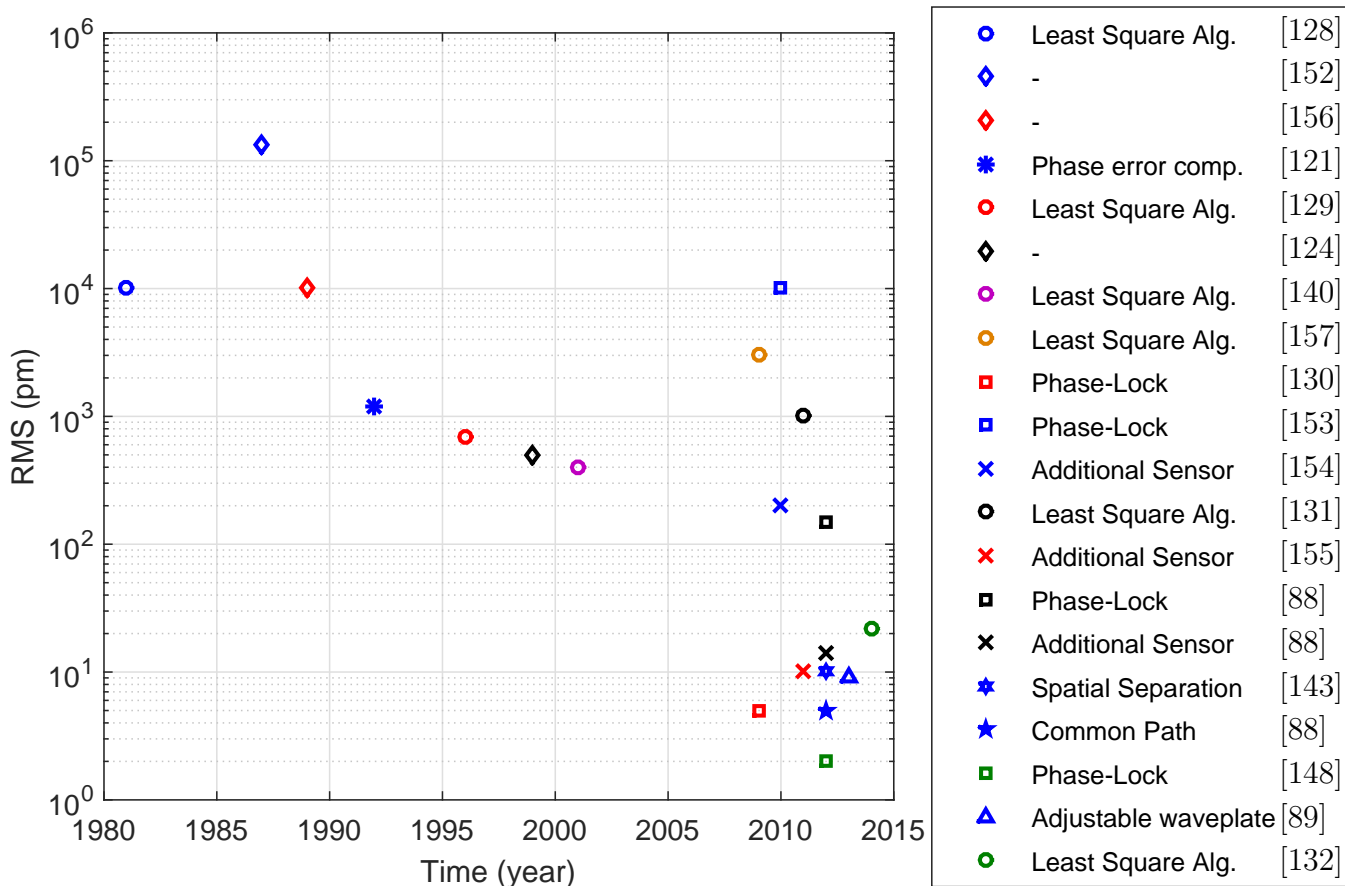


Figure 2.11: Time evolution of the non-linearities in RMS. The RMS values plotted are directly taken from the papers. The shape of the marker corresponds to an improvement or feature of the interferometer as explained in the legend. Note that the diamond marker corresponds to simple Michelson interferometers without any additional feature. Figure used from [30] with permission.

2.3 Readout model

In order to understand the working principle and the limitations of the homodyne interferometer used to sense the motion of the inertial sensor, a detailed model has been developed. After introducing the optical setup, this section describes the optical model. The first step consists in identifying the sources of noise that contribute to the signal. The second step is to compare the model to experimental data for validation.

2.3.1 Description of the readout

The Michelson interferometer integrated in the inertial sensor and its corresponding optical setup are shown in Fig. 2.12. The interferometer is based on the scheme developed by Ponceau et al. [103] as it has one of the best readout resolution, see table 2.1. The optical setup includes three photodiodes (Thorlabs PDA50B-EC). The additional photodiode helps to remove the fluctuations of power. The laser used is the Koheras Adjustik X15 from NKT connected to a collimator (Thorlabs F240APC-1550). The other optics are listed in table 2.3. The mirrors are replaced by corner cubes (Thorlabs PS974M-C) to ensure that the reflected beam is parallel to the incoming beam. In fact, in case of large displacement the reflected

2.3. Readout model

beam at the surface of a flat mirror can be deviated out of the photodiode active area. In practice, the reflected beam is not superimposed with the incoming beam due to the geometry of the corner cube. One corner cube is fixed to the inertial mass. Therefore, the relative displacement measured by the interferometer corresponds to the relative motion between the inertial mass and the payload.

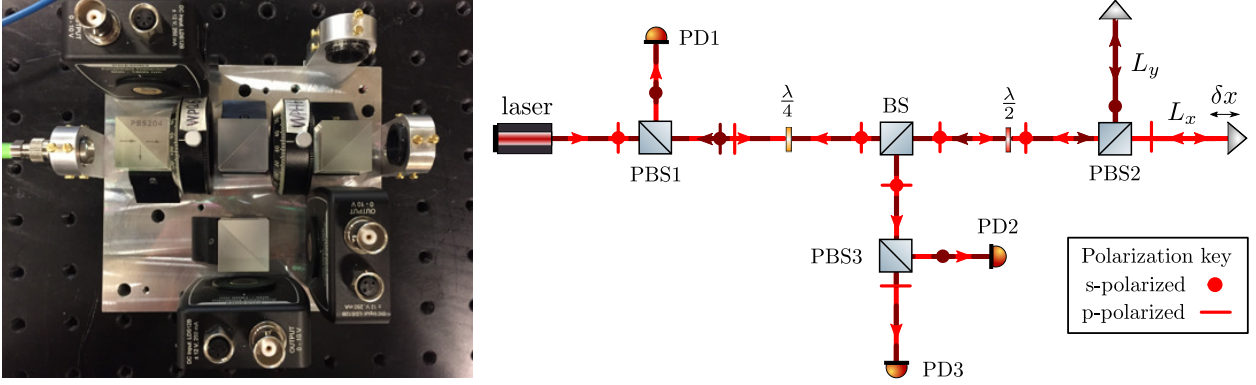


Figure 2.12: Top view (left) of the compact homodyne interferometer used to measure the motion of the inertial mass [141] and its corresponding optical setup (right).

The input field coming from the laser is defined by

$$E_{in} = E_0 \begin{bmatrix} 0 \\ 1 \end{bmatrix} e^{-i\omega t}, \quad (2.19)$$

where E_0 is the amplitude of the field and $\omega = 2\pi\frac{c}{\lambda}$.

Based on the Jones Matrix representation given in table 2.3, the power at the three photodiodes can be estimated knowing the amplitude of the input power $P_0 = E_0^2$ and the arm length difference $\Delta L = L_x - L_y$

$$PD1 = \frac{P_0}{8}(1 + \cos(2k\Delta L)), \quad (2.20)$$

$$PD2 = \frac{P_0}{8}(1 - \sin(2k\Delta L)), \quad (2.21)$$

$$PD3 = \frac{P_0}{8}(1 + \sin(2k\Delta L)). \quad (2.22)$$

Using Eq. (2.14) and Eq. (2.15), the relative displacement between the inertial mass and the payload can be recovered.

2.3.2 Identification of the sources of noise

Three different sources of noise are identified independently; the photodiode noise, the relative intensity noise and the phase noise of the laser. For each noise, an experiment is conducted and a model representing accurately the noise is set.

Table 2.3: List of the optics used in the interferometer and their corresponding Jones matrix given when the waveplates have the correct inclination with respect to the fast axis and when they have a inclination of an angle ϕ and the properties of the Thorlabs components. The quarter waveplate is assumed to be inclined with a 45° angle with respect to the fast axis and the half waveplate with a 22.5° angle.

Type	Thorlabs reference	Jones matrix	Jones matrix with Thorlabs parameters and inclination ϕ
Quarter waveplate	WPQ10E-1550	$\frac{1}{2}e^{-i\frac{\pi}{4}} \begin{bmatrix} 1+i & 1-i \\ 1-i & 1+i \end{bmatrix}$	$e^{-i\frac{\pi}{4}} \begin{bmatrix} \cos^2 \phi + i \sin^2 \phi & (1-i) \cos \phi \sin \phi \\ (1-i) \cos \phi \sin \phi & \sin^2 \phi + i \cos^2 \phi \end{bmatrix}$
Half waveplate	WPH10E-1550	$\frac{1}{\sqrt{2}}e^{-i\frac{\pi}{2}} \begin{bmatrix} 1 & 1 \\ 1 & -1 \end{bmatrix}$	$e^{-i\frac{\pi}{2}} \begin{bmatrix} \cos^2 \phi - \sin^2 \phi & 2 \cos \phi \sin \phi \\ 2 \cos \phi \sin \phi & \sin^2 \phi - \cos^2 \phi \end{bmatrix}$
BS R	BS018	$\frac{1}{\sqrt{2}} \begin{bmatrix} 1 & 0 \\ 0 & 1 \end{bmatrix}$	$\begin{bmatrix} \sqrt{0.5} & 0 \\ 0 & \sqrt{0.53} \end{bmatrix}$
BS T	BS018	$\frac{1}{\sqrt{2}} \begin{bmatrix} 1 & 0 \\ 0 & 1 \end{bmatrix}$	$\begin{bmatrix} \sqrt{0.42} & 0 \\ 0 & \sqrt{0.39} \end{bmatrix}$
PBS R	PBS204	$\begin{bmatrix} 1 & 0 \\ 0 & 0 \end{bmatrix}$	$0.97 \begin{bmatrix} 1 & 0 \\ 0 & 10^{-3} \end{bmatrix}$
PBS T	PBS204	$\begin{bmatrix} 0 & 0 \\ 0 & 1 \end{bmatrix}$	$0.96 \begin{bmatrix} 10^{-3} & 0 \\ 0 & 1 \end{bmatrix}$

Photodiode noise

The intensity measured at the active area of the photodiode is converted into current by energy transfer from the photons to the electrons. The current is then fed into a transimpedance amplifier, see Fig. 2.13. The output voltage is

$$V_{out} = -RI_{PD} , \quad (2.23)$$

where R is the resistance of the resistor, called the transimpedance gain, and I_{PD} is the current generated when photons are converted into electrons at the photodiode.

The photodiode used, the *PDA50B2* from Thorlabs, has a variable gain from 0 dB to 70 dB, hence, the resistance can be tuned between 1.51 k Ω and 4.75 M Ω .

In a photodiode, we can identify three different sources of noise listed in table 2.4. In addition, we have to consider the analog to digital conversion (ADC) error due to the limited number of bits of the digital system measuring the signal.

The circuit of the photodiode including these sources of noises is shown in Fig. 2.13. The output measured is

$$V_{out} = V_{th} + V_{ADC} + V_{1/f} + R(I_{PD} + I_{Dark} + I_{shot} + I_{1/f}) , \quad (2.24)$$

where V_{th} is the thermo-electrical noise, V_{ADC} is the noise of the analog to digital conversion, $V_{1/f}$ is the Flicker noise of the part of the circuit post OPA, I_{Dark} is the dark current (60 μ A

2.3. Readout model

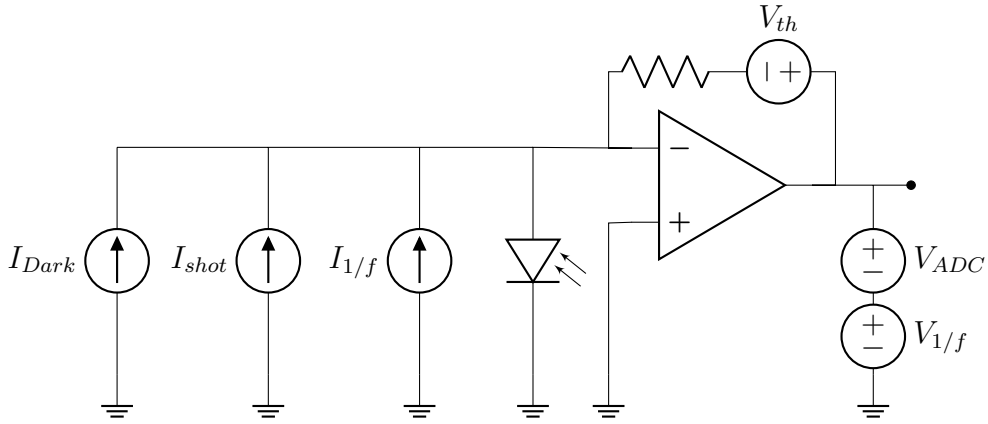


Figure 2.13: Transimpedance amplifier of the photodiode. The current coming from the active area of the photodiode is connected to the inverting input of the OPA. The current then circulates through the resistor and the corresponding voltage can be measured at the output. The different sources of noise are included.

for the PDA50B-EC), I_{shot} is the shot noise and $I_{1/f}$ is the Flicker noise of the part of the circuit before the OPA.

Description of the experiment: The photodiodes are placed in the dark, without any beam pointed to the active area, and the signal is recorded. The experiment was conducted for different values of the transimpedance gain from 0 dB to 50 dB. The signal was recorded using a National Instrument data acquisition system (DAQ) PXIe. The resulting ASD are the solid lines in Fig. 2.14.

From Fig. 2.14, we can see that for a gain lower than 20 dB, the photodiode ASD is the same. As the noise does not change depending on the gain of the transimpedance circuit below 20 dB, we can assume that below 20 dB, the dominant sources of noise are the noises related to the electronic circuits after the OPA (mostly due to the DAQ), see Fig. 2.13. Above 20 dB, the dominant Flicker noise at low frequency is the one related to electronics before the OPA which is amplified by the transimpedance gain.

Description of the model of the photodiode noise: The sources of noises are generated based on their definition given in table 2.4 and the data given by the manufacturer. In addition, based on the experiments, the gains of the two flicker noises, $I_{1/f}$ and $V_{1/f}$, are chosen to fit the data: $K = 10^{-6}$ V for the Flicker noise of the electronics after the OPA and $K = 6.6 \cdot 10^{-11}$ A for the Flicker noise of the electronics amplified by the transimpedance gain.

The resulting noises are then summed in the time domain and the ASD of the final signal is evaluated.

The model of the photodiode is compared with the experiment for different values of the gain in Fig. 2.14. Below 100 Hz, the model fits well the experimental data for all values of gain considered here.

Table 2.4: List of the sources of noise in the measuring system including the receiver photodiode, the electronic amplification circuit and the ADC. The equation characterizing their amplitude spectral density (ASD) and their definition are provided.

Type	Formula	Unit	Description
Shot noise	$\sqrt{2q(I + I_{Dark})}$	A/ $\sqrt{\text{Hz}}$	Due to the quantum nature of particles and photons, two photons with the same energy will not create the same number of pairs of electron-hole (q is an electric charge, I is the current in the photodiode) [30]
Thermo-electrical noise (Johnson-Nyquist)	$\sqrt{4k_BTR}$	V/ $\sqrt{\text{Hz}}$	Due to energy dissipation in the resistor (R is the resistor, T is the temperature, k_B is the Boltzmann constant)
1/f noise (Flicker)	$\frac{K}{f^{0.5}}$	V/ $\sqrt{\text{Hz}}$	Due to resistance fluctuation in all electronic components (K is a gain)
ADC noise	$\frac{q/2^n}{\sqrt{12f_N}}$	V/ $\sqrt{\text{Hz}}$	Due to the limited number of bits (q is the maximum voltage measured, n is the number of bits, f_N is the Nyquist frequency), see section 1.3.3

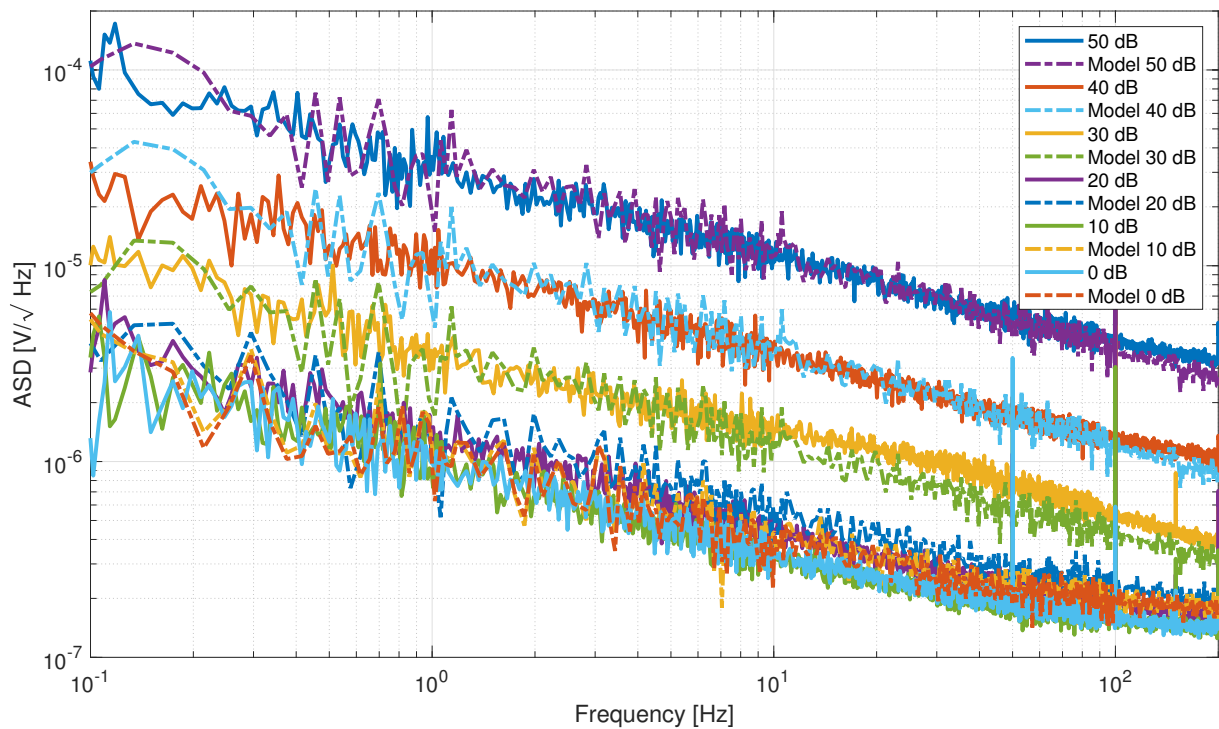


Figure 2.14: ASD of the photodiode signal measured experimentally (solid lines) and modeled (dashed lines) for different values of the gain.

Relative intensity noise

The intensity emitted by a laser fluctuates with time. One reason among others comes from the fact that the number of photons emitted by the laser and their energy at a certain time

2.3. Readout model

is not constant. This fluctuation is quantified by the laser relative intensity noise (RIN) [158]

$$RIN = \frac{\Phi_P}{P_0^2}, \quad (2.25)$$

where Φ_P is the power spectral density (PSD) (W^2/Hz) of the fluctuation of the laser power around the average power P_0 .

Description of the experiment: The laser is split at the beamsplitter in two and the two signals are measured by a photodiode, as shown in Fig. 2.15. Two measurements were made in the dark, one with and one without the laser turned on.

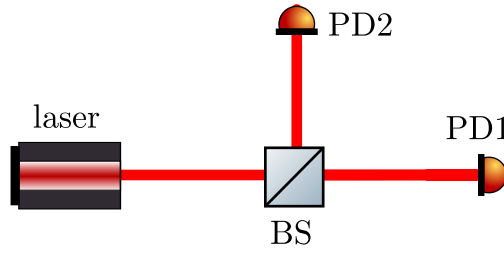


Figure 2.15: *The experiment conducted to identify the RIN: the incoming beam is split in two and each signal is measured by a photodiode.*

Description of the RIN model: In the time domain, the voltage measured at the photodiode when the laser is turned on is 9 V . A simulated laser signal has been generated with a power defined by [158]

$$P(t) = |P_0(1 + \delta P(t))|, \quad (2.26)$$

where $\delta P(t)$ is a time domain signal whose PSD matches the PSD of the RIN of the laser.

The corresponding RIN is a white Gaussian noise with a PSD amplitude of -132 dBc/Hz . The intensity P_0 is set so that the voltage at the photodiode is 9 V too. The RIN is kept constant at low frequency. This is recommended by the manufacturer who had not the information for the Koheras Adjustik X15 but had it down to 10 Hz for the Koheras Adjustik E15.

When adding the simulated laser power (converted into volts) to the signal of the photodiode measured when the laser is turned off, we can get an estimation of the “Laser turned on” curve.

The ASD of the two experiments and of the RIN model are shown in Fig. 2.16. You can see that the white Gaussian RIN does not fit the experiment.

By adjusting the RIN model to the experimental measurement (green dashed curve in Fig 2.16), the RIN model fits the data perfectly. The new RIN model is a white noise filtered by the following transfer function $F_{RIN}(s)$

$$F_{RIN}(s) = \frac{(2\pi \cdot 3 \times 10^2)^3 \cdot 2\pi \cdot 4}{4\pi^2 \cdot 50 \cdot (2\pi \cdot 18)^2} \frac{(s + 2\pi)(s + 2\pi \cdot 18)^2(s + 2\pi \cdot 50)}{s(s + 2\pi \cdot 4)(s + 2\pi \cdot 3 \times 10^2)^3}. \quad (2.27)$$

Validation of the new RIN model: The origin of the peak around 1 kHz in Fig. 2.16 can be confirmed thanks to Fig. 2.17. The signal from one of the two photodiodes when the laser is on and its corresponding noise are shown. To calculate the noise, a huddle test [159] is performed between the signals recorded by the two photodiodes. As the peak disappears it means that the two signals share the same noise source. The common signal between these two datasets is the laser. Consequently, we can assume that the peak comes from the laser itself as stated above and more precisely from the RIN of the laser, see equation (2.26).

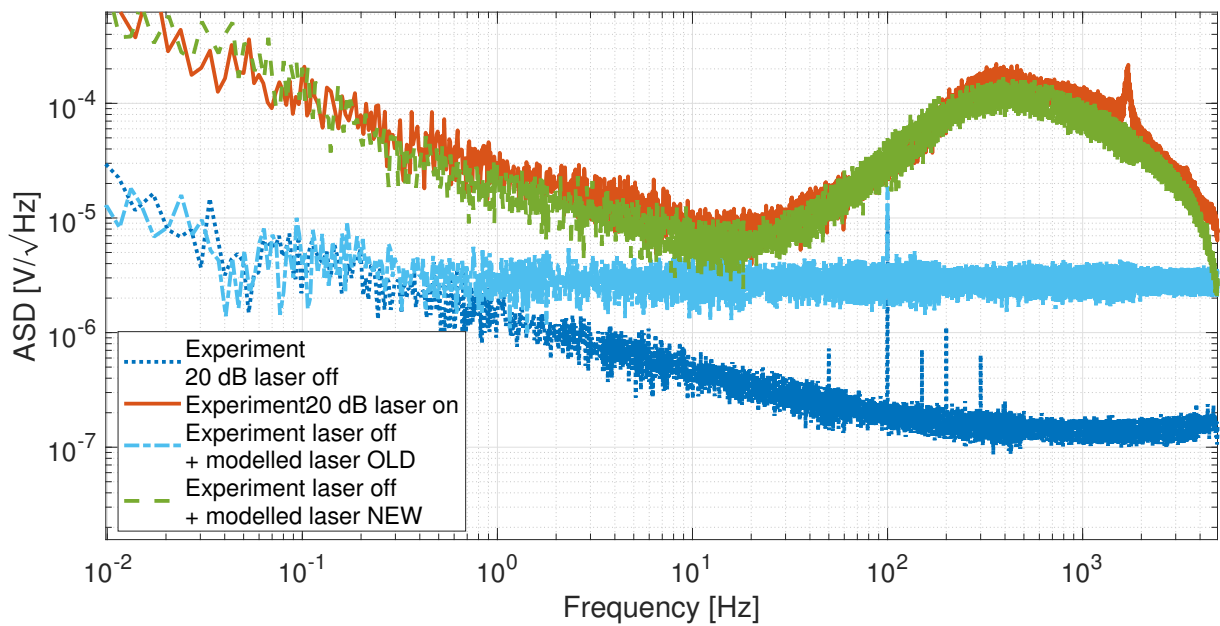


Figure 2.16: *ASD of the two experiments, laser turned off (dark blue dotted curve) and laser turned on (solid orange curve) and the fit of the experiment with the initial model of the RIN (light blue dashed dot curve) and the new one (green dashed).*

2.3. Readout model

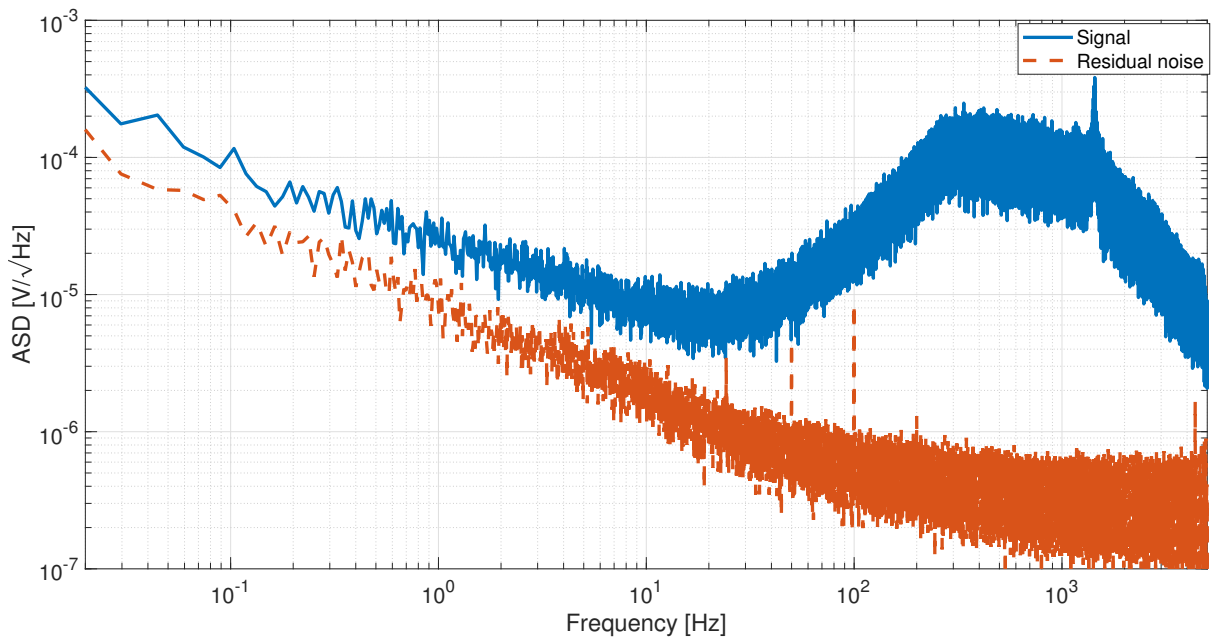


Figure 2.17: ASD of the signal measured by one photodiode when the laser is turned on (solid blue) and of the uncoherent signal between the two signals measured by the photodiodes (orange dashed).

Phase noise

A laser is never perfectly monochromatic due to quantum noise (essentially spontaneous emission) and changes in the properties of the cavity (refractive index of air fluctuations or cavity length fluctuations). Therefore, the frequency is distributed around the carrier frequency, see Fig. 2.18.a. The distribution has a lorentzian profile for most lasers, including semi-conductors laser [160].

The lorentzian profile can be characterized by the spectrum linewidth, also called the full width at half maximum (FWHM).

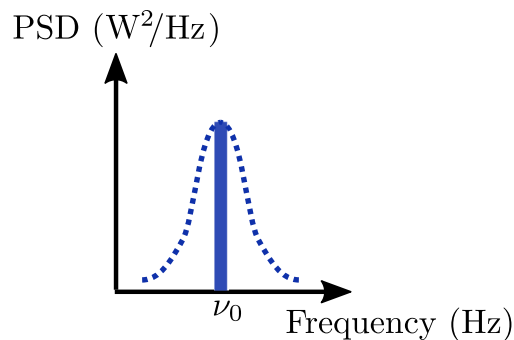


Figure 2.18: PSD of the optical frequency spectrum around the carrier frequency ν_0 in a perfect monochromatic laser (solid) and in a laser with frequency noise (dashed).

The frequency noise affects the signal of a Michelson interferometer because the two beams that recombine have not traveled the same distance. For a simple Michelson interferometer,

the beams that propagate in the two arms are

$$E_1 = E_0 e^{i(2kx_1 - (\omega_0 + \Delta\omega(t))t)}, \quad (2.28)$$

$$E_2 = E_0 e^{i(2kx_2 - (\omega_0 + \Delta\omega(t + \Delta t))(t + \Delta t))}, \quad (2.29)$$

where $\omega_0 = 2\pi\nu_0$ is the phase corresponding to the carrier frequency and $\Delta\omega(t) = 2\pi\Delta\nu(t)$ the corresponding frequency noise; Δt is the time delay due to the difference of distance traveled in the two arms.

Defining $\Delta L = 2(x_2 - x_1)$ the length difference between the two arms, the corresponding time delay is $\Delta t = \frac{\Delta L}{c}$ and hence, the corresponding phase noise is

$$n_{phase}(t) = \frac{2\pi\Delta L}{c} \Delta\nu(t). \quad (2.30)$$

- Identification of the phase noise of the Koheras Adjustik E15:

No identification of the phase noise of the Koheras Adjustik X15 has been found in the literature. On the contrary, measurement of the phase noise of the Adjustik E15 are published. In addition, the manufacturer ensures that the phase noise of the Adjustik X15 is lower than the Adjustik E15. From the results published, an overestimation of the phase noise of the Adjustik X15 can be deduced.

The different phase-noise measurement methods are explained in appendix E.

From the literature: Two papers present the phase noise of the Koheras Adjustik E15. Llopis *et al.* [161] measured the phase noise using the self-homodyne and the self-heterodyne methods. Okamoto *et al.* [162] used also the self-homodyne method to identify the phase noise.

The different phase noises of the Koheras Adjustik E15 given in the literature are shown in fig. 2.19. The phase noises of the Koheras Adjustik E15 and X15 given by the manufacturer are also plotted.

As expected the phase noise measured using the self-heterodyne method (blue square) is larger than when using the beat-note method (purple round).

Note that as the phase noise of the Koheras Adjustik series is supposed to be low, there is a possibility that all the signals shown are an overestimation of the real noise. To verify this, the phase noise with the lowest amplitude identified has been injected in the model of the Michelson interferometer presented in the next section. The estimated phase noise was indeed too big. Therefore, a fit of the phase noise given by the manufacturer with the laser that was already used to plot fig. 2.21 has been kept.

2.3.3 Description of the readout model

The model of the interferometer developed represents the optical set-up of Fig. 2.6 based on the Jones matrix formalism. It includes the ground motion measured experimentally and the parameters of the measurement: power, environmental conditions, etc. The properties of the optics are based on the datasheet of the products used and include their imperfections, see

2.3. Readout model

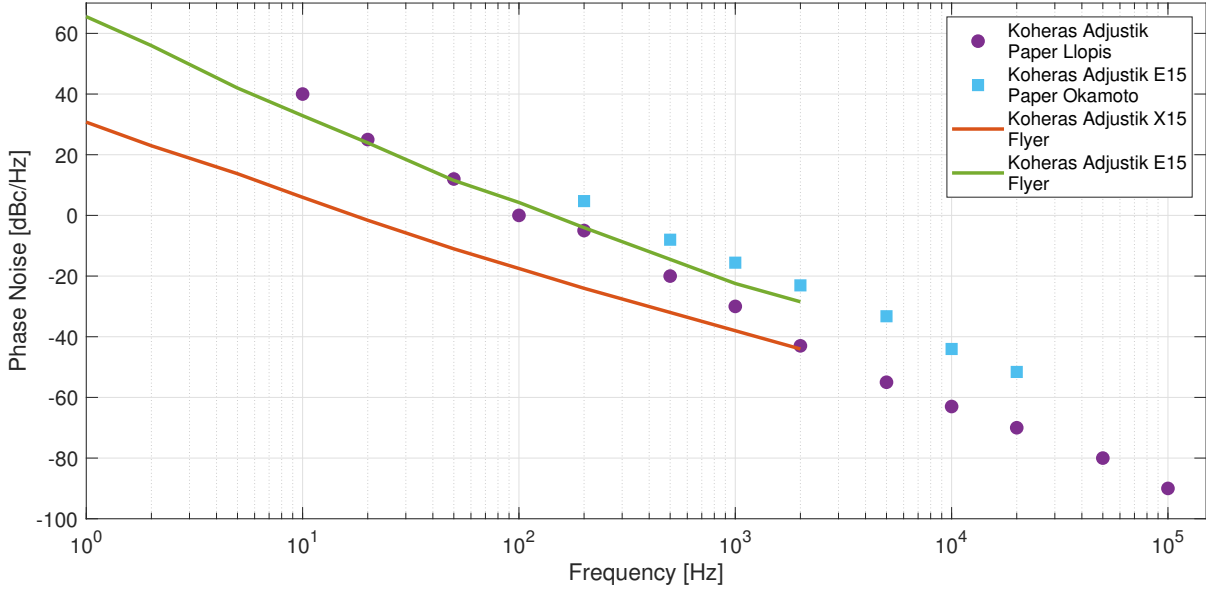


Figure 2.19: Phase noise of the Koheras Adjustik E15 measured using the beat-note method (purple dot), the self-heterodyne method (light blue square) and given by the manufacturer (solid green). The solid orange curve is the phase noise of the Koheras Adjustik X15.

table 2.3.

Moreover, the slow drift of the signal is identified and tuned as it dominates the low-frequency information. In Fig. 2.20, the drift of the signal measured by a horizontal inertial sensor over 80 seconds of measurement is shown; the signal drifts over more than 20 μm . The ASD confirms that this slow drift contributes only at low frequency. The long term drift is fitted by a third order polynomial and integrated to the readout model.

Finally, the noises identified in the previous sections are included in the model of the interferometer.

To validate the readout model, the time domain signal, the Lissajous figure and the ASD of the three photodiodes have first been compared to different sets of data. The Lissajous figure is the ellipse obtained when plotting the two quadrature signals, one in function of the other. Once it was proven that the model of the interferometer reproduces properly the interferometer, the displacement extracted from the model has been compared to the experimental one.

Adding the noises to the readout model

When considering the fitted model of the RIN, using the filter given in Eq. (2.27), and the detector noise, the actual ASD obtained with the model of the interferometer at each photodiodes underestimates at low frequency the ASD measured experimentally when the mirrors are blocked, as shown in Fig. 2.21. After a careful study, the fit of the low frequency drift as illustrated in Fig. 2.20 and the effect of the optics motion due to thermal fluctuations have been included to fit the measurement. To represent the motion of the optics, a Flicker noise combined with a white noise is generated that depends on the temperature and pressure.

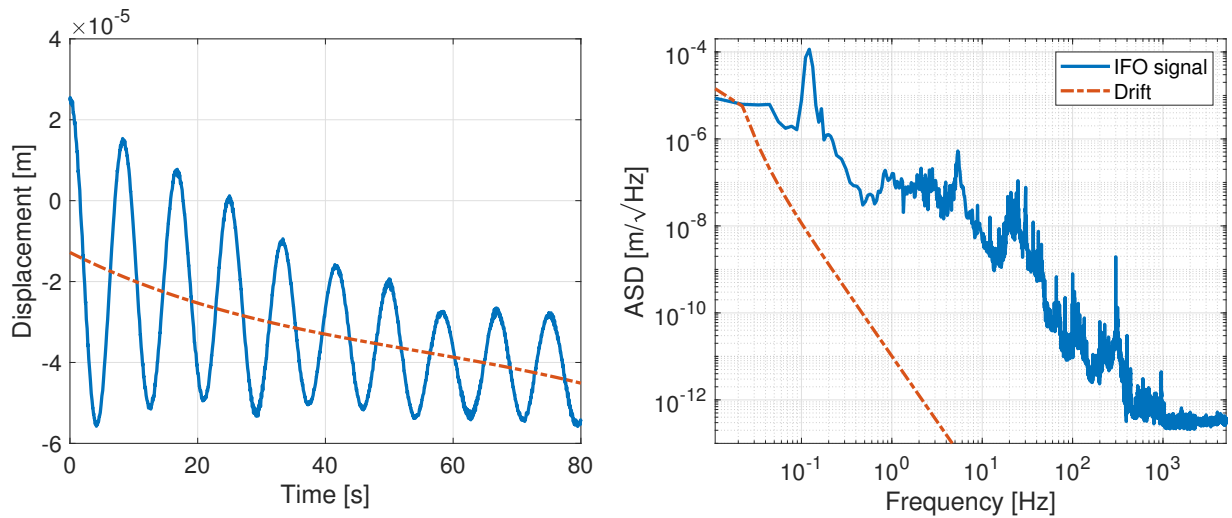


Figure 2.20: Example of drift of the signal measured by the interferometer. The signal measured (solid blue) and the fit of the drift (dash-dotted red) are shown in the time domain (left) and in ASD (right).

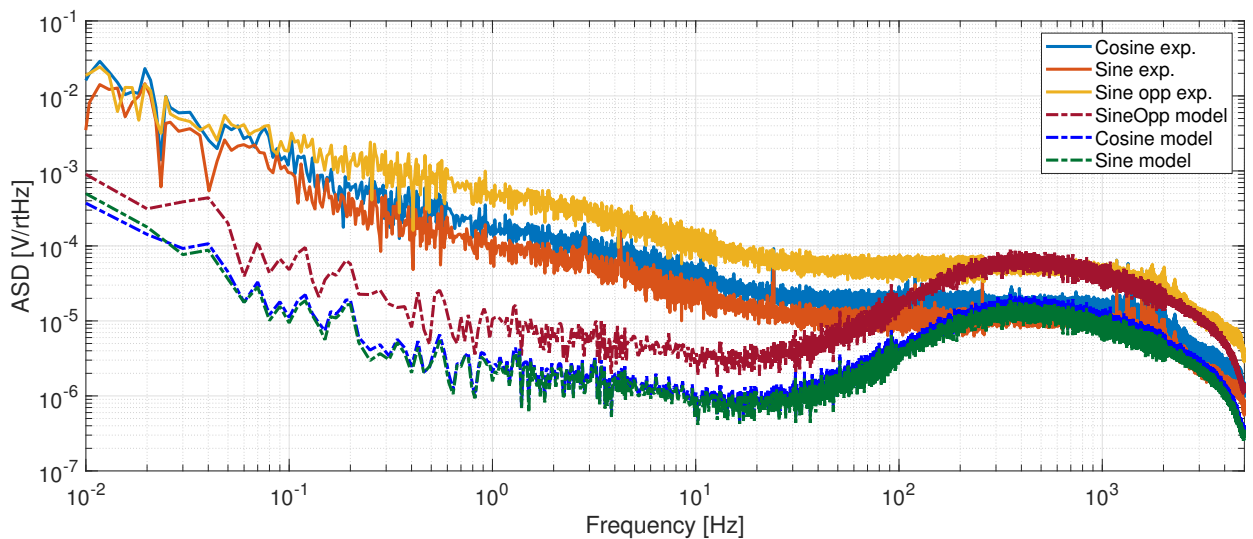


Figure 2.21: ASD of the signal measured at each photodiode measured experimentally (solid) and obtained with the model of the interferometer (dashed) when considering the fitted model of the RIN and the photodiode noise.

2.3.4 Comparison with experimental data

The final validation of the interferometer model consists in comparing the displacement extracted from the readout model to the experimental results when the mass is blocked and when it is free to move. The blocked-mass results will help to see if the estimation of the resolution of the sensor is correct.

The results for the pendulum blocked in air are shown in Fig. 2.22. The model of the interferometer reproduces properly the experiment except for the small peaks above 1 Hz. These peaks are resonances of the mountings holding the optics and are not included in the model.

2.3. Readout model

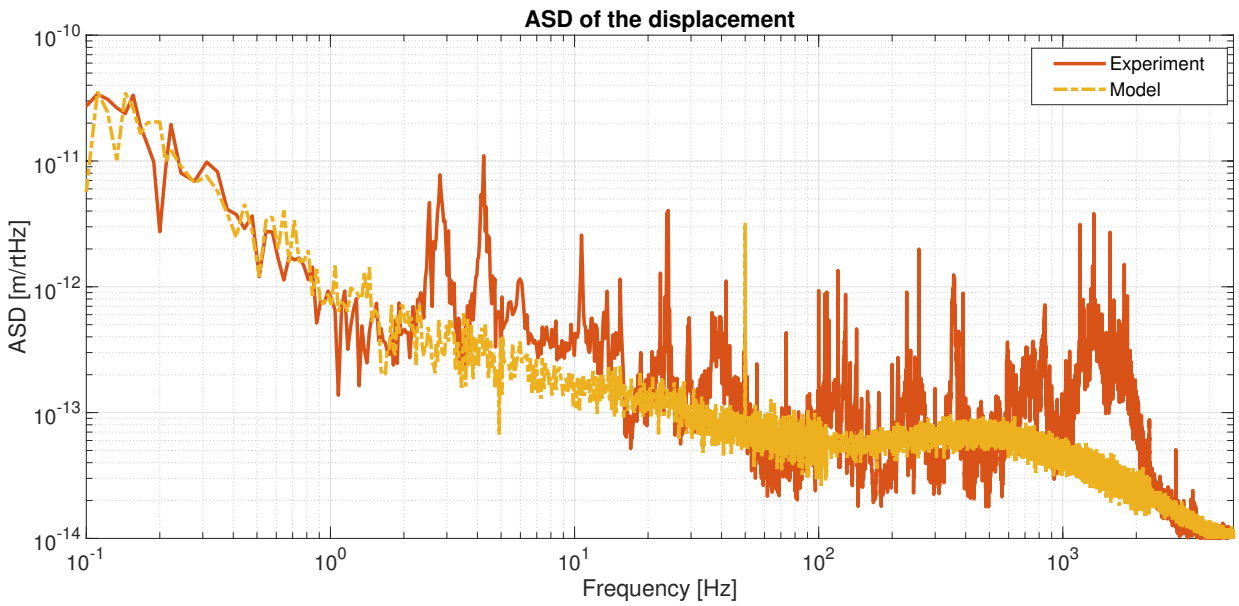


Figure 2.22: ASD of displacement measured experimentally (solid red) and obtained numerically (dash-dotted yellow) when the mass is blocked and the interferometer is in air. Except the peaks above 1 Hz due to vibration of the mountings, the model fits the experiment.

Finally, the readout model has been compared to a measurement when the interferometer measures the motion of a horizontal inertial sensor in air. The motion injected in the readout model was measured by a Guralp CMG-6T placed next to the inertial sensor. The ground motion signal was then multiplied by the sensitivity of the inertial sensor (resonance frequency at 0.12 Hz and damping $\xi = 0.1$). The comparison is shown in Fig. 2.23. Overall, the model of the interferometer reproduces properly the readout signal. Some peaks corresponding to the excitation of the mountings are visible above 10 Hz. For illustration, the estimated resolution of the interferometer is also plotted. It is evaluated by canceling the motion injected to the model.

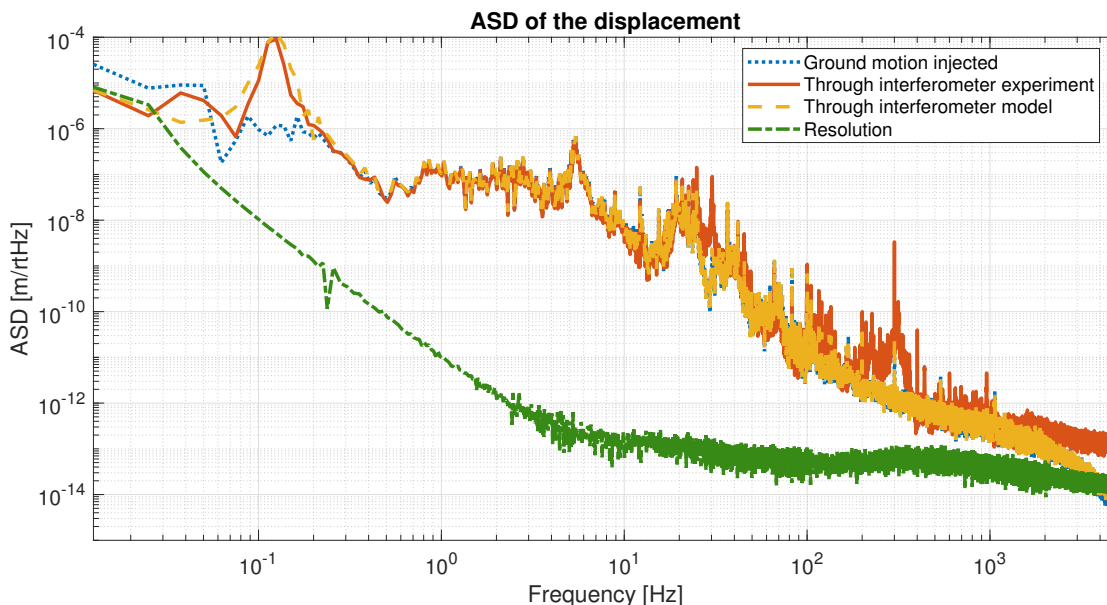


Figure 2.23: ASD of displacement measured experimentally (solid red) and obtained numerically (dashed yellow) for the horizontal inertial sensor in air. The motion injected in the interferometer is also shown (solid blue) and is under the yellow curve. The resolution of the sensor (dash-dotted green) is calculated by canceling the ground motion in the simulation.

2.3.5 Noise budgeting

The noise budget helps to understand the limitations of the resolution, and consequently will help to improve the resolution of the interferometer. In fact, the model of the interferometer presented in the previous section reproduces properly the resolution. Therefore, by tuning the different sources of noise in the model, we can identify which noise dominates which frequency range. This study is shown in Fig. 2.24 where each curve shows the resolution of the interferometer after progressively canceling the different sources of noise.

As expected the slow drift of the signal dominates the low frequency domain. At higher frequencies, the motion of the optics is dominating the signal up to 100 Hz. Above this frequency, the RIN is the main contributor to the noise of the signal.

Note that the other sources of noise of the photodiode have been tested but they were all giving a signal lower than the Flicker noise plotted in Fig. 2.24.

In conclusion, to improve the resolution, the drift of the signal and the motion to the optics due to transmission of motion from the mountings and due to thermal noise need to be investigated. For the later, placing the sensor inside a vacuum chamber can reduce this effect.

2.4. Resolution of the inertial sensor

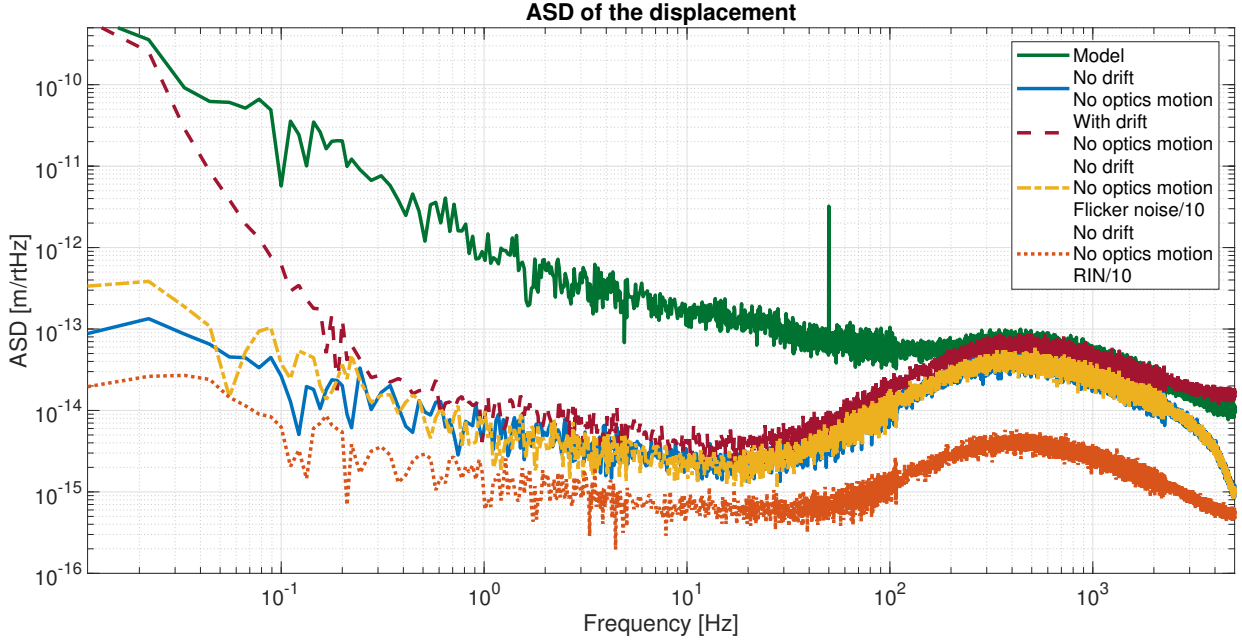


Figure 2.24: ASD of the resolution of the sensor (green) when tuning the different sources of noise: without drift and optics motion (solid blue), with drift and without optics motion (dark red dashed), with no drift, no optics motion and the flicker noise reduced of one order of magnitude (yellow dashed) and the same but when reducing the RIN of an order of magnitude (red dashed).

2.4 Resolution of the inertial sensor

The mechanical system and the optical readout are both sources of noise limiting the resolution of the device. The resolution of the optical readout is studied in section 2.3.

In section 1.2, damping in the suspension of passive systems has been introduced and corresponds to a dissipation of energy. Damping also occurs inside a material. This phenomenon is known as internal damping and corresponds to the energy dissipated, depending on the temperature. In a sensor, the dissipation of energy due to internal damping of the mechanical part is affecting the sensor resolution.

According to the fluctuation-dissipation theory, the thermal noise PSD due to internal damping is defined by [163]

$$\Phi_{th} = \frac{4k_B T \omega_0^2 \Phi_0}{m\omega((\omega_0^2 - \omega^2)^2 + k^2 \phi_0^2)} \quad [m^2/Hz] . \quad (2.31)$$

where k_B is the Boltzmann constant, T the ambient temperature, Φ_0 the loss factor, defined as $1/Q$, the inverse of the quality factor, $\omega_0 = 2\pi f_0$ where f_0 is the resonance frequency of the inertial sensor.

By summing the contribution to the signal measured of the readout noise and of the thermal noise of the inertial sensor, one can estimate the resolution of the sensor. In order to estimate the resolution with which the payload motion is evaluated from the relative

displacement measured between the payload and the inertial mass, the resolution of the signal has to be multiplied by the inverse of the sensor dynamics, Eq. (2.2). The thermal noise and the dynamics are evaluated based on the properties listed in table 2.5 from Ref. [141].

Table 2.5: Resonance frequency, Q factor and inertial mass of the vertical inertial sensor (VINS) and horizontal inertial sensor (HINS) measured in Ref. [141] and used for the estimation of the thermal noise.

	f_0 (Hz)	Q	m (kg)
VINS	0.253	30.01	0.6
HINS	0.108	14.51	0.3

The estimated resolution is shown in Fig. 2.25 for the horizontal inertial sensor (HINS) and in Fig 2.26 for the vertical inertial sensor (VINS). Both resolutions are dominated by sensor readout noise above 1 Hz. Thermal noise is dominating the low frequency domain as its ASD has a $\omega^{-5/2}$ slope, see Eq. (2.31).

Finally, the resolution of the two inertial sensors are compared with that of the GS-13 and the T240 in Fig. 2.27. The resolution of the inertial sensors characterized here overpass that of commercial products of more than one order of magnitude between 0.05 Hz and 5 Hz.

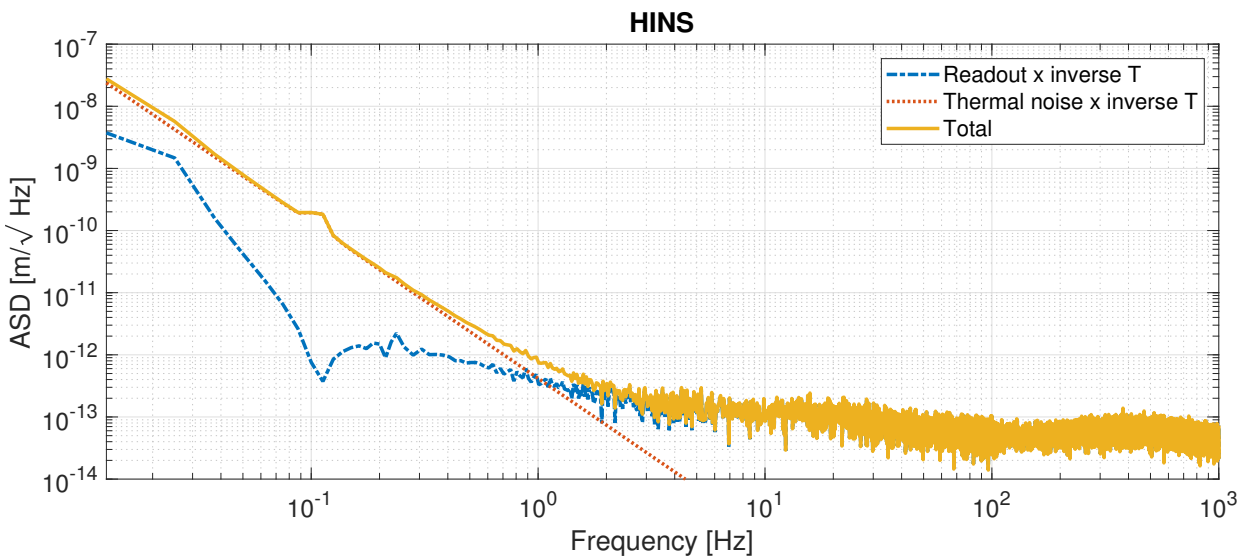


Figure 2.25: ASD of the estimated resolution of the HINS (solid yellow) when considering readout's resolution [141] (dash-dotted blue) and thermal noise (dotted red)

2.5. Summary

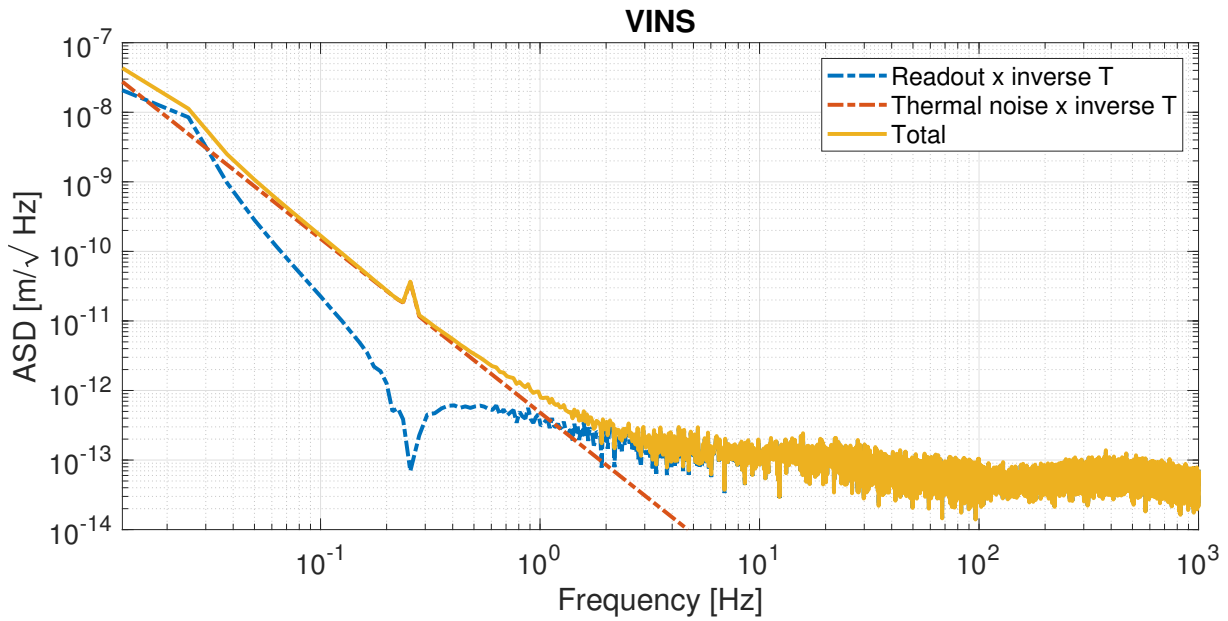


Figure 2.26: ASD of the estimated resolution of the VINS (solid yellow) when considering readout's resolution [141] (dash-dotted blue) and thermal noise (dotted red).

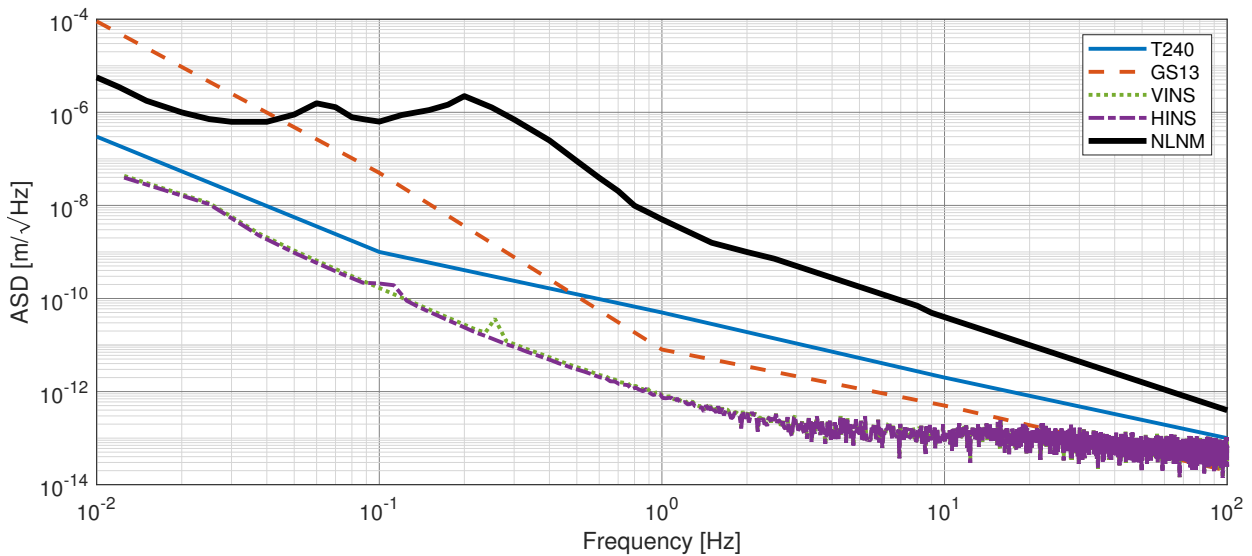


Figure 2.27: ASD of the estimated resolution of the VINS (dash-dotted purple) and the HINS (dotted green). The resolution of the T240 (solid blue) and the GS-13 (dashed red) are also shown. For indication, the new low noise model (NLNM) is shown (solid black).

2.5 Summary

In this chapter, the working principle of inertial sensors has been introduced. To obtain a good resolution, it has been highlighted that the motion of the inertial mass should be measured with an interferometric readout. The existing interferometers have been reviewed to study their resolution and understand their limitations and ways to reduce these. The optical setup of the Michelson interferometer used here is described. The numerical

characterization of this interferometer allows to understand the current resolution of the interferometer.

Finally, an estimated resolution of the inertial sensors has been evaluated by considering the resolution of the readout and the thermal noise of the inertial system. The inertial sensors present a better resolution than commercial products and are thus good candidates for the active isolation platform. The mechanics of the inertial sensor is studied in the next chapter.

Chapter 3

Inertial and liquid sensors

Contents

3.1 Gravity coupling in inertial sensors	67
3.1.1 Limitations for vertical control	67
3.1.2 Limitations for horizontal control	71
3.2 Decoupling strategies	74
3.3 Review of tiltmeters	77
3.4 The liquid sensor	79
3.4.1 Sensitivity	80
3.4.2 Noise budgeting	82
3.4.3 Coupling study	86
3.5 Summary	90

In order to measure the 6 degree-of-freedom (d.o.f.) of the platform, one should measure motion in the horizontal and in the vertical direction. Two spring-mass systems are used as inertial sensors; one pendulum oscillating around a horizontal axis to measure vertical motion and one pendulum oscillating around the vertical axis to measure horizontal motion. The readout described in chapter 2 is combined with these mechanics to sense the motion of the inertial mass suspended by the pendulum.

The sensor dynamics of an ideal inertial sensor is made of a pair of zeros at 0 Hz and a pair of complex conjugate poles at the frequency of the spring-mass mode of the inertial sensor, see Eq. (2.2).

In practice, inertial sensors are not perfect instruments. In comparison to the ideal sensor that measures only the motion in one degree of freedom, a real inertial sensor measures a coupled signal between different degrees of freedom due to its intrinsic sensitivity to the inclination of the payload in a gravitational field.

In this chapter, the sensitivity of inertial sensors to rotation is studied. Then, the mechanical system of the vertical and the horizontal inertial sensors is presented. The effect of the gravity coupling on the sensor dynamics is presented. Possible solutions to cope with this coupling

involve the use of a tiltmeter. A prototype of liquid sensor is characterized. As this sensor cannot measure exclusively the rotation, its sensitivity to translation is also studied.

3.1 Gravity coupling in inertial sensors

When subjected to rotation, the inertial mass of the inertial sensor moves because of gravity, see Fig. 3.1.a for a horizontal inertial sensor (HINS) and Fig. 3.1.b for a vertical inertial sensor (VINS). As the sensor can not make the distinction between a motion induced by a rotation or a translation of the platform of mass m , the signal measured contains both information. If the translation and rotation of the ground are defined respectively by w and θ , the equation of motion x_i of the inertial mass m_i , when including the effect of gravity, is in the Laplace domain

$$m_i s^2 X_i = k_i(W - X_i) + c_i s(W - X_i) + m_i g \sin \Theta . \quad (3.1)$$

From this equation of motion, the signal measured by the inertial sensor, the relative motion between the payload and the inertial mass $Y = X_i - W$, can be deduced. Assuming small motion, $\sin \Theta \approx \sin \Theta_0 + \Delta\Theta \cos \Theta_0$ and a null initial condition

$$(m_i s^2 + c_i s + k_i)Y = -m_i s^2 W + m_i g \Delta\Theta \cos \Theta_0 , \quad (3.2)$$

$$Y = \frac{-m_i s^2}{m_i s^2 + c_i s + k_i} W + \frac{m_i g \cos \Theta_0}{m_i s^2 + c_i s + k_i} \Delta\Theta . \quad (3.3)$$

At low frequency, the rotation dominates the signal measured by the inertial sensor [24]. This relation depends on the static inclination of the sensor around which the sensor oscillates θ_0 . For a VINS, θ_0 is around $\pi/2$ and for a HINS, it is around 0.

3.1.1 Limitations for vertical control

The VINS used is made of a STS-1V [92]. The interferometric readout is placed on top of the mechanism as seen in Fig. 3.2. On the picture, one can see the corner cube attached to the moving mass. The STS-1V can be represented as a pendulum suspended by a vertical spring and dashpot [96]. In practice, a leaf-spring is used to compensate gravitational force. In order to understand the dynamics of the sensor, a Simscape model has been developed. The Simscape library [164] from Matlab permits to model the interaction between bodies under the gravity field. As this is a toolbox from Simulink, Simscape is user friendly and allows to tune the parameters easily. Moreover, CAD can be properly imported in the model. These reasons justifies the choice of Simscape to model the sensors dynamics.

Based on CAD drawings and the working principle, the inertial sensor dynamics is modeled.

To study the effect of tilt-translation coupling on the VINS, a Simscape model of the sensor placed on a stage that can move vertically and in rotation is developed. The system represents the experiment conducted to validate the integration of the VINS developed in an active isolation stage [165].

The system is made of an extended structure, suspended as a pendulum capable to rotate

3.1. Gravity coupling in inertial sensors

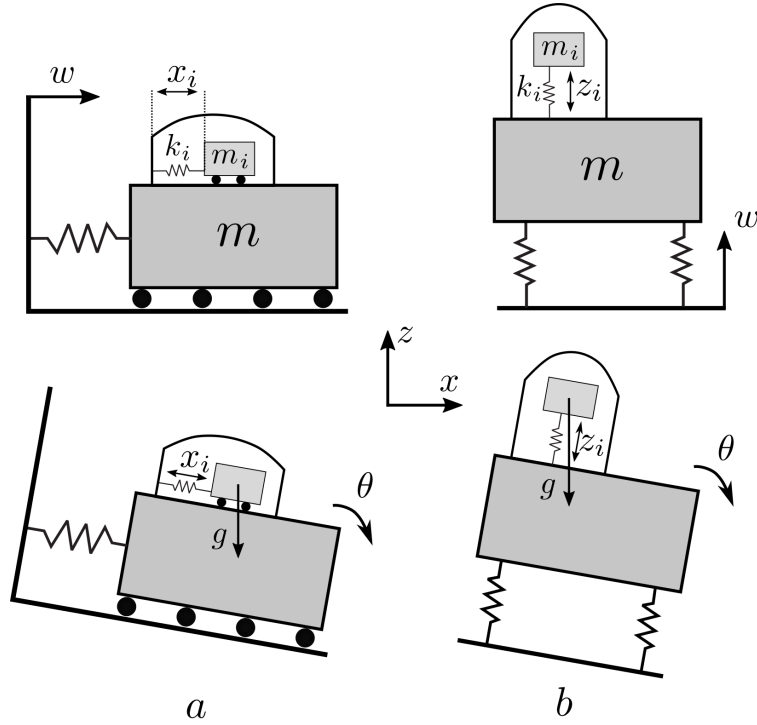


Figure 3.1: Horizontal (a) and vertical (b) inertial sensor's sensitivity to translation (top) and tilt (bottom) due to the gravity.

around a knife hinge, whose motion is sensed by a VINS, see Fig. 3.3. A vertical actuator developed in Ref. [166] is placed below the extended structure. The scheme of the corresponding Simscape model is shown in Fig. 3.3 where the VINS is represented by a pendulum.

The transfer function between the actuator and the inertial sensor obtained experimentally and numerically is shown in Fig. 3.4. To obtain a good plant identification at low frequency, several sine excitation experiments have been conducted, each at a different frequency. From Fig. 3.4, we can see that the Simscape model reproduces correctly the experiment and that the vertical inertial sensor is properly modeled in Simscape.

Due to the gravity coupling, there is a pair of complex conjugate zeros at 0.06 Hz in addition to the poles corresponding to the resonance of the system at 1.8 Hz and that of the sensor at 0.3 Hz. These zeros moves to 0 Hz if the pendulum of the sensor is perfectly perpendicular to gravity, which corresponds to the perfect inertial sensor dynamics. To better understand the origin of the zeros, the equations of motion of the system are calculated using the Lagrangian derivation, knowing the kinetic energy T and the potential energy V of the system

$$T = \frac{1}{2}m_1 l_{m1}^2 \dot{\theta}_1^2 + \frac{1}{2}m_2(l_1^2 + h^2 + 2l_1 h \sin \theta_{supp})\dot{\theta}_1^2 + \frac{1}{2}m_2 \left[l_2^2(\dot{\theta}_2 + \dot{\theta}_1)^2 + 2l_2(\dot{\theta}_2 + \dot{\theta}_1)\dot{\theta}_1(h \sin \theta_2 + l_1 \cos(\theta_2 - \theta_{supp})) \right] , \quad (3.4)$$

$$V = \frac{1}{2}k_{\theta_1}\theta_1^2 + m_1 l_{m1} g \sin(\theta_1 + \theta_{m1}) + \frac{1}{2}k_{\theta_2}\theta_2^2 + m_2 g(l_1 \sin(\theta_1 + \theta_{supp}) + h \cos \theta_1 + l_2 \sin(\theta_2 + \theta_1)) . \quad (3.5)$$

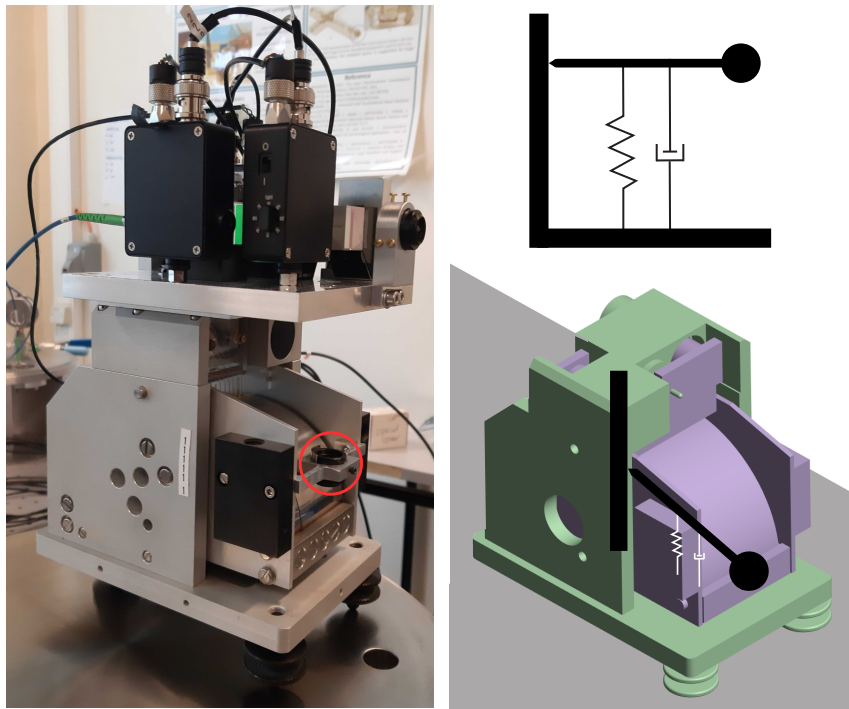


Figure 3.2: *The vertical inertial sensor. Left: picture of the mechanism with the interferometer on top. The corner cube connected to the inertial mass is encircled in red. Top right: sketch of its working principle. Bottom right: Simscape representation of the sensor. The moving part (purple) is connected to the rigid part (green) with a vertical spring.*

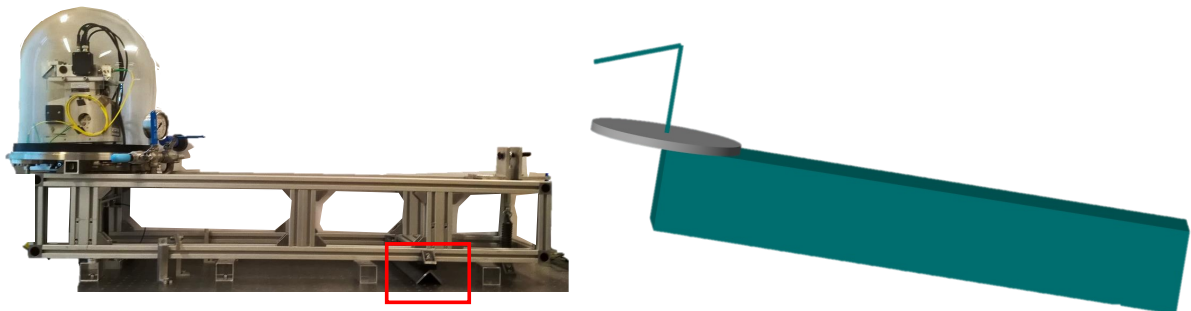


Figure 3.3: *Picture of the experimental stage studied in [165](left). The sensor is placed inside a vacuum chamber, the actuator is at the bottom left of this picture and the hinge (surrounded in red) and spring are at the bottom right of the picture. The corresponding Simscape model (right) includes a grey cylinder that represents the base of the vacuum chamber which weight 20 kg and hence cannot be neglected.*

The parameters used are represented in Fig. 3.5 and their assigned values are listed in table 3.1.

The equations are linearized for small motion around the equilibrium inclination of the payload θ_{01} and the equilibrium inclination of the sensor's pendulum θ_{02} .

3.1. Gravity coupling in inertial sensors

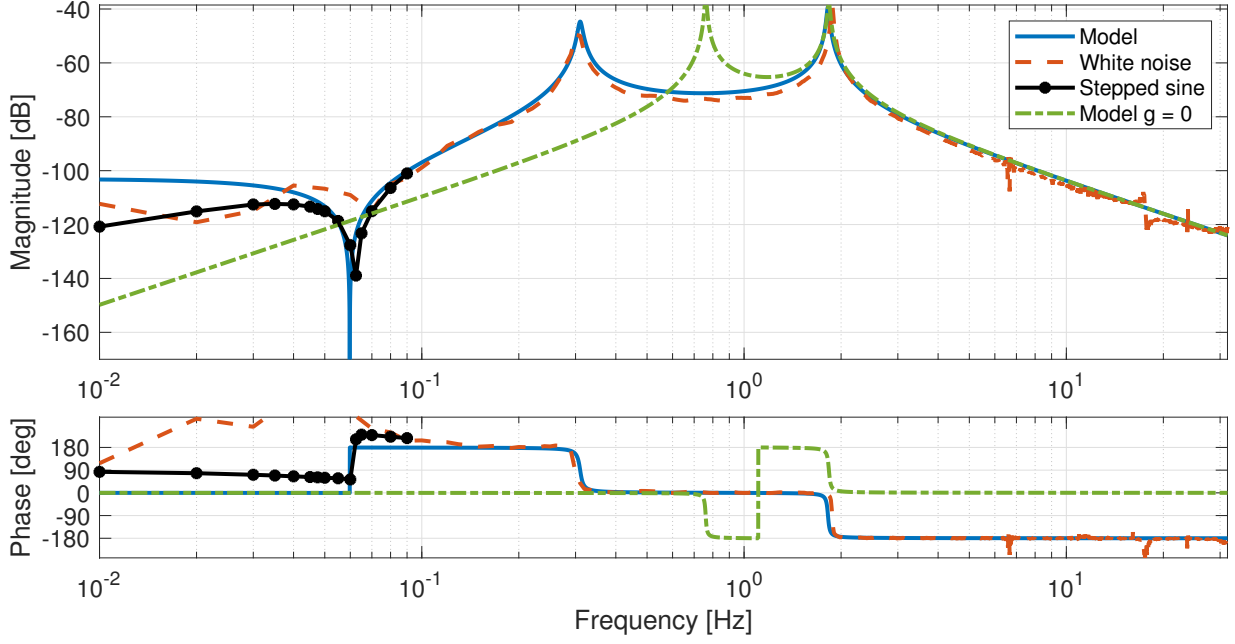


Figure 3.4: Plant measured experimentally with a white noise excitation (dashed orange), with a series of sine excitations (black dots) and obtained with the *sim*scape model (solid blue). Note that the experimental plant is multiplied by a low pass filter (cutoff frequency 0.1 Hz) [165]. The transfer function modeled in absence of gravity is also shown (dash-dotted green).

$$\begin{aligned}
 & [m_1 l_{m1}^2 + m_2 (l_1^2 + h^2 + l_2^2 + 2l_1 h \sin \theta_{supp}) + 2m_2 l_2 (h \sin \theta_{02} + l_1 \cos(\theta_{02} - \theta_{supp}))] \ddot{\theta}_1 \\
 & + [m_2 l_2^2 + m_2 l_2 (h \sin \theta_{02} + l_1 \cos(\theta_{02} - \theta_{supp}))] \ddot{\theta}_2 \\
 & + [k_{\theta_1} - m_1 g l_{m1} \sin(\theta_{01} + \theta_{m1}) - m_2 g l_1 \sin(\theta_{01} + \theta_{supp}) - m_2 g h \cos \theta_{01} \\
 & - m_2 g l_2 \sin(\theta_{02} + \theta_{01})] \theta_1 - m_2 g l_2 \sin(\theta_{02} + \theta_{01}) \theta_2 = F l \cos \theta_{01} ,
 \end{aligned} \tag{3.6}$$

$$\begin{aligned}
 & m_2 l_2^2 \ddot{\theta}_2 + [m_2 l_2^2 + m_2 l_2 (h \sin \theta_{02} + l_1 \cos(\theta_{02} - \theta_{supp}))] \ddot{\theta}_1 + [k_{\theta_2} - m_2 g l_2 \sin(\theta_{02} + \theta_{01})] \theta_2 \\
 & - m_2 g l_2 \sin(\theta_{02} + \theta_{01}) \theta_1 = 0 .
 \end{aligned} \tag{3.7}$$

Table 3.1: Values assigned to the parameters of the 1 d.o.f. model (analytical and *sim*scape) whose motion is measured by the VINS.

Parameter	Value	Parameter	Value
m_1	25 kg	l_{m1}	0.98 m
m_2	0.6 kg	l	0.84 m
h	0.1 m	θ_{01}	-3.7°
l_2	0.1 m	θ_{02}	0°
$l_{contact}$	1.04 m	θ_{supp}	10°

From these two equations, the transfer function between the rotation of the pendulum θ_2 and the actuator force F can be deduced. Knowing the length of the pendulum l_2 , the

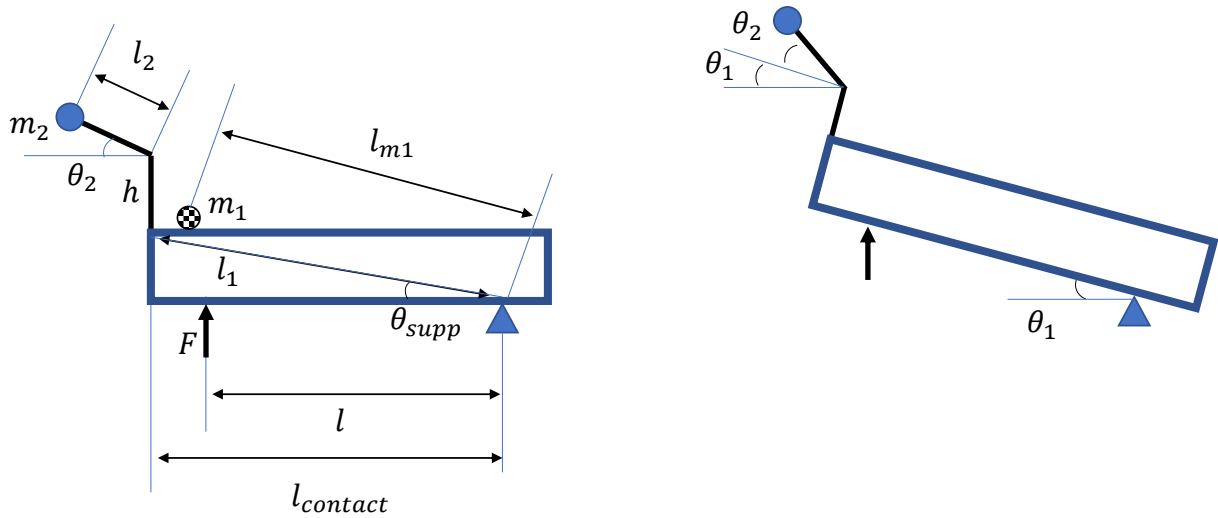


Figure 3.5: The double pendulum sketch at rest (left) and when the body is in motion (right).

relative displacement $l_2\theta_2$ corresponding to the signal measured by the VINS is evaluated for small displacement from the equations above. The static gain, poles and zeros obtained match the results shown in Fig. 3.4. The pair of undamped zeros z is located at

$$\omega_z = \pm \sqrt{\frac{-m_2gl_2 \sin(\theta_{02} + \theta_{01})}{m_2l_2^2 + m_2l_2(h \sin \theta_{02} + l_1 \cos(\theta_{02} - \theta_{supp}))}}. \quad (3.8)$$

As stated above, the location of the zeros depends on the static inclination of the inertial sensor in the gravity field. If the gravity is canceled, the pair of zeros moves to 0 Hz and the resonance frequency of the inertial sensor increases as the term proportional to θ_2 in Eq. (3.7) increases, see Fig. 3.4.

3.1.2 Limitations for horizontal control

The HINS is composed of a lab-made mechanism [141]. The sensor is made of a horizontal pendulum attached to the rigid part by a cross-spring hinge. The corner cube attached to the moving mass is visible in Fig. 3.6.

A Simscape model has also been developed to study the sensor dynamics.

The HINS has been characterized experimentally on a horizontal calibration stage. The horizontal stage is a table MB4545/M from Thorlabs placed on two LSP 2080 roller bearings from THX constraining the displacement to horizontal motion. The stage is excited by the piezoelectric transducer (PZT) APF705 from Thorlabs. To obtain the transfer function between the excitation, measured by a capacitive sensor, and the HINS, a white noise was injected to the PZT, see Fig. 3.8. To obtain a better resolution at low frequency, a sine excitation was injected at different frequencies between 0.01 Hz and 0.1 Hz.

The transfer function has two resonances, corresponding to the resonance frequency of the stage and of the inertial sensor. At low frequency, the transfer function shows a constant slope instead of the s^2 slope predicted by Eq. (3.3). The characterization stage was not

3.1. Gravity coupling in inertial sensors

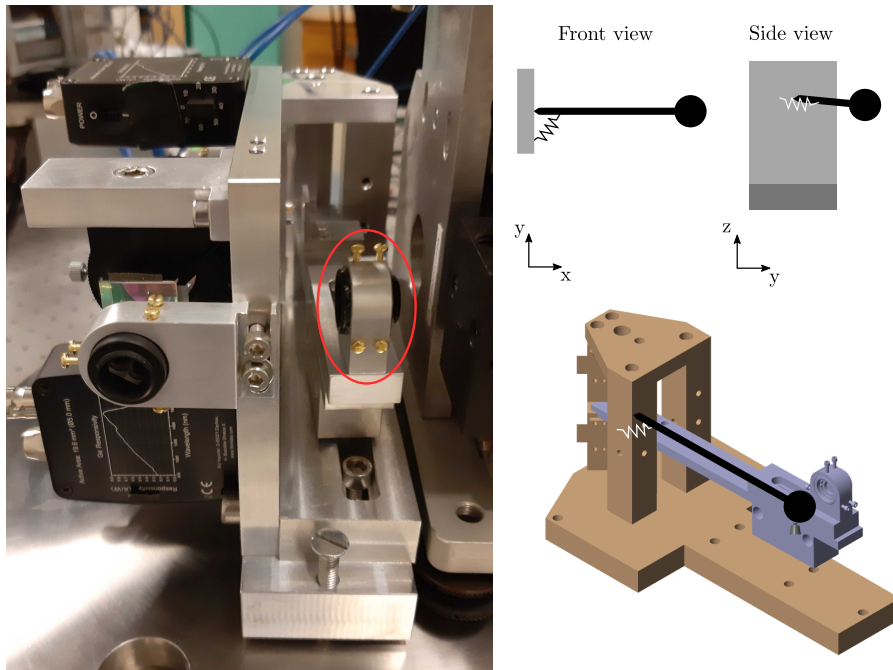


Figure 3.6: The horizontal inertial sensor. Left: picture of the mechanism with the interferometer on its left side. The corner cube connected to the inertial mass is encircled in red. Top right: sketch of its working principle. Bottom right: Simscape representation of the sensor. The moving part (purple) is connected to the rigid part (orange) with a rotational spring.

placed on a rigid optical table and hence, the motion injected was not a pure horizontal motion but a combination of translation and rotation.

To represent this stage, a Simscape model is developed based on the sketch shown in Fig. 3.7. The figure includes the definition of the parameters used to derive the equations of motion of the characterization stage. The values assigned to these parameters to fit the experiment are listed in table 3.2.

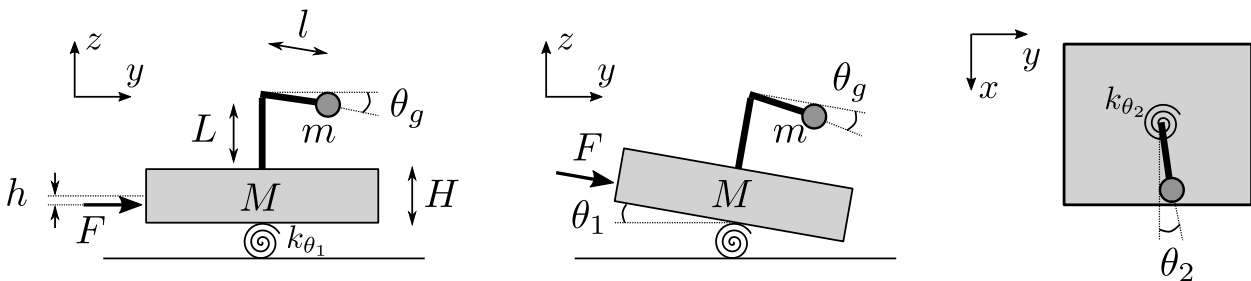


Figure 3.7: Model of the characterization stage for the HINS. Left: front view of the stage at rest with definition of the parameters used to derive the equations of motion. The angle θ_g represents the inclination of the pendulum with respect to the horizontal plane. Center: front view when the stage is tilted of an angle θ_1 . Right: top view of the system when the pendulum is tilted of an angle θ_2 .

Table 3.2: Values assigned to the parameters of the model (analytical and Simscape) of the calibration stage with the HINS.

Parameter	Value	Parameter	Value
M	6.6 kg	k_{θ_2}	1.1×10^{-4} N m/deg
m	0.3 kg	k_{θ_1}	7 N m/deg
h	3×10^{-2} m	θ_g	0.3°
H	12.7×10^{-2} m	θ_{01}	0°
L	5.7×10^{-2} m	θ_{02}	0°
l	0.14 m		

The kinetic energy T and potential energy V of the system are

$$T = \frac{1}{2}M\frac{H^2}{4}\dot{\theta}_1^2 + \frac{1}{2}m((2l^2 \sin \theta_g - 2l \cos \theta_2(H + L))\dot{\theta}_1\dot{\theta}_2 + l^2\dot{\theta}_2^2) + \frac{1}{2}m(l^2 \sin^2 \theta_2 + (L + H - l \sin \theta_g \cos \theta_2)^2)\dot{\theta}_1^2, \quad (3.9)$$

$$V = \frac{1}{2}k_2\theta_2^2 + mg(l \sin \theta_1 \sin \theta_2 + (L + H - l \sin \theta_g \cos \theta_2) \cos \theta_1) + \frac{1}{2}k_1\theta_1^2 + Mg\frac{H}{2} \cos \theta_1. \quad (3.10)$$

Using a Lagrangian derivation, the linearized equations of motion of the stage are obtained assuming small motion around the equilibrium inclination of the payload θ_{01} and the equilibrium inclination of the sensor's pendulum θ_{02}

$$\begin{aligned} & [M\frac{H^2}{4} + m(l^2 \sin^2 \theta_{02} + (H + L - l \sin \theta_g \cos \theta_{02})^2)]\ddot{\theta}_1 + ml[l \sin \theta_g - (H + L) \cos \theta_{02}]\ddot{\theta}_2 \\ & + [k_{\theta_1} - Mg\frac{H}{2} \cos \theta_{01} - mgl \sin \theta_{01} \sin \theta_{02} - mg \cos \theta_{01}(L + H - l \sin \theta_g \cos \theta_{02})]\theta_1 \\ & + mgl(\cos \theta_{02} \cos \theta_{01} - \sin \theta_g \sin \theta_{01} \sin \theta_{02})\theta_2 = Fh \cos \theta_{01}, \end{aligned} \quad (3.11)$$

$$\begin{aligned} & ml^2\ddot{\theta}_2 + ml[l \sin \theta_g - (H + L) \cos \theta_{02}]\ddot{\theta}_1 + mgl(\cos \theta_{02} \cos \theta_{01} - \sin \theta_g \sin \theta_{01} \sin \theta_{02})\theta_1 \\ & + [k_{\theta_2} - mgl(\sin \theta_{02} \sin \theta_{01} - \sin \theta_g \cos \theta_{01} \cos \theta_{02})]\theta_2 = 0. \end{aligned} \quad (3.12)$$

From these equations, the transfer function between θ_2 , the motion of the pendulum of mass m , and the actuator F is deduced. There is a pair of real zeros z located at

$$\omega_z = \pm \sqrt{-\frac{g(\cos \theta_{02} \cos \theta_{01} - \sin \theta_g \sin \theta_{01} \sin \theta_{02})}{l \sin \theta_g - (H + L) \cos \theta_{02}}}. \quad (3.13)$$

The zeros are real because the numerator is always positive and the denominator negative as θ_g , θ_1 and θ_{02} are small.

The fitted model is also shown in Fig. 3.8. By multiplying θ_2/F by the length of the pendulum l and the stiffness of the suspension of the PZT APF705 from Thorlabs ($4 \cdot 10^4$ N/m), the modeled transfer function between the displacement measured by the HINS and the motion induced by the actuator is deduced.

A good match is obtained between the model and the experiment below 10 Hz. The flexible modes above 10 Hz are not reproduced as the model considers only rigid bodies.

3.2. Decoupling strategies

Again, the model when canceling gravity is also shown in Fig. 3.8. The pair of zeros of the sensor dynamics moves to 0 Hz, according to Eq. (3.13).

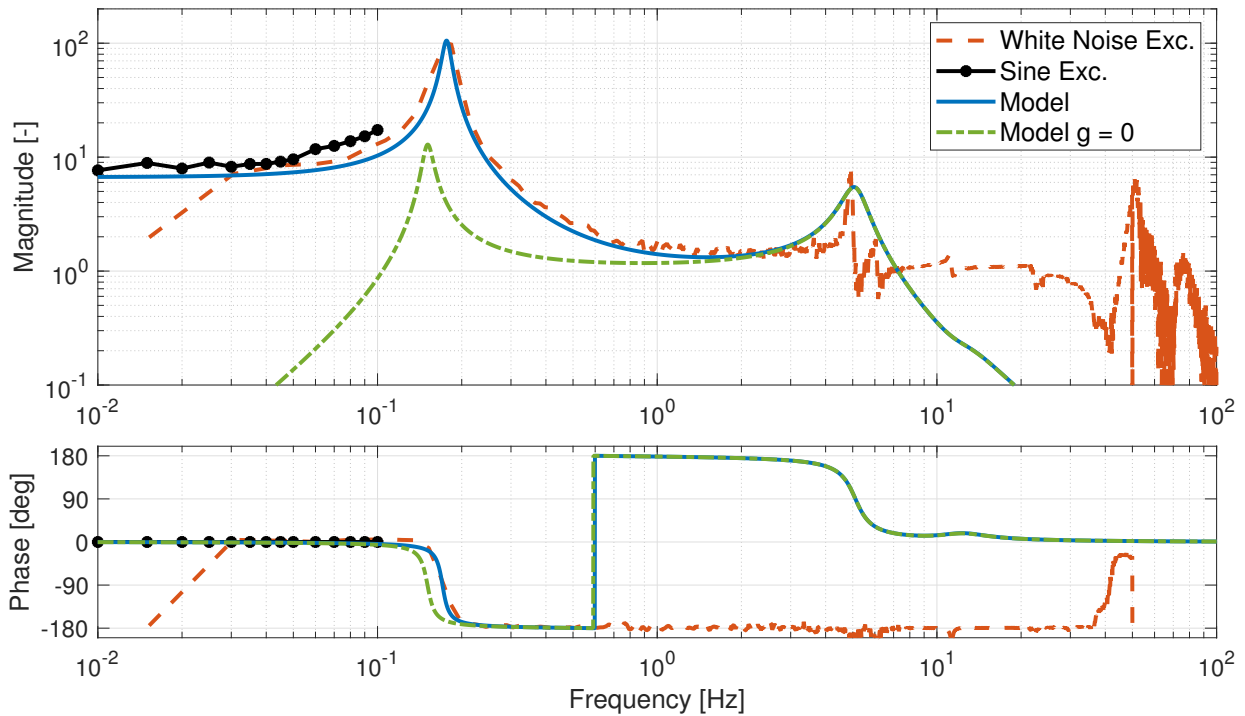


Figure 3.8: *Transfer function between the motion induced by the actuator and the signal measured by the HINS. The excitation is measured by a capacitive sensor. The experimental transfer function measured by exciting with a white noise is shown in dashed orange, with a series of sine excitation in dotted black and obtained with the Simscape model in solid blue. The transfer function modeled in absence of gravity is also shown (dash-dotted green).*

3.2 Decoupling strategies

The signal measured by an inertial sensor is dominated at low frequency by the rotation of the payload and/or that of the ground due to gravity as shown in section 3.1.

In addition, we have seen that the static inclination of an inertial sensor has an influence on its dynamics at low frequency as shown in section 3.1.1 and section 3.1.2. Instead of having a pair of zeros at 0 Hz, the pair of zeros is at a higher frequency.

To reduce the coupling between the translation and the rotation of the sensors and hence, improve the dynamics at low frequency, several solutions can be implemented. On one hand, there are solutions to mechanically decouple the translation from rotation. On the other hand, one can subtract the tilt from the signal measured by the inertial sensor. This solution involves to use a tiltmeter to sense the inclination of the platform.

Mechanical decoupling

Some designs developed reduce the rotation of the inertial sensor relatively to the payload by using a guide [82, 167, 168]. In Ref. [167], the spring guiding the motion of the HINS is made of vertical blades connected to the ground, see Fig. 3.9.a. It constrains the motion of the HINS and thanks to this improvement, the performance of the active isolation platform has been improved from a cumulative acceleration spectrum at 100 Hz of $46 \mu\text{m/s}^2$ to $37 \mu\text{m/s}^2$. As mentioned, this only reduces the relative rotation of the inertial sensor to the payload. If the payload has a static inclination, the guide can not prevent the sensor from moving due to the gravity, see Fig. 3.9.c.

In Ref. [83], a guide made of hinges reduces the sensitivity of HINS to vertical excitation at low frequency (below the suspension modes of the platform i.e. below 1 Hz) by two order of magnitudes.

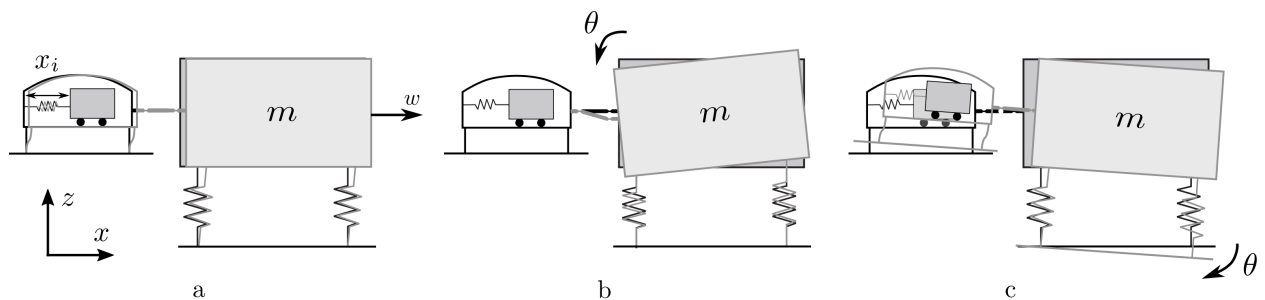


Figure 3.9: *HINS constrained by vertical blades [82] and subjected to different motion. (a) Translation of the payload, (b) rotation of the payload and (c) rotation of the ground. The inertial sensor is not sensitive to the tilt of the payload but it cannot make the distinction between translation of the payload and rotation of the ground.*

In order to mitigate the sensitivity of inertial sensor to absolute rotation, other solutions have been developed. First, the sensor is suspended in Ref. [169], see Fig. 3.10.a. When subjected to tilt, the suspended sensor rotates around the joint and it remains perpendicular to gravity. With this configuration, the sensitivity to tilt of the HINS has been reduced of three orders of magnitude below the suspension modes of the system. Note that this is made at the expense of a reduction of sensitivity of the sensor to translation below the tilt mode frequency of the suspended platform.

Second, the horizontal sensor can be made of a double pendulum [170], see Fig. 3.10.b. From the horizontal relative motion between the two suspended masses, one can recover the horizontal motion of the supporting structure. This idea has not been tested experimentally.

To compare the performance of the proposed solutions, the tilt-translation ratios of the methods are shown in Fig. 3.11; they correspond to the sensitivity of the sensor to the ground rotation over that to the ground horizontal motion. Note that the curves shown here are only valid below the frequency of the suspension mode.

The solutions are compared with the sensitivity to tilt of the classical inertial sensor at low frequency. From Eq. (3.3), the tilt-translation coupling is g/s^2 for a HINS. This ratio is unchanged when using blades to guide and vertical hinges to constrain the motion of the sensor. Indeed, as shown in Fig. 3.9.c, the sensor is still sensitive to ground rotation with

3.2. Decoupling strategies

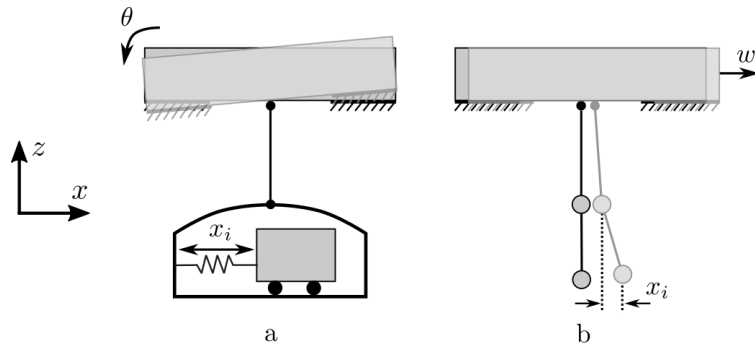


Figure 3.10: Solutions to reduce the tilt-horizontal coupling in a HINS. (a) HINS suspended on a pendulum [169] when subjected to ground rotation θ . (b) Representation of the double pendulum sensor [170]. When the ground moves horizontally w , the relative distance between the masses of the two pendulums varies.

this configuration.

When suspending the sensor, the sensor is assumed to be highly decoupled from rotation at low frequency. This concept has been tested experimentally by suspending the sensor with two wires and due to friction forces and some misalignments, the decoupling is less effective; It reduces still by more than two orders of magnitude the ratio in comparison to the classical case.

The double pendulum has the same theoretical performance as the suspended sensor. This concept has never been tested experimentally but it is expected that the reduction of ratio will also be affected by friction forces.

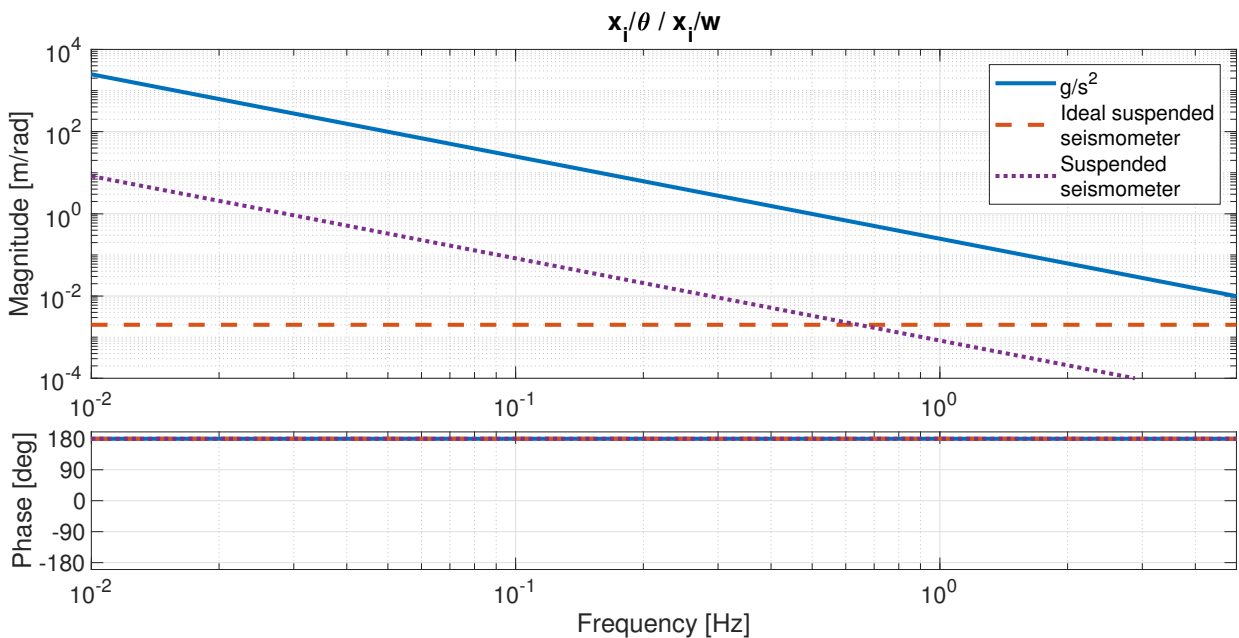


Figure 3.11: Tilt-translation sensitivity of inertial sensors for different decoupling solution compared with the classical HINS ratio (solid blue). The modeled suspended sensor (dashed red) reduces drastically the ratio at low frequency [169]. The experimental version of the suspended sensor (dotted purple) shows mild performance. Note that the ratios shown here are only valid below the frequency of the suspension mode where the tilt is dominating the signal measured by inertial sensors.

Canceling tilt from inertial sensor signal

In Ref. [171], the signal from a tiltmeter has been used to subtract the tilt motion measured by a T240 which reduced by one order of magnitude the coupling between 5 mHz and 100 mHz. For the isolation stage developed in this thesis, two solutions with a tiltmeter can be considered to reduce the dominance of the rotation at low frequency.

- Sensor correction: the signal from a tiltmeter is used to correct the signal of the inertial sensor.
- Cascade control: an inner control loop with a tiltmeter is closed to reduce the static inclination of the payload and inertial control is applied in an outer loop.

For both solutions, studied in chapter 4, a tiltmeter is required that is sufficiently insensitive to horizontal acceleration and has a good resolution at low frequency.

Note that the tiltmeter will be used to measure the rotation around the x and the y axis (not the z-axis) as these are the inclinations that influence the gravity coupling in inertial sensors.

3.3 Review of tiltmeters

There exists different types of rotation sensors but some can only measure the relative inclination between two bodies [172]. In order to measure the inclination of the payload relative to the gravity, the inclination has to be measured by comparison with a reference. The reference can be a balanced beam placed on a pivot, see Fig. 3.12. A relative displacement sensor measures the relative motion Δx between the balanced beam and the ground. Knowing the distance L between the pivot and the point where the sensor is located, the angle can be recovered $\theta = \Delta x/L$. The pivot is usually made of thin flexures with a thickness on the order of $10 \mu\text{m}$ [173, 174]. To reduce the tilt-horizontal coupling, the center of mass of the beam has to be aligned with the pivot.

The resolution of tiltmeter using the balance beam principle reaches $0.2 \text{ nrad}/\sqrt{\text{Hz}}$ above 0.1 Hz in Ref. [173] and $0.1 \text{ nrad}/\sqrt{\text{Hz}}$ above 50 mHz for a force-balanced version in Ref. [174].

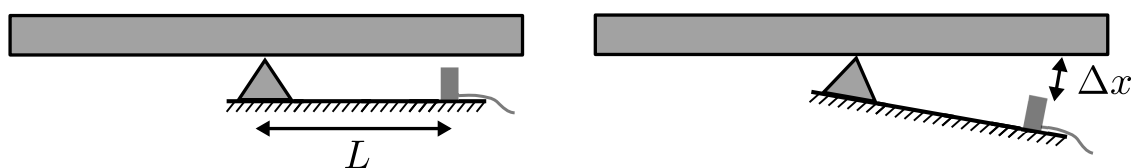


Figure 3.12: *The beam-pivot principle: the relative distance between the ground and the beam Δx is measured and the inclination is recovered from this signal. The beam is the reference and remains perpendicular to gravity, even when the platform is tilted (right).*

The reference can also be the surface of a liquid which is presumably always perpendicular to the total acceleration felt by the liquid that includes gravity and horizontal acceleration of the ground. A laser is pointing to the liquid surface, reflected by the liquid and its intensity is measured by a quadrant-photodiode. In case of rotation, the whole setup is inclined except the liquid surface, see Fig. 3.13. Therefore, the incident angle on the liquid surface varies

3.3. Review of tiltmeters

with the tilt of the setup.

A four quadrants photodiode (QUAD-PD) is a photodiode whose active area is divided into four parts. When the laser is deviated, some areas receive a larger intensity. From this difference in intensity, the displacement of the beam spot on the photodiode can be recovered and the angle deduced.

Knowing the distance traveled by the beam L and the displacement of the beam spot from the center of the photodiode Δx , the angle measured is

$$\theta = \frac{\Delta x}{2L} . \quad (3.14)$$

The resolution of the liquid sensor can be improved by adjusting precisely the size of the laser's cross section. The beam's section is easily adjusted with an iris or a ff' optical assembly i.e. two lenses are positioned at a distance equivalent to the sum of their focal length, f and f' , from each other.

The resolution obtained with this sensor is below $0.5 \text{ nrad}/\sqrt{\text{Hz}}$ between 0.01 Hz and 1 Hz [175].

The resolution of the tiltmeter using a liquid reference and a balanced beam found in the literature are similar. However, the resolution of the liquid sensor is difficult to understand as no noise budget is available. In addition, the surface of a liquid is inclined with horizontal acceleration. The sensitivity to translation of the liquid sensor has to be studied.

The next section presents the liquid sensor developed and the different experiments led to characterize it: sensitivity, noise budgeting and sensitivity to translation.

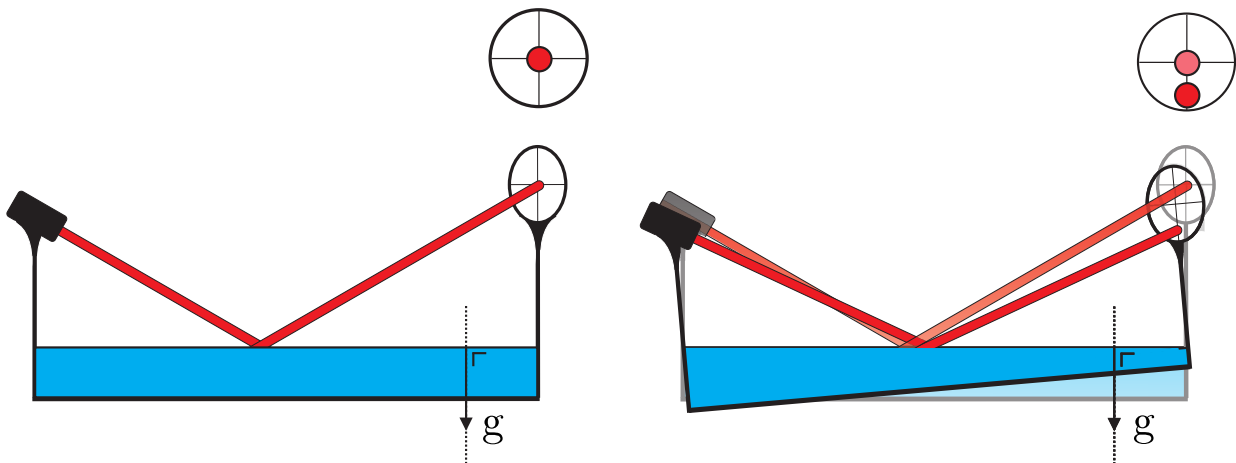


Figure 3.13: Working principle of the liquid sensor when the only acceleration is the gravity g : The beam is aligned with the center of the quadrant photodiode at rest (left). When the structure is tilted, the laser and the photodiode are tilted but the liquid surface remains perpendicular to gravity (right). The transparent illustration shows the path of the laser without tilt. For indication, the location of the beam spot on the photodiode is illustrated for both cases on top of the figures.

3.4 The liquid sensor

The liquid sensor developed at PML is shown in Fig. 3.14. The readout is based on the prototype developed in Ref. [175]. A 60 cm long horizontal frame supports the whole readout. On one side of the frame the red light laser is fixed. The light emitted is reflected by one beamsplitter and transmitted by a second one to reach the surface of the liquid mirror. The light reflected by the mirror is reflected by the second beamsplitter and its intensity is measured by a quadrant photodetector placed at the other end of the frame.

The liquid mirror is a small volume of Mercury, chosen for his liquid state at ambient temperature and its reflectivity. To avoid any oxidation, the Mercury is sealed with Nitrogen in a container, see Fig. 3.14.b.

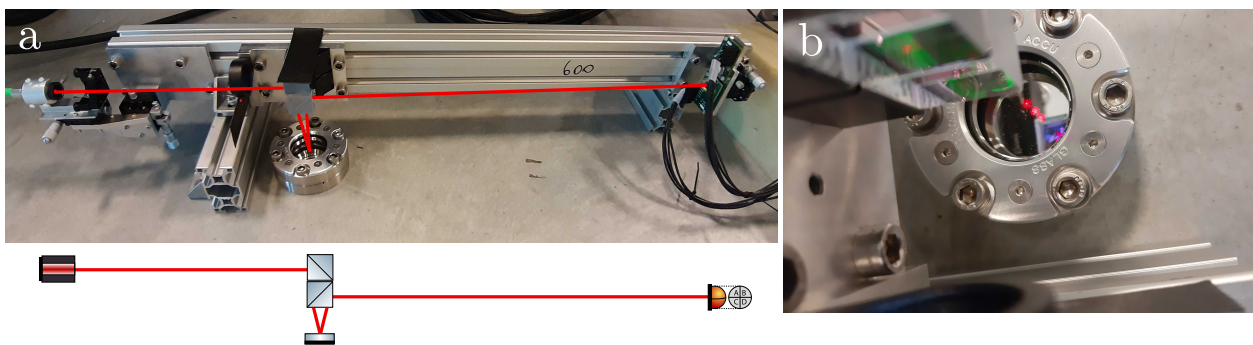


Figure 3.14: Sensor with a liquid mirror as a reference: (a) Optical system from left to right: the laser beam is reflected by the beamsplitter and arrives at the surface of the liquid mirror. After reflection by the mirror, it is reflected by a second beamsplitter and is measured by the photodiode. (b) The liquid mirror is made of Mercury sealed with Nitrogen to avoid oxidation.

The active area of the QD50-0-SD quadrant-photodiode has a diameter of 8 mm. Based on the diameter of the detector, the beam spot has to be 4 mm to have the best working range which is ± 2 mm. Indeed, on one hand, if the beam spot is larger, one part of the beam will be out of the active area before the beam travels the 2 mm distance, see Fig. 3.15.c. On the other hand, a beam smaller than 4 mm diameter will have a smaller working range as the spot will be on two active areas with a smaller displacement, see Fig. 3.15.d.

As the distance between the laser and the photodiode is 60 cm, the largest inclination measured is $\pm \frac{2}{2 \times 600} = \pm 0.1^\circ$.

One liquid sensor can be used to measure the rotation around the two horizontal axes, see Fig. 3.16. In fact, if the beam of the sensor is aligned with the y axis, the left-right signal, corresponding to the difference between the two left active areas and the two right ones, gives the inclination around this axis. The top-bottom signal gives the rotation around the x axis.

In order to characterize the liquid sensor, several experiments have been conducted which are explained hereafter: sensitivity, noise budget and study of the coupling between translation and rotation.

3.4. The liquid sensor

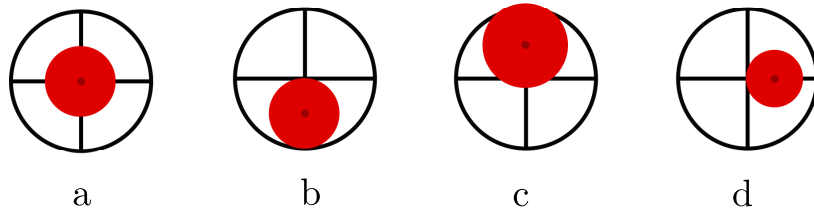


Figure 3.15: Illustration of the effect of the beam spot's diameter on the quadrant photodiode. The darker point shows the center of the beam spot for indication. (a) Beam centered with a diameter equal to half of the diameter of the photodiode active area. (b) Beam with a diameter equal to half of the diameter of the photodiode active area and placed at the largest distance possible. (c) Beam with a larger spot size. The beam moves out of the active area for a smaller distance than the maximum range that can be traveled. (d) Beam with a smaller spot size. The whole beam is in the two right active areas of the photodiode for a smaller distance than the maximum range traveled.

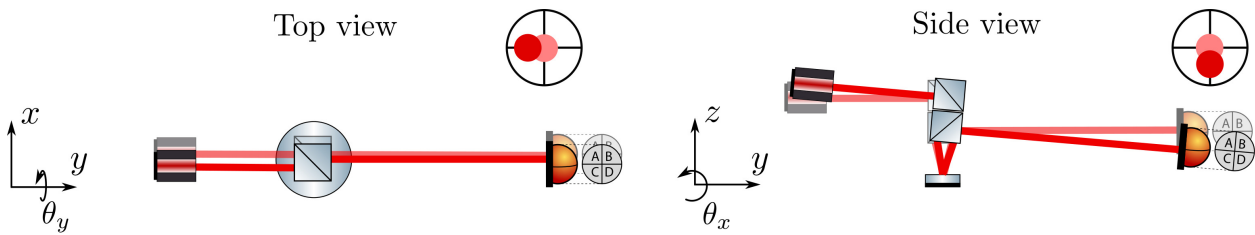


Figure 3.16: The liquid sensor is sensitive to the two rotations around the horizontal axis: the sensitivity to θ_y is shown with the top view (left) and the sensitivity to θ_x with the side view (right). A front view of the quadrant photodiode is drawn to show the beam spot before (light red) and after (dark red) rotation.

3.4.1 Sensitivity

The relationship between the voltage measured and the angle is obtained by inserting several metric feeler gauges of 0.1 mm thick below one foot of the sensor. The resulting sensitivity test is shown in Fig. 3.17. As the distance between the two feet is 47 cm, the angle induced by adding one blade is 0.012° .

From this first experiment, we can see that the liquid sensor is sensitive to DC inclination and that the noise of the sensor is sufficiently low to measure the inclination.

The voltage measured in function of the angle imposed to the sensor is shown in Fig. 3.18. Despite a small discrepancy in the measurement, the sensor is linear in the range tested, i.e. over 0.05° . Using these results, the sensitivity of the liquid sensor can be determined and is 306.75 V/rad.

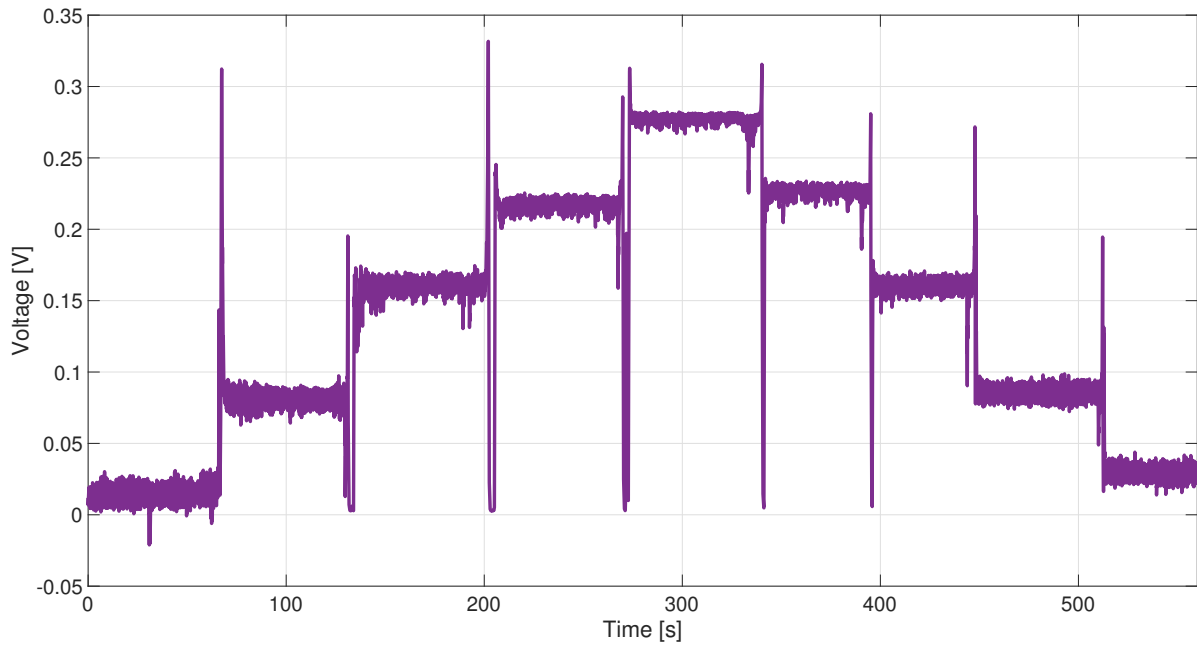


Figure 3.17: Time record of the sensitivity test of the liquid sensor: blades of 0.1 mm thickness are inserted below one foot of the sensor.

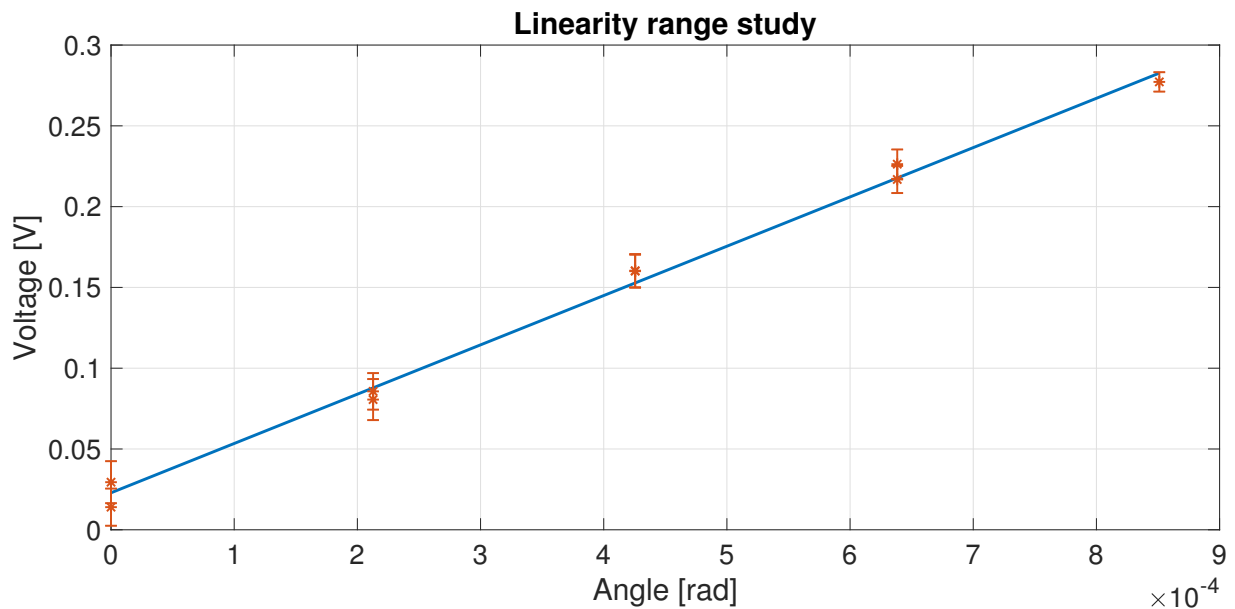


Figure 3.18: Sensitivity test of the liquid sensor: the voltage measured is shown in function of the angle imposed to the sensor (dots) and the corresponding error bars. For indication, the linear fit using the sensitivity of the sensor is shown (solid line) . The measurement can be considered as linear in the whole range tested.

3.4. The liquid sensor

3.4.2 Noise budgeting

An experimental noise budgeting is performed to study the limitations of the current sensor. The contributions of the different parts of the sensors are studied by conducting several measurements listed in table 3.3. Here, the following sources of noise are considered: analog to digital conversion (ADC), photodiode electronics, laser noise and mirror motion. To study the contribution of the mirror, first a broadband dielectric mirror BB1-E04 from Thorlabs reflects the beam and second, the liquid mirror is used. The noise budgeting is studied for both top-bottom and left-right signals.

Moreover, the QUAD photodiode provides a "sum signal" that corresponds to the sum of the signals measured by the four active areas of the photodiode. The impact of normalizing the signals by this sum signal is also studied.

Table 3.3: *List of experiments conducted to evaluate the noise budgeting of the liquid sensor. The first measurement corresponds to the identification of the ADC noise.*

Photodiode	Laser	Type of mirror	Normalized signal
OFF	OFF	-	-
ON	OFF	-	-
ON	ON	solid	NO
ON	ON	solid	YES
ON	ON	liquid	NO
ON	ON	liquid	YES

The amplitude spectral density (ASD) of the different tests is shown in Fig. 3.19 for the left-right and top-bottom signals. We can see that the noise from the photodiode is not limiting the resolution as the ASD measured with the photodiode plugged is the same as the ASD of the ADC only. When using the solid mirror, the noise increases at low frequency. This noise can be reduced by one order of magnitude when the signal is normalized by the sum signal of the photodiode. This means that the low frequency noise added corresponds to the intensity noise of the laser. Therefore, it is not surprising that normalizing the signal by the total amount of power measured by the photodiode reduces the fluctuation of intensity. The peaks around 10 Hz correspond to resonances of the system and are not reduced when the signal is normalized.

When the liquid mirror is used, the sensor measures some signal and hence the ASD is increased in the whole bandwidth. However, a look at the surface of the Mercury helps to understand that the signal measured does not correspond to the rotation; there are some ripples at the surface. In fact, the Mercury is shaking due to horizontal ground motion and hence, the surface of the mirror does not remain flat. From this measurement, we can understand that the liquid reference of the sensor needs to be more viscous. For information, the viscosity of Mercury is $1.25 \cdot 10^{-3}$ Pa s at 25 °C, which is close to the viscosity of water at the same temperature.

The resonances of the system are again visible around 10 Hz. An additional resonance at 3.6 Hz is visible and corresponds to the resonance of the liquid moving inside its container.

Note that some oils with a viscosity respectively one, two and three orders of magnitude larger have been tested to replace Mercury. Two solutions have been investigated to obtain a good reflection at the surface of these oils: put a small rectangle with a thin gold foil floating at the surface of the oil or mix the oil with aluminum particles with a size smaller than $70 \mu\text{m}$. However none of these solutions gave satisfactory results.

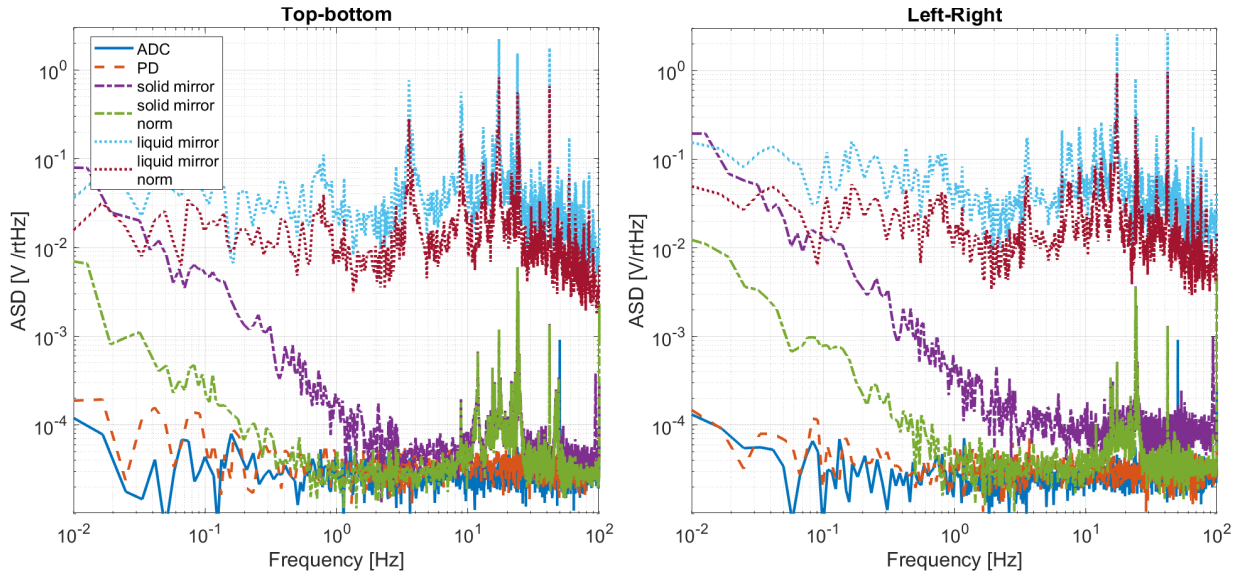


Figure 3.19: ASD of the noise budgeting of the liquid sensor for the different measurements listed in table 3.3 for the top-bottom signal (left) and the left-right signal (right).

The resolution of the actual sensor is compared to the requirement of the tiltmeter resolution defined by the laser interferometer gravitational-wave observatory (LIGO) for its isolation stages [24] in Fig. 3.20. This rotation goal specifies the resolution of the tiltmeter needed to be integrated in the LIGO isolation platforms to cope with tilt coupling. The current liquid sensor developed does not meet this requirement.

For comparison, the resolution of the precision laser inclinometer (PLI) [175] developed at CERN is also shown. This sensor is based on the same working principle and meets the LIGO requirements. Using a data acquisition system (DAQ) with a better resolution and by selecting a more viscous liquid, one can expect to improve the current resolution of the liquid sensor and meet the LIGO requirements.

Influence of the spot location on the quadrant photodetector

Several tests have been recorded for different location of the beam spot on the QUAD-PD to study if the location has an influence on the noise. The different locations are illustrated in Fig. 3.21.

The ASD of the measurements made at the different spot location are shown in Fig. 3.22. The peaks above 10 Hz correspond to resonances of the system as explained above. If the spot moves to the bottom (to the right), the ASD of the noise is increased at low frequency in this direction i.e. the top-bottom direction (the left-right direction). On the

3.4. The liquid sensor

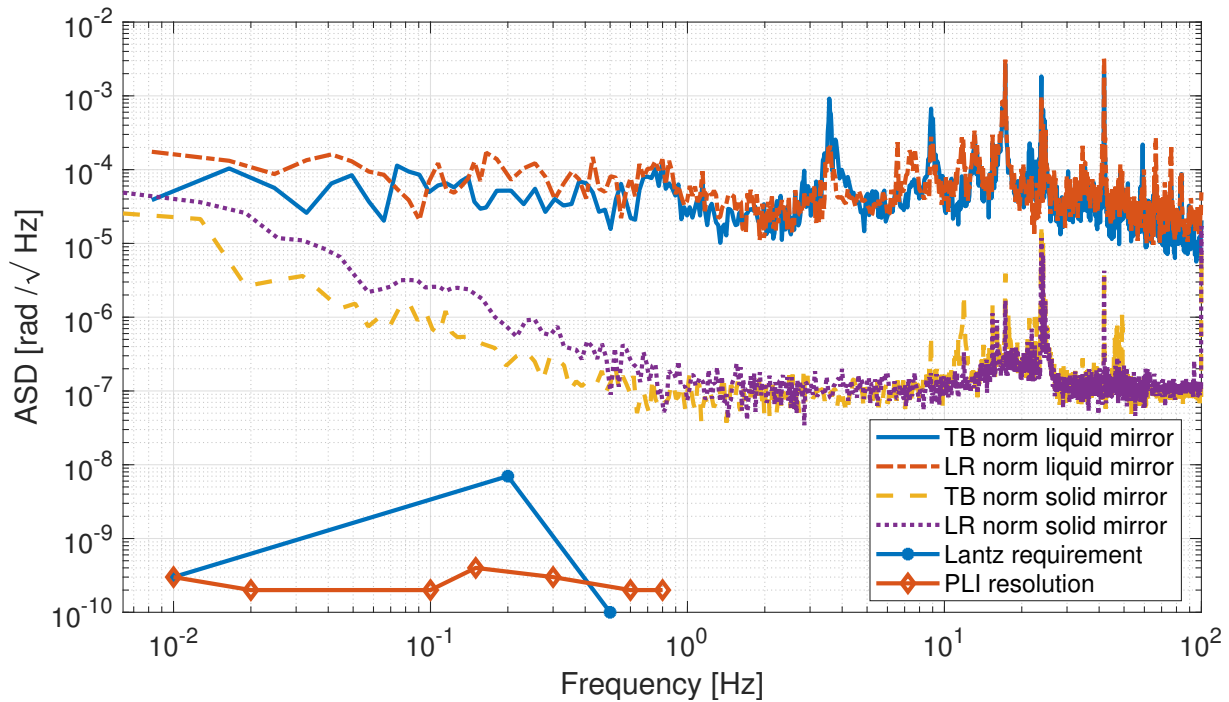


Figure 3.20: ASD of the resolution of the sensor with and without liquid mirror and with normalization by the sum signal compared to the requirement of resolution for the next generation of LIGO detectors [24]. The resolution of the precision laser inclinometer, based on the same working principle is also shown (red diamonds).

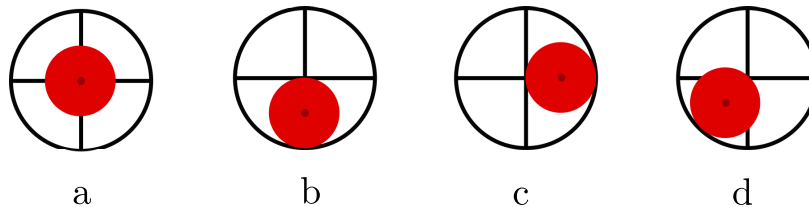


Figure 3.21: The beam spot location on the QUAD-PD to study if this has an effect on the noise measured: (a) center, (b) bottom, (c) right and (d) bottom-left.

contrary, the amplitude of the noise in the transverse direction is unchanged, i.e. the left-right direction when the spot moves to the bottom (the top-bottom direction when the spot moves to the right).

Similarly, if the spot moves to a combination of both directions, both signals see an increase of the amplitude of the ASD of the noise at low frequency.

The ASD of the normalized signals for all tests have the same amplitude. Therefore, to avoid an influence of the spot location on the amplitude of the noise, the normalized signal should be used. This conclusion was already partially understood in the previous section as the ASD of the noise when using a solid mirror is reduced after normalization.

One advantage of the normalization is that it permits to cancel the intensity noise from the signal. Indeed, without normalization, if the spot is not perfectly centered, the relative intensity noise (RIN) of the laser is partially canceled. In that case, if the RIN carried by the

laser is $RIN(\omega)$, the remaining intensity noise RIN_{sensor} is

$$RIN_{sensor}(\omega) = a RIN(\omega) - b RIN(\omega) , \quad (3.15)$$

where a is the proportion of intensity on two parts of the QUAD-PD and b , the proportion on the two other parts ($a + b \approx 1$).

This noise is canceled when the beam is centered ($a = b$) but increases when the spot moves on the QUAD photodiode ($a \neq b$). On the contrary, when normalizing the signal, the fluctuation of intensity is reduced no matter the location of the spot on the photodetector.

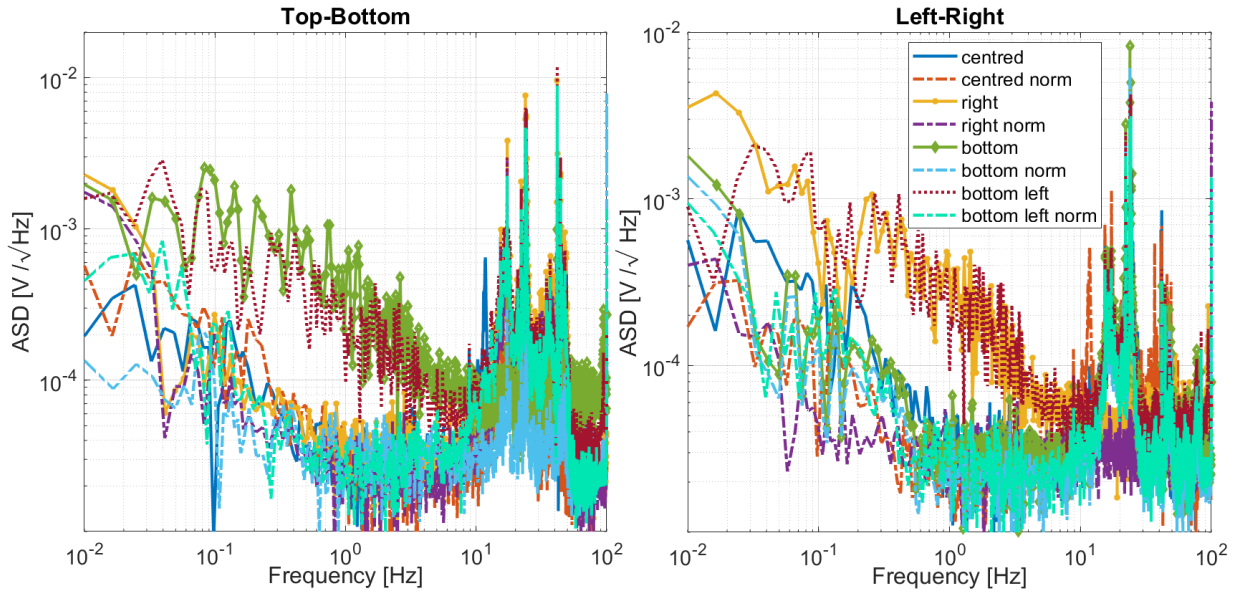


Figure 3.22: ASD of the top-bottom signal (left) and left-right signal (right) measured by the sensor for different locations of the beam on the QUAD-PD. When normalizing the signal (dashed dot curves), the ASD is not influenced by the location of the spot on the photodiode.

Influence of air fluctuations on the noise

In Ref. [175], the precision laser inclinometer is placed inside an enclosure to avoid air fluctuations. The effect of air on the sensor developed is tested by placing a fan in the path traveled by the beam. This experiment is tested with the broadband dielectric mirror from Thorlabs.

The results are shown in Fig. 3.23. The income of air clearly increases the amplitude of the ASD below the resonances of the system. Note that normalizing the signal does not reduce the effect of air fluctuations. In fact, while the RIN can be canceled by normalizing the signal as the four quadrants of the detector measure the same value, the air fluctuation affects the four quadrants differently. Therefore, the noise of the signal corresponding to the sum of the four quadrant is not identical to the noise of the difference between two pairs of quadrant. This test justifies the importance of placing the liquid sensor inside an enclosure, such as a vacuum chamber, to prevent the sensor of being influenced by air fluctuations.

3.4. The liquid sensor

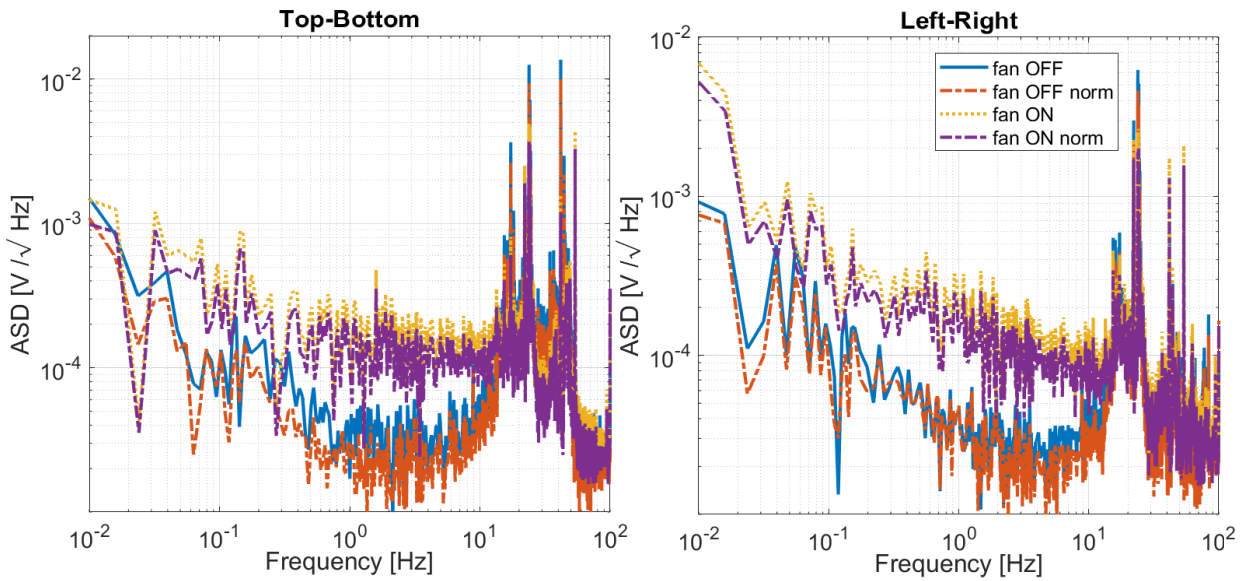


Figure 3.23: ASD of the top-bottom signal (left) and left-right signal (right) measured by the sensor when the fan is turn off (solid blue) and on (yellow dotted). For both cases, the normalized signal is shown in dashed dot curve.

3.4.3 Coupling study

Tiltmeters are also sensitive to horizontal displacement of their base; we saw in the previous section that the surface of the liquid mercury does not remain still due to ground motion. Moreover, as stated above in the case of the balanced beam tiltmeter, the pivot has to be carefully centered with the center of mass (COM) to reduce this coupling [174]. In fact, if the COM is not at the same height as the pivot, the tiltmeter acts as a pendulum and is sensitive to translation, see Fig. 3.24.

If the tiltmeter is too sensitive to translation, it can not be used to reduce the coupling of inertial sensors. Therefore, to characterize a tiltmeter, its sensitivity to horizontal excitation needs to be studied.

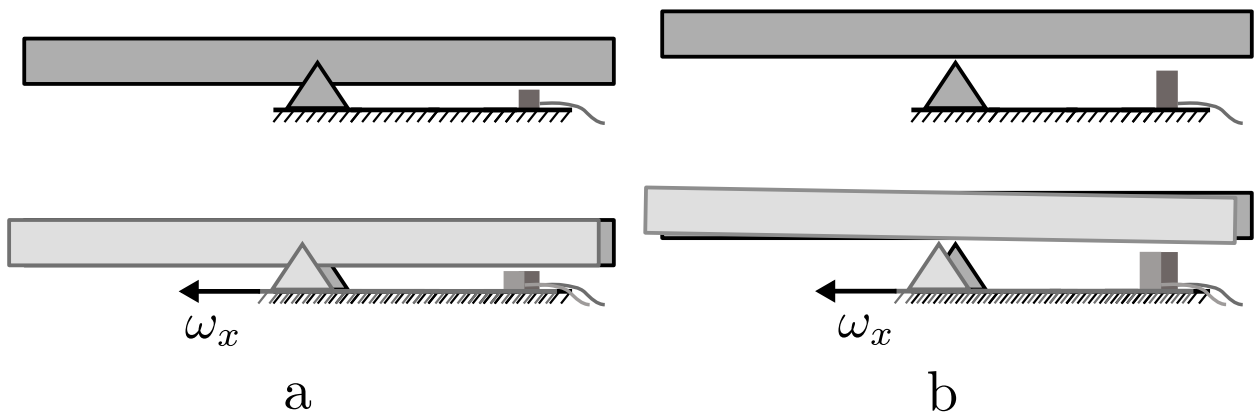


Figure 3.24: Balanced beam tiltmeter with the pivot located at the COM (a) and below the center of mass (b). When excited by horizontal ground motion ω_x , the beam is inclined when the pivot is not located at the center of mass.

The test bench developed to study this effect is shown in Fig. 3.25. In order to quantify the sensitivity of the liquid sensor to horizontal translation, the sensor is placed on top of two stages. The first stage is a Thorlabs breadboard MB4575/M that lies on two LSP 2080 roller bearings from THX allowing only horizontal motion. This stage is driven by a Thorlabs PZT actuator APF705. On top of this stage, a Thorlabs breadboard MB4545/M is placed on a hinge and a Cedrat Technologies PZT actuator APA-100M. When this stage is actuated, the breadboard rotates around the joint. The PZTs are driven by a Thorlabs MDT693B 3-channel Open Loop piezoelectric controller.

When one stage is actuated, the other is rigidly blocked by tightening screws.

Note that the mirror used is a broadband dielectric mirror BB1-E04 from Thorlabs. In fact, as explained, the viscosity of the Mercury is not large enough and hence, there are ripples at the surface of the liquid due to horizontal translation. The mirror is placed above the joint. Otherwise, the mirror would be subjected to tilt and vertical motion when the rotation stage is excited.

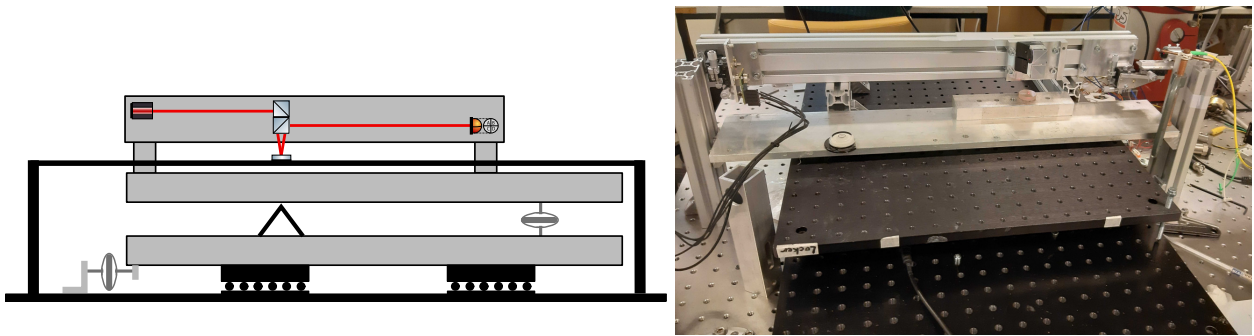


Figure 3.25: *Illustration (left) and picture (right) of the test bench to study the sensitivity of the sensor to translation and rotation. A bubble is placed on the beam supporting the mirror to verify the inclination of the beam.*

Two types of excitation are injected in the actuators: a white noise to identify the broadband transfer function between 0.1 Hz and 100 Hz and a set of sine excitation to recover the information at low frequencies. The transfer function between the sensor and the horizontal excitation and with the tilt excitation are shown in Fig. 3.26.

The coherence between the signal measured by the sensor and the horizontal excitation is poor at low frequency. However, the sine excitations permit to characterize the sensor in that range. Note that both transfer functions are flat in a large bandwidth at low frequency.

As mentioned, the goal of this experiment is to characterize the sensitivity of the sensor to horizontal translation. In fact, if the sensor is too sensitive to translation, it can not be used as a reference for tilt measurement. In order to quantify this sensitivity, the test bench is used to excite an inertial sensor, the Guralp CMG-6T, and compare the transfer functions obtained with those of the sensor. The Guralp is placed above the vertical actuator so that it is sensitive to the rotation imposed by the vertical PZT, see Fig. 3.27.

The transfer function between the vertical motion measured by the Guralp and the tilt excitation and the horizontal excitation are shown in Fig. 3.28. To recover the displacement from the signal measured by the Guralp, the data has to be multiplied by the inverse of its

3.4. The liquid sensor

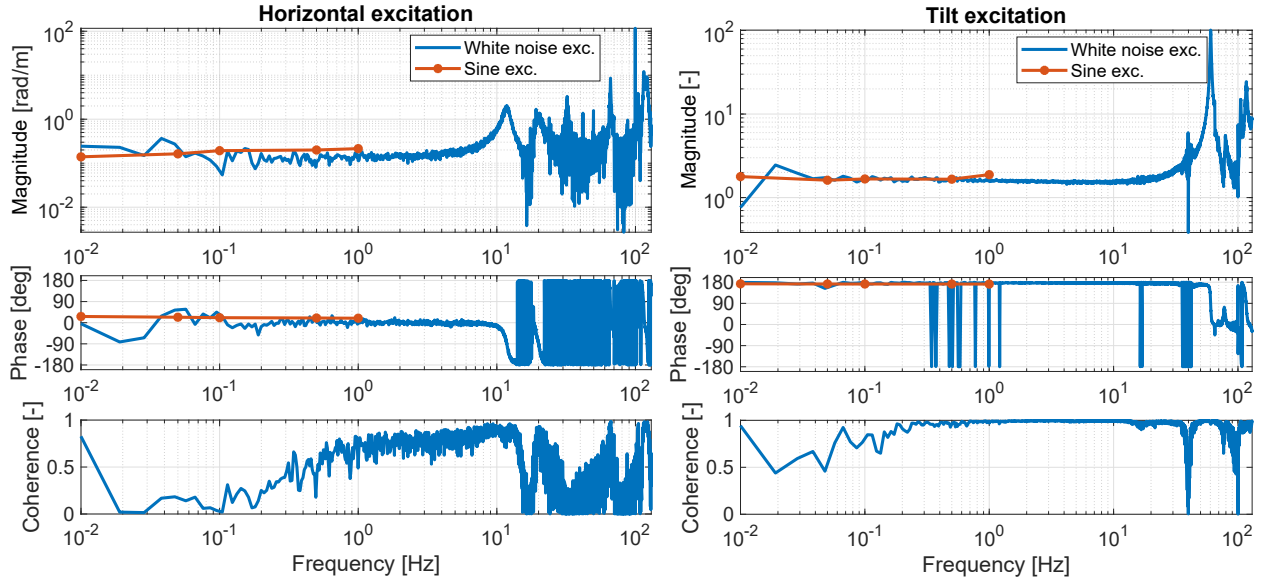


Figure 3.26: Transfer function between the rotation measured by the sensor's frame when using a broadband dielectric mirror rigidly connected to the ground and the horizontal excitation (left) and the tilt excitation (right). The transfer function obtained with the white noise excitation (solid blue) gives a broadband information between 0.1 Hz and 100 Hz. The set of sine excitations (red dots) complete this information at low frequency.

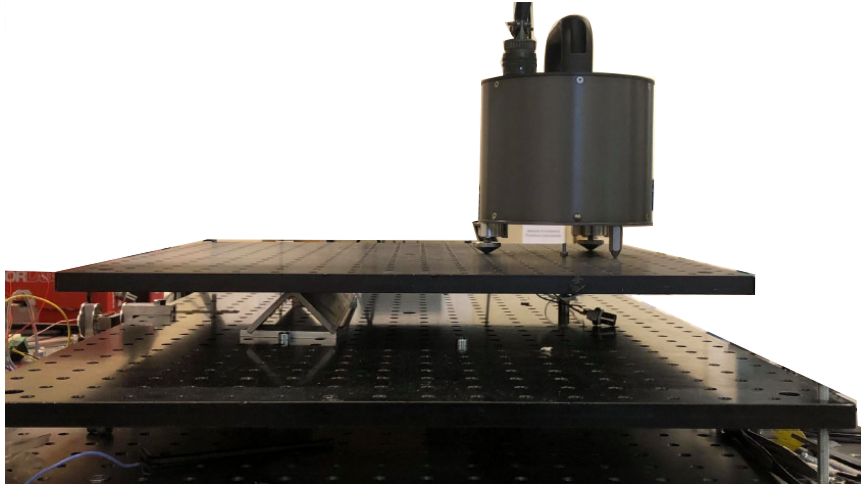


Figure 3.27: Picture of the test bench to study the sensitivity of inertial sensor to translation and rotation. The Guralp is located above the vertical PZT.

dynamics which is basically a high-pass filter with a cutoff frequency around 0.1 Hz and a low-pass filter with a cutoff frequency around 100 Hz

$$S_{Guralp} = 585.8 \times 10^8 \frac{s^2}{s^6 + 549.8s^5 + 10^5s^4 + 1.2 \times 10^7s^3 + 5.8 \times 10^8s^2 + 2.7 \times 10^7s + 6.4 \times 10^5} \quad (3.16)$$

Regarding the response to horizontal excitation, the decreasing slope below 0.1 Hz corresponds thus to the inverse of the high-pass filter. The response to rotation shows the g/s^2 slope which characterizes the sensitivity of inertial sensors to tilt at low frequency, see Eq. (3.3).

Note that due to the Guralp's dynamics, the useful signal is limited to the bandwidth between 0.1 Hz and 100 Hz.

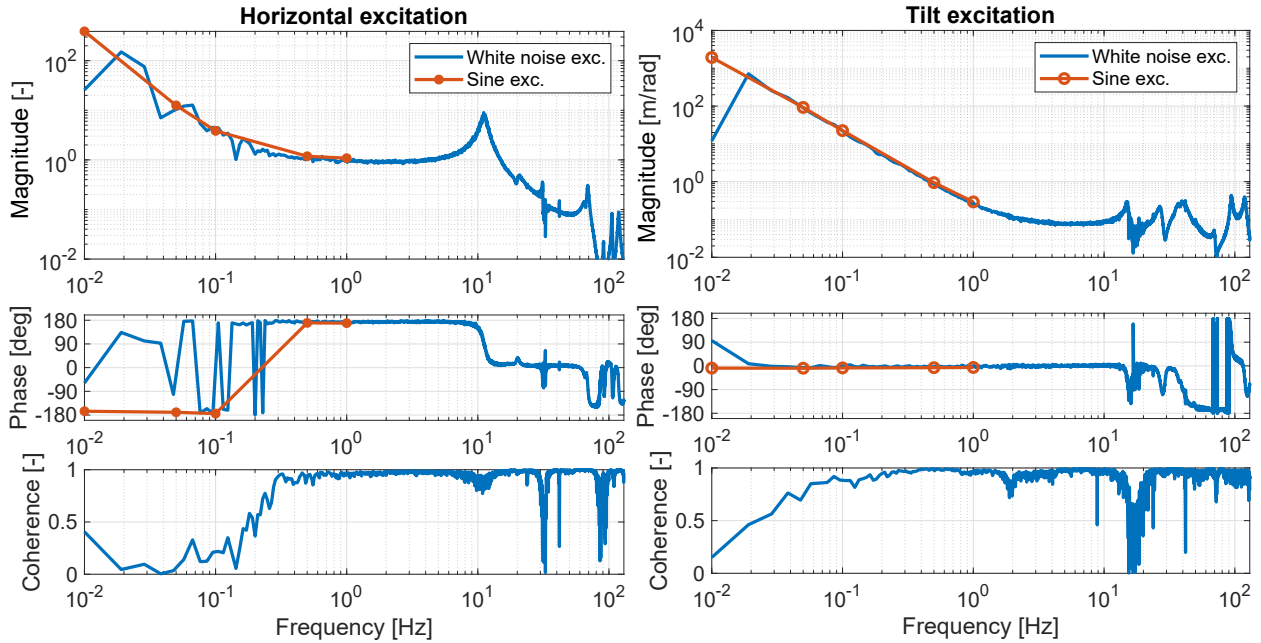


Figure 3.28: Transfer function between the vertical motion measured by the Guralp CMG-6T and the horizontal excitation (left) and the tilt excitation (right). The transfer function obtained with the white noise excitation (solid blue) gives a broadband information between 0.1 Hz and 100 Hz. The set of sine excitations (red dots) complete this information at low frequency.

For comparison, the dynamics of the beam-rotation-sensor (BRS) [171] is as follows: Above the resonance frequency of the BRS at 8.9 mHz, its sensitivity to tilt and the sensitivity to translation are flat and the ratio response to translation over response to tilt is $3 \cdot 10^{-5}$ rad/m. The sensor with the solid mirror developed here is less decoupled as this ratio is 10^{-1} rad/m. In conclusion, the test bench developed to study the coupling of inertial sensors and tiltmeters is efficient. In addition, the resolution of the sensor developed here has to be improved and the coupling study has to be reproduced using the liquid reference.

The sensitivity to translation of the rotation sensor tested here is explained in the next section.

Model of the sensor

The sensor placed on the test bench in the previous section uses a mirror connected to the ground as a reference. If the mirror is inclined with respect to the ground, it can be sensitive to translation as illustrated in Fig. 3.29.

The sensitivity of the sensor to translation can be understood with a geometric construction, see the zoom of Fig. 3.29 in Fig. 3.30. When the sensor moves horizontally of a distance x to the right, this is equivalent to moving the mirror of the same distance to the left. Knowing that the mirror is inclined with respect to the ground of an angle θ_0 , the additional distance d traveled by the beam before reflection by the mirror is

$$d = x \tan \theta_0 . \quad (3.17)$$

3.5. Summary

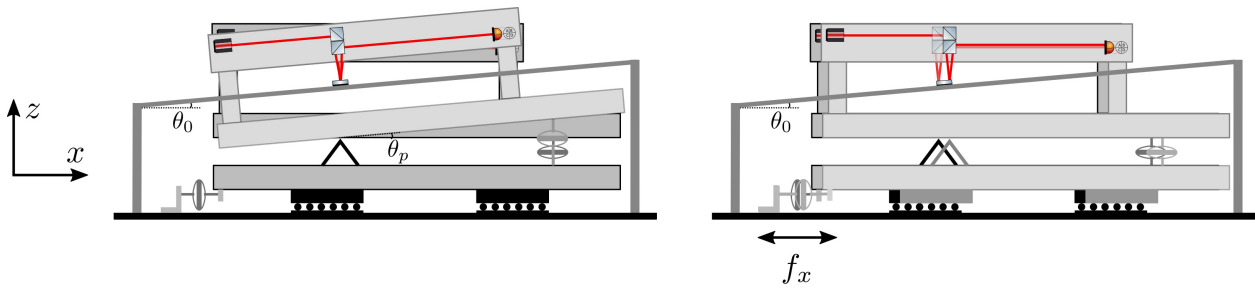


Figure 3.29: Effect of the rotation of the platform (left) and of the horizontal translation (right) on the sensor when the solid mirror is inclined of an angle θ_0 with respect to the ground.

Therefore, the reflected beam is parallel to the initial reflected beam but translated of the distance $2s$ where

$$s = d \sin \theta_0 . \quad (3.18)$$

From this result, the deviation of the beam on the photodiode Δx can be evaluated

$$\Delta x = h \cos 45^\circ = 2s \sin(45^\circ - \theta_0) \cos 45^\circ . \quad (3.19)$$

Assuming that L is the distance between the beamsplitter and the photodiode, the signal measured by the sensor θ_m due to the inclination of the platform θ_p and to its translation x is

$$\theta_m = 2\theta_p + \frac{\sqrt{2} \sin^2 \theta_0 \sin(45^\circ - \theta_0)}{L \cos \theta_0} x . \quad (3.20)$$

From this result, we can see that to prevent the sensor with a solid mirror of being sensitive to horizontal translation, the mirror has to be perfectly horizontal $\theta_0 = 0$.

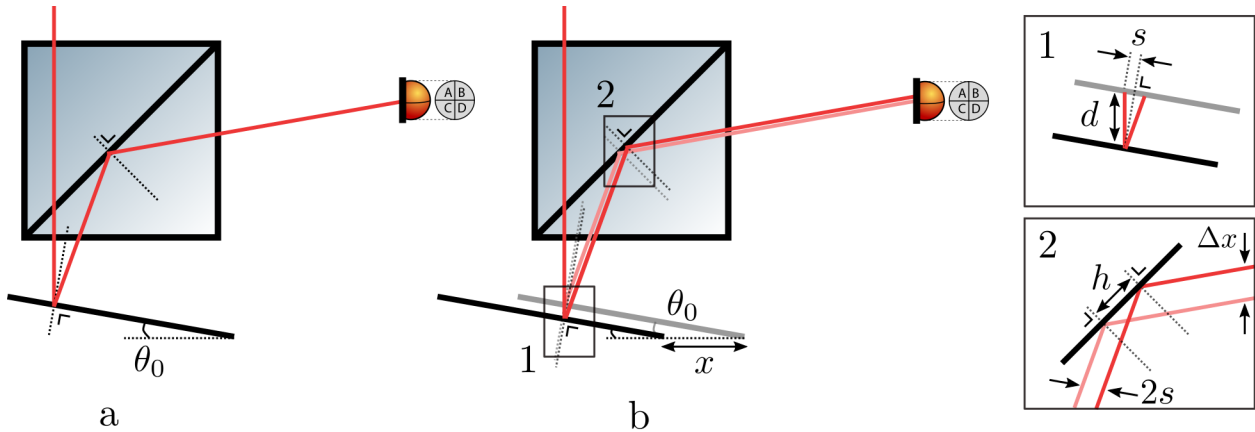


Figure 3.30: Exaggerated view of the beam propagation on the beamsplitter and reflected by the mirror (solid line below the beamsplitter) (a) before translation of the sensor and (b) after a translation of the sensor of a distance x . The frames 1 and 2 zoom on different parts of the figure (b).

3.5 Summary

The effect of the sensitivity of inertial sensors to tilt has been studied in this chapter. The dynamics of inertial sensors is changed as the frequency of the pair of zeros is not at 0 Hz

but depends on the inclination of the sensor in the gravitational field. Existing solutions to reduce this sensitivity are presented. Some involve to modify the mechanics while others involve to use a tiltmeter to sense the rotation and subtract it from the signal measured.

We have seen that we can build a liquid sensor by measuring the inclination of a payload by comparison to the surface of a liquid. The liquid should have good reflectivity and hence, liquid Mercury has been tested here. However, the viscosity of liquid Mercury is not large enough and hence, a liquid sensor using the surface of Mercury as the reference is too sensitive to translation. As explained, a good solution consists in using some oils, more viscous, and find a way to integrate a reflective material in this oil. Finally, a test bench to study the sensitivity of tiltmeters and inertial sensors to translation and rotation has been developed. The response of inertial sensors to tilt and translation obtained matches the expectations given in Eq. (3.3).

Chapter 4

Inertial control

Contents

4.1	Translation control	93
4.2	Translation-rotation control	95
4.2.1	Control with an ideal sensor	95
4.2.2	Inertial control	98
4.3	MIMO control	102
4.3.1	Centralized frame	103
4.3.2	Singular value decomposition	106
4.4	Coupling mitigation techniques	111
4.4.1	Cascade control	111
4.4.2	Sensor correction	118
4.4.3	Tilt subtraction	121
4.4.4	Control performance comparison	122
4.5	Summary	123

In Chapter 3, it has been shown that the signal measured by inertial sensors is a coupled tilt-translation signal due to the effect of gravity acting on the inertial mass. The impact of this coupling on inertial control is studied here.

In this chapter, inertial isolation is first applied on a 1 degree-of-freedom (d.o.f.) system. A 2 d.o.f. system is then introduced that can move horizontally and rotate. In addition, the reduction of the effect of gravity thanks to decoupling methods dedicated to multiple input/multiple output (MIMO) control is studied. To understand the effect of using inertial sensors in a feedback loop, the performance obtained with an ideal sensor are also presented for comparison. The solutions mentioned in chapter 3 to cope with coupling are investigated.

4.1 Translation control

Consider the spring-mass system shown in Fig. 4.1. The body of mass m_2 can only move horizontally and is connected to the ground by a spring of stiffness k_h . To isolate the payload from the ground horizontal motion ω_x , the actuator f_h and a sensor are added to the system. Here, we want to study the performance of inertial control hence, we are considering an ideal absolute sensor, see Fig. 4.1.a, measuring x_2 , the absolute motion of the body, and an inertial sensor measuring x_i , the relative displacement between the inertial mass and the body, see Fig. 4.1.b. This helps to see how inertial control with an inertial sensor compares to the ideal case.

The parameters used in the model are given in table 4.1.

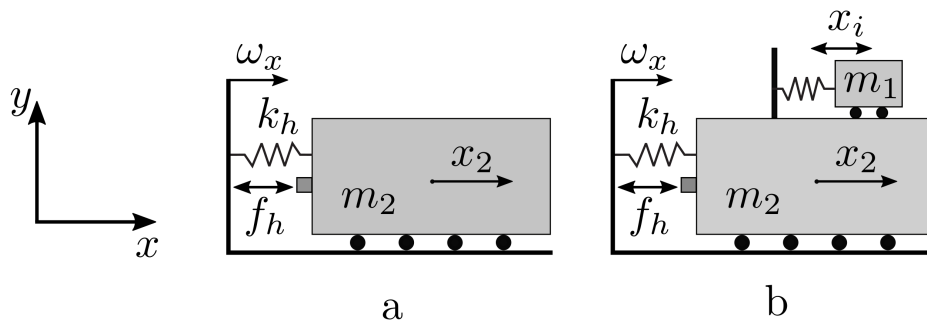


Figure 4.1: Sketch of the 1 dof system. The parameters are shown on the left figure and the degrees of freedom, the actuator and the ground motions considered are shown on the two right figures. In Fig. (a), the motion is measured with an ideal absolute sensor and in Fig. (b) with an inertial sensor.

Table 4.1: Values assigned to the parameters of the 1 d.o.f. model.

	Mass		Stiffness
m_1	0.3 kg	k_1	1 N/m
m_2	6.6 kg	k_h	10^4 N/m

The plant measured with an ideal displacement sensor corresponds to a transfer function with a pair of complex conjugate poles at $\sqrt{k_h/m_2}$. The gain is set to 10^6 to reduce by two orders of magnitude the motion of the body. The controller is the gain and a lead to ensure enough phase margin at the crossover frequency above the resonance

$$H(s) = 10^6 \frac{120}{30} \frac{s + 2\pi 30}{s + 2\pi 120}. \quad (4.1)$$

The open loop is shown in Fig. 4.2; there is 30° of phase margin.

When measured with an inertial sensor, the plant has now two pairs of complex conjugate poles, one corresponding to the spring-mass system made of the payload m_2 and the spring k_h and one corresponding to the spring-mass system of the inertial sensor, see Fig. 4.2. In addition, there is a pair of zeros at 0 Hz, similarly to the transmissibility evaluated in

4.1. Translation control

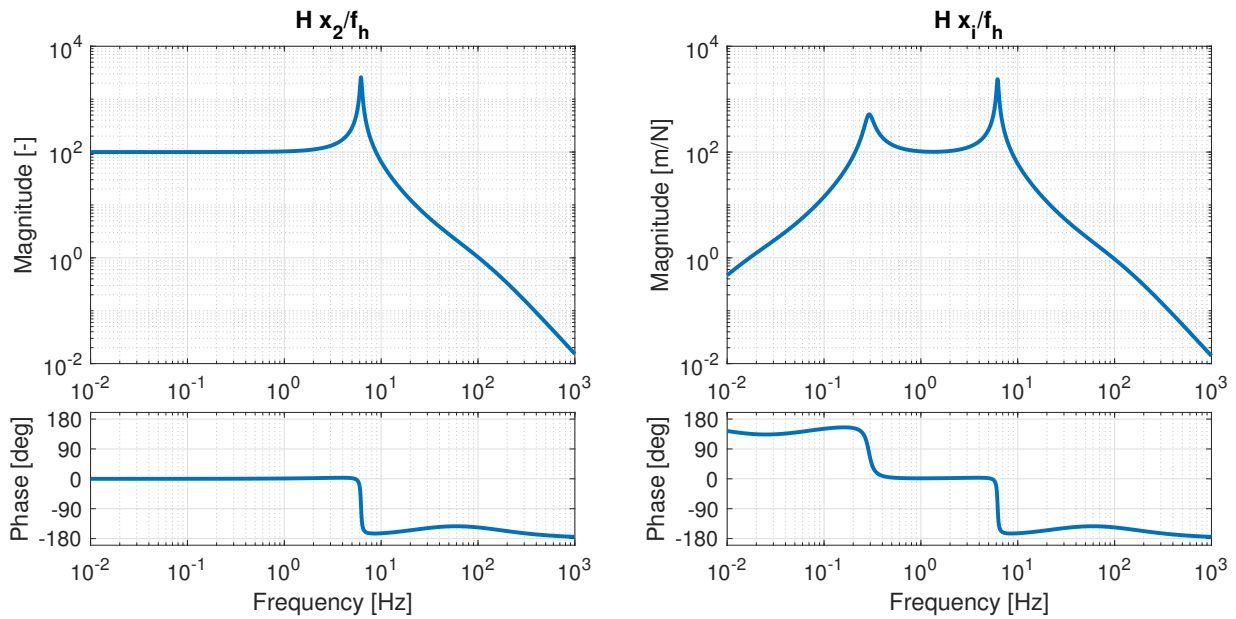


Figure 4.2: Open loop when using an ideal absolute sensor (left) and an inertial sensor (right).

Eq. (2.2). To ensure phase margins at the two crossover frequencies, a lead and a lag are needed

$$H(s) = -5.5 \cdot 10^6 \frac{120 \times 0.01 (s + 2\pi 30)(s + 2\pi 0.06)}{30 \times 0.06 (s + 2\pi 120)(s + 2\pi 0.01)}. \quad (4.2)$$

Phase margins larger than 35° are guaranteed for the two crossover frequencies.

The performance is shown in Fig. 4.3 where we can see that the two methods effectively reduce the motion of the payload x_2 of two orders of magnitude. Below the resonance of the inertial sensor, the inertial control is not working. Indeed, at low frequency, the inertial mass moves together with the payload and hence, the relative displacement measured by the inertial sensor is null. Therefore there is no control force injected at low frequency.

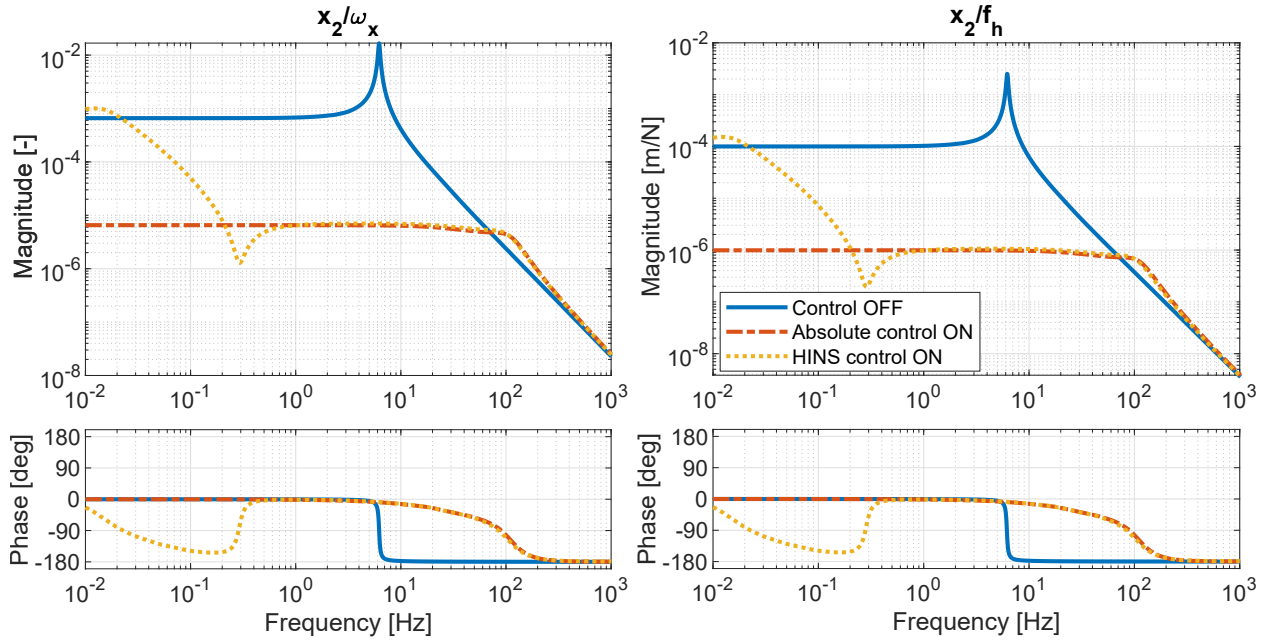


Figure 4.3: Transmissibility and plant of the 1 d.o.f. system when measuring the motion x_2 of the payload without control (solid blue), with control using an ideal absolute sensor (dashed red) and with inertial control (dotted yellow).

4.2 Translation-rotation control

In section 3.1.1 and section 3.1.2, we have shown that the dynamics of inertial sensors is sensitive to the rotation of the payload. The 1 d.o.f. model used in the previous section cannot represent this coupling. Therefore it is modified to become a 2 d.o.f. model by placing the payload on a slider. The effect on inertial control is studied here.

4.2.1 Control with an ideal sensor

Let's consider the 2 d.o.f. stage presented in Fig. 4.4. The mass m_2 lays on a slider allowing only horizontal motion x and rotation θ . In the figure, h is the height of the body m_2 ; l_f is the distance between the center of mass of m_2 and the force f_h applied on the body in the horizontal direction and h_f in the vertical direction; l_k is the distance in the horizontal direction between the center of mass of m_2 and the point where the stiffness k_h and k_v are supporting the payload. The values assigned to these parameters are given in table 4.2. The springs transmit the ground motion characterized by the horizontal ground motion ω_x and rotational ground motion ω_θ .

The sensor of mass m_1 is rigidly connected to the body and the motion measured x_1 is the absolute motion of the mass m_1 .

Table 4.2: Values assigned to the parameters of the 2 d.o.f. model.

	Mass	Stiffness	Lengths	Heights
m_1	0.3 kg	k_h 10^4 N/m	l_f 0.2 m	h_f $-5 \cdot 10^{-3}$ m
m_2	6.6 kg	k_v 10^4 N/m	l_k 0.22 m	h $1.27 \cdot 10^{-2}$ m

4.2. Translation-rotation control

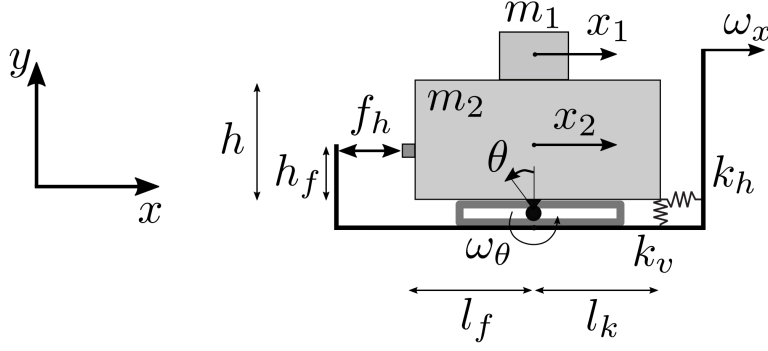


Figure 4.4: Sketch of the 2 d.o.f. stage. The parameters and the degrees of freedom, the actuator and the ground motions considered are represented.

The kinetic energy T and potential energy V of the system, assuming that $m_1 \ll m_2$, are

$$T = \frac{1}{2}m_2(\dot{x}_2^2 + \frac{h^2}{4}\dot{\theta}^2 - h\dot{x}_2\dot{\theta}\cos\theta), \quad (4.3)$$

$$V = m_2g\frac{h}{2}\cos\theta + \frac{1}{2}k_h(\omega_x - x_2)^2 + \frac{1}{2}k_v l_k^2(\sin\omega_\theta - \sin\theta)^2. \quad (4.4)$$

Using the Lagrangian derivation, the linearized equations of motion of the coupled system in the Laplace domain, assuming small motion (θ and ω_θ represent both small variations around $\theta_0 = 0$ and $\omega_{\theta,0} = 0$), are

$$m_2s^2x_2 - m_2\frac{h}{2}s^2\theta = f_h + k_h(\omega_x - x_2), \quad (4.5)$$

$$m_2\frac{h^2}{4}s^2\theta - m_2\frac{h}{2}s^2x_2 = -h_f f_h + k_v l_k^2(\omega_\theta - \theta) + m_2\frac{h}{2}g\theta. \quad (4.6)$$

From these equations, the motion measured is deduced $x_1 = x_2 - (h + \frac{h_s}{2})\theta$.

The transmissibilities and plant of the stage are shown in Fig. 4.5. The first mode at 6 Hz corresponds to a pure horizontal displacement of the payload at $\omega_0 = \sqrt{k_h/m_2}$. The second mode corresponds to a pure rotation of the payload. We can see that the motion x_1 is less sensitive to the ground rotation than to the ground translation.

To isolate the payload, the following controller made of a gain and two leads is applied to the plant:

$$H(s) = 10^6 \frac{20.200}{5.50} \frac{(s + 2\pi 5)(s + 2\pi 50)}{(s + 2\pi 20)(s + 2\pi 200)}. \quad (4.7)$$

The open loop of the system x_1/f_h is shown in Fig. 4.6. Based on the open loop, we can see that the phase margins at the crossover frequency is 45° and that the isolation bandwidth is larger than 100 Hz. The performance is presented in Fig. 4.7 when considering the motion x_2 at the center of mass of the body m_2 . When closing the loop, the horizontal motion is reduced by two orders of magnitude and hence, the transmissibility with the horizontal ground motion ω_x is also reduced by two orders of magnitude. Regarding the transmissibility of ground rotation ω_θ to the payload motion x_2 , the resonance corresponding to the horizontal suspension $\sqrt{k_h/m_2}$ is isolated and hence it disappears from this transmissibility.

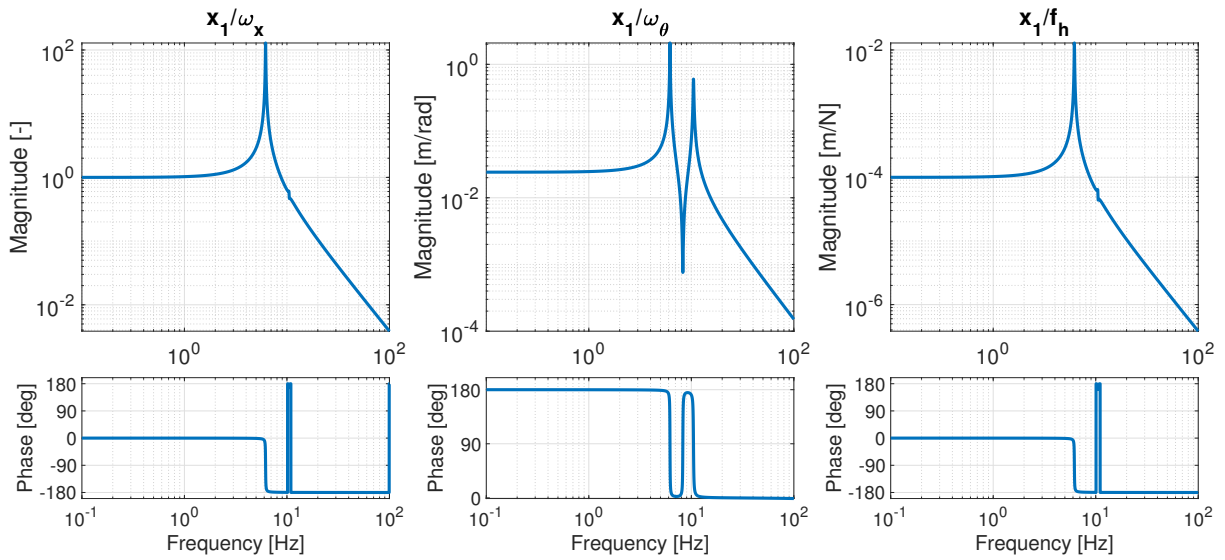


Figure 4.5: Transmissibilities with ground translation ω_x (left) and ground rotation ω_θ (center) and plant (right) of the motion x_1 of the 2 d.o.f. stage.

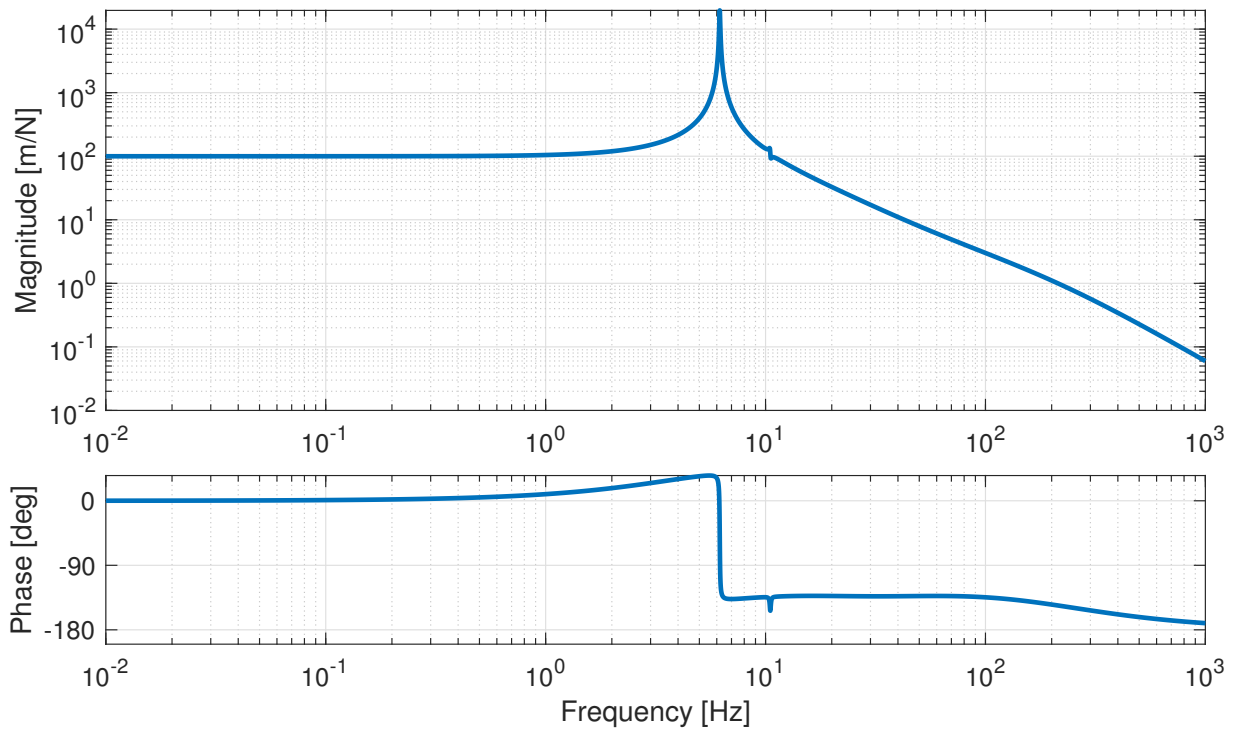


Figure 4.6: Open loop of the system, transfer function from the horizontal force f_h to the signal measured x_1 .

With this first ideal model, a stable closed loop can easily be designed in order to reduce the horizontal motion of the body m_2 without increasing the coupling with other directions. However, it is not possible to use an ideal absolute sensor in practice. Instead, inertial sensors are used to sense the motion of the payload. In the next section, the effect of using an inertial sensor on the control performance is presented.

4.2. Translation-rotation control

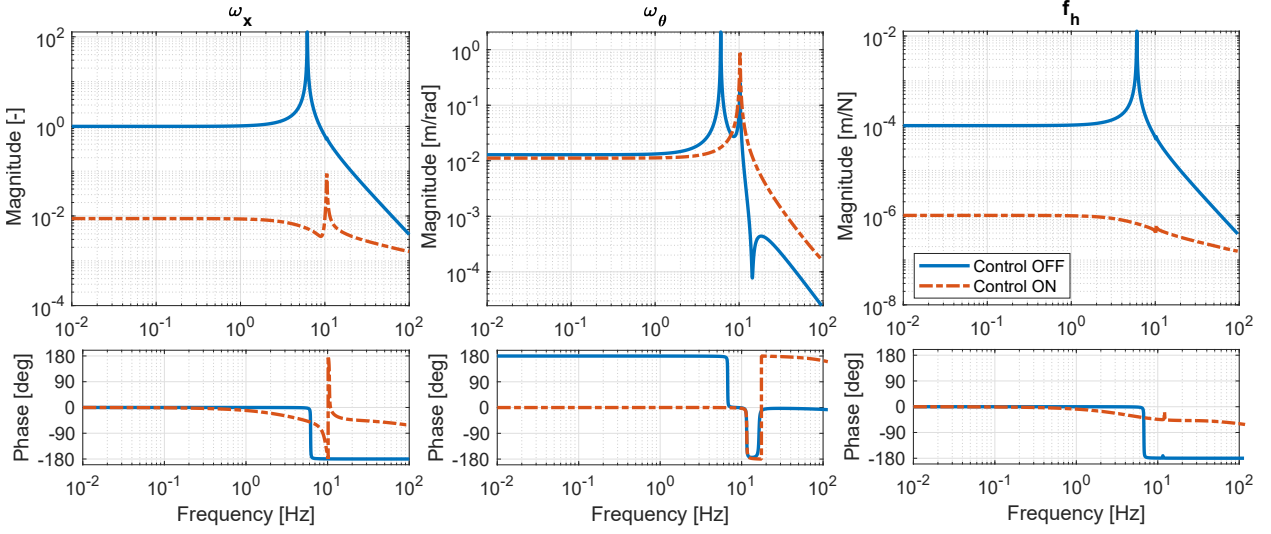


Figure 4.7: Performance of the closed loop. Transmissibilities with ground translation ω_x (left) and ground rotation ω_θ (center) and plant (right) of the motion x_2 at the center of mass of the body m_2 without control (solid blue) and with control (dashed red).

4.2.2 Inertial control

The body m_1 initially rigidly connected to the body m_2 to represent the ideal absolute sensor is now connected by a spring of stiffness k_1 to represent an inertial sensor in Fig. 4.8. The values assigned to the parameters are the same, see table 4.2. The height of the inertial sensor h_s is 0.01 m, its mass m_1 is 0.3 kg and the spring k_1 has a stiffness of 1 N/m.

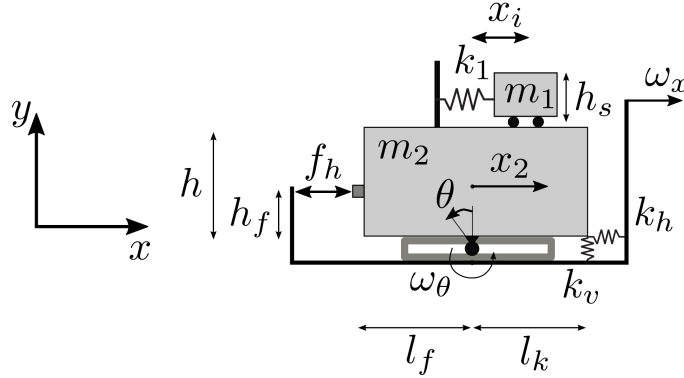


Figure 4.8: Sketch of the 2 d.o.f. platform with the horizontal inertial sensor. The parameters and the three degrees of freedom considered are presented.

The variable x_i measured by the horizontal inertial sensor (HINS) corresponds now to the relative displacement between the center of mass of the body m_2 and that of the inertial mass m_1 .

The kinetic energy T and potential energy V of the system, assuming that $m_1 \ll m_2$, are

$$\begin{aligned}
 T = & \frac{1}{2}m_2(\dot{x}_2^2 + \frac{h^2}{4}\dot{\theta}^2 - h\dot{x}_2\dot{\theta}\cos\theta) + \frac{1}{2}m_1(\dot{x}_i^2 + (x_i^2 + (h + \frac{h_s}{2})^2)\dot{\theta}^2 + \dot{x}_2^2) \\
 & + m_1(\dot{x}_2(\dot{x}_i\cos\theta - x_i\dot{\theta}\sin\theta - (h + \frac{h_s}{2})\dot{\theta}\cos\theta) - (h + \frac{h_s}{2})\dot{x}_i\dot{\theta}),
 \end{aligned} \tag{4.8}$$

$$\begin{aligned}
 V = & m_2 g \frac{h}{2} \cos \theta + \frac{1}{2} k_h (\omega_x - x_2)^2 + \frac{1}{2} k_v l_k^2 (\sin \omega_\theta - \sin \theta)^2 \\
 & + m_1 g \left(\left(h + \frac{h_s}{2} \right) \cos \theta + x_1 \sin \theta \right) + \frac{1}{2} k_1 x_i^2 .
 \end{aligned} \tag{4.9}$$

The linearized equations of motion of the coupled system, assuming small motion and that $m_1 \ll m_2$, are

$$m_1 s^2 x_i - m_1 \left(h + \frac{h_s}{2} \right) s^2 \theta + m_1 s^2 x_2 = -k_1 x_i - m_1 g \cos \theta_0 \theta , \tag{4.10}$$

$$m_2 s^2 x_2 - m_2 \frac{h}{2} s^2 \theta = f_h + k_h (\omega_x - x_2) + k_1 x_i , \tag{4.11}$$

$$I s^2 \theta - m_2 \frac{h}{2} s^2 x_2 = -h_f f_h + k_v l_k^2 (\omega_\theta - \theta) + k_1 \left(h + \frac{h_s}{2} \right) x_i + m_1 \left(h + \frac{h_s}{2} \right) g \theta + m_2 \frac{h}{2} g \theta . \tag{4.12}$$

The transmissibilities and the plant are compared to those measured without sensor dynamics in Fig. 4.9. In addition to the suspension modes observed in the previous section, there is the mode corresponding to the inertial spring-mass system $\sqrt{\frac{k_1}{m_1}}$. Moreover, the signal is more coupled at low frequency with the ground rotation as already discussed in chapter 3. In fact, the static gain of the transfer function x_i/ω_θ is

$$\left. \frac{x_i}{\omega_\theta} \right|_{s=0} = - \frac{m_1 g k_v l_k^2}{k_1 (l_k^2 k_v - m_2 g \frac{h}{2})} . \tag{4.13}$$

As expected, gravity g is responsible for the coupling of the signal measured by the inertial sensor with ground rotation at low frequency. Equation (4.13) shows that if the payload rotates, the body m_1 falls in the gravity field if $g \neq 0$. On the contrary, in absence of gravity, the body m_1 does not move with the rotation of the stage.

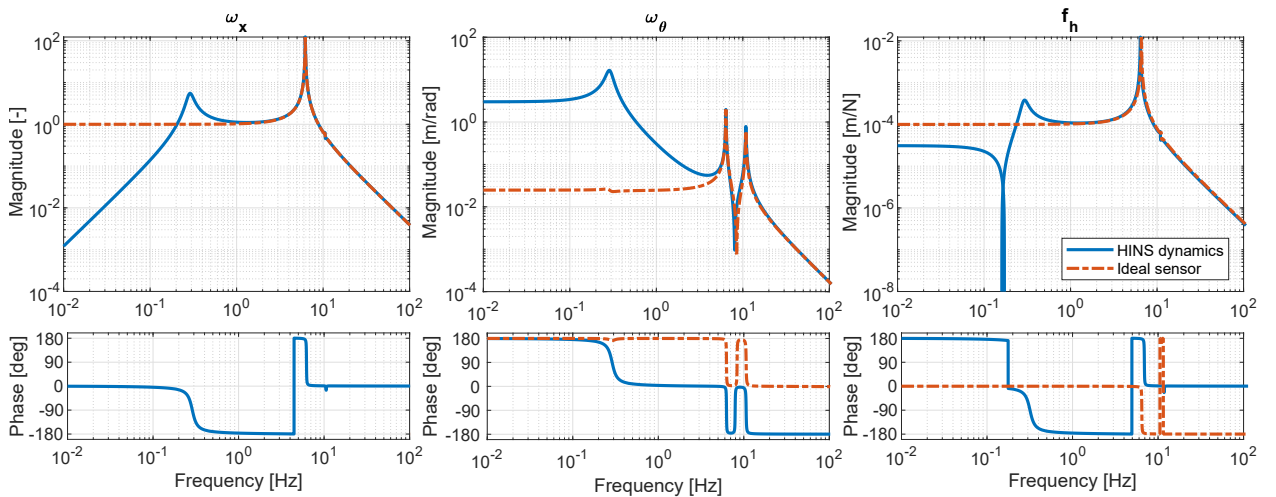


Figure 4.9: Transfer functions between different excitations and the inertial sensor (solid blue) or the ideal absolute sensor (dashed red): transmissibility with ground translation ω_x (left), transmissibility with ground rotation ω_θ (center) and plant (right).

4.2. Translation-rotation control

In Fig. 4.10, the plant is represented for different locations h_f of the actuating force. The corresponding pole-zero map is also plotted. The poles are not influenced by the location of the actuator. On the contrary, the zeros due to the tilt-horizontal coupling of the sensor are moving from a pair of positive and negative real zeros to a pair of positive and negative purely imaginary zeros if the force actuates below or above the joint. To evaluate the location of the zeros, let's consider the numerator of the transfer function x_i/f_h which has two pairs of zeros and three pairs of poles

$$\begin{aligned}
 & -m_1 s^4 \left(I + m_2 h_f \left(\frac{h}{2} + \frac{h_s}{2} \right) \right) \\
 & -m_1 s^2 \left(k_v l_k^2 + \left(h + \frac{h_s}{2} \right) h_f k_h - m_1 g \left(h + \frac{h_s}{2} \right) - m_2 g \frac{h}{2} - h_f m_2 g \right) \\
 & + m_1 g k_h h_f = 0 .
 \end{aligned} \tag{4.14}$$

To calculate the frequencies corresponding to the two pairs of zeros, let's assume that $t = s^2$ and rewrite Eq. (4.14) as $at^2 + bt + c$, where $a = I + m_2 h_f \left(\frac{h}{2} + \frac{h_s}{2} \right)$, b is the coefficient of the s^2 term in Eq. (4.14) and $c = -h_f k_h g$.

The roots $\pm \sqrt{\frac{-b - \sqrt{b^2 - 4ac}}{2a}}$ are canceled by the pair of poles corresponding to the vertical suspension mode as this mode is not excited by the horizontal actuator. The second pair of zeros $\pm \sqrt{\frac{-b + \sqrt{b^2 - 4ac}}{2a}}$ obtained from Eq. (4.14) comes from the dynamics of the inertial sensor. Note that in absence of gravity, this pair of zeros is at 0 Hz as the term $c = -g k_h h_f$ is canceled. Due to the gravitational field, the zeros are located at a higher frequency and depending on the sign of h_f , the roots of the polynomial are real or imaginary.

Here, the pair of zeros is at a frequency around 0.1 Hz and will have consequences on the isolation performance as shown hereafter.

Given the plant shown in Fig. 4.10 with the force located 5 mm below the slider point, the following lead-lag controller is applied in order to isolate the payload in the horizontal direction

$$H(s) = 10^6 \frac{14.7}{15.75} \frac{(s + 2\pi 0.3)^2 (s + 2\pi 5)(s + 2\pi 35)}{(s + 2\pi 0.07)^2 (s + 2\pi 20)(s + 2\pi 150)} . \tag{4.15}$$

The open-loop is shown in Fig. 4.11. In the same figure, the plant when the loop is closed is presented. Here, the amplitude of motion is only reduced of one order of magnitude. In fact, there is a pair of undamped complex zeros at 0.16 Hz. The effect of this pair of zeros is visible when looking at the transmissibilities between x_2 and the two directions of ground motion imposed in Fig. 4.12; the peak at 0.16 Hz is due to the migration of a pair of complex poles of the closed loop to the pair of complex zeros of the open loop. Here, the zeros are undamped hence if the gain is further increased, the damping of the poles moving to these undamped zeros will further decrease. The gain chosen here is thus a compromise between good performance and not a large amplification of the closed loop at the frequency of the pair of zeros.

To evaluate the performance of the control loop, the transmissibilities between the horizontal motion of the center of mass of the body m_2 and the two ground motions injected ω_x and ω_θ are shown in Fig. 4.12. The control loop achieves to reduce the transmission of horizontal ground motion of one order of magnitude between 0.5 Hz and 10 Hz. However, this performance

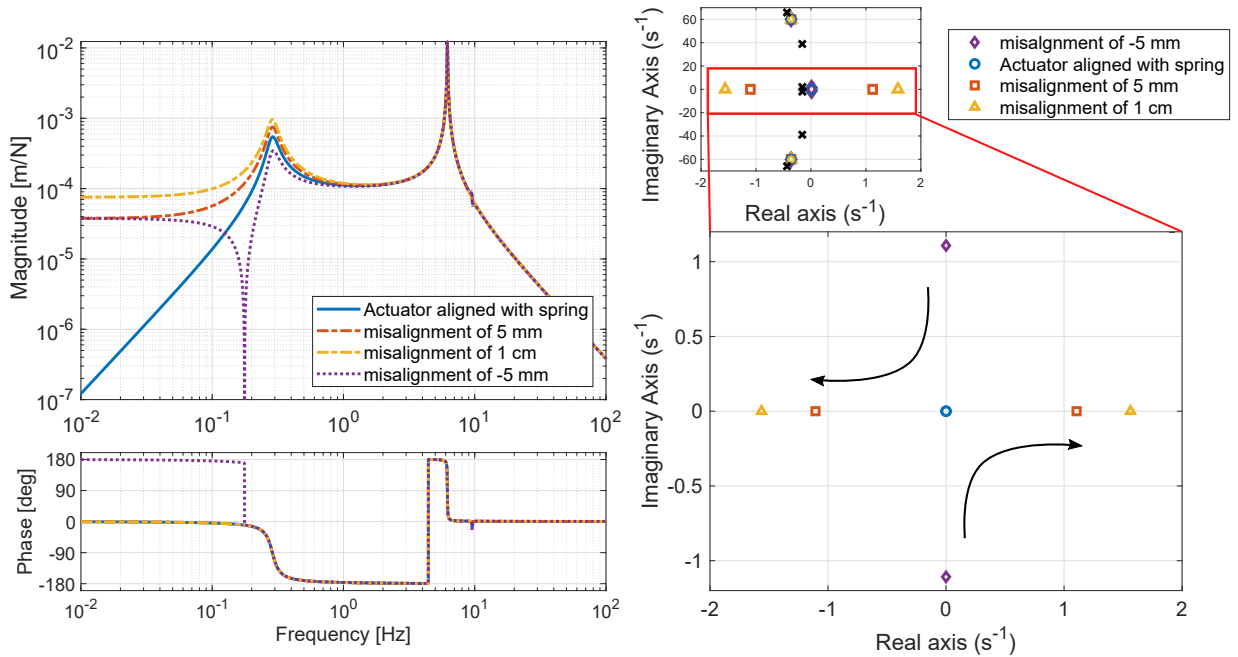


Figure 4.10: Plant for different location h_f of the actuator f_h . The poles and zeros corresponding to different locations of the force f_h are shown on the top right figure where the poles are the black crosses. A zoom on the zeros near the origin is shown on the bottom right.

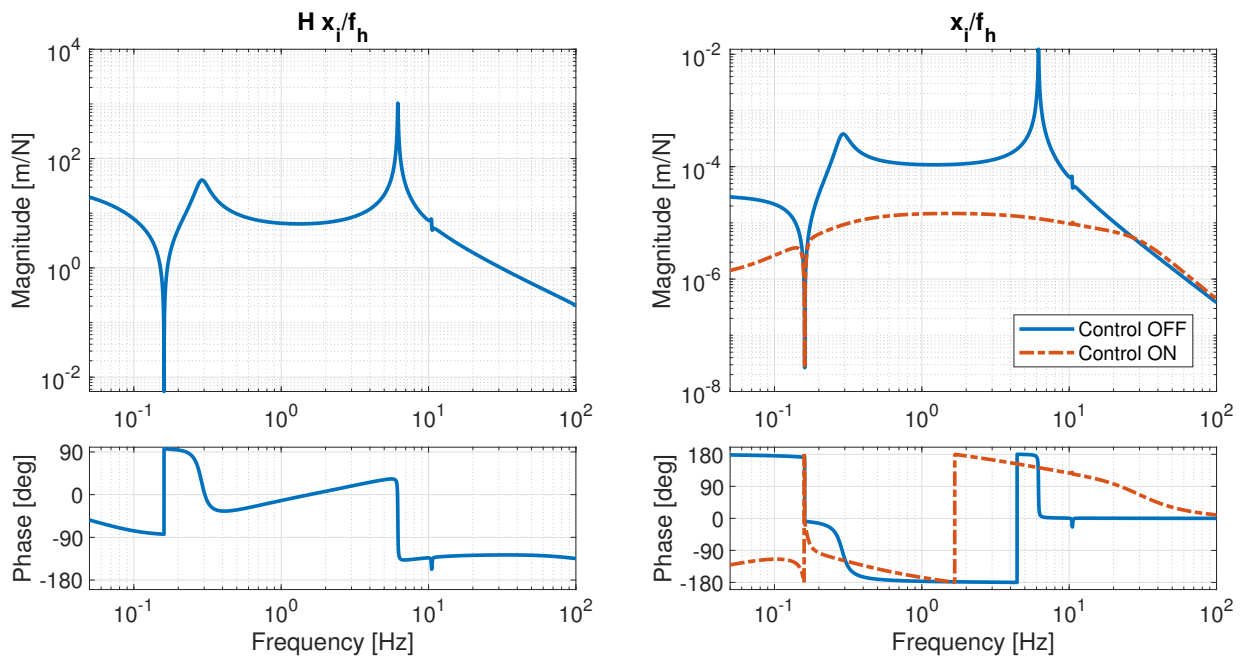


Figure 4.11: Open loop of the system when using an inertial sensor (left) and performance of the closed loop on the plant (right).

is made at the expense of an increase of coupling at low frequency between the horizontal motion of the payload and the rotation of the ground. The coupling is magnified because the signal measured by the HINS is not x_2 , the pure horizontal translation of the center of mass

4.3. MIMO control

m_2 , but $x_1 - x_2 + (h + \frac{h_s}{2})\theta$. Therefore, when closing the loop, some tilt is injected in the system.

Inertial control allows to reduce the translation of the payload but in return, it increases the tilt coupling. The effect of decoupling methods and other solution are studied hereafter to reduce this magnification.

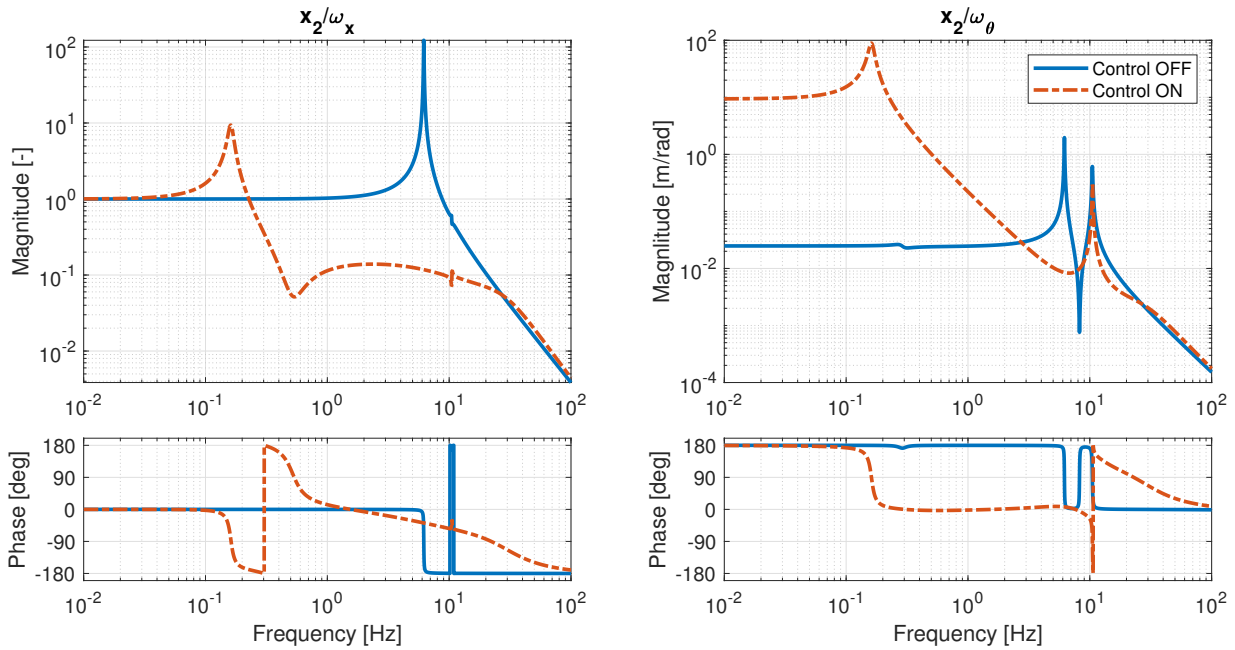


Figure 4.12: *Transmissibility between the horizontal motion of the payload of mass m_2 and the two directions of ground motion injected to the platform: horizontal ω_x (left) and rotation ω_θ (right) with (dashed red) and without (solid blue) inertial control. The resonance at 0.16 Hz is due to the migration of the poles of the closed loop to the zeros of the open loop of the system. The low frequency coupling to ground tilt is amplified by the inertial control.*

4.3 MIMO control

When coping with coupled MIMO systems, one solution proposed is to project the system in a decoupled frame. To study the impact of decoupling techniques on the 2 d.o.f. stage considered here, there is a need to introduce a second pair of sensor and actuator, see Fig. 4.13. In fact, to recover all the degrees of freedom from one system, we need to use the same number of sensor and actuators as the number of degrees of freedom.

Here, the additional actuator is a vertical actuator f_v and the additional sensor is an absolute vertical sensor measuring $y_3 = l_v\theta$. Note that the conclusions made with the absolute vertical sensor are also valid for an absolute rotation sensor as there is only a gain between these two signals.

A vertical actuator is exerting a force at the same location as the horizontal actuator.

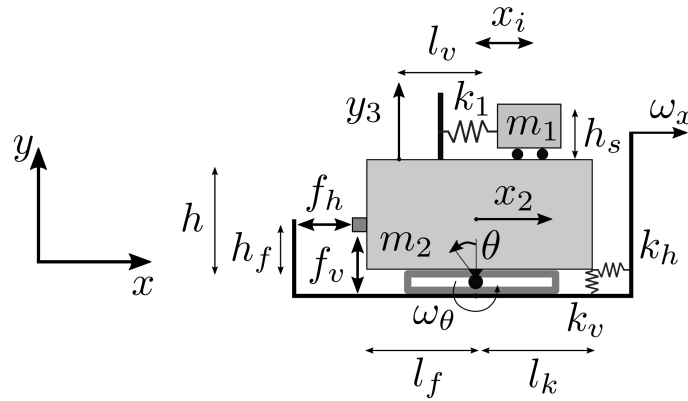


Figure 4.13: Sketch of the 2 d.o.f. stage with the additional vertical sensor y_3 . The additional force f_v is acting on the same point as the horizontal force f_h . The parameters are shown on the left figure and the three degrees of freedom considered are shown on the right figure.

The 2x2 plant of the resulting MIMO system is shown in Fig. 4.14. The HINS is sensitive to the vertical actuator due to the tilt-horizontal coupling. In fact, when a vertical force is applied, the platform rotates. For comparison, the same plant considering an ideal absolute sensor measuring the motion x_1 , see section 4.2.1, is also represented.

4.3.1 Centralized frame

Centralized control consists in controlling the degrees of freedom independently, i.e. the degree of translation and the degree of rotation here. The plant is projected from the local coordinates of the sensors and actuators into the global coordinates of the payload to isolate. The projection matrices are called the Jacobian matrices. The new plant is

$$G_{cen} = J_s^{-1} G_{dec} (J_a^T)^{-1}, \quad (4.16)$$

where G_{cen} is the plant in the centralized coordinates, G_{dec} is the original plant in the local coordinates, the post-compensator J_s is the Jacobian matrix allowing to project the sensor local coordinates in the global coordinates and the pre-compensator J_a is the Jacobian matrix allowing to project the actuators local coordinates into the global coordinates.

The global coordinates are defined in a frame centered at a specified origin. Usually, the origin of the frame is at the center of mass (COM) of the payload, hence m_2 , where the mass matrix of the system is decoupled. The resulting system is decoupled at high frequency as the mass term is dominating the high frequency dynamics of the system. To decouple at low frequency, it has been shown in Ref. [176] that projecting at the center of stiffness (COK) can reduce the coupling between the degrees of freedom. Again, this can be justified by the dynamics of the system as at low frequency, the stiffness term is dominating the equation of motion. These two options are discussed hereafter.

4.3. MIMO control

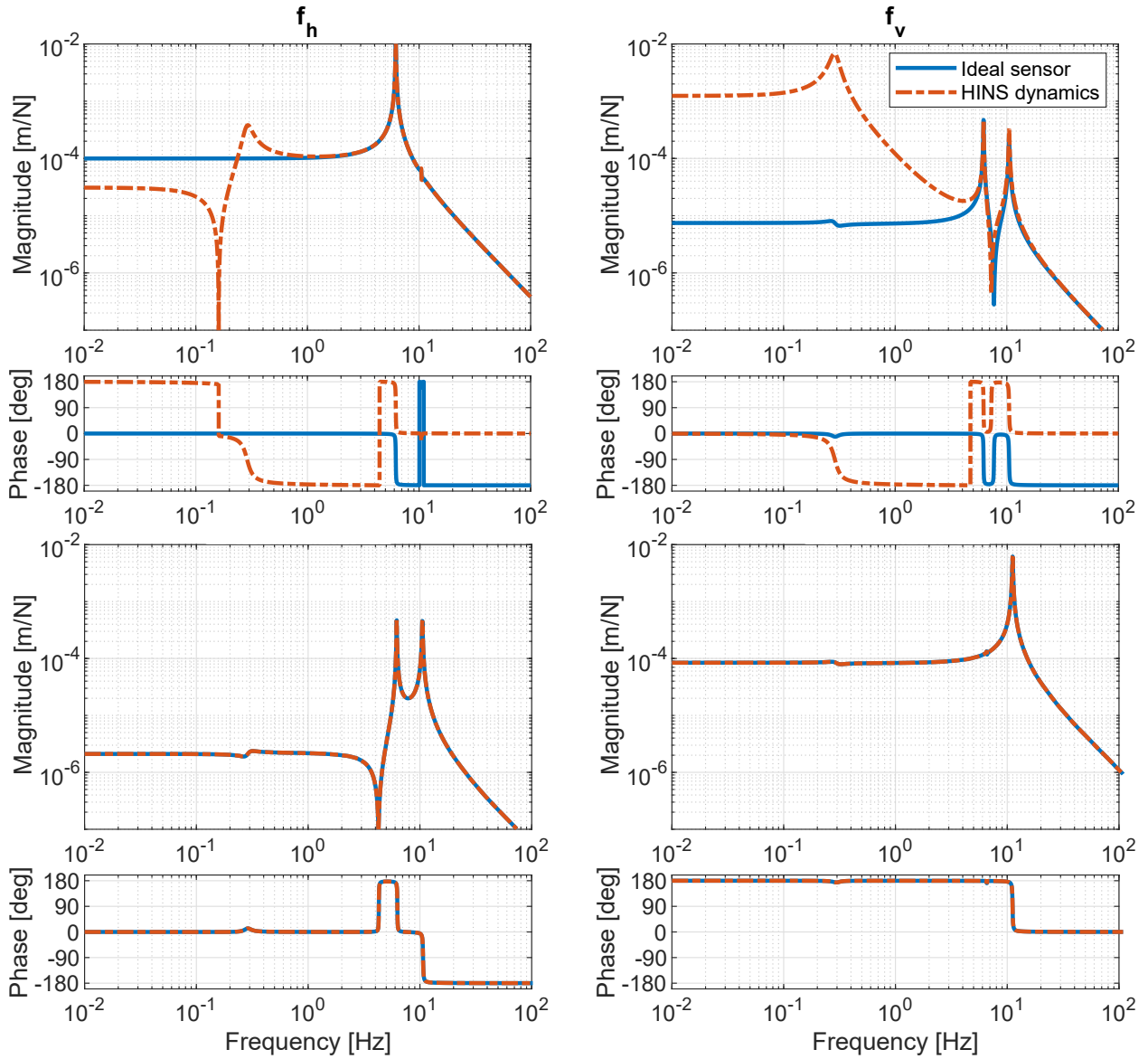


Figure 4.14: Plant of the 2×2 MIMO system. The horizontal displacement (top line) is measured by an ideal absolute sensor (solid blue) or a HINS (dashed red) and the vertical displacement (bottom line) is measured by an absolute vertical sensor.

Centralized frame with its origin at the center of mass

In order to project the system in the frame of the degrees of freedom centered at the COM of m_2 , the Jacobian of the sensors J_s and of the actuators J_a are

$$J_s = \begin{bmatrix} \partial x_1 / \partial x & \partial x_1 / \partial \theta \\ \partial y_3 / \partial x & \partial y_3 / \partial \theta \end{bmatrix} = \begin{bmatrix} 1 & -\frac{h+h_s}{2} \\ 0 & l_v \end{bmatrix}, \quad (4.17)$$

$$J_a = \begin{bmatrix} \partial f / \partial f_h & \partial M / \partial f_h \\ \partial f / \partial f_v & \partial M / \partial f_v \end{bmatrix} = \begin{bmatrix} 1 & \frac{h}{2} - h_f \\ 0 & -l_f \end{bmatrix}. \quad (4.18)$$

Knowing the Jacobians, the system is projected in the centralized frame by applying Eq. (4.16). The resulting system is shown in Fig. 4.15 for the system with and without HINS

dynamics. Each diagonal term shows only one resonance, corresponding to one mode of the system. Regarding the non-diagonal term of the system without sensor dynamics, we can see that at high frequency, the decoupling is decreased as expected from projecting at the COM. However, the projection in the centralized frame for the system with HINS dynamics does not improve the coupling.

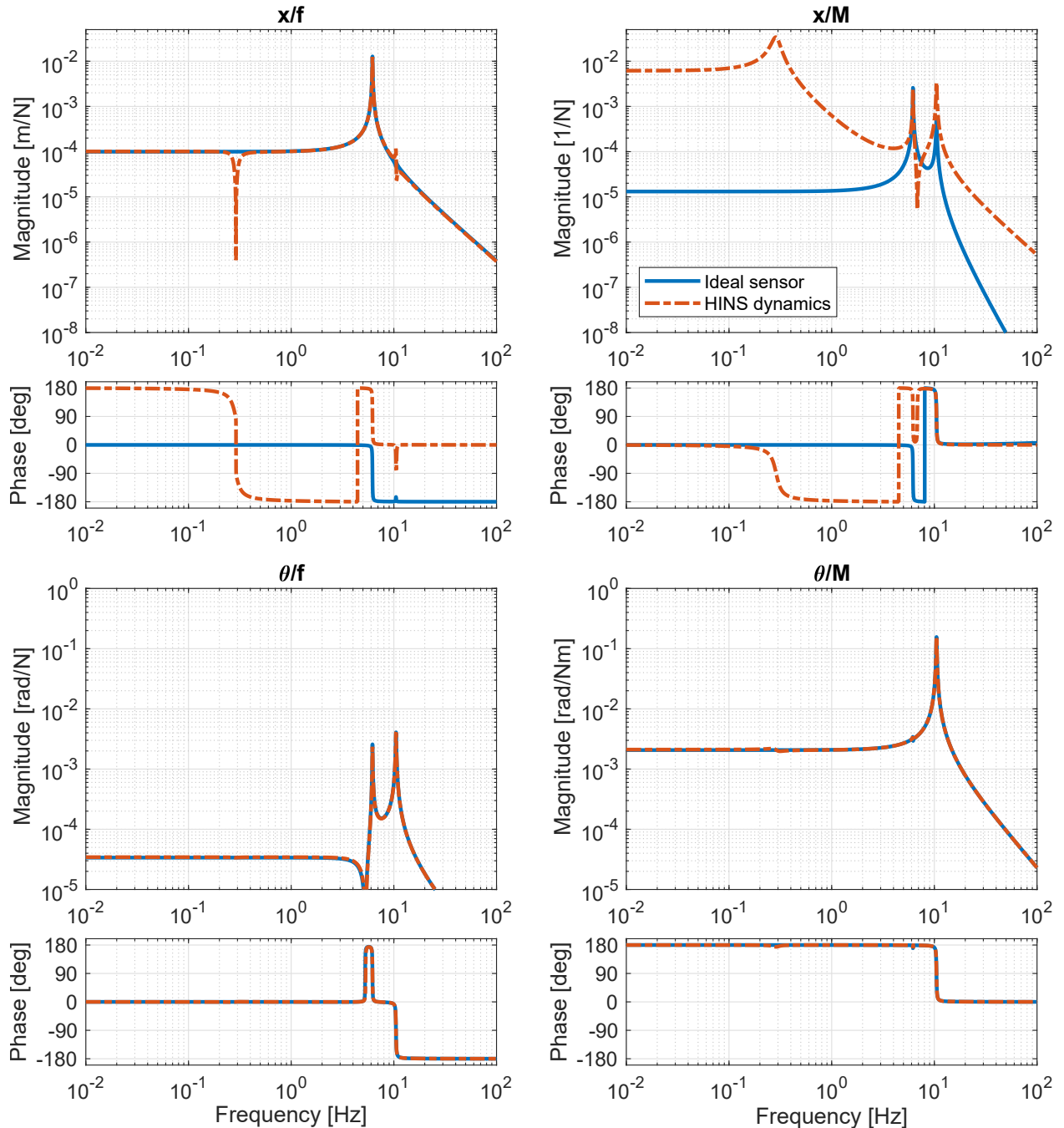


Figure 4.15: Plant of the 2×2 MIMO system projected in the centralized frame at the COM. The horizontal displacement is measured by an ideal absolute sensor (solid blue) or a HINS (dashed red) and the vertical displacement is measured by an absolute vertical sensor.

4.3. MIMO control

Centralized frame with its origin at the center of stiffness

The sensors and actuators Jacobians to project at the COK varies slightly from the previous one. In fact, the center of stiffness is any point in the horizontal line passing through the slider as exerting a vertical force in this plane induces a pure rotation and exerting a horizontal force, a pure translation.

$$J_s = \begin{bmatrix} 1 & -h - \frac{h_s}{2} \\ 0 & l_v \end{bmatrix} \text{ and } J_a = \begin{bmatrix} 1 & -h_f \\ 0 & -l_f \end{bmatrix}. \quad (4.19)$$

The resulting centralized system with and without sensor dynamics is shown in Fig. 4.16. Again, the two diagonal terms have one resonance, each corresponding to one of the two modes of the platform. In addition, as predicted, the projection at the COK reduces the low frequency coupling of the sensor signal when the sensor dynamics is not considered. Unfortunately, the coupling is not improved for the sensor when including HINS dynamics.

Neither the centralized projection at the COM or COK permits to decoupled the system when considering HINS dynamics. The projection of the system G_{dec} in the centralized frame centered at the COK, G_{cen} , for the element $\frac{x}{M}$ gives

$$G_{cen}(1, 2) = (J_s^{-1}(1, 1)G_{dec}(1, 2) + J_s^{-1}(1, 2)G_{dec}(2, 2))J_a^{-T}(2, 2) \quad (4.20)$$

$$= (G_{dec}(1, 2) + \frac{h + h_s/2}{l_v}G_{dec}(2, 2))\frac{-1}{l_f}. \quad (4.21)$$

The phase of x_1/f_v is opposite to the phase of y_3/f_v , when multiplied by the gains specified above and these two terms have the same amplitude. Therefore, the two terms $G_{dec}(1, 2)$ and $G_{dec}(2, 2)$ cancel each other at low frequency in the case without sensor dynamics. However, when considering the HINS dynamics, the amplitude of x_i/f_v is three orders of magnitude larger and hence, the two terms do not cancel each other. Therefore, projecting in the centralized frame does not permit to deal with the coupling due to inertial sensor dynamics.

4.3.2 Singular value decomposition

The singular value decomposition (SVD) allows to project the system into a new frame where the system is fully decoupled for each frequency and the directions obtained are orthogonal to each other [68]

$$G_{dec}(\omega) = U(\omega) \Sigma(\omega) V^H(\omega), \quad (4.22)$$

where $\Sigma(\omega)$ is a diagonal matrix whose elements are the singular values for a specific frequency, the post-compensator $U(\omega)$ is the matrix which allows to project the local sensor coordinates into the coordinates of the singular values for a specific frequency and the pre-compensator $V^H(\omega)$ is the projection matrix from the local actuator coordinates to the coordinates of the singular values at the frequency ω . A proper definition of how these quantities are evaluated can be found in appendix D.

In order to have real U and V^H projection matrices, the SVD can be applied on a real approximation of the plant [68].

From Eq. (4.22), the SVD has to be applied to all frequencies to decouple the plant at each frequency. However, an approximate decoupling can be performed, i.e., the decomposition

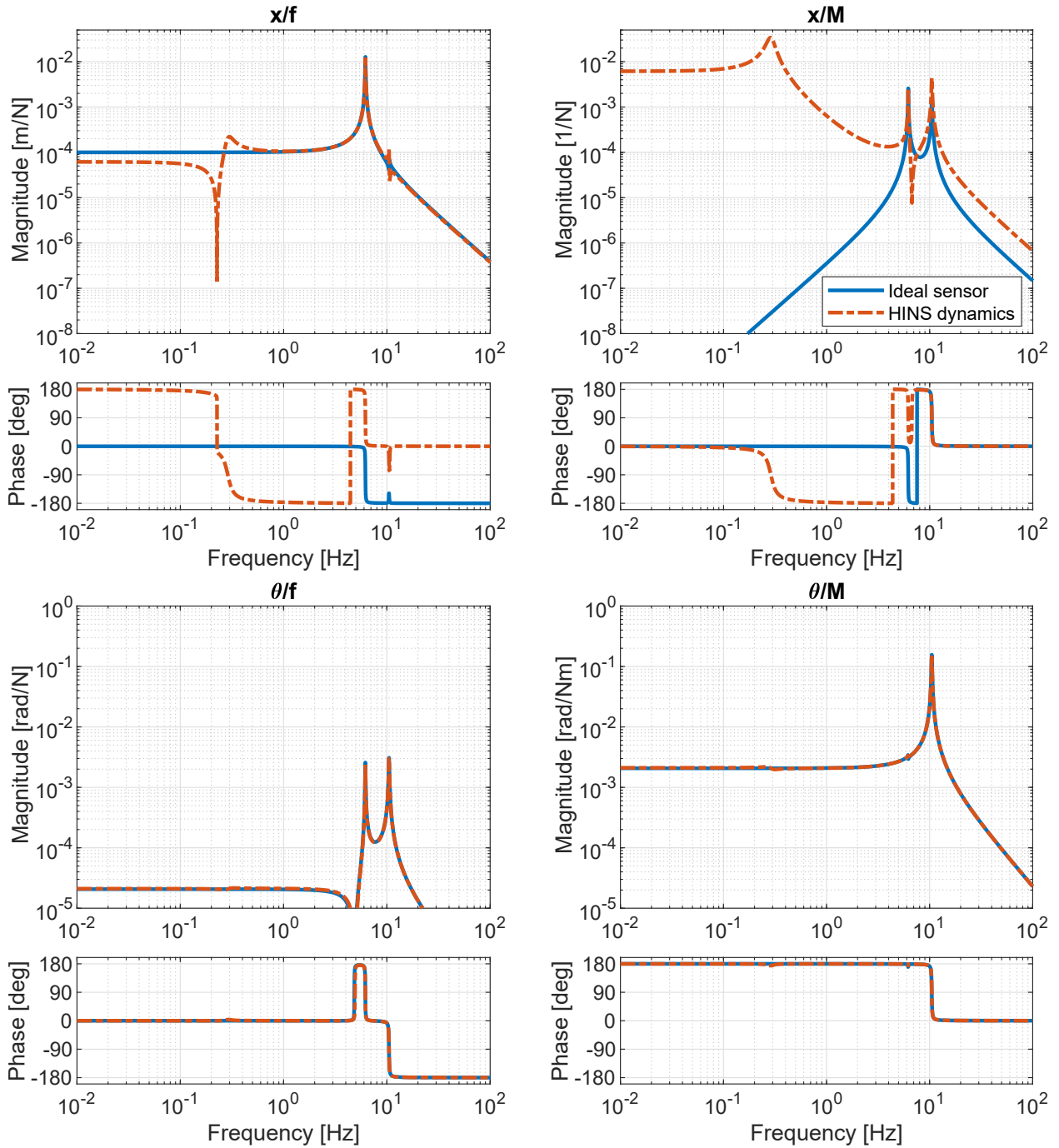


Figure 4.16: Plant of the 2×2 MIMO system projected in the centralized frame at the COK. The horizontal displacement is measured by an ideal absolute sensor (solid blue) or a HINS (dashed red) and the vertical displacement is measured by an absolute vertical sensor.

is calculated for a given frequency and the projection matrices are applied to the whole frequency range [68]. Approximate decoupling is preferred for reducing computation time. The SVD can be evaluated at the crossover frequency to guarantee decoupling of the system around this frequency. The system in the new frame becomes

$$G_{svd}(\omega) = U^{-1}(\omega_0) G_{dec}(\omega) (V^H)^{-1}(\omega_0), \quad (4.23)$$

4.3. MIMO control

where ω_0 is the crossover frequency.

Singular values are sorted from the largest one to the smallest one. Therefore, if the same gain is applied to all singular values, in practice the gain of the open loop transfer function will be different for each singular value and the isolation will be smaller for the smallest ones. If one wants to isolated all directions in the same way, each diagonal term can be normalized by its steady state gain.

Here, to apply the approximate SVD, the frequency chosen has to be carefully selected in order to decouple the low frequency content of the signal.

Above 1 Hz, the amplitude of x_i/f_h is larger than the amplitude of the non-diagonal term x_i/f_v , see Fig. 4.14. Therefore, the SVD will not improve the decoupling if the frequency used to evaluate the matrices U and V is chosen above 1 Hz.

Two frequencies have been tested: at 0.5 Hz, above the resonance frequency of the inertial sensor and at 0.05 Hz, below the resonance frequency of the HINS. The SVD when applied on the system with ideal sensor is shown in Fig. 4.17 and with inertial sensor in Fig. 4.18.

When applied to the system without sensor dynamics, the results are similar and the system is decoupled at low frequency. In addition, each diagonal element contains only one mode as expected from SVD. In addition, the decoupling is stronger at the frequency chosen to compute SVD.

However SVD does not allow to decouple the system with the HINS. To understand this difference, the inverse of the projection matrices obtained when using an ideal sensor and an inertial sensor are compared. The inverse of the U matrices are similar and are close to an identity matrix, at the exception of one sign. However, the columns of the inverse of the V^H matrices are switched. This permutation is due to the fact that the transfer function x_i/f_v has a larger amplitude at low frequency than the transfer function x_i/f_h . Due to this permutation, the diagonal and non-diagonal elements of the system are switched with SVD for the two frequencies at which the matrices are evaluated, see Fig. 4.14. Consequently, at low frequency the first singular value is indeed well decoupled but this is not the case of the second singular value.

This model has highlighted the fact that SVD is probably not a solution to decouple a system when some non-diagonal elements have an amplitude larger than the diagonal element of the system.

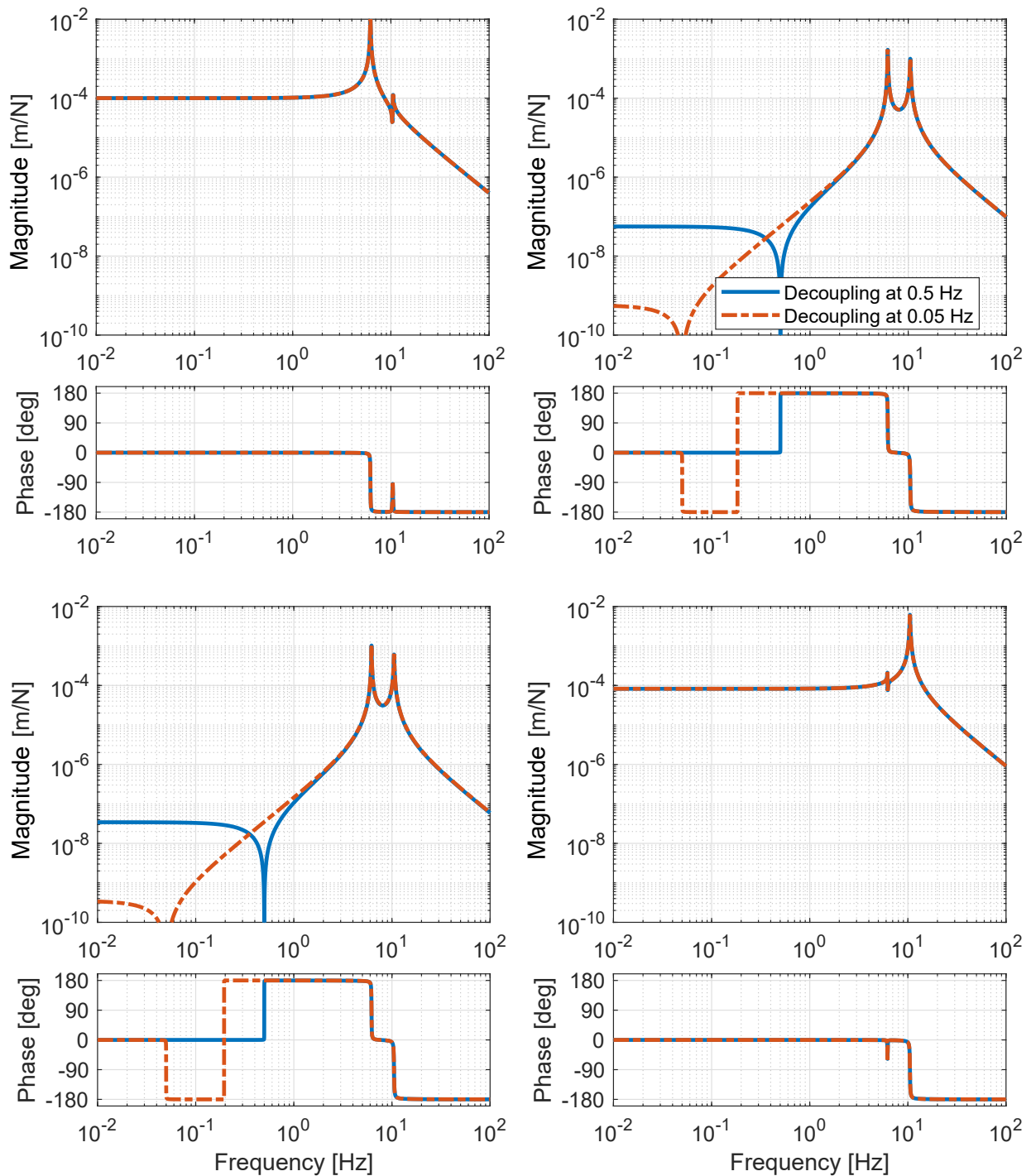


Figure 4.17: Plant of the 2×2 MIMO system projected in the frame of the singular values using SVD evaluated at 0.5 Hz (solid blue) and 0.05 Hz (dash-dotted red). The horizontal displacement is measured by an ideal absolute sensor and the vertical displacement is measured by an ideal vertical sensor.

4.3. MIMO control

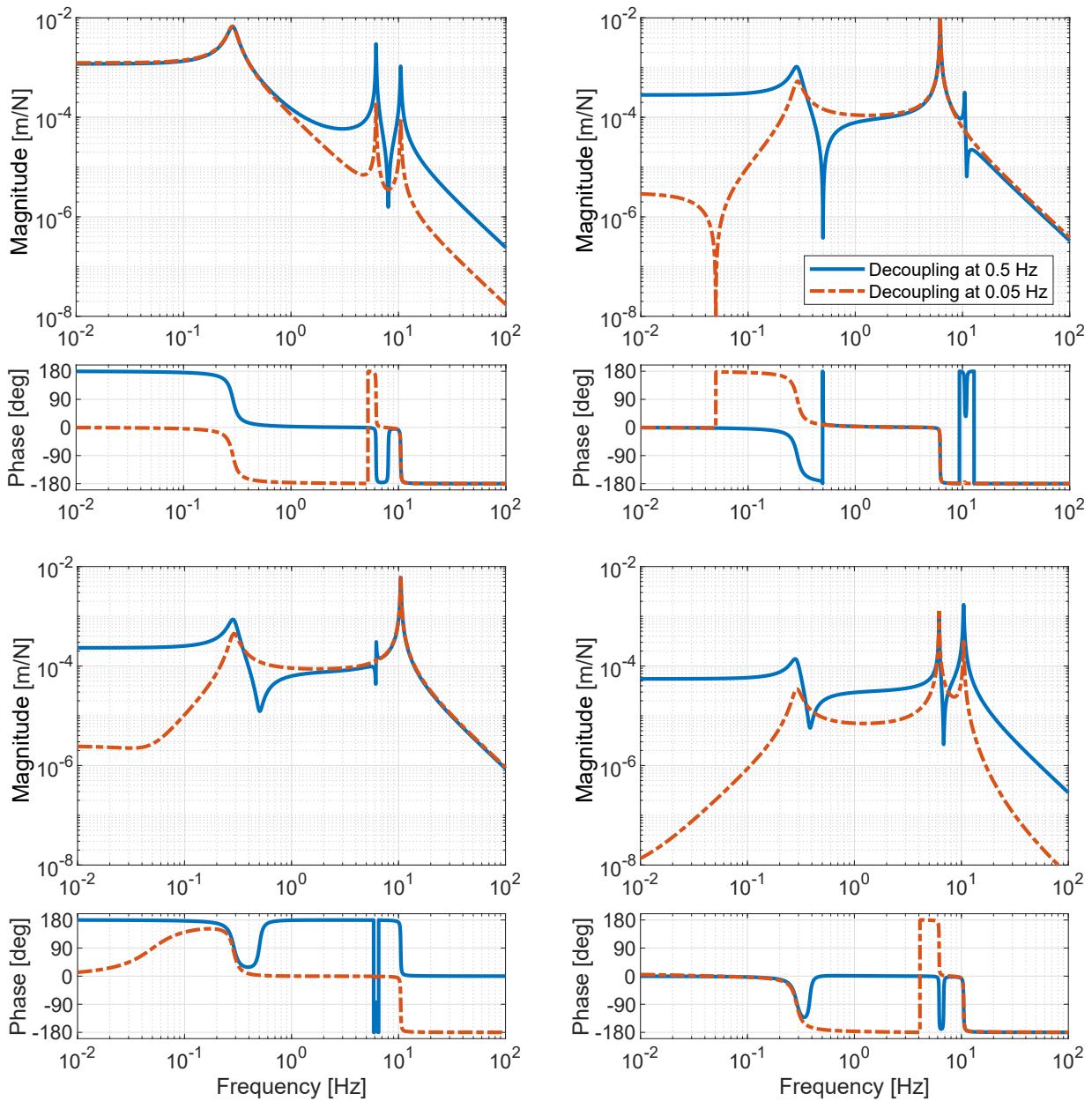


Figure 4.18: Plant of the 2×2 MIMO system projected in the frame of the singular values using SVD evaluated at 0.5 Hz (solid blue) and 0.05 Hz (dash-dotted red). The horizontal displacement is measured by a HINS and the vertical displacement is measured by an ideal vertical sensor.

4.4 Coupling mitigation techniques

At low frequency, the effect of gravity on the signal measured by an inertial sensor prevents the system of being decoupled. As shown in the previous section, projecting the system in another frame does not improve this issue. Other methods are investigated hereafter: cascade control, sensor correction and tilt subtraction.

4.4.1 Cascade control

As the tilt is dominating the signal of the inertial sensor at low frequency, one idea is to close a first inner loop that reduces the amplitude of the rotation, see Fig. 4.19. In order to see what type of vertical sensor is required to close this first loop, several options are tested: an inertial sensor, a relative displacement sensor and an ideal displacement sensor, see Fig. 4.20.

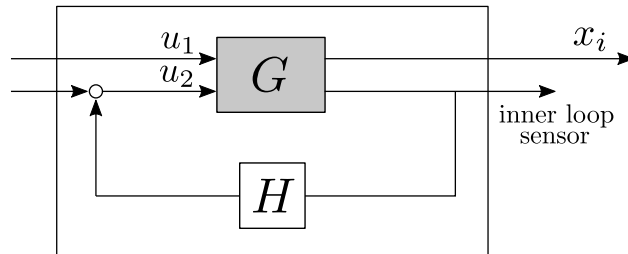


Figure 4.19: Block scheme of the first loop closed in the cascade control strategy.

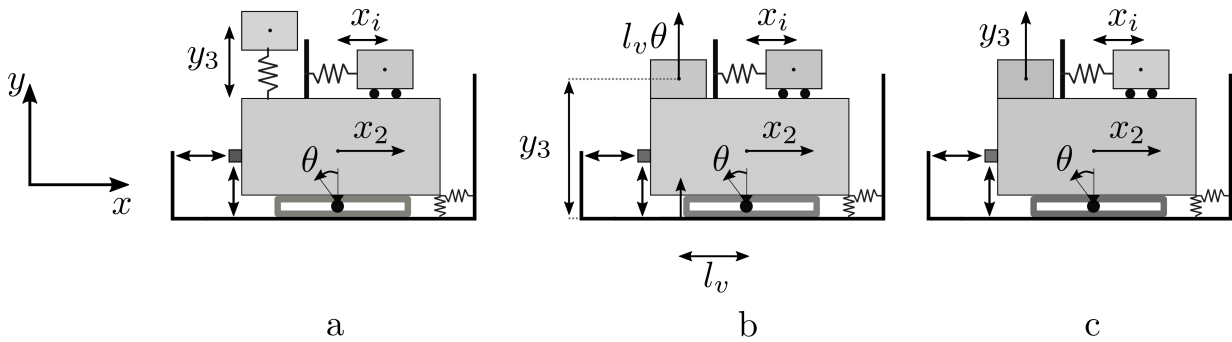


Figure 4.20: Options studied for the inner loop sensor. (a) inertial sensor, (b) relative sensor and (c) ideal sensor.

Inner loop with an inertial sensor

Let's consider the case presented in Fig. 4.20.a where the rotation is measured by a vertical inertial sensor. The spring suspending the inertial mass has a different stiffness than the horizontal sensor in order to have the resonance frequency at another value, considering the same weight for the inertial mass. In addition, the length of the spring at rest is designed to compensate the gravity sag due to the weight of the inertial sensor.

The open loop is shown in Fig. 4.21 when applying the same controller as in Eq. (4.15). The effect on the HINS can be seen in Fig. 4.22. The sensitivity of the sensor to ground rotation

4.4. Coupling mitigation techniques

is effectively reduced for frequencies above the zeros of the open loop.

In addition, when the inner loop is closed, the plant between the HINS and the horizontal actuator has an additional pair of complex conjugates poles due to the pair of complex zeros of the open loop at 0.06 Hz. The resulting plant for the outer loop now contains three pairs of complex conjugates poles in a row which corresponds to a total phase delay of -540° . It is not possible to design a stable controller on such a system.

Not surprisingly, adding another inertial sensor does not improve the performance as the sensor added is also coupled.

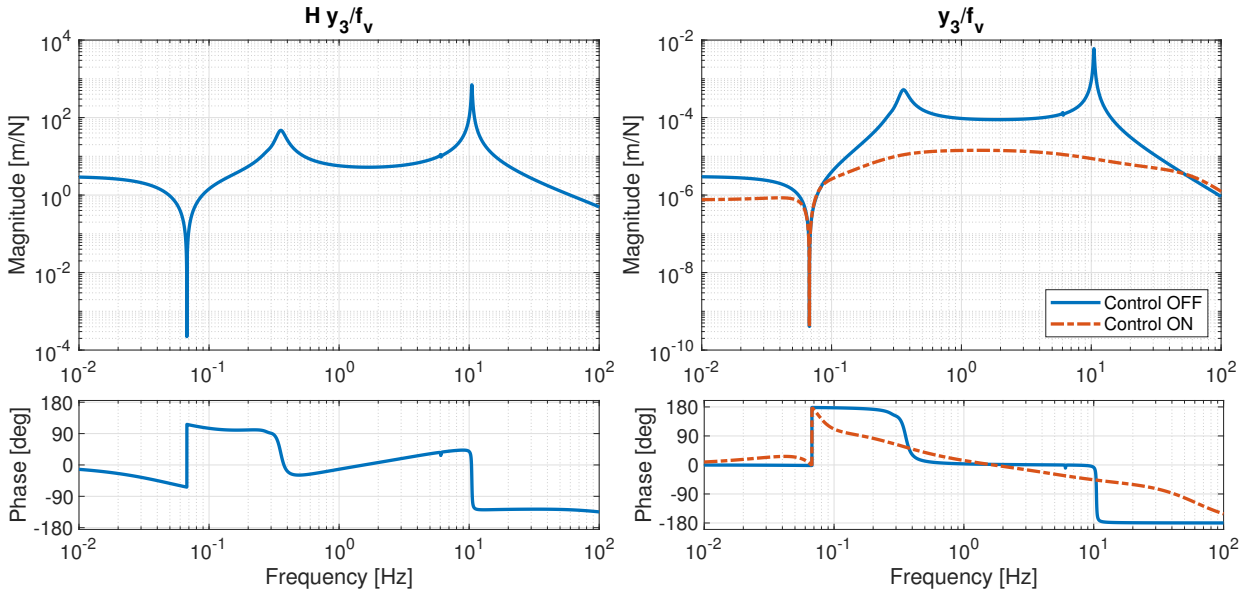


Figure 4.21: Open loop (left) and plant (right) of the inner loop using a vertical inertial sensor. The plant is shown without (solid blue) and with control (dash-dotted red).

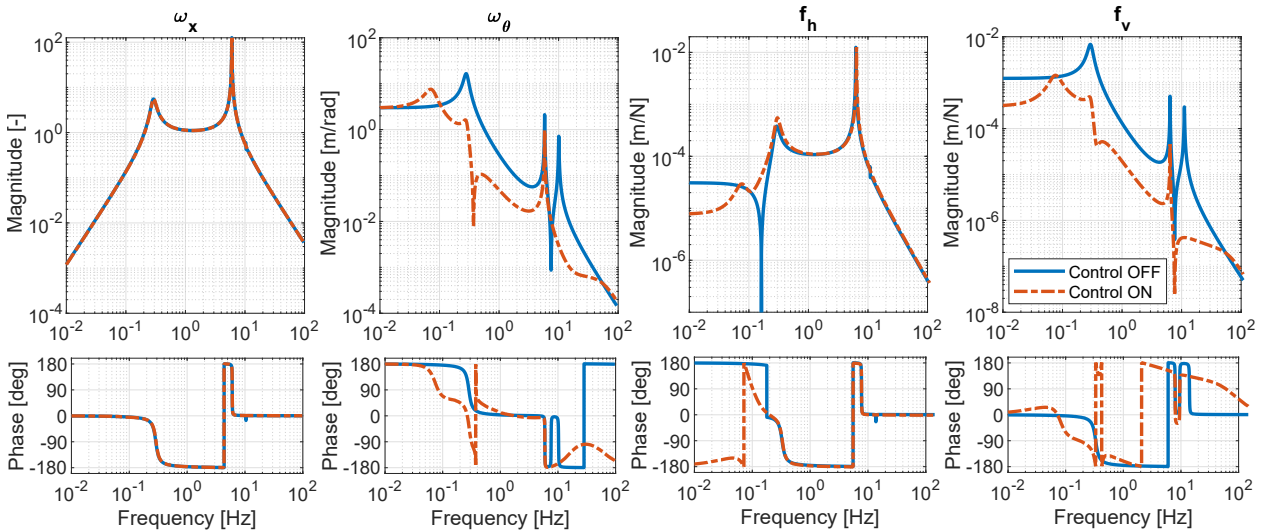


Figure 4.22: Transmissibilities with ground translation ω_x and ground rotation ω_θ and plant of the motion x_i of the 2 d.o.f. system without (solid blue) and with (dashed red) the inner loop closed using a vertical inertial sensor.

Inner loop with a relative sensor

The relative displacement sensor, represented in Fig. 4.20.b, measures the quantity $l_v(\theta - \omega_\theta)$. At low frequency, this quantity is canceled and hence, we cannot expect this method to reduce the tilt coupling at low frequency as shown here.

The controller applied is made of a gain and a lead

$$H(s) = 10^6 \frac{200 (s + 2\pi 50)}{50 (s + 2\pi 200)}. \quad (4.24)$$

The corresponding open loop is shown in Fig. 4.23. The relative rotation of the payload is effectively reduced. The effect of the relative sensor control on the HINS is shown in Fig. 4.24. As expected, the control has no effect on the transmission of ground rotation at low frequency. In addition, it increases the transmissibility with ω_θ at high frequency.

The effect of the inner loop on the plant can be observed on the last two figures of Fig. 4.24. First, the pair of zeros due to the tilt-horizontal coupling migrates to a lower frequency. This migration permits to increase the control bandwidth of the outer loop. Second, the amplitude of the transfer function from the vertical actuator f_v to the HINS is reduced of two order of magnitudes as the relative tilt of the payload is reduced. Consequently, the 2x2 plant becomes diagonally dominant, as required.

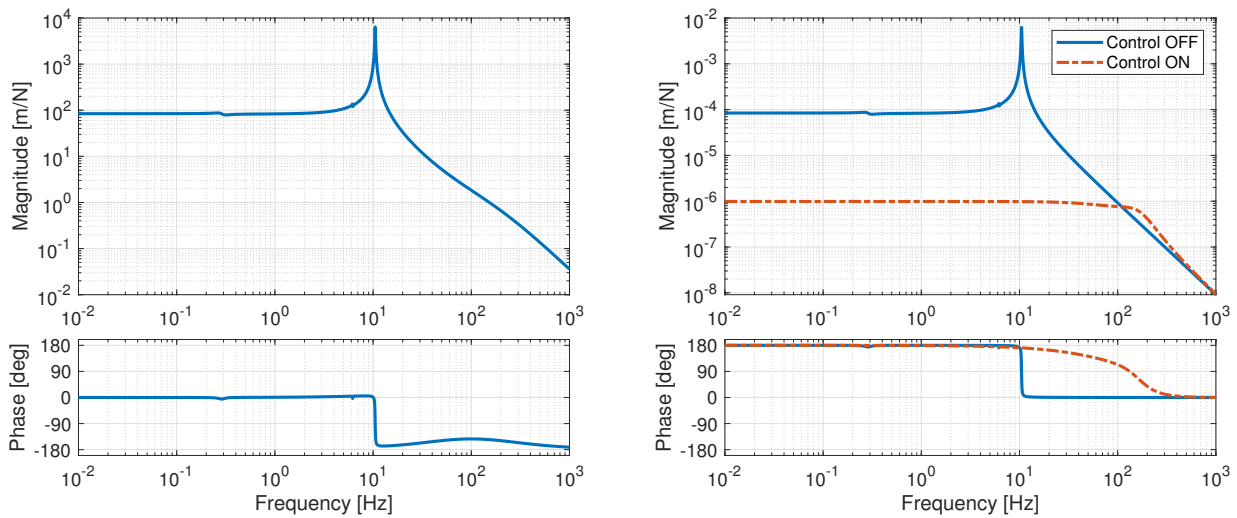


Figure 4.23: Open loop (left) and plant (right) of the inner loop using a vertical relative displacement sensor. The plant is shown without (solid blue) and with control (dash-dotted red).

Inner loop with an ideal sensor

The ideal displacement sensor measures the quantity $l_v\theta$, see Fig. 4.20.c. The open loop is identical to the one shown in Fig. 4.23, when using a relative displacement sensor. Therefore, the controller given in Eq. (4.24) is also applied. The effect of this control loop on the inertial sensor is also presented in Fig. 4.24. The effect on the transfer function from the actuator to the inertial sensor is similar to when using a relative displacement sensor. However, the transmission of the ground rotation is reduced of two order of magnitudes and there is no magnification at high frequency.

4.4. Coupling mitigation techniques

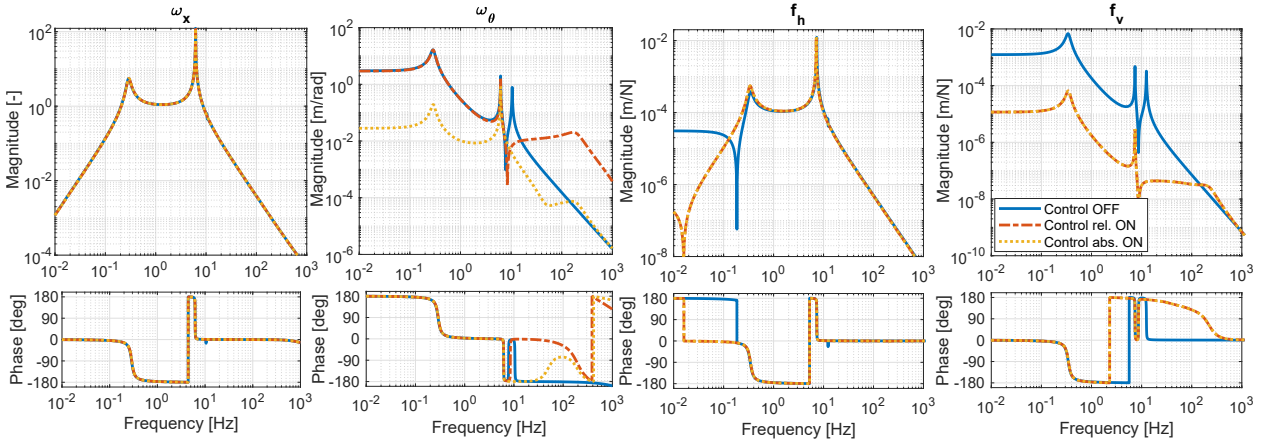


Figure 4.24: Transmissibilities with ground translation ω_x and ground rotation ω_θ and plant of the motion x_i of the 2 d.o.f. system without (solid blue) inner loop closed, with inner loop closed using a relative displacement sensor (dashed red) and with inner loop closed using an absolute displacement sensor (dotted yellow).

Comparing the control applied using the three types of sensor, the inner loop using inertial sensor does not improve the low frequency plant of the outer loop as the vertical inertial sensor (VINS) is also coupled at low frequency with rotation. The loop with a relative displacement sensor allows to decouple the plant without improving the transmission of ground rotation. The inner loop with an ideal displacement sensor is thus the best candidate to cope with the tilt-horizontal coupling; it allows to decouple the plant and reduces the sensitivity of the sensor to ground rotation.

Note that the results obtained with this ideal sensor will also be valid for an absolute rotation sensor.

Tiltmeter

We have seen that controlling the inclination with an ideal sensor reduces the amount of tilt transmitted to the inertial sensor and hence, modifies its dynamics. However, as shown in section 3.4.3, tiltmeters measure a coupled signal between rotation and translation. The beam-rotation-sensor (BRS) developed in Ref. [171] measures a signal corresponding to $\theta + 3 \cdot 10^{-5} x_2$ above the resonance frequency of the flexure. The sensor characterized in chapter 3 with the solid mirror from Thorlabs measures $\theta + 10^{-1} x_2$.

The inner loop of the cascade control is evaluated when using tiltmeters in the inner loop with these two different levels of coupling ($3 \cdot 10^{-5}$ and 10^{-1} rad/m) instead of an ideal sensor. The idea is to identify what is the largest sensitivity to translation that a tiltmeter can have that still permits to have satisfactory performance of the inner loop assuming that the resonance frequency of the flexure of the tiltmeter is the same as the one of the BRS at 8.9 mHz. The dynamics $D(s)$ of the tiltmeter to horizontal translation is [171]

$$D(s) = \frac{s^2}{s^2 + s\omega_0 0.1 + \omega_0^2}. \quad (4.25)$$

The plant used to close the inner loop is identical to the ideal absolute sensor plant in both cases. Therefore, the same controller as the one given in Eq. (4.24) is applied. The

effect on the transfer function between the inertial sensor x_i and the horizontal actuator f_h , the plant of the outer loop, is shown in Fig. 4.25.

When using the sensitivity of the BRS to horizontal motion, the inner loop has the same effect as when using an absolute tiltmeter. On the contrary, the sensor characterized in this thesis with the solid mirror is too sensitive to horizontal motion and hence, the inner loop is not effective. In addition, the resonance of the dynamics of the tiltmeter to horizontal translation, see Eq. (4.25), is visible at 8.9 mHz. In order to have an effect similar to the absolute tiltmeter, it appears that the translation to tilt ratio of the tiltmeter should be lower than 10^{-3} rad/m to have enough gain margin in the plant x_i/f_h .

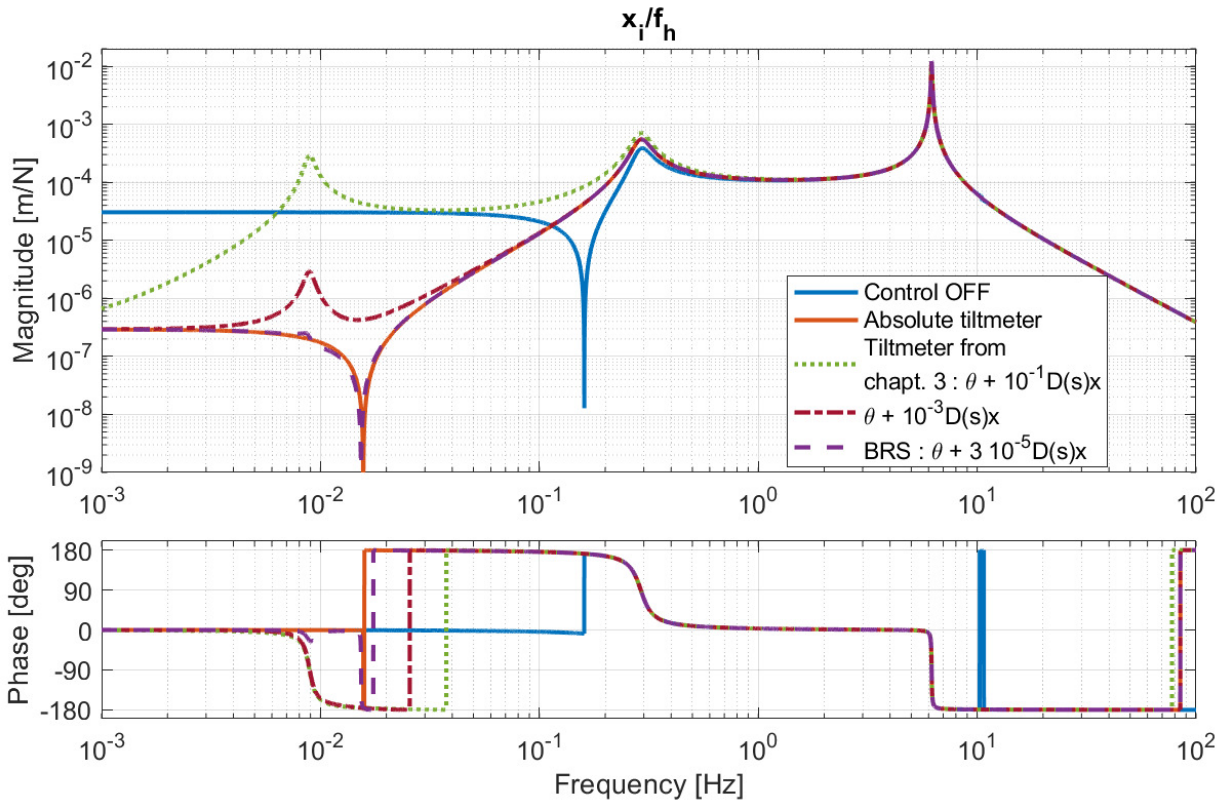


Figure 4.25: Plant between the HINS x_i and the horizontal actuator f_h of the 2 d.o.f. system without (solid blue) inner loop closed, with inner loop closed using an ideal tiltmeter (solid orange), the sensor characterized in chapter 3 (dotted green) and the tiltmeter that senses $\theta + D(s)10^{-3}x$ (dash-dotted red) and the BRS [173] (dashed purple). $D(s)$ is the dynamics of the tiltmeter given in Eq. (4.25).

Effect of the inner loop on centralized projection

The system obtained after closing the inner loop with an ideal sensor is projected in the centralized frame centered at the COM using the Jacobians defined in Eq. (4.17) and Eq. (4.18). The resulting d.o.f. are shown in Fig. 4.26. The amplitude of the non-diagonal elements is reduced and the pair of zeros for the first degree of freedom due to the dynamics of the HINS has now migrated to a smaller frequency, increasing the control bandwidth of the outer loop. The controller designed to isolate the resulting system can now be made of two independent

4.4. Coupling mitigation techniques

single input/single output (SISO) controllers applied to the diagonal elements. The effect of the inner loop is similar when projecting the system in a centralized frame centered at the COK.

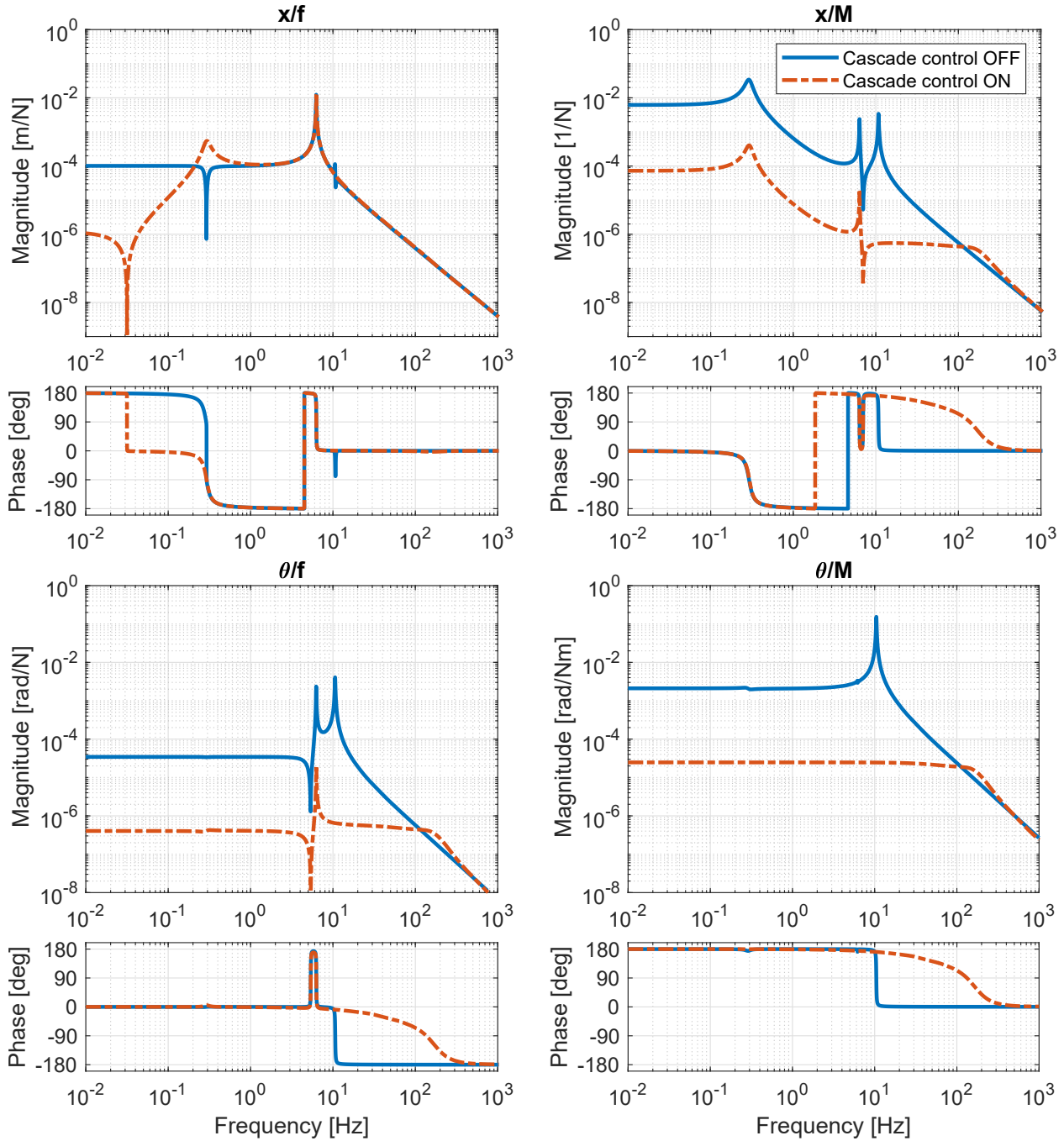


Figure 4.26: Plant of the 2×2 MIMO system projected in the centralized frame at the COM before (solid blue) and after (dashed red) closing the inner loop.

Effect of the inner loop on SVD

The system projected in the singular values frame when computing the SVD at 0.5 Hz is shown in Fig. 4.27. We can see that the system is decoupled above 0.1 Hz.

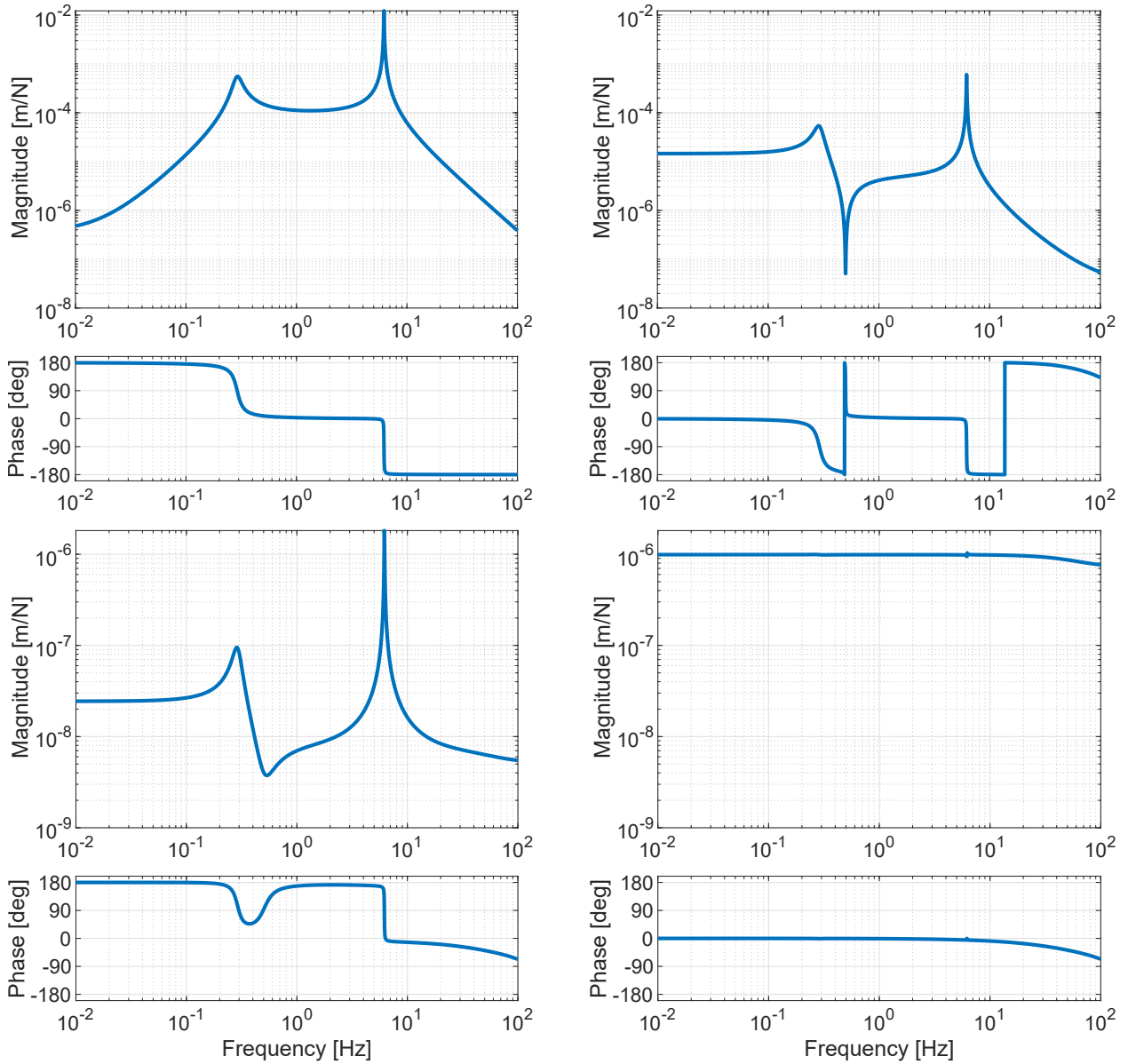


Figure 4.27: Plant of the 2×2 MIMO system projected in the frame of the singular values using SVD evaluated at 0.5 Hz after closing the inner loop.

The projection matrices evaluated at frequencies between the pair of zeros and poles of the sensor dynamics and those estimated for frequencies below the zeros of the sensor dynamics do not help to project in a frame where the system is decoupled. In these two cases, the system is decoupled at the frequency at which the SVD is evaluated but do not reduce coupling in the control bandwidth. This is easily understood with the shape of the red dashed curves of the first line of elements in Fig. 4.14, i.e. the transfer functions x_i/f_h and x_i/f_v . Below the resonance frequency, the non-diagonal term x_i/f_v has a larger amplitude, hence it will be considered as the dominant term by the SVD. The SVD decouples the resulting system at the specified frequency. However, as the term x_i/f_h has a increasing slope of s^2 above the evaluated frequency, the signal increases until the first mode. The smaller the frequency, the higher the amplitude of the non-diagonal term will be above the resonance

4.4. Coupling mitigation techniques

frequency of the inertial sensor. Therefore, due to this positive slope, the amplitude of the non-diagonal term is large and the system cannot be decoupled. This is illustrated in Fig.4.28, where the SVD matrices are evaluated at 0.01 Hz.

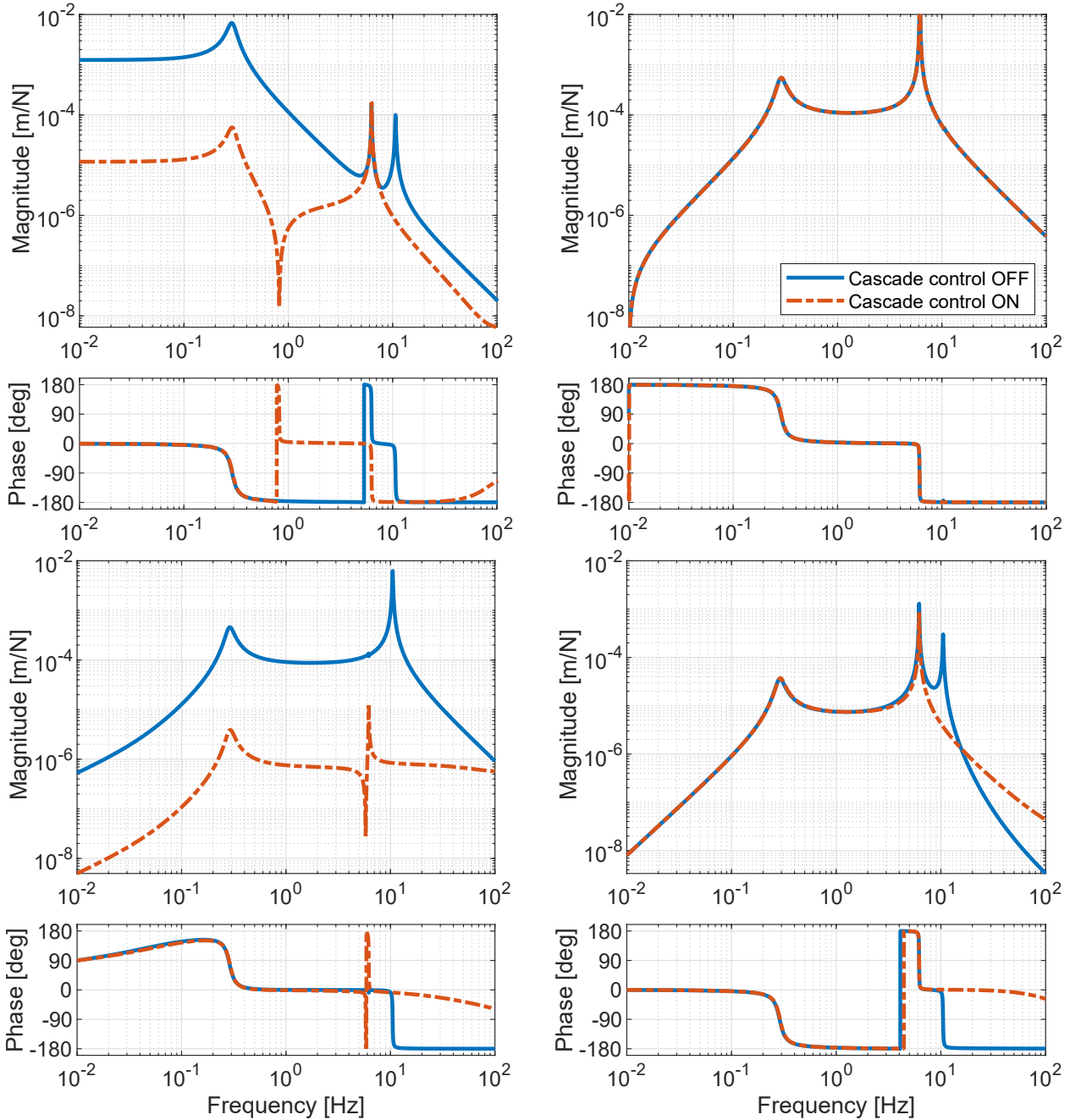


Figure 4.28: Plant of the 2×2 MIMO system projected in the frame of the singular values using SVD evaluated at 0.01 Hz before (solid blue) and after (dashed red) closing the inner loop.

4.4.2 Sensor correction

When taking into account the tilt-translation coupling, it has been shown in section 3.1.1 and section 3.1.2 that the dynamics D of the inertial sensor is composed of a pair of zeros

and a pair of complex conjugate poles

$$D(s) = \frac{s^2 + \omega_z^2}{s^2 + 2\xi\omega_p s + \omega_p^2}, \quad (4.26)$$

where ω_z is the resonance frequency of the zeros of the sensor dynamics;
 ω_p is the resonance frequency of the poles of the sensor dynamics;
 ξ is the damping factor of the poles of the sensor dynamics.

By comparison with the dynamics of an ideal inertial sensor, given in Eq. (2.2), the pair of zeros is not at 0 Hz. Depending on the architecture of the assembly, this pair of zeros can be a pair of undamped complex zeros or a pair of real zeros, as illustrated in Fig. 4.10. The signal measured by the inertial sensor can be corrected by multiplying it by the inverse of its dynamics.

The effect of the inverse of the dynamics applied to the plant is shown in Fig. 4.29. The zeros and the poles due to the inertial sensor dynamics are canceled for the plant x_i/f_h . However, the plant x_i/f_v contained at low frequency only the pair of poles related to the inertial sensor. This pole is canceled but in counterpart, there is now an undamped pair of complex poles at the frequency ω_z . Moreover, the static gain ω_z^2/ω_p^2 of the sensor dynamics in Eq. (4.26) is smaller than one as the frequency of the zero is smaller than the frequency of the pole. Consequently, the static gain of the plant is amplified and hence, the coupling is not reduced by multiplying by the inverse of the plant.

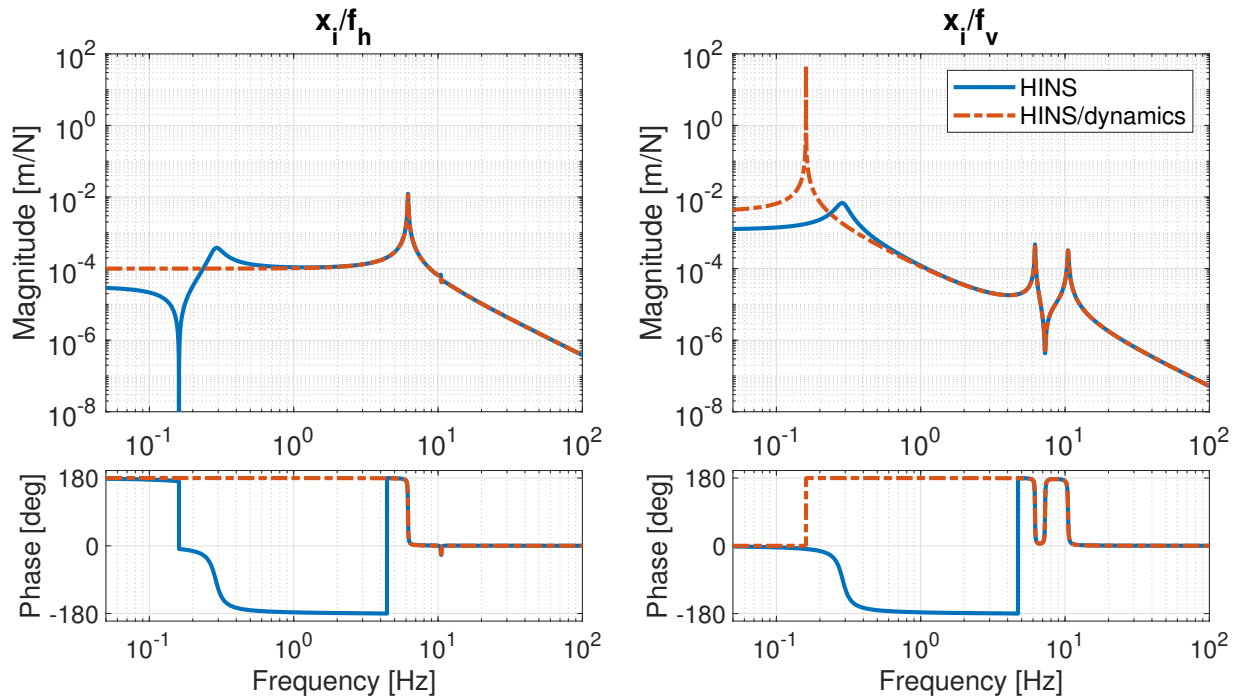


Figure 4.29: Control plant between the inertial sensor x_i and the horizontal f_h actuator (left) and with the vertical actuators f_v (right). The plant (solid blue) is multiplied by the inverse of the sensor dynamics (dashed red).

4.4. Coupling mitigation techniques

Even though sensor correction has no positive impact on the transfer function x_i/f_v , let's see what is its effect when closing the loop using the plant x_i/f_h . Based on Fig. 4.29, the controller applied is made of a lead to ensure phase margins at the crossover frequency

$$H(s) = 10^5 \frac{120 (s + 2\pi 10)}{10 (s + 2\pi 120) D(s)} . \quad (4.27)$$

This lead controller is multiplied by the inverse of the sensor dynamics.

To compare with Fig. 4.12 showing the closed loop performance of inertial control, the gain applied on the plant is chosen to reduce of one order of magnitude the motion x_i . The effect of the closed loop on the plant is shown in Fig. 4.30. The amplitude of the motion x_i is effectively reduced of one order of magnitude and hence, both plants are reduced. Note that the plant is not decoupled as would be needed to control the MIMO system. As stated above, the goal of the control loop is to reduce the motion of the payload, the body of mass m_2 . The effect of the control on the transmissibilities between x_2 and the two ground motion ω_x and ω_θ is shown in Fig. 4.31.

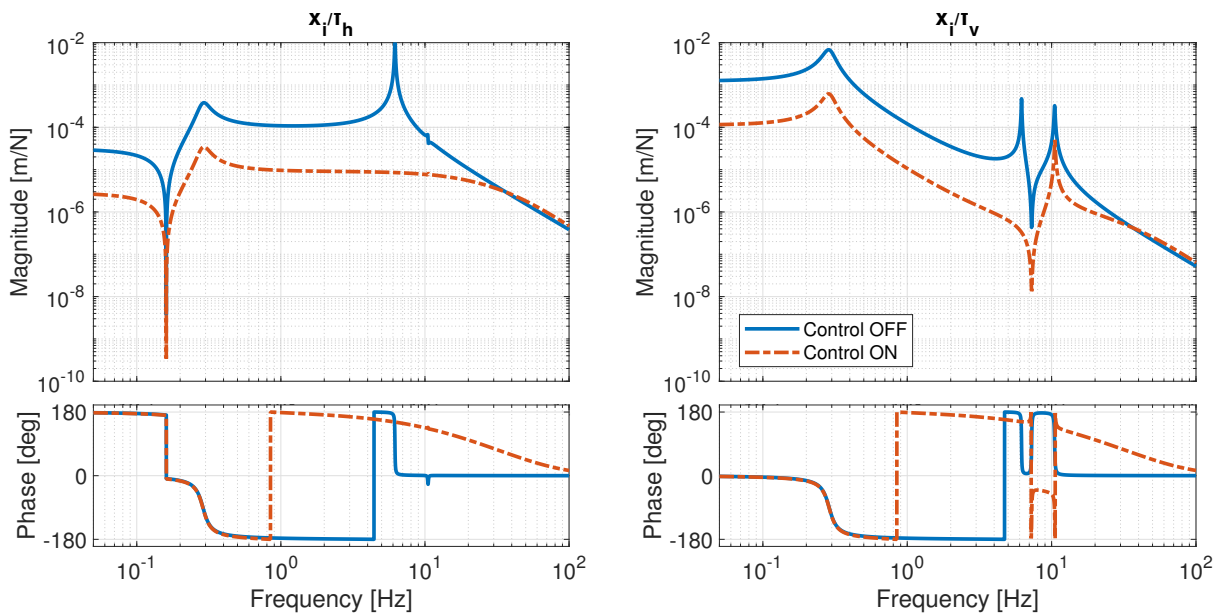


Figure 4.30: Plant between the inertial sensor x_i and the horizontal actuator f_h (left) and vertical actuator f_v (right). The plant is shown without (solid blue) and with inertial control (dashed red) when correcting the signal of the HINS by inverting its dynamics.

As shown by the transfer function x_i/f_v in Fig. 4.30, the sensor is more sensitive to rotation after sensor correction. Therefore, the motion of the payload x_2 is again coupled with ground rotation at low frequency due to the inertial control, similarly to inertial control without sensor correction studied in section 4.2.2.

In conclusion, using the inverse of the sensor dynamics does not solve the low frequency issues related to the tilt-translation coupling.

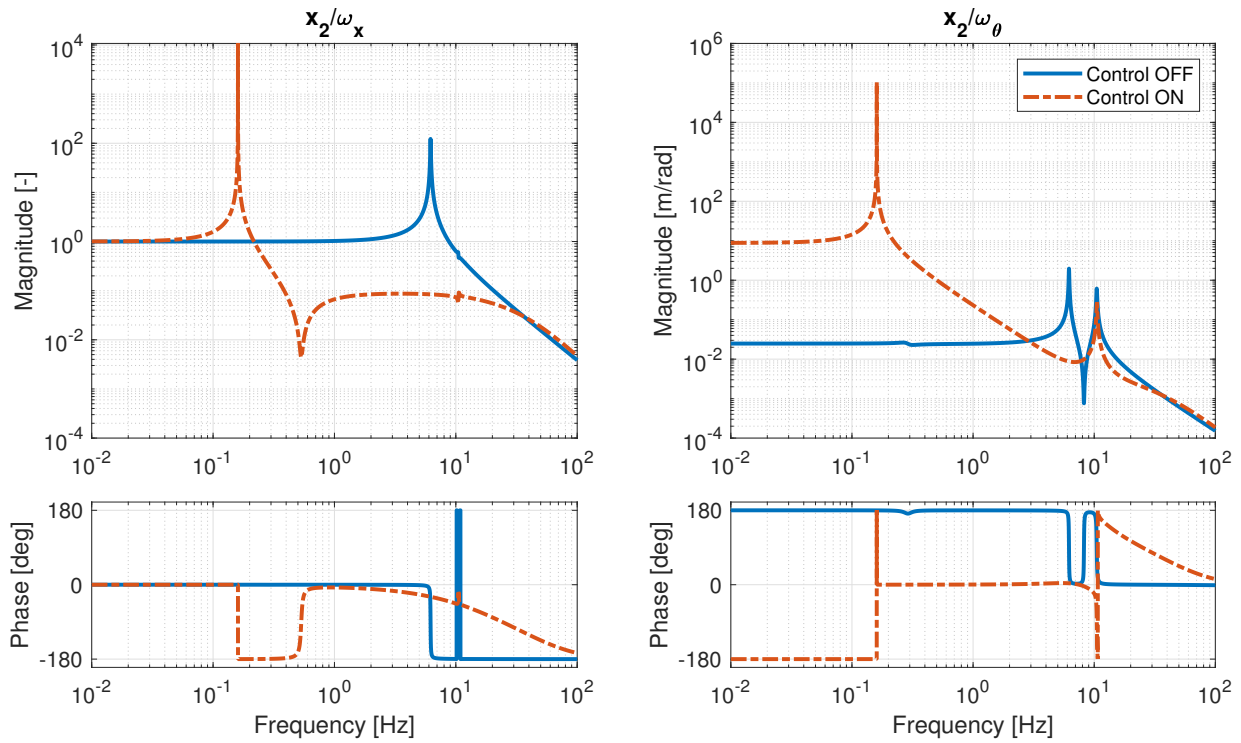


Figure 4.31: Transmissibility between the inertial sensor x_i and the horizontal ground motion ω_x and tilt ground motion ω_θ without (solid blue) and with (dashed red) inertial control when correcting the signal of the HINS by inverting its dynamics.

4.4.3 Tilt subtraction

In section 3.2, it is shown that the tilt signal can be subtracted from the signal measured by an inertial sensor by using an absolute rotation sensor [171].

Indeed, the contribution of the tilt signal to the signal measured by the inertial sensor is given in Eq. (3.3). Based on the equations of motion of the stage, see Eq. (4.10), the rotation can be removed using the signal measured by the ideal vertical sensor y_3 shown in Fig. 4.20. The corrected signal is

$$x_{corrected} = x_i + \frac{m_1 g}{m_1 s^2 + c_1 s + k_1} \frac{y_3}{l_v}. \quad (4.28)$$

The effect on the plant is shown in Fig. 4.32. For comparison, the plant measured when gravity is canceled is also plotted. In fact, if the rotation is subtracted properly, the resulting signal should correspond to the signal measured by the inertial sensor in the absence of a gravitational field.

As shown in the figure, the tilt-subtraction is efficient as the plant is now decoupled and the resulting transfer functions perfectly matches the no-gravity case.

In practice, the tiltmeter used measures a coupled tilt-translation signal, as explained in section 4.4.1. When considering a tiltmeter with the same sensitivity to translation as the BRS [173], the tilt subtraction is still effective. However, the tilt subtraction does not work when using a tiltmeter with the sensitivity of the sensor characterized in this thesis with the solid mirror. Tiltmeter with the translation to tilt ratio smaller than 10^{-3} rad/m is required

4.4. Coupling mitigation techniques

to have an effective tilt subtraction. Those conclusions are similar to what has been obtained when closing an inner loop with a tiltmeter in section 4.4.1.

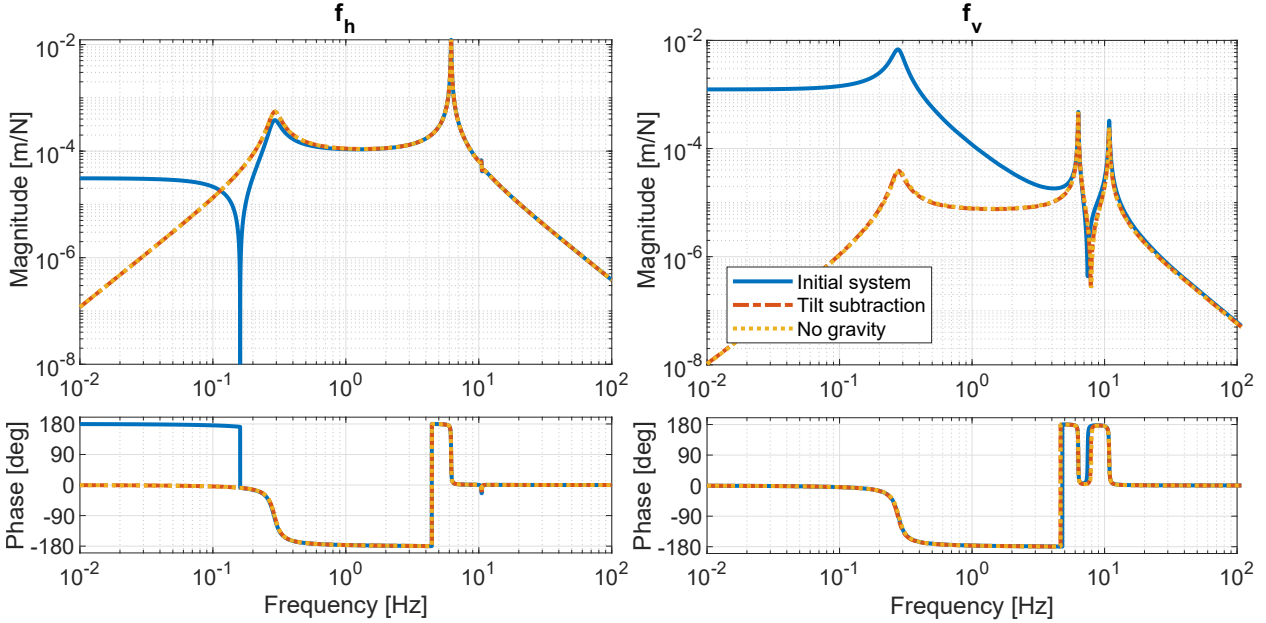


Figure 4.32: Plant (solid blue) between the inertial sensor x_i and the horizontal f_h and vertical f_v actuators. The signal after tilt subtraction (red dashed) matches the signal measured when the gravity is canceled (yellow dotted).

4.4.4 Control performance comparison

The following controller is applied between the HINS and the horizontal actuator on the system obtained with the inner loop closed using an ideal sensor, section 4.4.1, and on the system with the tilt subtracted from the HINS signal, section 4.4.3,

$$H(s) = 3 \cdot 10^6 \frac{120.0.01}{30.0.06} \frac{(s + 2\pi 0.06)(s + 2\pi 30)}{(s + 2\pi 0.01)(s + 2\pi 120)}. \quad (4.29)$$

The performance obtained when closing the loop on these two systems is shown in Fig. 4.33. Between 0.05 Hz and 50 Hz, the transmissibility x_2/ω_x is reduced of two orders of magnitude for the two methods. This frequency bandwidth corresponds to the region between the two crossover frequencies of the open-loops.

The transmissibility x_2/ω_θ at low frequency is either unchanged in the case of the tilt-subtraction or amplified at low frequency when applying the cascade control. The static gain obtained with the cascade control is however smaller than the static gain of the closed loop system with only one inertial control loop as shown in Fig. 4.12.

To understand the effect of the controllers on the transmissibility x_2/ω_θ , the transmissibilities between the inertial sensor x_i and the ground rotation ω_θ are shown in Fig. 4.34. As discussed earlier, it is the fact that the inertial sensor is sensitive to ground rotation that increases the coupling between the motion x_2 of the body m_2 and the ground rotation when

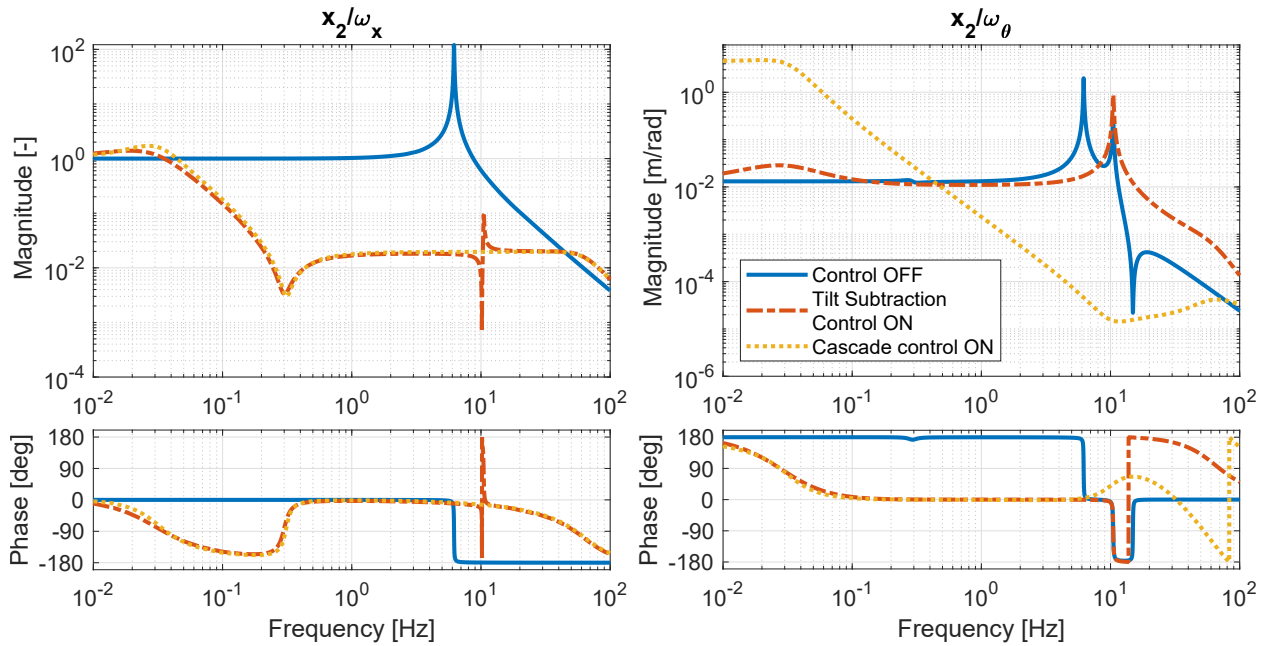


Figure 4.33: Transmissibility between the motion x_2 of the body m_2 and the horizontal ground motion ω_x and tilt ground motion ω_θ without control (solid blue), with the controller H applied on the HINS when the tilt signal is subtracted (dash-dotted red) and when the cascade control is applied (dotted yellow).

applying inertial control.

The tilt-subtraction completely cancels this coupling, see Fig. 4.34, and hence, closing the loop does not affect the transmissibility x_2/ω_θ .

The inner loop reduces the amplitude of the static gain and hence, the static gain of the transmissibility x_2/ω_θ is also reduced. Increasing the gain of the inner loop further reduces the amplitude of the static gain. However, the gain of the inner loop can not be arbitrary increased and the stability of the closed loop system has to be investigated. Therefore, tilt subtraction is the most promising solution among these two ideas.

Note that in practice, a reduction by five orders of magnitude of the sensitivity of the inertial sensor to rotation is not realistic. In fact, the resolution of the tiltmeter will limit the ability to subtract the tilt signal. For example, the BRS achieves to reduce of one order of magnitude the sensitivity of the Trillium T240 to rotation between 6 to 90 mHz [171]. It was demonstrated in Ref. [171] that the reduction was limited by the resolution of the tiltmeter and by the fact that the inertial sensor and the tiltmeter were not located on the same platform and hence, were sensitive to different local inclinations of the ground.

4.5 Summary

In this chapter, we have studied the effect of inertial control on a 2 d.o.f. isolation stage. Due to the inertial sensor dynamics, the signal measured by the inertial sensor is a combination of translation and rotation. Consequently, when closing the loop, the payload becomes coupled with rotation. Two ideas can reduce this effect: the cascade control with an inner loop

4.5. Summary

controlling the inclination and tilt-subtraction. Among them, tilt subtraction improves the most the control plant at low frequency and hence, the performance of the isolation platform. In addition, it has been shown that existing tiltmeters can be used to apply this solution as long as the ratio between their sensitivity to translation and to tilt is lower than 10^{-3} rad/m.

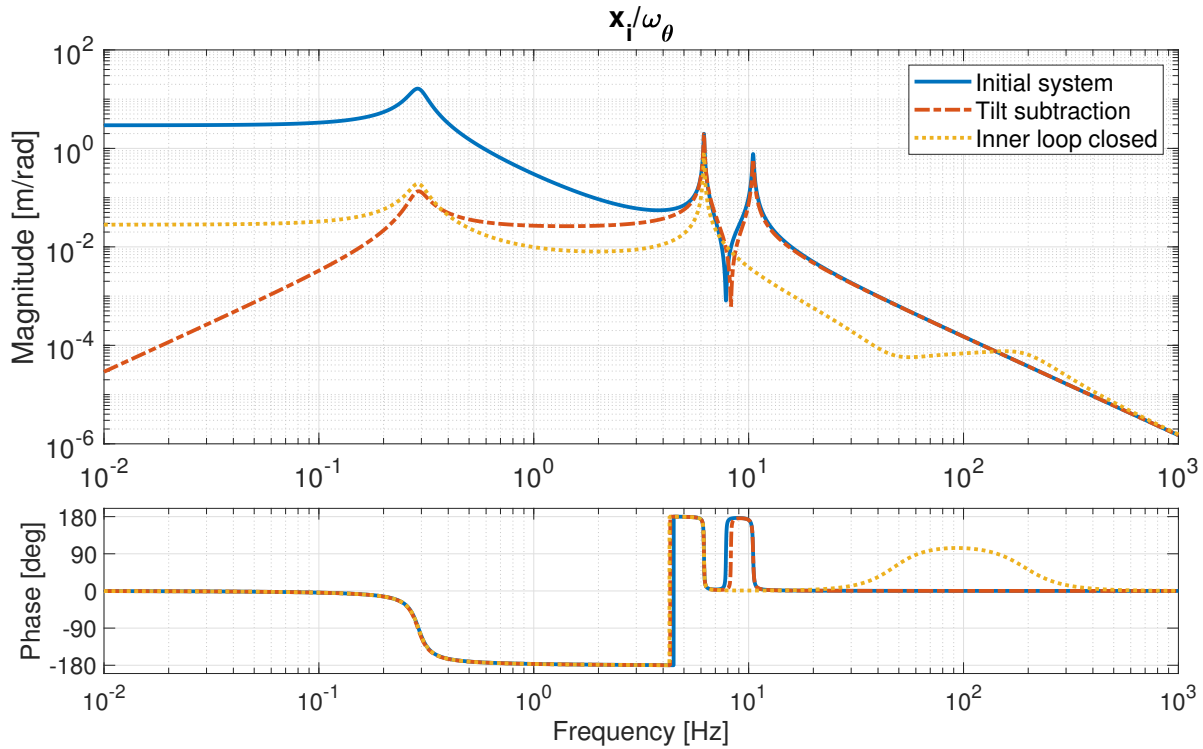


Figure 4.34: *Transmissibility between the signal measured by the inertial sensor x_i and the tilt ground motion ω_θ for the initial system (solid blue), the system with the tilt signal subtracted from the HINS signal (dash-dotted red) and when the inner loop of the cascade control is applied (dotted yellow). Tilt subtraction reduces the most the sensitivity of the inertial sensor to the rotation of the ground which justifies why there is no magnification of the amplitude at low frequency of the transfer function x_2/ω_θ in Fig. 4.33.*

Chapter 5

Experimental inertial control

Contents

5.1	Description of the platform	125
5.1.1	Yuanda isolators	126
5.1.2	Current amplifier	129
5.2	Identification of the system	130
5.3	Isolation	134
5.3.1	Vertical decentralized control	135
5.3.2	Horizontal decentralized control	135
5.3.3	Performance	138
5.3.4	Liquid sensor on the platform	141
5.4	Summary	142

The effect of inertial control on coupling has been studied numerically in chapter 4. The inertial sensors characterized in chapter 2 and in chapter 3 are assembled on a 6 degree-of-freedom (d.o.f.) active isolation platform to apply inertial control experimentally. In this chapter, the active isolation stage is described and the different elements of the system are characterized. Decentralized inertial control strategies are then studied.

5.1 Description of the platform

The isolation stage assembled is shown in Fig. 5.1. It is made of an active isolation platform supported by a passive platform. For clarity, all these elements and their interactions are represented in Fig. 5.2.

The passive platform is made of a rectangular table supported by four springs OS25/200 from Christie & Grey. The active isolation stage is placed on top of this passive one: a hexagonal table of 157 kg is supported by three Yuanda isolators. The voice coils inside the isolators are fed with a homemade current amplifier.

On top of the hexagonal payload, three sensors units are made of one horizontal inertial sensor (HINS) and one vertical inertial sensor (VINS) each, presented in chapter 3. Each

5.1. Description of the platform

pair is sealed inside a vacuum chamber BJ-12-SF from Applied Vacuum Engineering. The bell jar can maintain a pressure of 10 mbar. The feedthroughs of the vacuum chambers are below the plate hence, a homemade support was designed to ensure enough height for the connectors, see Fig. 5.3. Each vacuum chamber support weights 8 kg and the holes for the screws are unique for each of the three supports in order to match the holes of the hexagonal table. The part is extruded to reduce the mass in a way that guarantees enough rigidity. The first internal mode is calculated with a FEM software and is at 1916 Hz.

Two Koheras Adjustik X15 with a 1550 nm wavelength are used to feed the six interferometers. Two 1x4 splitters from Muquans UFS1560-1x4 are used to divide the incoming beam into three beams and the outputs of each splitter feed half of the interferometers used. The signal coming from the sensors is processed by the dSpace Scalexio with a sampling frequency of 10 kHz to feed the actuators through the homemade current amplifier. The characterization of these equipments is presented hereafter.

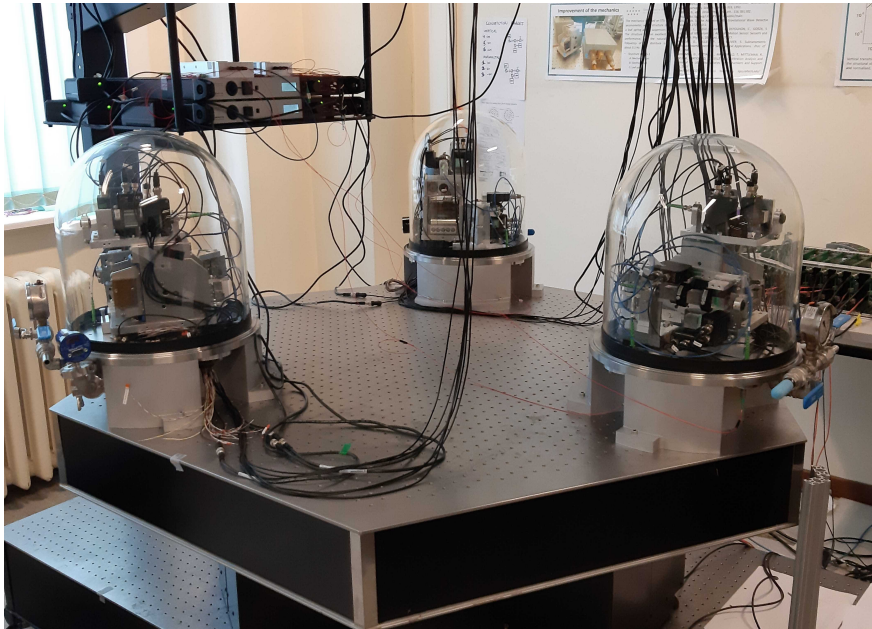


Figure 5.1: *Picture of the active isolation platform mounted on the passive stage. The data acquisition system and current amplifier are not visible.*

5.1.1 Yuanda isolators

The isolators from Yuanda Tech, shown in Fig. 5.4, are made of horizontal and vertical springs. Each isolator contains adaptive negative stiffness springs in the vertical direction. Inside each isolator, there is a pair of horizontal and vertical voice coil actuators (transducer constant is 2.8 N/A for horizontal voice coils and 2 N/A for vertical ones). The isolators are designed to support a weight between 50 kg and 125 kg each. The isolators can be leveled independently to tune the static inclination of the payload.

Two experiments are conducted to characterize these isolators. First, each isolator is tested independently and second, the three isolators are placed below the hexagonal payload. The first test aims to verify that the isolators have a similar response. The second test helps to

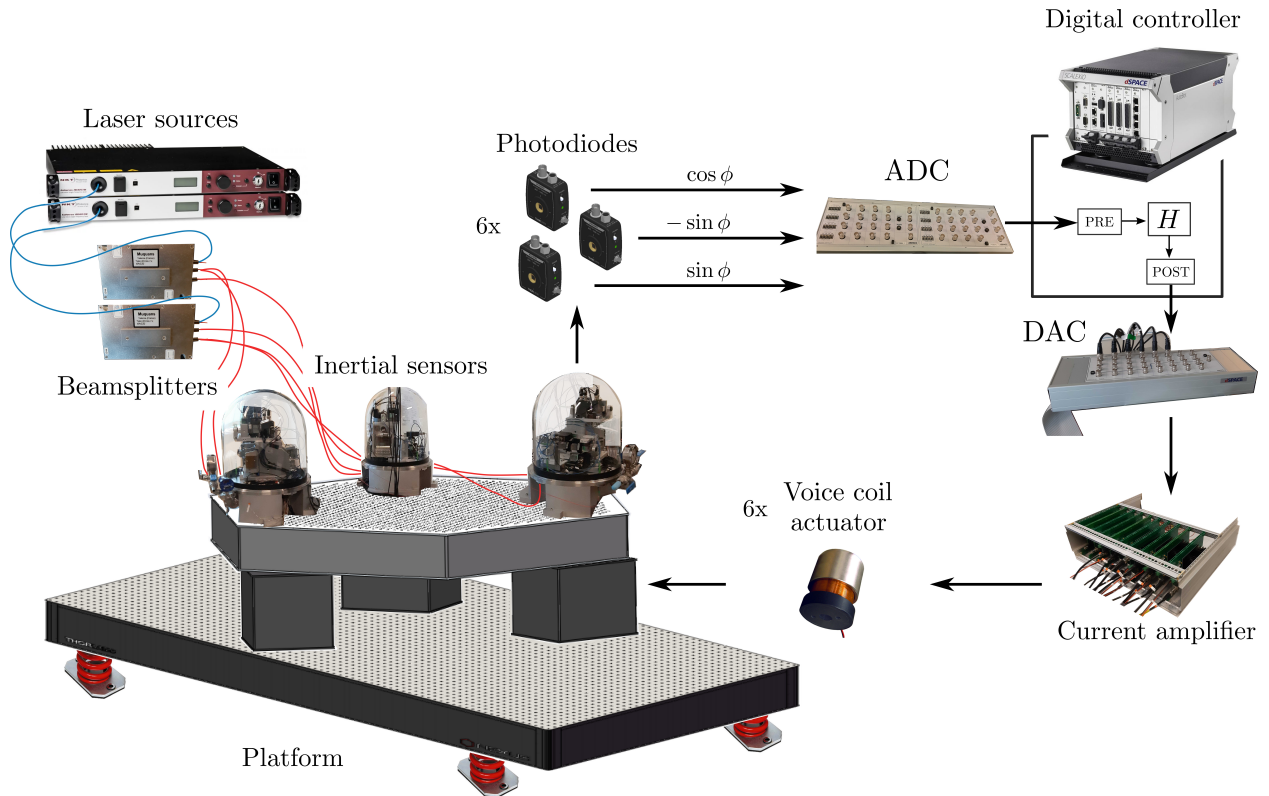


Figure 5.2: Schematic diagram illustrating the interactions between the different parts of the active isolation platform. "PRE" and "POST" correspond to the pre-compensator and post-compensator matrices applied to project the signal of the six sensors into the frame where the controller is applied and to project the corresponding control signal in the frame of the actuators.

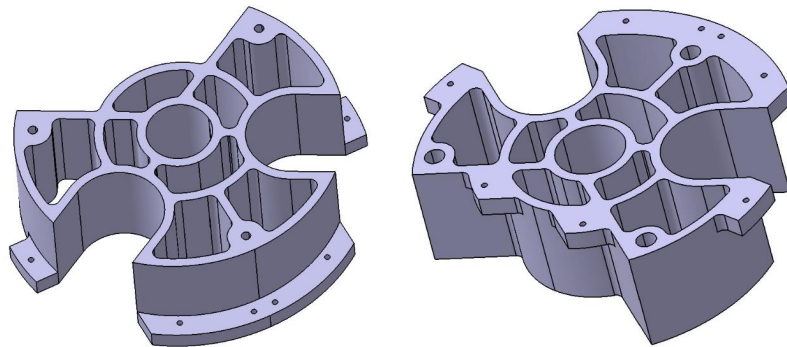


Figure 5.3: CAD of the vacuum chamber supports. The screws' holes of each support is unique to match the holes on the hexagonal breadboard.

characterize the suspension system of the 6 d.o.f. platform, more precisely to measure the resonance frequency of the suspension and flexible modes.

Characterization of the isolators tested independently

To characterize one isolator, it is excited with a white noise (cutoff frequency 200 Hz) and the motion at the top of the isolator is sensed with an accelerometer ICP 353B34 from PCB.

5.1. Description of the platform

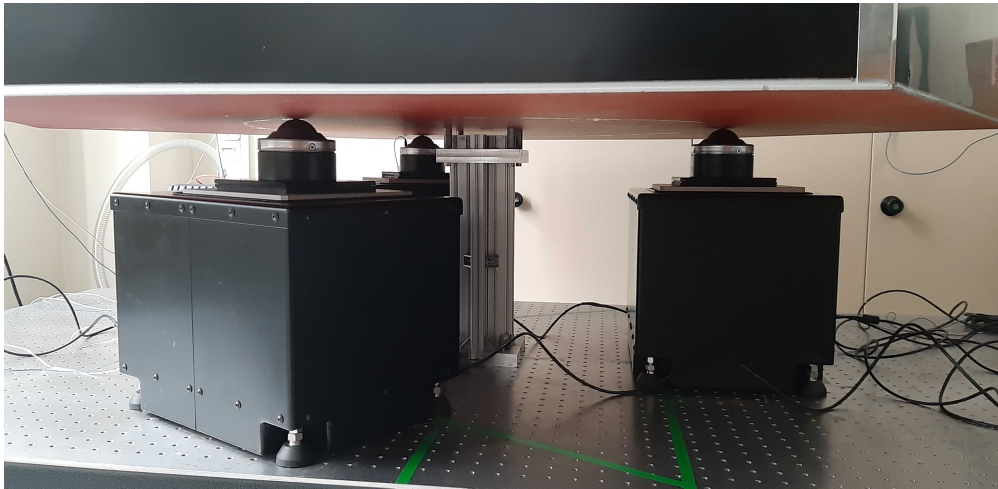


Figure 5.4: Picture of the three isolators. A sphere is used to have the smallest contact point between the isolators and the hexagonal table. A guide is put at the center of mass for safety reasons; there is no contact between the part connected to the hexagonal table and the part fixed to the bottom table except in case of accident.

In order to be in the working range of the isolators, a dummy mass of 60 kg is placed on top. The results for the three isolators in the vertical direction are shown in Fig 5.5.

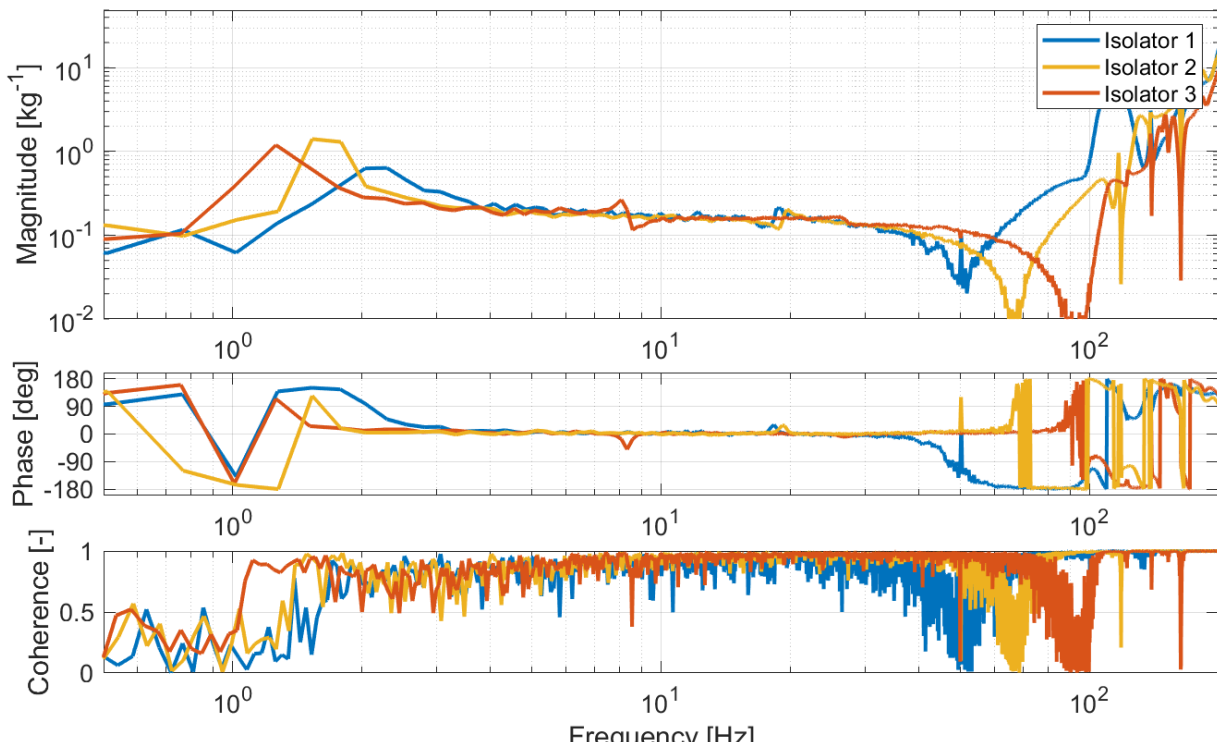


Figure 5.5: Transfer function between the vertical voice coil inside the isolator and an accelerometer placed on top. The suspension modes are around 1 Hz while the first internal modes appears above 100 Hz.

Characterization of the three isolators together

During this experiment, a dummy mass of 70 kg is placed on top of the hexagonal table. The motion of the table is measured by a Guralp CMG-6T, a seismometer that senses the velocity in the three directions. By integrating the signal and multiplying it by the inverse of its sensitivity and its dynamics, the absolute motion of the table can be estimated.

The control plant has been measured to characterize the system. It is obtained by injecting a white noise signal in an actuator and sensing the motion with the Guralp placed above the isolator excited. The plant allows to obtain the properties of the hexagonal table and its three supports.

Experimental results The plants measured between the vertical sensor and the aligned vertical actuator at the location of each isolator are plotted in Fig. 5.6. In this graph, the coherence is also plotted to show the quality of the measurement. The suspension modes of the platform are around 1 Hz while the flexible modes of the system have resonance frequencies above 100 Hz. Because the stiffness of the three isolators was not identical, there are three resonance frequencies corresponding to each suspension mode.

Comparison with a FEM model A reduced model has been developed to study the mode shapes of the system. The finite element model (FEM) represents the assembly described above without the inertial sensors. The rectangular table is meshed with tetrahedral elements with 3.5 cm side. To avoid calculation errors, the hexagonal payload needs a finer mesh; the tetrahedrons for the hexagonal table have a 2 cm side. From the frequency analysis carried out, the first 60 modes of the system are retained to generate a reduced model of the FEM [177, 178]. The parameters of this FEM have been tuned based on the measurements. Assuming that the masses of the parts given in the different datasheets are correct, the stiffnesses of the isolators and of the passive stage are tuned.

In Fig. 5.6, the model, in dotted line style, has a matching steady-state gain and the suspension modes in the same frequency band. In addition, the flexible modes start above 100 Hz and some modes are even matching, see the mode around 100 Hz and around 400 Hz.

Finally, even if not shown here, the off-diagonal terms of the plant measured experimentally match those extracted from the model; the resonances are in the same frequency band and the general shape is similar.

This comparison between FEM and experiments helps to confirm the physical understanding of the isolation stage.

5.1.2 Current amplifier

The homemade current amplifier converts the input voltage into current with a gain of 1/5 A/V. The current monitor output permits to verify the signal fed to the voice coils. From this signal, in volts, the current injected can be deduced as the gain is -5 V/A.

To verify that the electronics of the current amplifier does not induce any phase delay, a white noise is sent to the current amplifier and the signal from the current monitor is measured. The circuit has no effect on the phase as there is no phase delay measured between the signal injected in the current amplifier and the monitor signal. The transfer function obtained has

5.2. Identification of the system

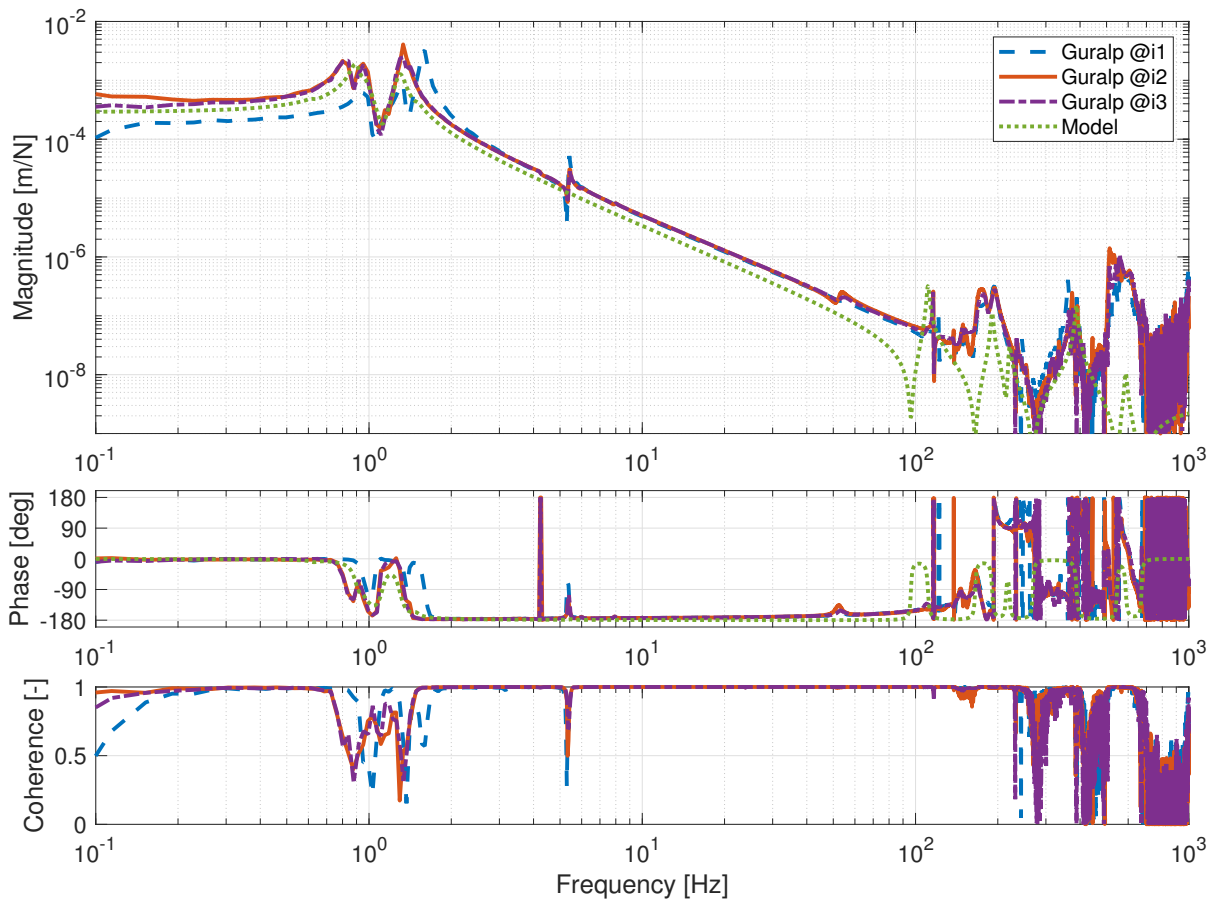


Figure 5.6: *Transfer functions measured between the vertical motion sensed by the Guralp placed above an isolator and the vertical actuator aligned. The "@i1", "@i2" and "@i3" refer to the three different isolators locations. The green dotted curve is obtained from the model for one pair of sensor/actuator.*

a constant amplitude of 5 and a phase of 180° . This experiments permits to prove that the signal from the current monitor is 180° shifted from the input signal. In addition, the measurement shows that above 100 Hz, the capacitors inside the current amplifier start to have an effect on the phase delay, which is out of the control bandwidth.

5.2 Identification of the system

The control plant is measured by injecting a white noise in one actuator and repeating the experiment for the six actuators. The amplitude of the noise is sufficient to have a good coherence between the actuator and each sensor in order to identify the 36 transfer functions representing the multiple input/multiple output (MIMO) system. Below 0.1 Hz, the coherence drops drastically. A series of sine excitation is conducted to recover the information between 10 mHz and 100 mHz. The diagonal elements of the plant are shown in Fig. 5.7, in Fig. 5.8 and in appendix F.

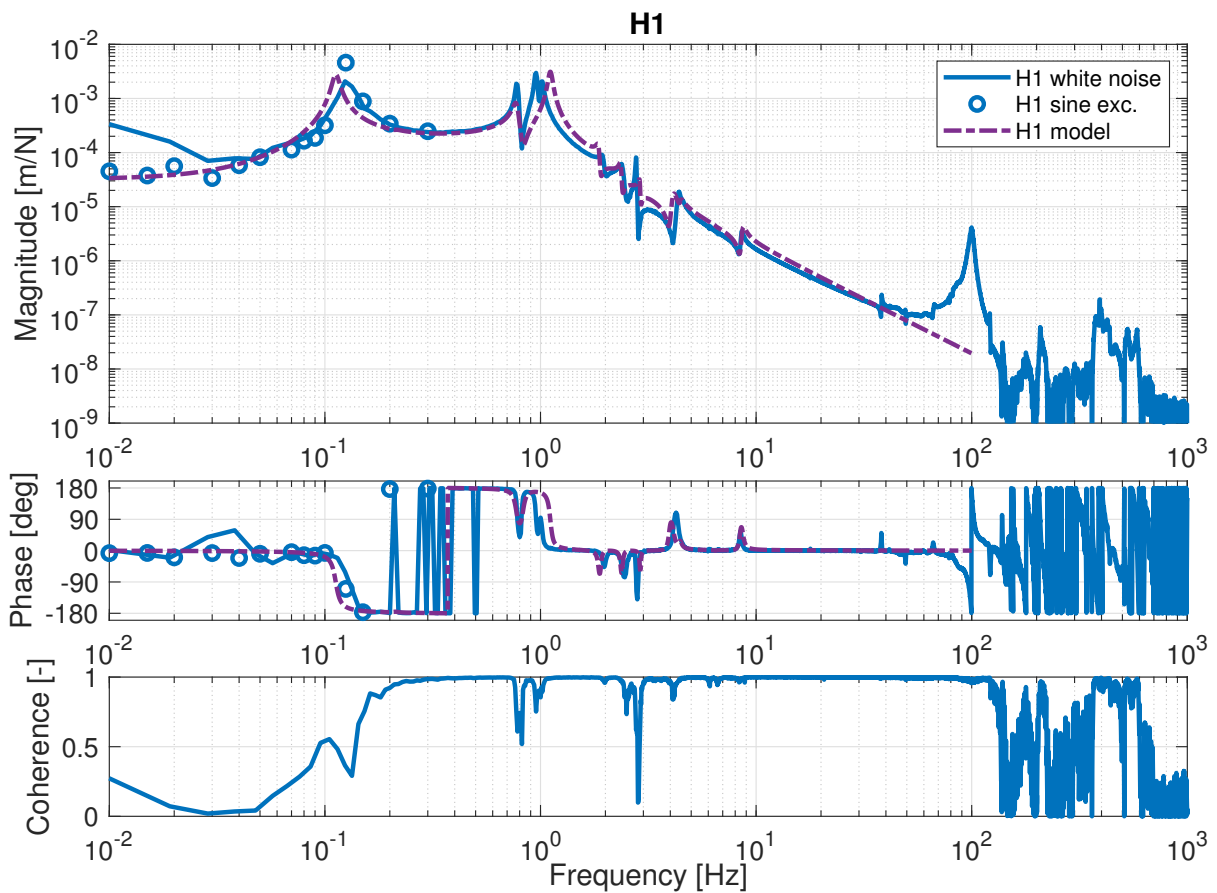


Figure 5.7: Transfer function and coherence between the signal injected in the horizontal actuator *H1* and the aligned *HINS 1*. The identification is performed using a sine excitation (dots) at low frequency (below 0.1 Hz) and a white noise at higher frequencies (solid line). The same transfer functions extracted from the *simscape* model is shown (dash-dotted purple).

To ease the description of the plant, the location of the pairs of sensor/actuator is numbered anti-clockwise, assuming that the origin of the axis is in the middle of the hexagonal table and that the axis are oriented as shown in Fig. 5.9:

- location 1 is on the positive x-axis side.
- location 2 is on the negative x-axis side and on the positive y-axis side.
- location 3 is on the negative x-axis side and on the negative y-axis side.

At low frequency, the transfer function between the *HINS* and the horizontal actuators, see Fig. 5.7 and Appendix F, shows the behavior predicted: a static gain and the resonance frequency corresponding to the spring-mass system of the inertial sensor. Based on the sensor dynamics, this implies that there is a pair of real zeros below the resonance frequency. Similarly, for the vertical transfer functions in Fig. 5.8 and in Appendix F, the pair of complex conjugate zeros due to the effect of gravity are visible at a frequency below the resonance frequency of the inertial sensor.

Between 0.8 Hz and 1 Hz, the resonance frequencies corresponding to the horizontal suspension

5.2. Identification of the system

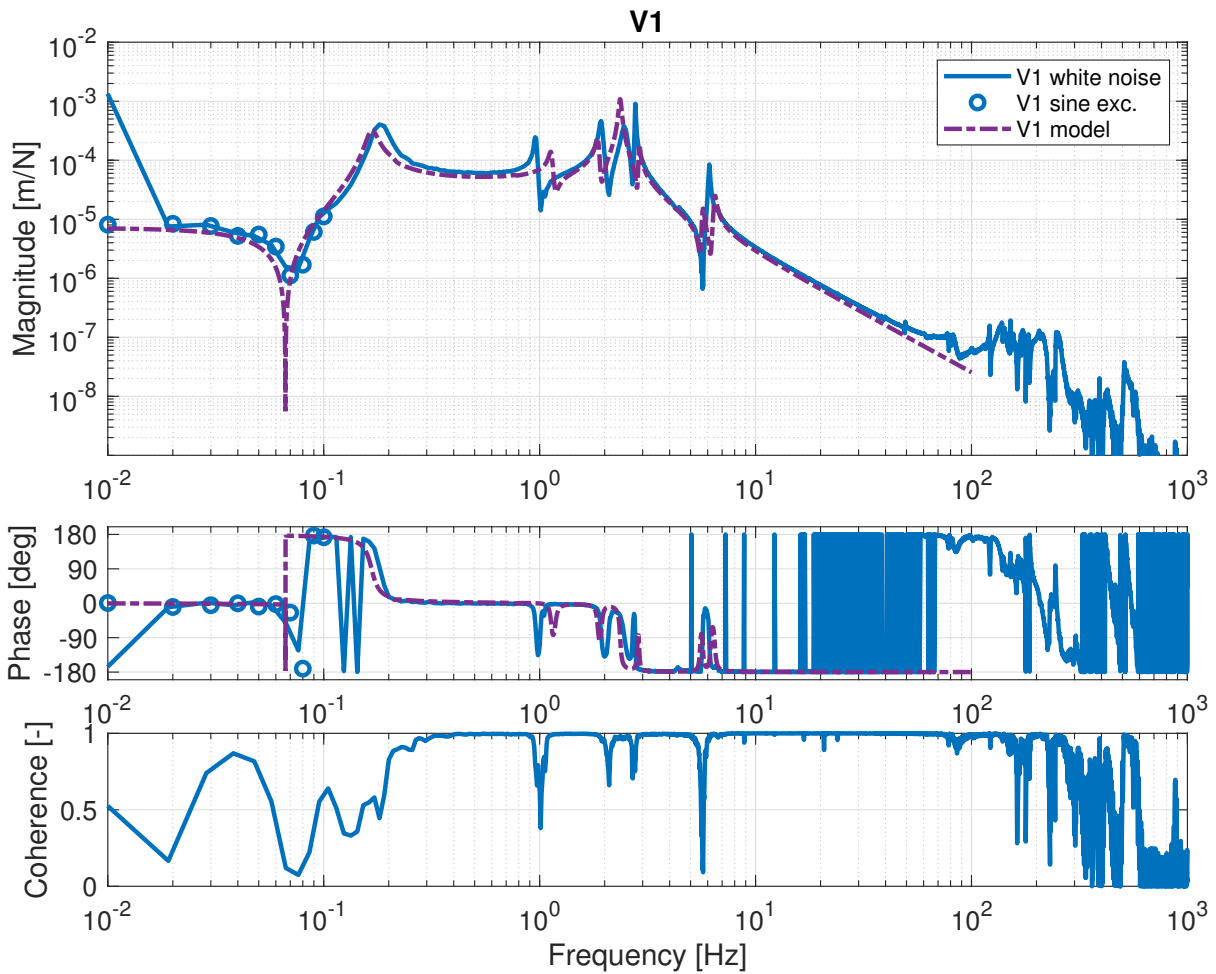


Figure 5.8: Transfer function and coherence between the signal injected in the vertical actuator V1 and the aligned VINS 1. The identification is performed using a sine excitation (dots) at low frequency (below 0.1 Hz) and a white noise at higher frequencies (solid line). The same transfer functions extracted from the Simscape model also shown (dash-dotted purple).

modes of the three isolators appear. They are not perfectly identical because the isolators are not placed perfectly. Unfortunately, due to a failure of one isolator, it is not possible to correct the position. The resonance frequencies of the vertical suspension modes of the isolators are around 2 Hz. Finally, the resonances around 5 Hz correspond to the suspensions modes of the passive stage below the isolators.

Understanding the physical meaning of the poles was facilitated by the Simscape model of the complete isolation platform, see Fig. 5.9. The identification of the poles was studied by adjusting the parameters of the model until a good match was obtained, see Fig. 5.7 and Fig. 5.8. The Simscape model permits to quantify the asymmetry of the isolators location, the direction of application of their force and the misorientation and inclination of the inertial sensors.

Moreover, the control laws applied in the next section will be tested on the model to predict their performance.

As stated in chapter 4, the horizontal inertial sensor is sensitive to vertical excitation,

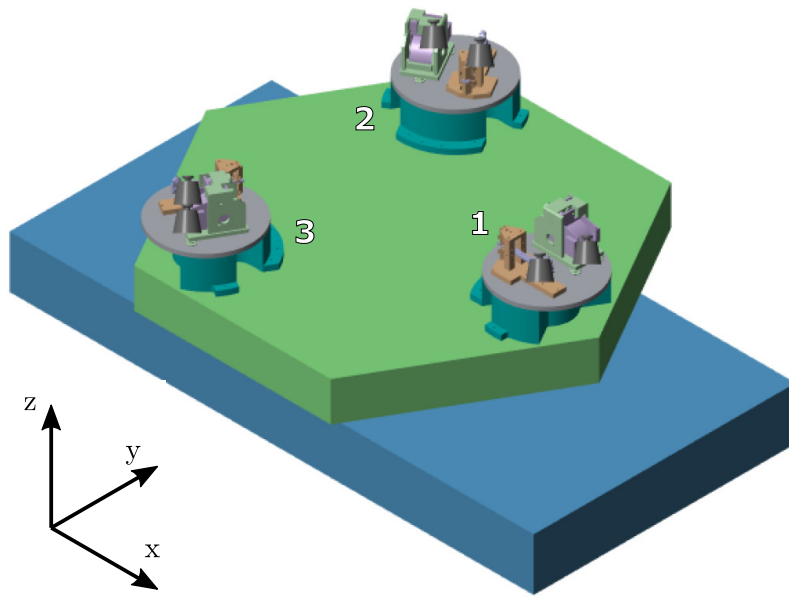


Figure 5.9: Visualization of the simscape model made of the rectangular and hexagonal tables. The vacuum chamber supports, the platform of the vacuum chamber and the three vertical and horizontal inertial sensors are included.

see Fig. 4.14. The same response is observed here, as shown in Fig. 5.10. The static gain of the transfer function between the HINS and the vertical actuator is larger than the transfer function when considering a horizontal excitation. This is thus a consequence of the tilt-horizontal coupling of inertial sensors. It confirms that the observations made in chapter 4 can be transposed to the 6 d.o.f. system and that the solutions studied to cope with the coupling can be tested on the platform.

5.3. Isolation

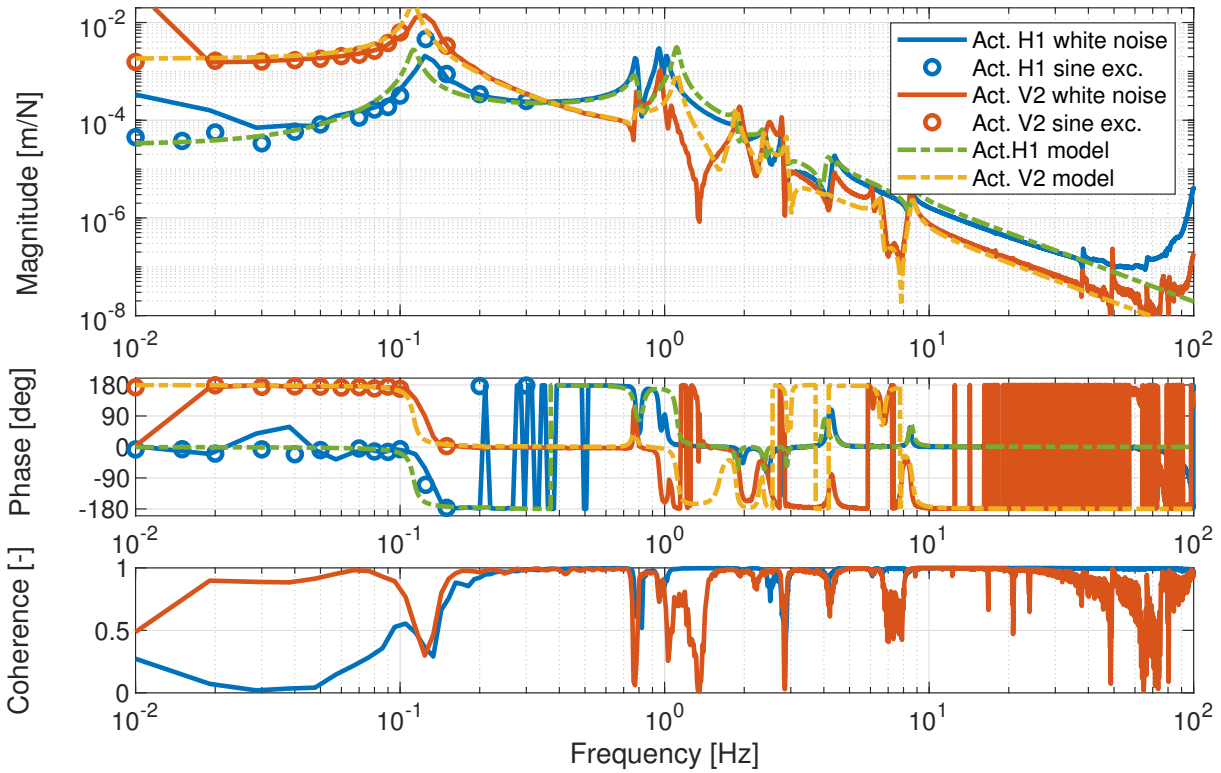


Figure 5.10: *Transfer function and coherence between the signal injected in the horizontal actuator H1 and the aligned HINS (blue) and between the vertical actuator V2 and the same HINS (orange). The identification is performed using a sine excitation (dots) at low frequency (below 0.1 Hz) and a white noise at higher frequencies (solid line). The model is also shown (dash-dotted green and yellow).*

5.3 Isolation

To study the performance of inertial control on the 6 d.o.f. isolation stage, decentralized control is applied. First, the three vertical loops are closed simultaneously. In fact, closing one vertical loop at a time has an impact on the inclination of the table and hence, on the signal measured by the HINS. In addition, isolation in the vertical direction has also a positive impact on the relative inclination of the platform and hence, it is a good practice to close first the vertical loops.

The performance of the three vertical loops and the three horizontal loops are studied separately. The final performance obtained when closing all loops are then compared with the predictions made on the model.

Note that a high-pass filter is added to every control loop to reject any DC gain in the interferometer signal (cutoff frequency at 0.01 Hz). In addition, a low-pass filter with a cutoff frequency at 50 Hz is applied to avoid magnification of the flexible modes.

5.3.1 Vertical decentralized control

The following controller, made of a gain, one lead and one lag, is applied on the plant to guarantee stability margins:

$$H(s) = 8 \cdot 10^5 \frac{0.05 \cdot 40}{0.5^2} \frac{(s + 2\pi \cdot 0.5)^2}{(s + 2\pi \cdot 40)(s + 2\pi \cdot 0.05)}. \quad (5.1)$$

The transfer function between VINS2 and actuator V2 is shown in Fig 5.11 with and without feedback. Between 0.1 Hz and 10 Hz, the amplitude of the platform is reduced by almost one order of magnitude.

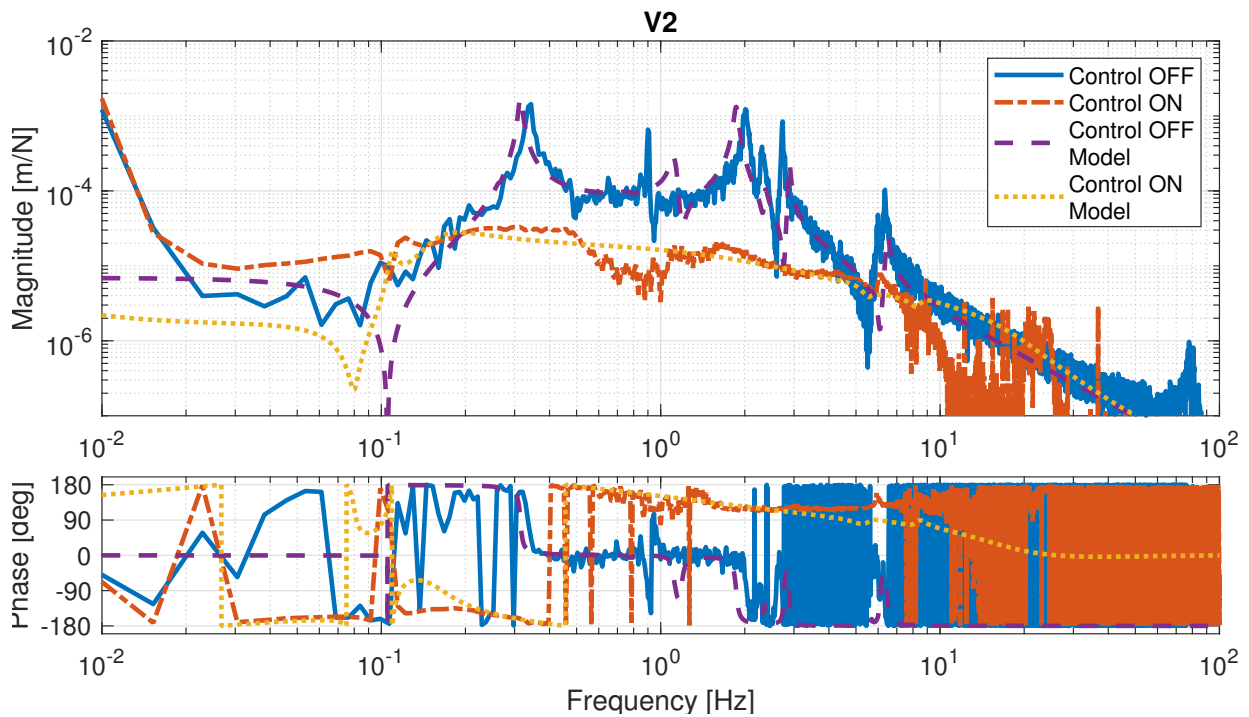


Figure 5.11: *Experimental transfer function between VINS 2 and vertical actuator 2 without control (solid blue) and with control (dash-dotted red) and the same transfer function extracted from the Simscape model without control (dashed purple) and with control (dotted yellow).*

5.3.2 Horizontal decentralized control

To isolate the payload in the horizontal directions, a controller made of two lags and one lead is applied to the platform isolated in the vertical direction

$$H(s) = 5 \cdot 10^5 \frac{0.01 \cdot 20}{0.5 \cdot 0.3} \frac{(s + 2\pi \cdot 0.3)(s + 2\pi \cdot 0.5)}{(s + 2\pi \cdot 20)(s + 2\pi \cdot 0.01)}. \quad (5.2)$$

The transfer function between HINS1 and actuator H1 is shown in Fig. 5.12 with and without control. The amplitude is not reduced much but the controller gain cannot be increased. Indeed, the static gain is too large and hence, if the gain is further increased, the pair of real zeroes around 0.03 Hz is amplified.

5.3. Isolation

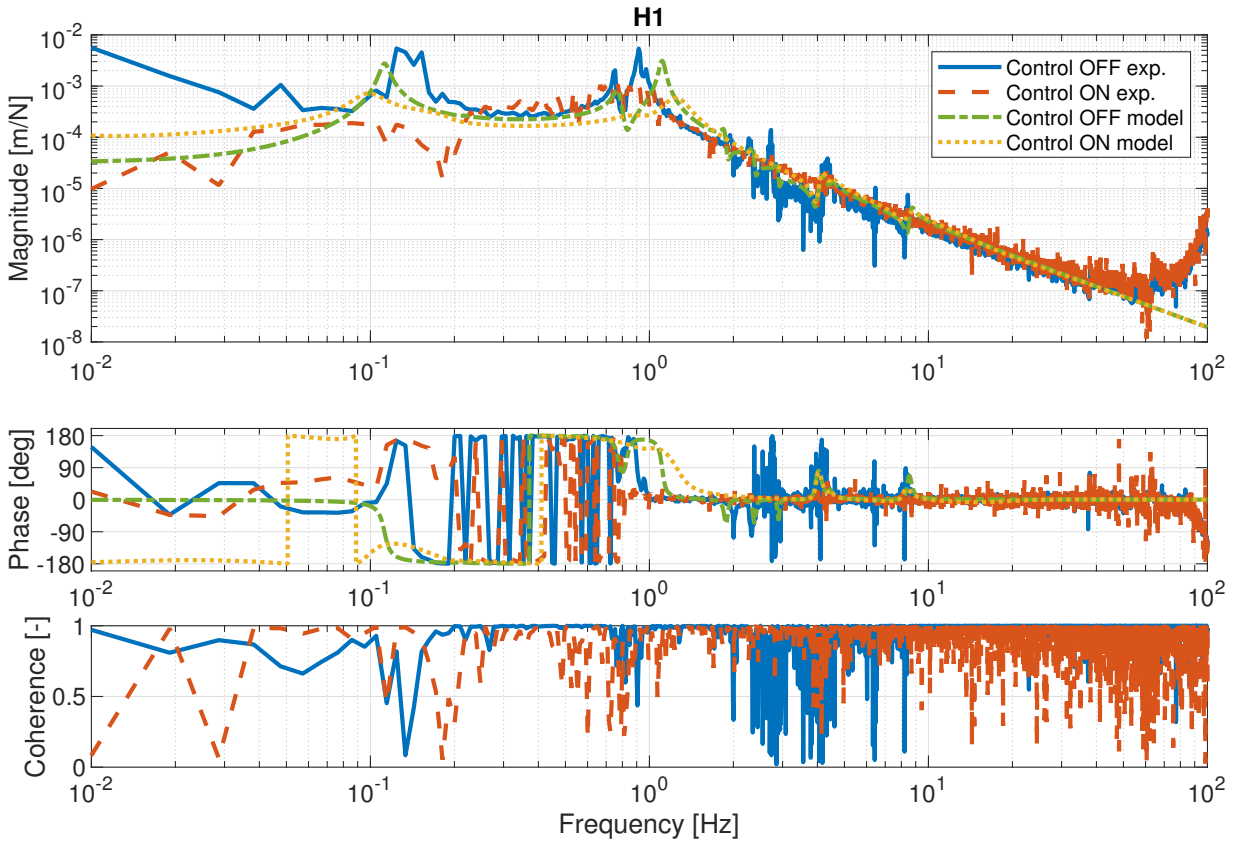


Figure 5.12: *Experimental transfer function between HINS 1 and horizontal actuator 1 without control (solid blue) and with control (dashed red) and the same transfer function extracted from the Simscape model without control (dash-dotted green) and with control (dotted yellow).*

To increase the controller gain, one idea is to reduce the static gain of the transfer function between HINS and horizontal actuator. By tilting the pendulum of the HINS on the model studied in section 3.1.2, the static gain is reduced. In counterparts, this increases the resonance frequency of the inertial sensor and hence, reduces the control bandwidth.

The HINS have been inclined and the effect of this new inclination on the transfer function between HINS3 and the actuator H3 is shown in Fig. 5.13. The static gain is effectively reduced by increasing the inclination of the pendulum.

The following controller is applied on the new system for the three pairs of horizontal sensor/actuator

$$H(s) = 4 \cdot 10^4 \frac{0.05 \cdot 10}{0.2} \frac{(s + 2\pi \cdot 0.2)(s + 2\pi)}{(s + 2\pi \cdot 10)(s + 2\pi \cdot 0.05)}. \quad (5.3)$$

The performance of the horizontal inertial control is shown in Fig. 5.14. By reducing the static gain, the inertial control has indeed better performance.

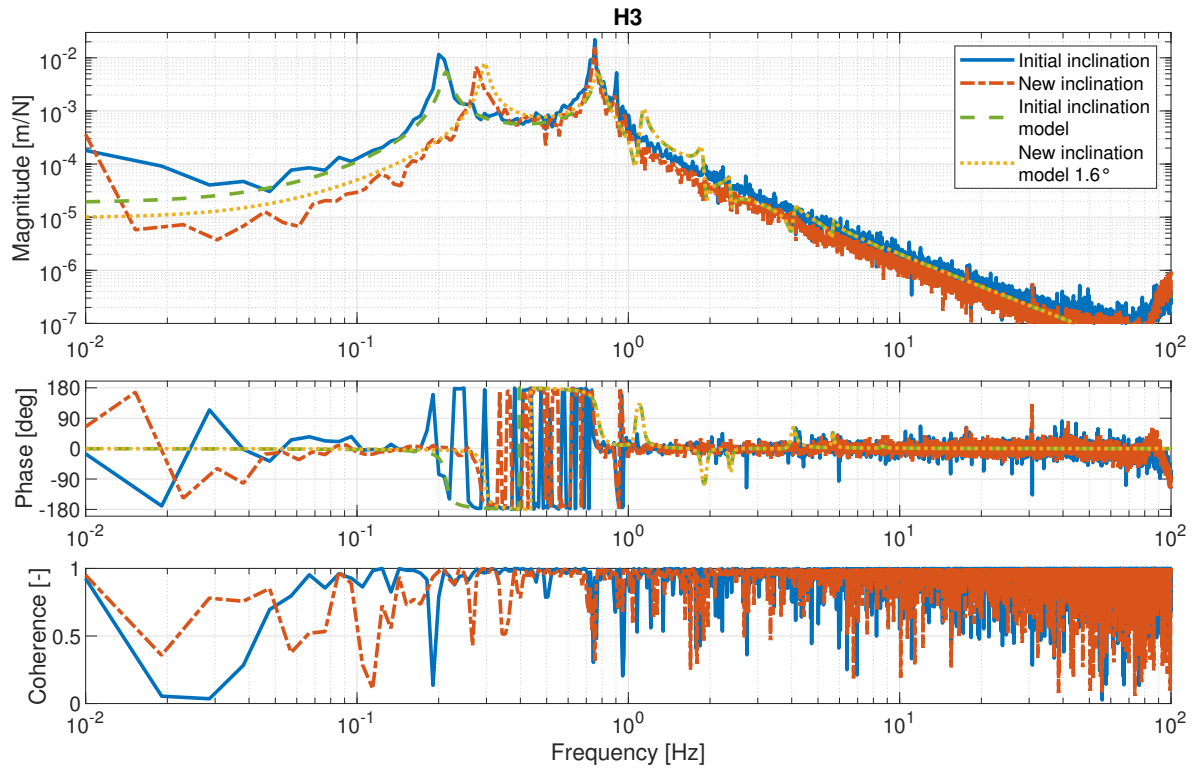


Figure 5.13: Experimental transfer function between HINS 3 and the horizontal actuator 3 with the initial inclination of the pendulum (solid blue) and with the inclination increased (solid red) and the same transfer function extracted from the simscape model with initial inclination (dashed green) and with the new inclination (dotted yellow).

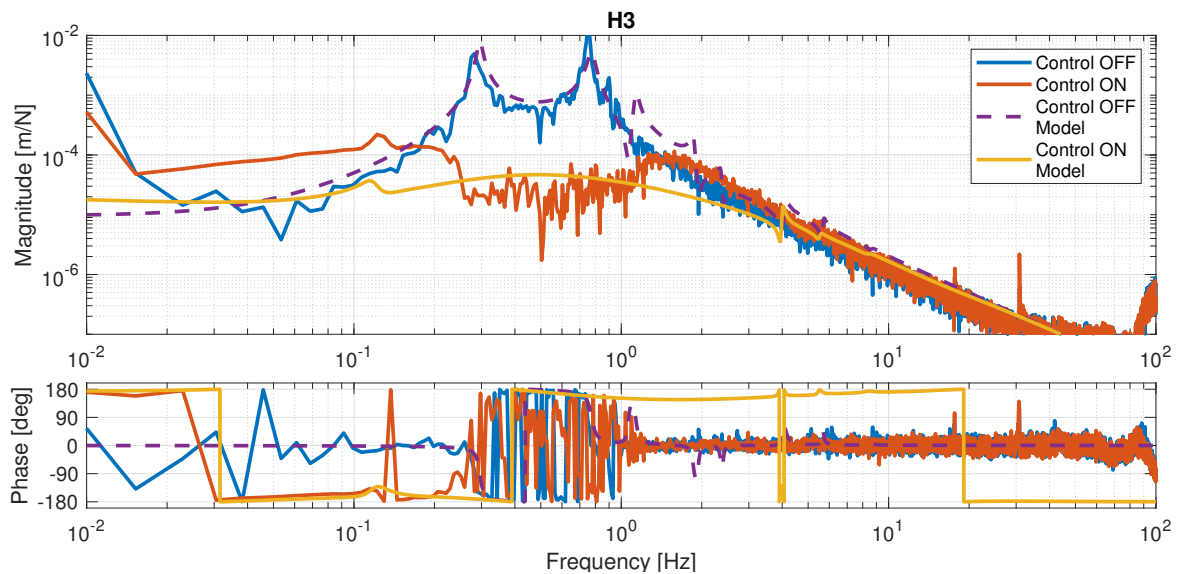


Figure 5.14: Experimental transfer function between HINS 3 and horizontal actuator 3 without control (solid blue) and with control (dash-dotted red) and the same transfer function extracted from the simscape model without control (dash-dotted purple) and with control (dotted yellow).

5.3. Isolation

5.3.3 Performance

To evaluate the reduction of transmitted ground motion obtained thanks to inertial control, the transmissibilities are measured by placing one Guralp CMG-6T on the ground and one at the center of the hexagonal payload. The resulting transmissibilities are shown in Fig. 5.15 for the vertical direction and in Fig. 5.16 for the horizontal direction when closing all loops. The transmissibilities are shown only between 0.1 Hz and 10 Hz, i.e. in the sensitivity bandwidth of the Guralp.

As expected, the control bandwidth in the vertical direction is larger than in the horizontal direction. The peak around 4 Hz is not isolated as it corresponds to one suspension mode of the rectangular table with the four springs (passive stage) supporting the whole system.

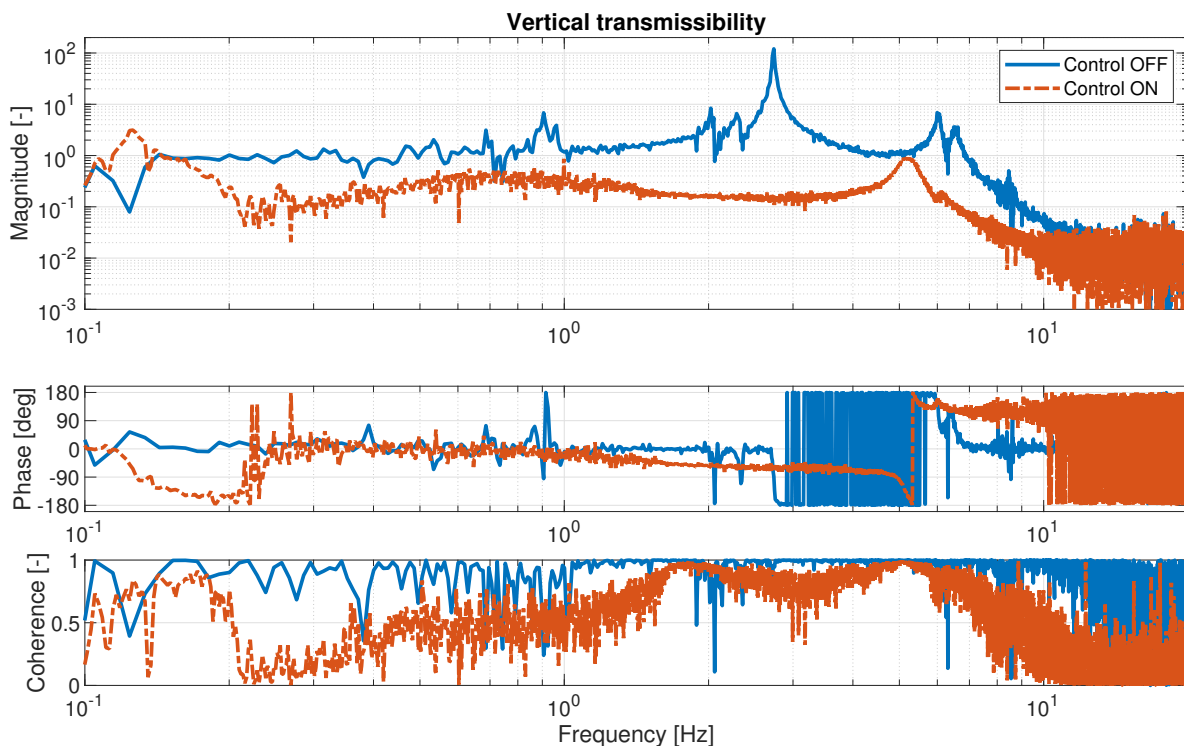


Figure 5.15: *Transmissibility in the vertical direction without control (solid blue) and with control (dash-dotted red).*

Moreover, to quantify the reduction of the amplitude of the platform's motion by comparison to the amplitude of the ground motion, the amplitude spectral density (ASD) is shown in Fig. 5.17 for the vertical direction and in Fig. 5.18 for the horizontal direction. In the horizontal direction, the passive system isolates the platform from ground motion above 2 Hz. In the vertical direction, the passive system isolates above 7 Hz and the active system isolates at low frequency. The residual ASD of the platform has a lower amplitude in the vertical direction than the ground motion. However, this is not the case in the horizontal direction below 300 mHz.

For indication, the performance of the HAM-ISI developed at LIGO is also shown [179]. In the horizontal direction, the ground motion at LIGO is already smaller than the motion of

the platform developed when the control is on. In the vertical direction, the residual motion of the stage developed here is smaller and hence, the stage can reduce the motion of the HAM-ISI. However, the reduction is far from that obtained using the HAM-ISI.

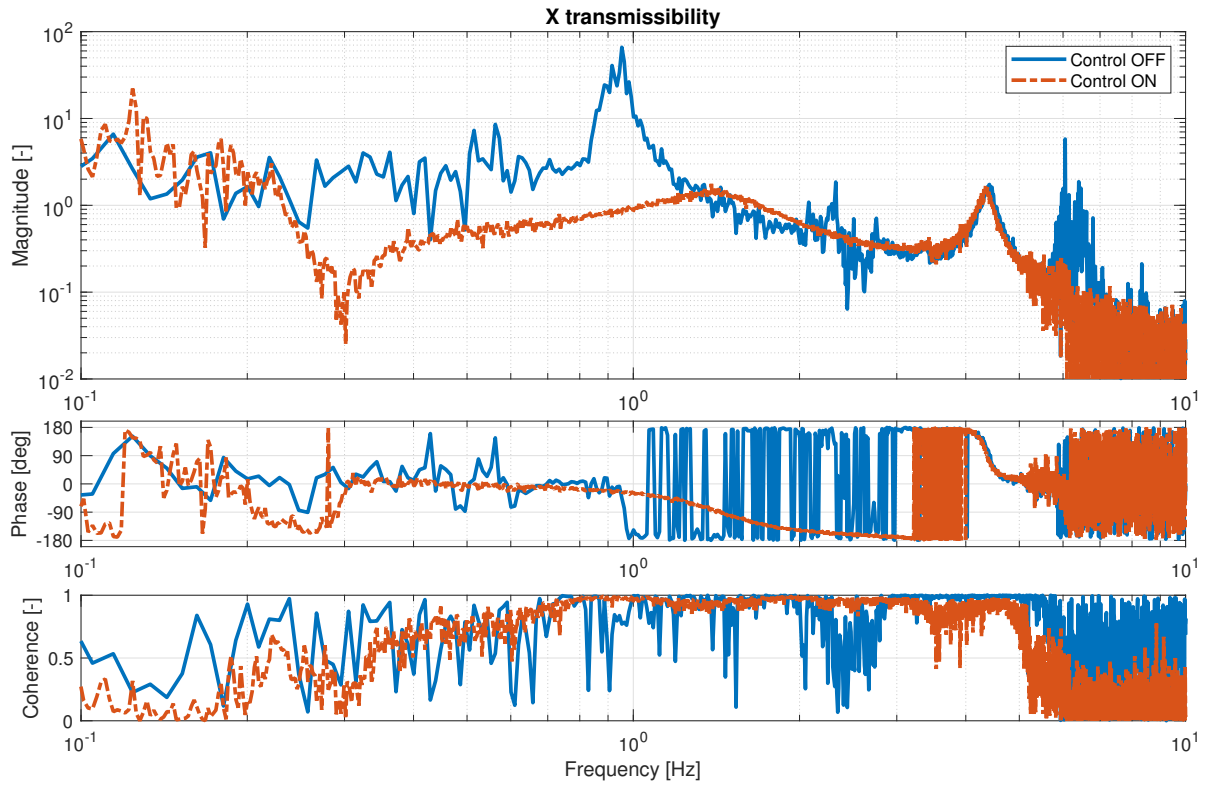


Figure 5.16: *Transmissibility in the horizontal direction without control (solid blue) and with control (dash-dotted red).*

5.3. Isolation

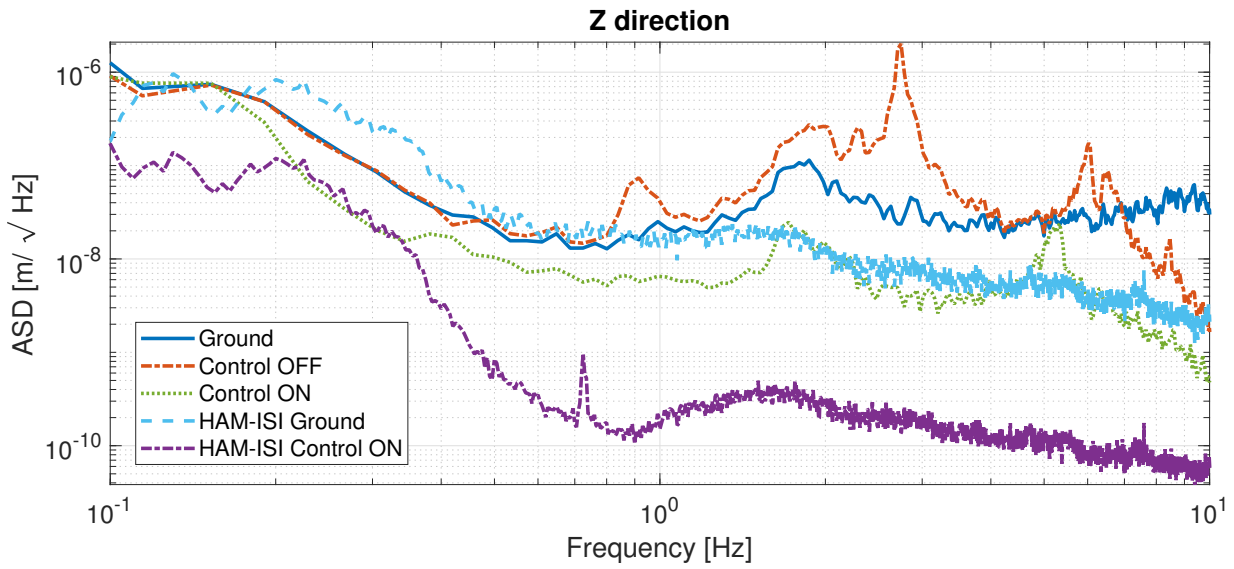


Figure 5.17: ASD measured by the Guralp in the vertical direction of the ground motion (solid blue), of the platform without control (dash-dotted red) and with control (dotted green). For indication, the performance of the HAM-ISI from LIGO is also presented: the ground motion measured on site (dashed light blue) and the residual motion of the platform when the controller is on (dash-dotted purple).

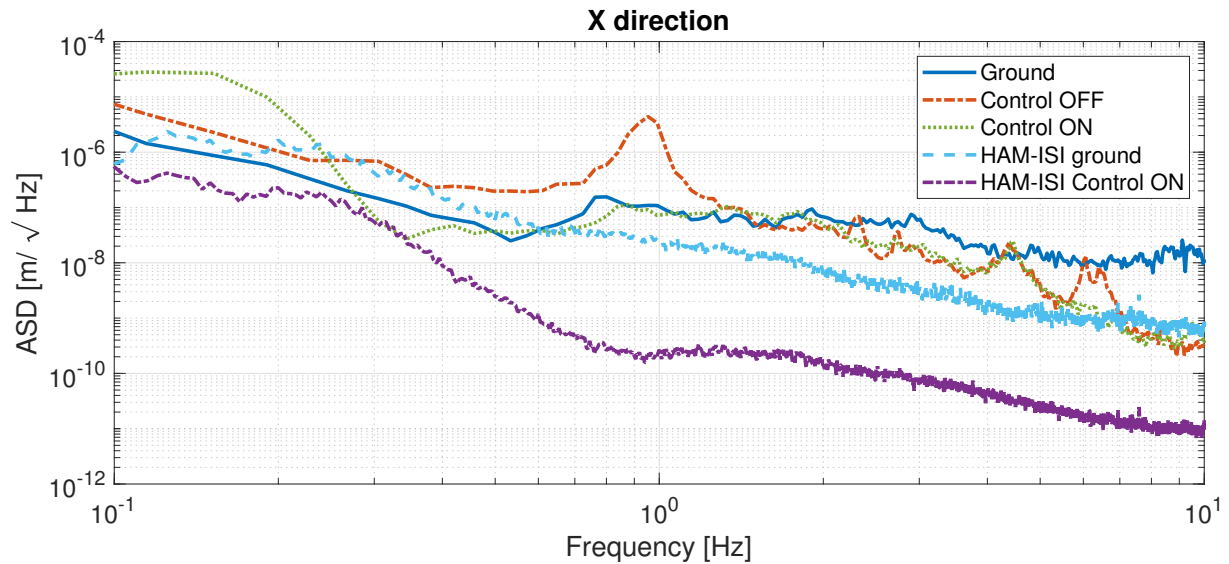


Figure 5.18: ASD measured by the Guralp in the horizontal direction of the ground motion (solid blue), of the platform without control (dash-dotted red) and with control (dotted green). For indication, the performance of the HAM-ISI from LIGO is also presented: the ground motion measured on site (dashed light blue) and the residual motion of the platform when the controller is on (dash-dotted purple).

5.3.4 Liquid sensor on the platform

As shown in chapter 3, the resolution of the liquid sensor developed is not sufficient, mainly because the Mercury is too sensitive to ground motion. For comparison, the liquid sensor is placed on the 6 d.o.f. platform, see Fig. 5.19, to see if this affects the resolution.

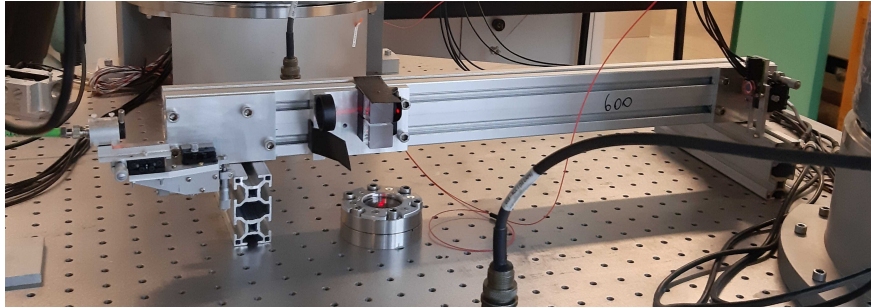


Figure 5.19: *Picture of liquid sensor placed on the isolation table. Some additional counterweights were added to maintain the horizontal inclination of the table.*

Above the frequency of the suspension modes, i.e. above 1 Hz, we expect to see a reduction of the amplitude of the motion. For comparison, the resolution of the liquid sensor on the rigid optical table, shown in Fig. 3.19, and on the ground are also shown in Fig. 5.20. The amplitude of the signal when placed on the optical table is much larger than on the ground as the table is supported by legs without any isolation system. As expected, when placed on the hexagonal table, the amplitude of the signal is reduced above 1 Hz. The resolution of the liquid sensor is improved and reaches the photodiode noise at high frequency. However, the resolution is not sufficient to reach the requirement presented in Fig. 3.20 even at high frequency.

Placing the liquid sensor on the passive stage did not improve the low-frequency resolution as required here. The need to find a better liquid with good reflective properties as stated in section 3.4.2, is confirmed here.

Note that the resonance of the liquid at 3.6 Hz is visible on the curves.

5.4. Summary

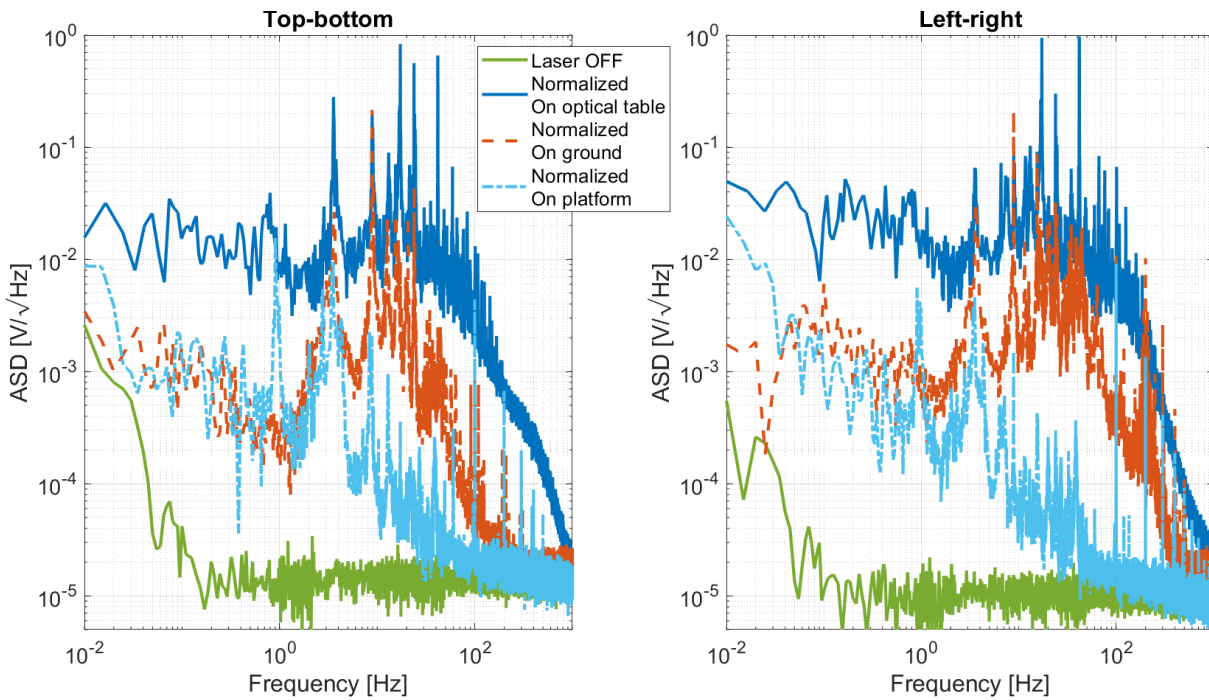


Figure 5.20: ASD of the normalized signals measured by the liquid sensor (top-bottom signal on the left and left-right signal on the right) when the Mercury is placed on an optical table (solid blue), on the ground (dashed red) and on the hexagonal platform - passive stage (dash-dotted light blue). For comparison the photodiode noise is also shown (solid green); it is measured by turning off the laser.

5.4 Summary

In this chapter, the parts of the active isolation platform have been characterized independently before characterizing the complete system. The system identification permits to validate the simscape model developed.

The performance obtained with decentralized control are promising as the payload is isolated above the frequency of the zeroes of the sensor dynamics, 0.07 Hz in the vertical direction and 0.02 Hz in the horizontal direction; regarding vertical control, the motion has been reduced by one order of magnitude between 0.1 Hz and 10 Hz. In the horizontal direction, inclining the pendulum permits to increase the controller gain and to reduce by one order of magnitude the horizontal motion between 0.1 Hz and 1 Hz.

Finally, when placing the liquid sensor on the stage, the noise of the sensor is reduced but the resolution is still not sufficient.

Conclusions and Perspectives

Conclusions

In this thesis, the importance of isolating sensitive equipment at low frequency from external disturbances in several directions has been investigated. To mitigate the effect of external disturbances such as ground motion, inertial control is required. However current isolation tables are limited at low frequency due to sensor resolution.

To overcome this limitation, two inertial sensors with an interferometric readout are developed, one measuring the vertical motion, the vertical inertial sensor (VINS), and one measuring the horizontal motion, the horizontal inertial sensor (HINS). The interferometric readout improved the resolution. The current resolution of the two inertial sensors has been studied thanks to a numerical model using Jones Matrix representation and is 10^{-12} m/ $\sqrt{\text{Hz}}$ at 1 Hz. In addition, the working principle of the inertial sensors has been studied based on the equations of motion and a simscape model. It has been demonstrated that both models reproduce the experimental results. Therefore, simscape is a convenient tool to represent sensor dynamics in a gravitational field.

The identification of the sensor dynamics has highlighted the effect of tilt-translation coupling; Sensor signal is dominated by tilt at low frequency. Moreover, the pair of complex zeros move from 0 Hz to a higher frequency and can become a pair of real zeros, depending on the sensor's mechanics and the architecture of the platform.

Although projecting the system in a decoupled frame has no effect on the sensor dynamics, it has been demonstrated that controlling the rotation or subtracting the tilt from the sensor signal can move the zeros of the dynamics to low frequency, increasing the inertial control bandwidth at low frequency.

Both decoupling methods can work using tiltmeters that have a sensitivity to translation lower than 10^{-3} rad/m. In addition, it has been demonstrated that the control performance are met when subtracting the tilt from the inertial sensor signal.

In order to mitigate the effect of rotation on the sensor signal, a tiltmeter is needed. Tiltmeter are not only sensitive to rotation but also to translation. The effect of this sensitivity on the performance of the tilt-subtraction methods has been studied. The maximum sensitivity of the tiltmeter to translation has been quantified and some tiltmeters developed in the literature are already below this limit.

A liquid sensor has been developed and characterized in this thesis as liquid sensor with a resolution that meets the LIGO tiltmeter's requirements has been found in the literature [175]. The liquid Mercury used as the reflecting surface has too many ripples and hence, a new

Perspectives and further works

liquid more viscous and with good reflective properties has to be identified to have a working sensor. It is expected that the liquid sensor is sensitive to horizontal acceleration of the ground and hence, this sensitivity can be studied on the calibration stage developed in this thesis.

A complete 6 degree-of-freedom (d.o.f.) active isolation platform using interferometric inertial sensors has been developed.

The Simscape model of the complete assembly reproduces properly the experimental results. Simscape has proven to be a very promising tool to study a complex system and predict the performance of any controller applied on the system.

The system identification confirmed the effect of inertial sensor dynamics on the control plant. In addition, it confirms that the solutions proposed to reduce the sensitivity to tilt of inertial sensors should be applied.

This thesis presents the first active isolation system that uses inertial sensors with an interferometric readout. The resulting control performance of a decentralized inertial controller are promising. Both vertical and horizontal motion could be reduced of one order of magnitude in the sub-Hz domain.

Finally, some of the results presented here are the result of a collaboration between a lot of people involved with me and a next generation of people that will continue the work initiated here. Some will focus on the sensors resolution and some on the control aspect. Therefore, here are some ideas that might hopefully help them in the future.

Perspectives and future work

Through the experiments and the simulations, I could face some issues or used some tools that can be improved. My thoughts regarding the modifications of different aspects of the isolation stage are summarized hereafter.

Inertial sensors

The homodyne interferometric readout of the inertial sensors has been complexified from a $\frac{\lambda}{8}$ setup because this waveplate is not available on the market. One possible application of the inertial sensors is to control the isolators of the future Einstein Telescope. For this instrument, several dozens of sensors are needed. Hence, for a large amount of waveplates, I think that it is possible to negotiate with a manufacturer to produce the desired amount of $\frac{\lambda}{8}$ waveplates and simplify the readout, see Fig. 2.4. An additional photodiode can be added prior to the beamsplitter for power monitoring.

Regarding the interferometric readout, the holder maintaining and aligning the collimator can be improved. In fact, right now, the collimator is attached with six adjustable screws to its support for an alignment in 2 rotational d.o.f., see Fig. 5.21. While adjusting the screws, the operator noticed several times that not the six screws are fixing the collimator due to a bad positioning. Note that only 2 d.o.f. need to be adjusted hence another solution, inspired from commercial products can be preferred: the collimator is rigidly attached to a

first support. This support is connected to the platform holding the whole interferometer by two adjustable screws. Such systems can be small and suited for compact interferometers.



Figure 5.21: Actual collimator holder (left), when holding the collimator (center) and commercial kinematic mount that can be more suited to hold and adjust the inclination of the collimator (right)¹.

When measuring the resolution of the interferometer in chapter 2, we could see some peaks around 10 Hz, due to the modes of the optical mounts. The prism holder currently used is the PAD-20 from OptoSigma. The beamsplitter is clamped to the mount by tightening a screw. To damp some of the resonances, thin rubber pads could be placed between the holder and the beamsplitter and at the end of the screw.

Finally, the design of the HINS was not optimized for two reasons. First, the interferometric readout is connected vertically to the base of the pendulum and hinder the motion of the pendulum, see Fig. 5.22. Therefore, the range of the pendulum is reduced almost by half and it is hard to align the pendulum at its middle position. Second, the foot of the HINS is large and it is difficult to place the HINS and VINS inside the vacuum chamber without blocking some feedthrough. Reducing the size of the sensors can definitely ease their positioning.

Gravity decoupling In this thesis, it has been shown that the sensitivity of inertial sensors to tilt can be improved by mechanically decoupling the inertial sensor or by subtracting/-canceling the tilt. In order to compare these solutions, they can be tested on the pendulum presented in section 3.1.1. Indeed, the inertial sensor and the tiltmeter can be easily connected to the extended structure. The inertial sensor should then be suspended from the payload, similarly to Ref. [169]. The effect of these two solutions on the control plant can then be identified and one can try to control the 1 d.o.f. platform.

Vacuum chamber

The electric connector on the vacuum side can not be sealed to the electric feedthrough of the vacuum chamber. Due to the limited space inside the chamber, the feedthrough is below the VINS and hence, it can be slightly disconnected when adjusting the sensor. A sealed connector should be preferred, which is already the case on the air side of the connector.

¹https://www.thorlabs.de/newgrouppage9.cfm?objectgroup_id=1492

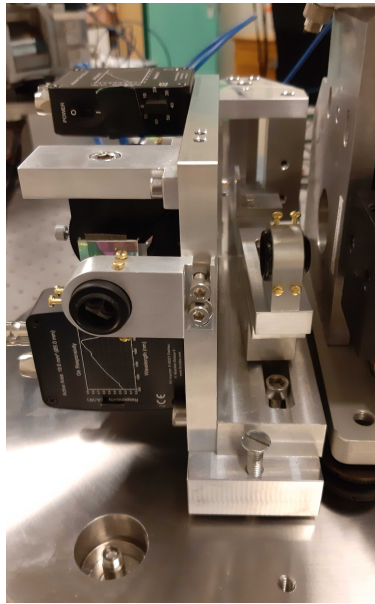


Figure 5.22: *Front view of the HINS. The interferometric readout on the left blocks the pendulum and reduces its working range.*

Isolators

Regarding voice coil actuators, a good practice is to attach the magnet to the sensitive equipment and the coil to the ground. In this configuration, the heat induced by the current in the coil is transferred to the ground [180]. In the future, if isolation stages are used in series to isolate a sensitive payload, the heat transfer has to be carefully addressed especially if the stages are working at cryogenic temperatures.

Data acquisition system

Currently, there are 32 analog to digital conversion (ADC) channels available on the dSpace Scalexio data acquisition system (DAQ). For future experiments, this amount of measurement channels will not be enough. The current and future number of channels needed to measure all the useful information is listed in table 5.1. For performance indication, sensors measuring ground motion and out of loop sensors (monitors) are needed. Other control laws can also be considered. The relative sensors can be used for high frequency control by applying sensors fusion filters. Additional sensors can be used to damp the suspension modes for a HAC/LAC configuration. In addition, the isolation stage is going to be used in future experiments to stabilize a gravimeter.

Depending on the application and the type of controller implemented, the number of channels needed varies from 30 to more than 40 which exceeds the number of channels available on the Scalexio. Several solutions can be investigated to overcome this. First, another ADC card can be added to the Scalexio. Second, two MicroLabBox from dSpace can be synchronized (each includes 24 channels); one DAQ will measure the controlled channels and the second one, the channels for performance. Finally, other DAQ system such as SpeedGoat can be considered.

Table 5.1: *Number of channels needed for each type of sensor currently used or used for future applications.*

Quantity	Sensor	Currently used
18	Inertial sensors	YES
6	Current monitor output	YES
3	Liquid sensor	NO
3	Ground motion	NO
3	Performance monitor	NO
6	Relative displacement sensors	NO
6	Sensors for damping	NO
TBD	Gravimeter	NO

Modelisation

All Simscape models in this thesis represent properly the suspension modes of the platform and its behavior under gravity. The rigid body modes are thus properly represented by the models and hence, the model is correct at low frequency. However, the flexible modes are not included so far. They can be added by including the reduced model of each part in the Simscape model using the block *reduced order flexible solid* from the *Simscape Multibody* library.

Liquid sensor

Besides the improvement of the liquid sensor resolution, it is important to find a way to adjust the inclination of the table so that it is perfectly flat. The current method to adjust the inclination of the table is by placing a bubble level and center it. In addition, the sensor has to be calibrated; the beam spot has to be in the middle of the quadrant photodetector when the sensor is horizontal. It is important in the future to define a proper calibration procedure. For example, one can measure with a laser pointer the height of the payload at different corners.

A calibration stage can be designed based on existing stages. At ESRF for example, the granite below the object that is sampled is adjusted using μm -resolution inclinometer and AirLoc levelers to adjust the inclination.

Control law

Different improvements can be investigated to reduce further the transmission of external disturbances to the stage.

First, it has been explained in section 1.3.3, that sensor fusion can be used to extend the control bandwidth; A relative displacement sensor can be used at high frequency to become independent of the flexible modes.

Second, once the resolution of the liquid sensor is improved, the solutions proposed in chapter 4 to reduce the effect of tilt coupling can be tested experimentally.

Finally, only classical control methods using inertial sensors have been considered to isolate the platform so far. Optimal controllers are more suited to deal with a coupled system when it is characterized properly. Therefore, it is interesting to compare the performance obtained with inertial control when including the tilt-reduction methods with that obtained with an optimal controller. For example, linear-quadratic regulator (LQR) can be applied on the states of the system.

In practice, it is never possible to have a direct access to the states of the system. One can use a Kalman filter to estimate the states, giving the noise of the sensors, and apply LQR on the estimated states. This combination of states estimator and LQR is called the linear-quadratic gaussian regulator (LQG). If the sources of noise injected in the system are not Gaussian, some modifications can be applied to the Kalman filter estimator to still estimate the states properly [70].

References

- [1] C. Jarvis, D. Veal, B. Hughes, P. Lovelock, and M. Wagner, “6 degree of freedom micro-vibration test facility for european space agency,” in *ECSSMET*, 2016. Cited on pages iii, 1, 26, 30, and 178.
- [2] M.-K. Zhou, X. Xiong, L.-L. Chen, J.-F. Cui, X.-C. Duan, and Z.-K. Hu, “Note: A three-dimension active vibration isolator for precision atom gravimeters,” *Review of Scientific Instruments*, vol. 86, no. 4, p. 046108, 2015. Cited on pages v, 4, 30, and 178.
- [3] F. Matichard, B. Lantz, K. Mason, R. Mittleman, B. Abbott, S. Abbott, E. Allwine, S. Barnum, J. Birch, S. Biscans, *et al.*, “Advanced ligo two-stage twelve-axis vibration isolation and positioning platform. part 2: Experimental investigation and tests results,” *Precision engineering*, vol. 40, pp. 287–297, 2015. Cited on pages v, 26, 30, and 178.
- [4] H. Butler, “Acceleration feedback in a lithographic tool,” *Control Engineering Practice*, vol. 20, no. 4, pp. 453–464, 2012. Cited on page 1.
- [5] A. R. Carter, G. M. King, T. A. Ulrich, W. Halsey, D. Alchenberger, and T. T. Perkins, “Stabilization of an optical microscope to 0.1 nm in three dimensions,” *Applied Optics*, vol. 46, no. 3, pp. 421–427, 2007. Cited on page 1.
- [6] M. De Angelis, A. Bertoldi, L. Cacciapuoti, A. Giorgini, G. Lamporesi, M. Prevedelli, G. Saccorotti, F. Sorrentino, and G. Tino, “Precision gravimetry with atomic sensors,” *Measurement Science and Technology*, vol. 20, no. 2, p. 022001, 2008. Cited on pages 1 and 3.
- [7] F. Matichard, B. Lantz, R. Mittleman, K. Mason, J. Kissel, B. Abbott, S. Biscans, J. McIver, R. Abbott, S. Abbott, *et al.*, “Seismic isolation of advanced ligo: Review of strategy, instrumentation and performance,” *Classical and Quantum Gravity*, vol. 32, no. 18, p. 185003, 2015. Cited on page 1.
- [8] M. Verma, V. Lafarga, T. Dehaeze, and C. Collette, “Multi-degree of freedom isolation system with high frequency roll-off for drone camera stabilization,” *IEEE Access*, pp. 176188 – 176201, 2020. Cited on pages 1 and 179.
- [9] M. Lafarga, V. and Verma, G. Rodrigues, and C. Collette, “Multi degree of freedom micro-vibration isolator with frameless actuators,” in *1st Aerospace Europe Conference (Bordeaux, France)*, p. 007, 2020. Cited on page 1.
- [10] F. Decobert, D. Veal, C. Jarvis, B. Hughes, and M. Wagner, “Performance validation of a versatile vibration isolation system micro-vibration studies,” in *ECSSMET*, 2016. Cited on pages 1, 26, and 179.
- [11] P. Germain, D. Dekkers, and D. Manglunki, *Introduction aux accélérateurs de particules*. CERN, Geneva, 2014. Cited on pages 2 and 3.

REFERENCES

- [12] M. Minty and F. Zimmermann, *Measurement and control of charged particle beams*. Springer, 2003. Cited on page 2.
- [13] Communication group, “Guide du LHC - CERN faq,” Jul. 2013. Cited on pages 2 and 3.
- [14] C. Collette, S. Janssens, and D. Tshilumba, “Control strategies for the final focus of future linear particle collider,” *Nuclear Instruments and Methods in Physics Research Section A: Accelerators, Spectrometers, Detectors and Associated Equipment*, vol. 684, pp. 7–17, 2012. Cited on page 3.
- [15] C. Collette, S. Janssens, K. Artoos, A. Kuzmin, P. Fernandez-Carmona, M. Guinchard, R. Leuxe, and C. Hauviller, “Nano-motion control of heavy quadrupoles for future particle colliders: An experimental validation,” *Nuclear Instruments and Methods in Physics Research Section A: Accelerators, Spectrometers, Detectors and Associated Equipment*, vol. 643, no. 1, pp. 95–101, 2011. Cited on page 3.
- [16] J. Watchi, B. Ding, D. Tshilumba, K. Artoos, and C. Collette, “Coil-free active stabilisation of extended payloads with optical inertial sensors,” *Measurement Science and Technology*, vol. 29, no. 5, p. 054005, 2018. Cited on pages 3 and 36.
- [17] A. Peters, K. Y. Chung, and S. Chu, “Measurement of gravitational acceleration by dropping atoms,” *Nature*, vol. 400, no. 6747, pp. 849–852, 1999. Cited on page 3.
- [18] M. Schmidt, A. Senger, M. Hauth, C. Freier, V. Schkolnik, and A. Peters, “A mobile high-precision absolute gravimeter based on atom interferometry,” *Gyroscopy and Navigation*, vol. 2, no. 3, p. 170, 2011. Cited on pages 3, 30, and 178.
- [19] M.-K. Zhou, Z.-K. Hu, X.-C. Duan, B.-L. Sun, L.-L. Chen, Q.-Z. Zhang, and J. Luo, “Performance of a cold-atom gravimeter with an active vibration isolator,” *Physical Review A*, vol. 86, no. 4, p. 043630, 2012. Cited on pages 3 and 4.
- [20] X. Wu, Z. Pagel, B. S. Malek, T. H. Nguyen, F. Zi, D. S. Scheirer, and H. Müller, “Gravity surveys using a mobile atom interferometer,” *Science advances*, vol. 5, no. 9, p. eaax0800, 2019. Cited on page 4.
- [21] Z.-K. Hu, B.-L. Sun, X.-C. Duan, M.-K. Zhou, L.-L. Chen, S. Zhan, Q.-Z. Zhang, and J. Luo, “Demonstration of an ultrahigh-sensitivity atom-interferometry absolute gravimeter,” *Physical Review A*, vol. 88, no. 4, p. 043610, 2013. Cited on page 4.
- [22] J. M. Hensley, A. Peters, and S. Chu, “Active low frequency vertical vibration isolation,” *Review of scientific instruments*, vol. 70, no. 6, pp. 2735–2741, 1999. Cited on pages 4, 30, and 178.
- [23] B. Fang, I. Dutta, P. Gillot, D. Savoie, J. Lautier, B. Cheng, C. G. Alzar, R. Geiger, S. Merlet, F. P. Dos Santos, *et al.*, “Metrology with atom interferometry: Inertial sensors from laboratory to field applications,” in *Journal of Physics: Conference Series*, vol. 723, p. 012049, IOP Publishing, 2016. Cited on page 4.
- [24] B. Lantz, R. Schofield, B. O’reilly, D. Clark, and D. DeBra, “Requirements for a ground rotation sensor to improve advanced ligo,” *Bulletin of the Seismological Society of America*, vol. 99, no. 2B, pp. 980–989, 2009. Cited on pages 4, 5, 67, 83, and 84.
- [25] M. Haelterman, *Physique Generale: Chapitre 6 - Physique moderne*. Brussels, BE: Presses Universitaires de Bruxelles, 2010. Cited on page 5.

-
- [26] R. X. Adhikari, “Gravitational radiation detection with laser interferometry,” *Reviews of Modern Physics*, vol. 86, no. 1, p. 121, 2014. Cited on pages 5 and 6.
- [27] C. Cutler and E. E. Flanagan, “Gravitational waves from merging compact binaries: How accurately can one extract the binary’s parameters from the inspiral waveform?,” *Physical Review D*, vol. 49, no. 6, p. 2658, 1994. Cited on page 5.
- [28] R. T. DeRosa, *Performance of active vibration isolation in the advanced ligo detectors*. PhD thesis, Louisiana State University, 2014. Cited on pages 5, 6, and 9.
- [29] IPAC Communications & Education Team, “LIGO’s interferometer.” <https://www.ligo.caltech.edu/page/ligos-ifo>, 2020. Cited on page 6.
- [30] J. Watchi, S. Cooper, B. Ding, C. M. Mow-Lowry, and C. Collette, “Contributed review: A review of compact interferometers,” *Review of scientific instruments*, vol. 89, no. 12, p. 121501, 2018. Cited on pages 6, 32, 34, 36, 37, 39, 40, 41, 43, 45, 49, 53, and 173.
- [31] Abbott, B. P. et al., “Exploring the sensitivity of next generation gravitational wave detectors,” *Classical and Quantum Gravity*, vol. 34, no. 4, p. 044001, 2017. Cited on page 6.
- [32] Abbott, B. P. et al., “Observation of gravitational waves from a binary black hole merger,” *Physical review letters*, vol. 116, no. 6, p. 061102, 2016. Cited on page 6.
- [33] Abbott, B. P. et al., “Gw170817: observation of gravitational waves from a binary neutron star inspiral,” *Physical Review Letters*, vol. 119, no. 16, p. 161101, 2017. Cited on page 6.
- [34] M. Abernathy, F. Acernese, P. Ajith, B. Allen, P. Amaro Seoane, N. Andersson, S. Aoudia, P. Astone, B. Krishnan, L. Barack, *et al.*, “Einstein gravitational wave telescope conceptual design study,” Tech. Rep. ET-0106C-10, EGO, 2011. Cited on page 7.
- [35] H. Yu, D. Martynov, S. Vitale, M. Evans, D. Shoemaker, B. Barr, G. Hammond, S. Hild, J. Hough, S. Huttner, and *et al.*, “Prospects for detecting gravitational waves at 5 hz with ground-based detectors,” *Physical review letters*, vol. 120, no. 14, p. 141102, 2018. Cited on page 7.
- [36] S. J. Richman, *A multi-stage active vibration system*. PhD thesis, University of Colorado, 1992. Cited on pages 7 and 179.
- [37] S. Reilly and R. Leach, “Critical review of seismic vibration isolation techniques.” Tech. Rep. DEPC-EM 007, National Physical Laboratory, Middlesex, United Kingdom, 2006. Cited on pages 9, 13, and 29.
- [38] M. S. Longuet-Higgins, “A theory of the origin of microseisms,” *Philosophical Transactions of the Royal Society of London. Series A, Mathematical and Physical Sciences*, vol. 243, no. 857, pp. 1–35, 1950. Cited on page 10.
- [39] M. Van Camp, S. D. Williams, and O. Francis, “Uncertainty of absolute gravity measurements,” *Journal of Geophysical Research: Solid Earth*, vol. 110, no. B5, 2005. Cited on page 10.
- [40] M. Richardson and R. Potter, “Viscous vs. structural damping in modal analysis,” in *46th Shock and Vibration Symposium*, vol. 175, Citeseer, 1975. Cited on page 11.
- [41] A. Stochino, B. Abbot, Y. Aso, M. Barton, A. Bertolini, V. Boschi, D. Coyne, R. DeSalvo, C. Galli, Y. Huang, *et al.*, “The seismic attenuation system (sas) for the advanced ligo gravitational wave interferometric detectors,” *Nuclear Instruments and Methods in Physics*

REFERENCES

- Research Section A: Accelerators, Spectrometers, Detectors and Associated Equipment*, vol. 598, no. 3, pp. 737–753, 2009. Cited on page 12.
- [42] A. Wanner, G. Bergmann, A. Bertolini, T. Fricke, H. Lück, C. Mow-Lowry, K. Strain, S. Gossler, and K. Danzmann, “Seismic attenuation system for the aei 10 meter prototype,” *Classical and quantum gravity*, vol. 29, no. 24, p. 245007, 2012. Cited on page 12.
- [43] Y. Akiyama, T. Akutsu, M. Ando, K. Arai, Y. Arai, S. Araki, A. Araya, N. Aritomi, H. Asada, Y. Aso, *et al.*, “Vibration isolation system with a compact damping system for power recycling mirrors of kagra,” *Classical and Quantum Gravity*, vol. 36, no. 9, p. 095015, 2019. Cited on page 12.
- [44] C. Johnson and P. Wilke, “Protecting satellites from the dynamics of the launch environment,” in *AIAA Space 2003 Conference & Exposition*, p. 6266, 2003. Cited on page 13.
- [45] Y. Chen, B. Fang, T. Yang, and W. Huang, “Study of whole-spacecraft vibration isolators based on reliability method,” *Chinese Journal of Aeronautics*, vol. 22, no. 2, pp. 153–159, 2009. Cited on page 13.
- [46] A. Preumont, *Vibration control of active structures*, vol. 2. Springer, 1997. Cited on pages 13, 28, and 175.
- [47] L. Zuo, *Element and system design for active and passive vibration isolation*. PhD thesis, Massachusetts Institute of Technology, 2004. Cited on pages 13, 14, 18, and 175.
- [48] F. Matichard, B. Lantz, K. Mason, R. Mittleman, B. Abbott, S. Abbott, E. Allwine, S. Barnum, J. Birch, S. Biscans, *et al.*, “Advanced ligo two-stage twelve-axis vibration isolation and positioning platform. part 1: Design and production overview,” *Precision Engineering*, vol. 40, pp. 273–286, 2015. Cited on pages 13, 18, 30, and 178.
- [49] M. Plissi, C. Torrie, M. Husman, N. Robertson, K. Strain, H. Ward, H. Lück, and J. Hough, “Geo 600 triple pendulum suspension system: Seismic isolation and control,” *Review of scientific instruments*, vol. 71, no. 6, pp. 2539–2545, 2000. Cited on page 14.
- [50] P. Schellekens, N. Rosielle, H. Vermeulen, M. Vermeulen, S. Wetzels, and W. Pril, “Design for precision: current status and trends,” *Cirp Annals*, vol. 47, no. 2, pp. 557–586, 1998. Cited on pages 14, 25, 31, 172, 173, and 174.
- [51] M. Haelterman, *Physique Generale: Chapitre 5 - Oscillations et Ondes*. Brussels, BE: Presses Universitaires de Bruxelles, 2010. Cited on page 15.
- [52] G. Losurdo, *Ultra-low frequency inverted pendulum for the Virgo test mass suspension*. PhD thesis, Scuola Normale Superiore di Pisa, 1999. Cited on page 16.
- [53] J. Winterflood, *High performance vibration isolation for gravitational wave detection*. PhD thesis, University of Western Australia, 2001. Cited on pages 16, 17, and 18.
- [54] G. Losurdo, M. Bernardini, S. Braccini, C. Bradaschia, C. Casciano, V. Dattilo, R. De Salvo, A. Di Virgilio, F. Frasconi, A. Gaddi, *et al.*, “An inverted pendulum preisolator stage for the virgo suspension system,” *Review of scientific instruments*, vol. 70, no. 5, pp. 2507–2515, 1999. Cited on page 16.
- [55] R. DeSalvo, A. DiVirgilio, A. Errico, F. Guotong, I. Ferrante, F. Frasconi, A. Gaddi, A. Gennai, G. Gennaro, A. Giazotto, *et al.*, “Performances of an ultralow frequency vertical pre-isolator for

- the virgo seismic attenuation chains,” *Nuclear Instruments and Methods in Physics Research Section A: Accelerators, Spectrometers, Detectors and Associated Equipment*, vol. 420, no. 1-2, pp. 316–335, 1999. Cited on pages 16 and 18.
- [56] S. Reilly and R. Leach, “Critical review of seismic vibration isolation techniques.,” 2006. Not cited.
- [57] J. Winterflood and D. Blair, “A long-period conical pendulum for vibration isolation,” *Physics Letters A*, vol. 222, no. 3, pp. 141–147, 1996. Cited on page 16.
- [58] J. V. van Heijningen, “A fifty-fold improvement of thermal noise limited inertial sensitivity by operating at cryogenic temperatures,” *arXiv preprint arXiv:1909.12956*, 2019. Cited on page 16.
- [59] T. Zhang, H. Huang, F. Zhao, and J. Zhu, “A control strategy using negative stiffness for active vibration isolation,” in *2008 3rd IEEE International Conference on Nano/Micro Engineered and Molecular Systems*, pp. 712–716, IEEE, 2008. Cited on page 17.
- [60] J. Van Heijningen, A. Bertolini, E. Hennes, M. Beker, M. Doets, H. Bulten, K. Agatsuma, T. Sekiguchi, and J. Van Den Brand, “A multistage vibration isolation system for advanced virgo suspended optical benches,” *Classical and Quantum Gravity*, vol. 36, no. 7, p. 075007, 2019. Cited on page 17.
- [61] A. Stochino and R. de Salvo, “Performance improvement of the geometric anti spring (gas) seismic filter for gravitational waves detectors,” *SURF Report, T050239-00*, 2005. Cited on page 18.
- [62] M. Beccaria, M. Bernardini, E. Bougleux, S. Braccini, C. Bradaschia, C. Casciano, G. Cella, E. Cuoco, E. D’Ambrosio, G. De Carolis, *et al.*, “Extending the virgo gravitational wave detection band down to a few hz: metal blade springs and magnetic antisprings,” *Nuclear Instruments and Methods in Physics Research Section A: Accelerators, Spectrometers, Detectors and Associated Equipment*, vol. 394, no. 3, pp. 397–408, 1997. Cited on page 18.
- [63] J. Winterflood, D. G. Blair, and B. Slagmolen, “High performance vibration isolation using springs in euler column buckling mode,” *Physics Letters A*, vol. 300, no. 2-3, pp. 122–130, 2002. Cited on page 18.
- [64] E. Chin, K. Lee, J. Winterflood, L. Ju, and D. Blair, “Low frequency vertical geometric anti-spring vibration isolators,” *Physics letters A*, vol. 336, no. 2-3, pp. 97–105, 2005. Cited on page 18.
- [65] J. van Heijningen, J. Winterflood, and L. Ju, “Multi-blade monolithic euler springs with optimised stress distribution,” *arXiv preprint arXiv:2104.03734*, 2021. Cited on page 18.
- [66] A. Souleille, T. Lampert, V. Lafarga, S. Hellegouarch, A. Rondineau, G. Rodrigues, and C. Collette, “A concept of active mount for space applications,” *CEAS Space Journal*, vol. 10, no. 2, pp. 157–165, 2018. Cited on page 19.
- [67] R. Munnig Schmidt, G. Schitter, and A. Rankers, *The design of high performance mechatronics: high-Tech functionality by multidisciplinary system integration*. Ios Press, 2020. Cited on page 24.
- [68] S. Skogestad and I. Postlethwaite, *Multivariable feedback control: analysis and design*, vol. 2. Wiley New York, 2007. Cited on pages 25, 26, 106, and 107.

REFERENCES

- [69] C. Ding, *Vibration isolation control of a contactless electromagnetic suspension system*. PhD thesis, Technische Universiteit Eindhoven, 2013. Cited on pages 25 and 179.
- [70] M. G. Beker, *Low-frequency sensitivity of next generation gravitational wave detectors*. PhD thesis, Vrije University Amsterdam, 2013. Cited on pages 25 and 148.
- [71] H. Kwakernaak and R. Sivan, *Linear optimal control systems*, vol. 1. Wiley-interscience New York, 1972. Cited on pages 25 and 27.
- [72] J. Sabatier, P. Lanusse, P. Melchior, and A. Oustaloup, “Fractional order differentiation and robust control design,” in *CRONE, H-infinity and Motion Control*, Springer, 2015. Cited on pages 25 and 26.
- [73] H. Pu, X. Chen, Z. Zhou, and X. Luo, “Six-degree-of-freedom active vibration isolation system with decoupled collocated control,” *Proceedings of the Institution of Mechanical Engineers, Part B: Journal of Engineering Manufacture*, vol. 226, no. 2, pp. 313–325, 2012. Cited on pages 26 and 178.
- [74] J. Watchi, B. Ding, G. Zhao, and C. Collette, “Study of mimo control laws for seismic isolation of flexible payload,” in *7th International Conference on Control, Mechatronics and Automation (ICCMA)*, pp. 248–252, IEEE, 2019. Cited on page 26.
- [75] C. Collette and F. Matichard, “Sensor fusion methods for high performance active vibration isolation systems,” *Journal of sound and vibration*, vol. 342, pp. 1–21, 2015. Cited on page 26.
- [76] T. Dehaeze, M. Verma, and C. Collette, “Complementary filters shaping using h-infinity synthesis,” in *2019 IEEE 7th International Conference on Control, Mechatronics and Automation*, pp. 457–461, 2019. Cited on page 26.
- [77] L. Chamon, G. Quiqueto, and S. Bistafa, “The application of the singular value decomposition (svd) for the decoupling of the vibratory reproduction system of an aircraft cabin simulator,” in *SAE Technical Paper*, SAE International, 2010. Cited on page 26.
- [78] A. V. Oppenheim, R. W. Schaffer, and J. R. Buck, *Discrete-time signal processing*. New Jersey: Prentice-Hall, 1999. Cited on page 27.
- [79] W. S. Levine, *The control handbook*. CRC press, 2000. Cited on pages 27 and 28.
- [80] X. Li, *Simultaneous, fault-tolerant vibration isolation and pointing control of flexure jointed hexapods*. PhD thesis, University of Wyoming, 2000. Cited on pages 28 and 179.
- [81] J. R. Peterson, “Observations and modeling of seismic background noise,” Tech. Rep. 93-322, US Department of interior, Geological Survey, 1993. Cited on pages 29 and 30.
- [82] MI Partners, “Active vibration isolation at mi-partners,” 2010. Cited on pages 29, 30, 75, and 178.
- [83] N. Rijnveld, R. Braber, P. Fraanje, and T. van den Dool, “Low-frequency vibration isolation in six degrees of freedom: the hummingbird,” 2010. Euspen. Cited on pages 30, 75, and 178.
- [84] A. L. Y. Zenga, “Iterative siso feedback design for an active vibration isolation system,” Master’s thesis, Technische Univererseit Eindhoven, 2005. Cited on pages 29 and 178.
- [85] K. K.-L. Miu, *A low cost, DC-coupled active vibration isolation system*. PhD thesis, Massachusetts Institute of Technology, 2008. Cited on pages 29, 30, 32, 170, 174, and 178.

- [86] N. Bobroff, “Recent advances in displacement measuring interferometry,” *Measurement Science and Technology*, vol. 4, no. 9, p. 907, 1993. Cited on pages 30 and 42.
- [87] P. Kren and P. Balling, “Common path two-wavelength homodyne counting interferometer development,” *Measurement Science and Technology*, vol. 20, no. 8, p. 084009, 2009. Cited on page 30.
- [88] M. Pisani, A. Yacoot, P. Balling, N. Bancone, C. Birlikseven, M. Çelik, J. Flügge, R. Hamid, P. Köchert, P. Kren, *et al.*, “Comparison of the performance of the next generation of optical interferometers,” *Metrologia*, vol. 49, no. 4, p. 455, 2012. Cited on pages 30, 46, 48, and 49.
- [89] S. Xu., L. Chassagne, S. Topcu, L. Chen, J. Sun, and T. Yan, “Polarimetric interferometer for measuring nonlinearity error of heterodyne interferometric displacement system,” *Chin. Opt. Lett.*, vol. 11, p. 061201, Jun 2013. Cited on pages 30, 42, 46, 47, 48, and 49.
- [90] T. Schuldt, M. Gohlke, W. D., U. Johann, A. Peters, and C. Braxmaier, “Compact laser interferometer for translation and tilt metrology,” *International Journal of Optomechatronics*, vol. 1, no. 2, pp. 168–179, 2007. Cited on page 30.
- [91] A. Yacoot, M. Pisani, G. B. Picotto, U. Kuetgens, J. Flügge, P. Kren, A. Lassila, S. Seppä, R. Hamid, M. Celik, *et al.*, “Nanotrace: the investigation of nonlinearity in optical interferometers using x-ray interferometry,” in *Proceedings of 9th International Symposium on Measurement Technology and Intelligent Instruments*, pp. 216–221, Measurement Technology and Intelligent Instruments, Saint-Petersburg, 2009. Cited on pages 30 and 46.
- [92] E. Wielandt and G. Streckeisen, “The leaf-spring seismometer: Design and performance,” *Bulletin of the Seismological Society of America*, vol. 72, no. 6A, pp. 2349–2367, 1982. Cited on pages 30 and 67.
- [93] C. Collette, S. Janssens, P. Fernandez-Carmona, K. Artoos, M. Guinchard, C. Hauviller, and A. Preumont, “Review: Inertial sensors for low-frequency seismic vibration measurement,” *Bulletin of the Seismological Society of America*, vol. 102, no. 4, pp. 1289–1300, 2012. Cited on pages 35, 174, and 175.
- [94] M. J. Downs and K. Raine, “An unmodulated bi-directional fringe-counting interferometer system for measuring displacement,” *Precision Engineering*, vol. 1, no. 2, pp. 85–88, 1979. Cited on pages 36, 37, 38, and 45.
- [95] M. A. Zumberge, J. Berger, M. A. Dzieciuch, and R. L. Parker, “Resolving quadrature fringes in real time,” *Applied optics*, vol. 43, no. 4, pp. 771–775, 2004. Cited on pages 36, 44, and 47.
- [96] J. Otero, *Development and characterization of an observatory-class, broadband, non-feedback, leaf-spring interferometric seismometer*. PhD thesis, University of California, San Diego, 2009. Cited on pages 36, 42, 44, and 67.
- [97] C. Collette, F. Nassif, J. Amar, C. Depouhon, and S.-P. Gorza, “Prototype of interferometric absolute motion sensor,” *Sensors and Actuators A: Physical*, vol. 224, pp. 72–77, 2015. Cited on page 36.
- [98] M. Pisani, “Multiple reflection michelson interferometer with picometer resolution,” *Optics express*, vol. 16, no. 26, pp. 21558–21563, 2008. Cited on pages 37, 38, 40, and 44.
- [99] Z. Zhou, J. Winterflood, L. Ju, and D. Blair, “Investigation of a laser walk-off angle sensor and its application to tilt measurement in gravitational wave detectors,” *Physics Letters A*, vol. 280, no. 4, pp. 197–203, 2001. Cited on page 38.

REFERENCES

- [100] C. Joenathan, A. Bernal, Y. Woonghee, R. M. Bunch, and C. Hakoda, “Dual-arm multiple-reflection michelson interferometer for large multiple reflections and increased sensitivity,” *Optical Engineering*, vol. 55, no. 2, p. 024101, 2016. Cited on page 38.
- [101] R. Reibold and W. Molkenstruck, “Laser interferometric measurement and computerized evaluation of ultrasonic displacements,” *Acta Acustica united with Acustica*, vol. 49, no. 3, pp. 205–211, 1981. Cited on page 38.
- [102] I. Dániel, “Advanced successive phase unwrapping algorithm for quadrature output michelson interferometers,” *Measurement*, vol. 37, no. 2, pp. 95–102, 2005. Cited on pages 38 and 45.
- [103] D. Ponceau, P. Miller, and S. Olivier, “Subnanometric michelson interferometry for seismological applications,” in *Photonics Europe (International Society for Optics and Photonics)*, pp. 70030U–1–10, 2008. Cited on pages 39, 40, 45, and 49.
- [104] S. M. Aston, *Optical read-out techniques for the control of test-masses in gravitational wave observatories*. PhD thesis, University of Birmingham, 2011. Cited on pages 39 and 40.
- [105] M. Bradshaw, *nEUCLID: a new homodyne interferometer with space applications*. PhD thesis, University of Birmingham, 2015. Cited on pages 39 and 40.
- [106] J. Watchi, B. Ding, F. Matichard, and C. Collette, “Development of a high-resolution optical inertial sensor for sub-hz seismic isolation,” in *ISMA2016 USD2016 (ISMA conference (Leuven, Belgium))*, pp. 275–285, 2016. Cited on pages 39, 40, 44, and 45.
- [107] V. Greco, G. Molesini, and F. Quercioli, “Accurate polarization interferometer,” *Review of scientific instruments*, vol. 66, no. 7, pp. 3729–3734, 1995. Cited on pages 39 and 45.
- [108] S. J. Cooper, C. J. Collins, A. C. Green, D. Hoyland, C. Speake, A. Freise, and C. Mow-Lowry, “A compact, large-range interferometer for precision measurement and inertial sensing,” *Classical and Quantum Gravity*, vol. 35, no. 9, p. 095007, 2018. Cited on pages 39, 40, and 45.
- [109] M. Zumberge, J. Berger, J. Otero, and E. Wielandt, “An optical seismometer without force feedback,” *Bulletin of the Seismological Society of America*, vol. 100, no. 2, pp. 598–605, 2010. Cited on page 40.
- [110] F. Acernese, G. Giordano, R. Romano, and F. Barone, “Compact tunable monolithic sensors for vibration monitoring and control of structures and very low frequency–large band characterization of sites,” in *15th World Conference in Earthquake Engineering*, pp. 24–28, 2012. Cited on page 40.
- [111] Renishaw, “RLD10 plane mirror interferometer.” www.renishaw.com, 2017. Cited on page 40.
- [112] Zygo, “DynaFiz, dynamic metrology with confidence.” www.zygo.com, 2018. Cited on page 40.
- [113] DayOptronics, “AK-40 interferometer.” en.dayoptronics.cn, 2018. Cited on page 40.
- [114] M. J. Downs and W. Rowley, “A proposed design for a polarization-insensitive optical interferometer system with subnanometric capability,” *Precision Engineering*, vol. 15, no. 4, pp. 281 – 286, 1993. Cited on page 39.
- [115] K. Raine and M. J. Downs, “Beam-splitter coatings for producing phase quadrature interferometer outputs,” *Optica Acta: International Journal of Optics*, vol. 25, no. 7, pp. 549–558, 1978. Cited on page 39.

-
- [116] B. J. Slagmolen, D. A. Shaddock, M. Gray, and D. McClelland, “Frequency stability of spatial mode interference (tilt) locking,” *IEEE journal of quantum electronics*, vol. 38, no. 11, pp. 1521–1528, 2002. Cited on page 41.
- [117] D. Shaddock *et al.*, “Advanced interferometry for gravitational wave detection,” 2000. Cited on page 41.
- [118] H. Kogelnik and T. Li, “Laser beams and resonators,” *Proceedings of the IEEE*, vol. 54, no. 10, pp. 1312–1329, 1966. Cited on page 41.
- [119] C. Bond, D. Brown, A. Freise, and K. A. Strain, “Interferometer techniques for gravitational-wave detection,” *Living reviews in relativity*, vol. 19, no. 1, p. 3, 2016. Cited on page 41.
- [120] C.-M. Wu, S.-T. Lin, and J. Fu, “Heterodyne interferometer with two spatial-separated polarization beams for nanometrology,” *Optical and Quantum Electronics*, vol. 34, no. 12, pp. 1267–1276, 2002. Cited on pages 42 and 46.
- [121] W. Hou and G. Wilkening, “Investigation and compensation of the nonlinearity of heterodyne interferometers,” *Precision Engineering*, vol. 14, no. 2, pp. 91 – 98, 1992. Cited on pages 42, 44, 47, 48, and 49.
- [122] A. E. Rosenbluth and N. Bobroff, “Optical sources of non-linearity in heterodyne interferometers,” *Precision Engineering*, vol. 12, no. 1, pp. 7 – 11, 1990. Cited on page 42.
- [123] A. Ju, C. Zhong, and W. Hou, “The effect of laser source and {PBS} on the nonlinearity in heterodyne interferometer,” *Optik - International Journal for Light and Electron Optics*, vol. 126, no. 1, pp. 112 – 115, 2015. Cited on pages 42, 46, and 47.
- [124] F. Petru and O. Cip, “Problems regarding linearity of data of a laser interferometer with a single-frequency laser,” *Precision Engineering*, vol. 23, no. 1, pp. 39 – 50, 1999. Cited on pages 42, 44, 47, 48, and 49.
- [125] J. D. Ellis, *Field guide to displacement measuring interferometry*. Society of Photo-Optical Instrumentation Engineers, 2014. Cited on page 42.
- [126] P. L. Rosin, “A note on the least squares fitting of ellipses,” *Pattern Recognition Letters*, vol. 14, no. 10, pp. 799 – 808, 1993. Cited on page 44.
- [127] L. R. Watkins and M. J. Collett, “Ellipse fitting for interferometry. part 2: experimental realization,” *Appl. Opt.*, vol. 53, pp. 7697–7703, Nov 2014. Cited on page 44.
- [128] P. L. M. Heydemann, “Determination and correction of quadrature fringe measurement errors in interferometers,” *Appl. Opt.*, vol. 20, pp. 3382–3384, Oct 1981. Cited on pages 44, 48, and 49.
- [129] C.-M. Wu, C.-S. Su, and G.-S. Peng, “Correction of nonlinearity in one-frequency optical interferometry,” *Measurement Science and Technology*, vol. 7, no. 4, p. 520, 1996. Cited on pages 44, 48, and 49.
- [130] P. Gregorčič, T. Požar, and J. Možina, “Quadrature phase-shift error analysis using a homodyne laser interferometer,” *Opt. Express*, vol. 17, pp. 16322–16331, Aug 2009. Cited on pages 44, 46, 48, and 49.

REFERENCES

- [131] T. Požar and J. Možina, “Enhanced ellipse fitting in a two-detector homodyne quadrature laser interferometer,” *Measurement Science and Technology*, vol. 22, no. 8, p. 085301, 2011. Cited on pages 44, 48, and 49.
- [132] R. Köning, G. Wimmer, and V. Witkovský, “Ellipse fitting by nonlinear constraints to demodulate quadrature homodyne interferometer signals and to determine the statistical uncertainty of the interferometric phase,” *Measurement Science and Technology*, vol. 25, no. 11, p. 115001, 2014. Cited on pages 44, 48, and 49.
- [133] K. A. Goldberg and J. Bokor, “Fourier-transform method of phase-shift determination,” *Appl. Opt.*, vol. 40, pp. 2886–2894, Jun 2001. Cited on page 44.
- [134] M. J. Collett and G. J. Tee, “Ellipse fitting for interferometry. part 1: static methods,” *J. Opt. Soc. Am. A*, vol. 31, pp. 2573–2583, Dec 2014. Cited on page 44.
- [135] K. Emancipator and M. H. Kroll, “A quantitative measure of nonlinearity,” *Clinical chemistry*, vol. 39, no. 5, pp. 766–772, 1993. Cited on page 44.
- [136] M. J. Collett and L. R. Watkins, “Ellipse fitting for interferometry. part 3: dynamic method,” *J. Opt. Soc. Am. A*, vol. 32, pp. 491–496, Mar 2015. Cited on page 44.
- [137] C. Wang, E. D. Burnham-Fay, and J. D. Ellis, “Real-time fpga-based kalman filter for constant and non-constant velocity periodic error correction,” *Precision Engineering*, vol. 48, pp. 133–143, 2017. Cited on page 44.
- [138] P. de Groot, “Derivation of algorithms for phase-shifting interferometry using the concept of a data-sampling window,” *Appl. Opt.*, vol. 34, pp. 4723–4730, Aug 1995. Cited on page 44.
- [139] J. Schmit and K. Creath, “Window function influence on phase error in phase-shifting algorithms,” *Appl. Opt.*, vol. 35, pp. 5642–5649, Oct 1996. Cited on page 44.
- [140] T. Eom, J. Kim, and K. Jeong, “The dynamic compensation of nonlinearity in a homodyne laser interferometer,” *Measurement Science and Technology*, vol. 12, no. 10, p. 1734, 2001. Cited on pages 45, 48, and 49.
- [141] B. Ding, *Development of High Resolution Interferometric Inertial Sensors*. PhD thesis, Université libre de Bruxelles, 2021. Cited on pages 46, 50, 63, 64, and 71.
- [142] M. Pisani, G. Mana, and A. M. Nobili, “Design of an interferometric displacement sensor with picometer resolution for the galileo-galilei mission,” in *2015 IEEE Metrology for Aerospace (MetroAeroSpace)*, pp. 591–595, June 2015. Cited on page 46.
- [143] C. Weichert, P. Köchert, R. Köning, J. Flügge, B. Andreas, U. Kuetgens, and A. Yacoot, “A heterodyne interferometer with periodic nonlinearities smaller than ± 10 pm,” *Measurement Science and Technology*, vol. 23, no. 9, p. 094005, 2012. Cited on pages 46, 48, and 49.
- [144] M. Teran, V. Martín, L. Gesa, I. Mateos, F. Gibert, N. Karnesis, J. Ramos-Castro, T. Schwarze, O. Gerberding, G. Heinzl, *et al.*, “Towards a fpga-controlled deep phase modulation interferometer,” *Journal of Physics: Conference Series*, vol. 610, no. 1, p. 012042, 2015. Cited on page 46.
- [145] X. Wu, H. Wei, H. Zhang, L. Ren, Y. Li, and J. Zhang, “Absolute distance measurement using frequency-sweeping heterodyne interferometer calibrated by an optical frequency comb,” *Applied optics*, vol. 52, no. 10, pp. 2042–2048, 2013. Cited on page 46.

-
- [146] D. I. Robertson, E. D. Fitzsimons, C. J. Killow, M. Perreur-Lloyd, H. Ward, J. Bryant, A. M. Cruise, G. Dixon, D. Hoyland, D. Smith, *et al.*, “Construction and testing of the optical bench for lisa pathfinder,” *Classical and quantum gravity*, vol. 30, no. 8, p. 085006, 2013. Cited on page 46.
- [147] O. Gerberding, “Deep frequency modulation interferometry,” *Optics express*, vol. 23, no. 11, pp. 14753–14762, 2015. Cited on page 46.
- [148] M. Celik, R. Hamid, U. Kuetsgens, and A. Yacoot, “Picometre displacement measurements using a differential fabry–perot optical interferometer and an x-ray interferometer,” *Measurement Science and Technology*, vol. 23, no. 8, p. 085901, 2012. Cited on pages 46, 48, and 49.
- [149] F. G. Cervantes, L. Kumanchik, J. Pratt, and J. M. Taylor, “High sensitivity optomechanical reference accelerometer over 10 khz,” *Applied Physics Letters*, vol. 104, no. 22, p. 221111, 2014. Cited on page 46.
- [150] F. Guzman, O. Gerberding, J. T. Melcher, J. Stirling, J. R. Pratt, G. A. Shaw, and J. M. Taylor, “Optomechanical motion sensors,” in *ASPE 2015 Summer Topical Meeting, Precision*, 2015. Cited on page 46.
- [151] A. systems AG., “Attocube systems ag, vibration analysis of a positioner (anpz101) using the attofpsensor,” 2009. Cited on page 46.
- [152] N. Bobroff, “Residual errors in laser interferometry from air turbulence and nonlinearity,” *Appl. Opt.*, vol. 26, pp. 2676–2682, Jul 1987. Cited on pages 48 and 49.
- [153] F. Xie, J. Ren, Z. Chen, and Q. Feng, “Vibration-displacement measurements with a highly stabilised optical fiber michelson interferometer system,” *Optics & Laser Technology*, vol. 42, no. 1, pp. 208 – 213, 2010. Cited on pages 48 and 49.
- [154] V. Korpelainen, J. Seppä, and A. Lassila, “Design and characterization of {MIKES} metrological atomic force microscope,” *Precision Engineering*, vol. 34, no. 4, pp. 735 – 744, 2010. Cited on pages 48 and 49.
- [155] J. Seppä, V. Korpelainen, M. Merimaa, G. B. Picotto, and A. Lassila, “A method for linearization of a laser interferometer down to the picometre level with a capacitive sensor,” *Measurement Science and Technology*, vol. 22, no. 9, p. 094027, 2011. Cited on pages 48 and 49.
- [156] M. Tanaka, T. Yamagami, and K. Nakayama, “Linear interpolation of periodic error in a heterodyne laser interferometer at subnanometer levels [dimension measurement],” *IEEE Transactions on Instrumentation and Measurement*, vol. 38, pp. 552–554, Apr 1989. Cited on pages 48 and 49.
- [157] M. Gohlke, T. Schuldt, D. Weise, U. Johann, A. Peters, and C. Braxmaier, “A high sensitivity heterodyne interferometer as a possible optical readout for the lisa gravitational reference sensor and its application to technology verification,” *Journal of Physics: Conference Series*, vol. 154, no. 1, p. 012030, 2009. Cited on pages 48 and 49.
- [158] Packard and Hewlett, “Lightwave signal analysers measure relative intensity noise,” Tech. Rep. 71400, 1991. Cited on page 54.
- [159] L. G. Holcomb, “A direct method for calculating instrument noise levels in side-by-side seismometer evaluations,” Tech. Rep. 89-214, United States Department of the interior geological survey, Albuquerque, New Mexico, 1989. Cited on page 55.

REFERENCES

- [160] S.-P. Gorza and P. Kockaert, *Laser physics*. Brussels, BE: Presses Universitaires de Bruxelles, 2013. Cited on page 56.
- [161] O. Llopis, P.-H. Merrer, H. Brahim, K. Saleh, and P. Lacroix, “Phase noise measurement of a narrow linewidth cw laser using delay line approaches,” *Optics letters*, vol. 36, no. 14, pp. 2713–2715, 2011. Cited on pages 57 and 183.
- [162] T. Okamoto and F. Ito, “Laser phase noise characterization using parallel linear optical sampling,” *Journal of Lightwave Technology*, vol. 32, no. 18, pp. 3119–3125, 2014. Cited on pages 57 and 185.
- [163] P. R. Saulson, “Thermal noise in mechanical experiments,” *Physical Review D*, vol. 42, no. 8, p. 2437, 1990. Cited on page 62.
- [164] MathWorks, “Simscape - model and simulate multidomain physical systems.” <https://www.mathworks.com/products/simscape.html>, 2021. Cited on page 67.
- [165] G. Zhao, B. Ding, J. Watchi, A. Deraemaeker, and C. Collette, “Experimental study on active seismic isolation using interferometric inertial sensors,” *Mechanical Systems and Signal Processing*, vol. 145, p. 106959, 2020. Cited on pages 67, 69, and 70.
- [166] B. De Marneffe, *Active and passive vibration isolation and damping via shunted transducers*. PhD thesis, Université Libre de Bruxelles, 2007. Cited on page 68.
- [167] D. Laro, S. Van den Berg, J. Eisinger, and J. Van Eijk, “6-dof active vibration isolation without tilt-horizontal coupling,” in *Proc. of the 11th Euspen International Conference*, pp. 15–18, 2011. Cited on page 75.
- [168] N. Rijnveld and T. C. Van Den Dool, “Active vibration isolation and damping system,” 2016. US Patent 9,488,247. Cited on page 75.
- [169] F. Matichard, M. Evans, R. Mittleman, M. MacInnis, S. Biscans, K. Dooley, H. Sohler, A. Lauriero, H. Paris, J. Koch, *et al.*, “Modeling and experiment of the suspended seismometer concept for attenuating the contribution of tilt motion in horizontal measurements,” *Review of Scientific Instruments*, vol. 87, no. 6, p. 065002, 2016. Cited on pages 75, 76, and 145.
- [170] S. Xie, “Amélioration des systèmes d’isolation de grands instruments scientifiques, ULB,” Master’s thesis, Institut supérieur de l’automobile et des transports, 2013. Cited on pages 75 and 76.
- [171] K. Venkateswara, C. A. Hagedorn, J. H. Gundlach, J. Kissel, J. Warner, H. Radkins, T. Shaffer, B. Lantz, R. Mittleman, F. Matichard, *et al.*, “Subtracting tilt from a horizontal seismometer using a ground-rotation sensor,” *Bulletin of the Seismological Society of America*, vol. 107, no. 2, pp. 709–717, 2017. Cited on pages 77, 89, 114, 121, and 123.
- [172] J. Belfi, N. Beverini, F. Bosi, G. Carelli, A. Di Virgilio, E. Maccioni, A. Ortolan, and F. Stefani, “A 1.82 m 2 ring laser gyroscope for nano-rotational motion sensing,” *Applied Physics B*, vol. 106, no. 2, pp. 271–281, 2012. Cited on page 77.
- [173] K. Venkateswara, C. A. Hagedorn, M. D. Turner, T. Arp, and J. H. Gundlach, “A high-precision mechanical absolute-rotation sensor,” *Review of Scientific Instruments*, vol. 85, no. 1, p. 015005, 2014. Cited on pages 77, 115, and 121.
- [174] J. J. McCann, J. Winterflood, L. Ju, and C. Zhao, “A multi-orientation low-frequency rotational accelerometer,” *TBD*, vol. TBD, no. TBD, p. TBD, 2021. Cited on pages 77 and 86.

-
- [175] N. Azaryan, V. Batusov, J. Budagov, V. Glagolev, M. Lyablin, G. Trubnikov, G. Shirkov, J.-C. Gayde, B. D. Girolamo, D. Mergelkuhl, *et al.*, “The precision laser inclinometer long-term sensitivity in thermo-stabilized conditions,” Tech. Rep. E13-2015-35, Dzhelpev Lab. of Nuclear Problems, 2015. Cited on pages 78, 79, 83, 85, and 143.
- [176] T. Dehaeze, “Diagonal control using the SVD and the Jacobian Matrix,” tech. rep., Universite de Liege <https://orbi.uliege.be/handle/2268/260970>, 2021. Cited on page 103.
- [177] A. Deremaeker, “Model reduction in structural dynamics,” *Precision Mechatronics Lab., Belgium, internal note*, 2018. Cited on page 129.
- [178] R. Craig and M. Bampton, “Coupling of substructures for dynamic analyses,” *AIAA journal*, vol. 6, no. 7, pp. 1313–1319, 1968. Cited on page 129.
- [179] J. Kissel, “L1 HAM6 ISI eLIGO final performance measurements,” Tech. Rep. LIGO-T0900285-v1, LIGO, 2010. Cited on page 138.
- [180] D. Coyne *et al.*, “Design requirements for the in-vacuum mechanical elements of the advanced ligo seismic isolation system for the bsc chamber,” Tech. Rep. LIGO-E030180, LIGO, 2006. Cited on page 146.
- [181] A. Papoulis and S. U. Pillai, *Probability, random variables, and stochastic processes*. Tata McGraw-Hill Education, 2002. Cited on page 169.
- [182] A. M. Yaglom, *An introduction to the theory of stationary random functions*. Prentice Hall, Englewood Cliffs, New York, 1962. Cited on page 169.
- [183] C. F. Milo, M. R. Selmon, R. E. Hill, R. G. French, *et al.*, “Methods and apparatus for crossing total occlusions in blood vessels,” May 15 2001. US Patent 6,231,546. Cited on page 170.
- [184] J. Y. Chung and D. A. Blaser, “Transfer function method of measuring in-duct acoustic properties. i. theory,” *The Journal of the Acoustical Society of America*, vol. 68, no. 3, pp. 907–913, 1980. Cited on page 170.
- [185] L. B. White and B. Boashash, “Cross spectral analysis of nonstationary processes,” *IEEE Transactions on Information Theory*, vol. 36, no. 4, pp. 830–835, 1990. Cited on page 171.
- [186] B. N. Shapiro, *Adaptive modal damping for advanced LIGO suspensions*. PhD thesis, Massachusetts Institute of Technology, 2012. Cited on page 172.
- [187] S. Hellegouarch, L. Fueyo Roza, K. Artoos, P. Lambert, and C. Collette, “Linear encoder based low frequency inertial sensor,” *International Journal of Optomechatronics*, vol. 10, no. 3-4, pp. 120–129, 2016. Cited on page 173.
- [188] M. Haelterman, *Physique Generale: Chapitre 2 - Electrostatique*. Brussels, BE: Presses Universitaires de Bruxelles, 2010. Cited on pages 174 and 175.
- [189] L. F. Fueyo, F. Francqui, and C. Collette, “High sensitivity fbg accelerometer with stiffness adjustment,” in *78th EAGE Conference and Exhibition 2016*, vol. 2016, pp. 1–5, European Association of Geoscientists & Engineers, 2016. Cited on page 175.
- [190] Cedrat technologies, “Cedrat technologies - Innovation in mechatronics.” <https://www.cedrat-technologies.com/fr/technologies.html>, 2020. Cited on page 175.

REFERENCES

- [191] R. L. Hannah and S. E. Reed, *Strain gage users' handbook*. Springer Science & Business Media, 1992. Cited on page 176.
- [192] E. Udd and W. B. Spillman Jr, *Fiber optic sensors: an introduction for engineers and scientists*. John Wiley & Sons, 2011. Cited on page 176.
- [193] J.-S. Tao, G.-R. Liu, and K.-Y. Lam, "Design optimization of marine engine-mount system," *Journal of Sound and vibration*, vol. 235, no. 3, pp. 477–494, 2000. Cited on page 178.
- [194] J. van Eijk, D. Laro, J. Eisinger, W. Aarden, T. Michielsen, and S. van den Berg, "The ultimate performance in floor vibration isolation," *Microniek*, vol. 51, no. 2, pp. 13–19, 2011. Cited on page 178.
- [195] R. Kirchhoff, C. Mow-Lowry, G. Bergmann, M. Hanke, P. Koch, S. Köhlenbeck, S. Leavey, J. Lehmann, P. Oppermann, J. Wöhler, *et al.*, "Local active isolation of the aei-sas for the aei 10 m prototype facility," *Classical and Quantum Gravity*, vol. 37, no. 11, p. 115004, 2020. Cited on page 178.
- [196] T. Sutton, S. Elliott, M. Brennan, K. Heron, and D. Jessop, "Active isolation of multiple structural waves on a helicopter gearbox support strut," *Journal of Sound and Vibration*, vol. 205, no. 1, pp. 81–101, 1997. Cited on page 179.
- [197] R. G. Cobb, J. M. Sullivan, A. Das, L. P. Davis, T. T. Hyde, T. Davis, Z. H. Rahman, and J. T. Spanos, "Vibration isolation and suppression system for precision payloads in space," *Smart Materials and Structures*, vol. 8, no. 6, p. 798, 1999. Cited on page 179.
- [198] G. Losurdo, G. Calamai, E. Cuoco, L. Fabbroni, G. Guidi, M. Mazzoni, R. Stanga, F. Vetrano, L. Holloway, D. Passuello, *et al.*, "Inertial control of the mirror suspensions of the virgo interferometer for gravitational wave detection," *Review of Scientific Instruments*, vol. 72, no. 9, pp. 3653–3661, 2001. Cited on page 179.
- [199] R. Sugahara, M. Masuzawa, and H. Yamaoka, "Performance of an active vibration isolation system," in *IWAA*, (CERN, Geneva), 2004. Cited on page 179.
- [200] M. H. Kim, H. Y. Kim, H. C. Kim, D. Ahn, and D.-G. Gweon, "Design and control of a 6-dof active vibration isolation system using a halbach magnet array," *IEEE/ASME Transactions on Mechatronics*, vol. 21, no. 4, pp. 2185–2196, 2016. Cited on page 179.
- [201] M. Thier, R. Saathof, A. Sinn, R. Hainisch, and G. Schitter, "Six degree of freedom vibration isolation platform for in-line nano-metrology," *IFAC-PapersOnLine*, vol. 49, no. 21, pp. 149–156, 2016. Cited on page 179.
- [202] D. B. Newell, *Six degree of freedom active vibration isolation at 1 Hz and above*. PhD thesis, University of Colorado, 1994. Cited on page 179.
- [203] Y. Du, R. A. Burdisso, and E. Nikolaidis, "Control of internal resonances in vibration isolators using passive and hybrid dynamic vibration absorbers," *Journal of Sound and Vibration*, vol. 286, no. 4-5, pp. 697–727, 2005. Cited on page 179.
- [204] T. Ametek, "Cleanbench laboratory table." <https://www.techmfg.com/products/labtables/cleanbench63series>, 2016. Cited on page 180.
- [205] Newport, "Guardian[®] active isolation workstations." <https://www.newport.com/f/guardian-active-isolation-workstations>, 2016. Cited on page 180.

- [206] Thorlabs, “Optical table supports: Active vibration isolation.” https://www.thorlabs.de/newgrouppage9.cfm?objectgroup_id=1095&pn=PTS602, 2016. Cited on page 180.
- [207] Kinetic Systems, *Brochure: 9100 Series VIBRAPLANE Workstations... For Load Ranges up to 1300 lbs.* Kinetic Systems, Inc., Massachusetts, USA, 2016. Cited on page 180.
- [208] MS NOISE, “Table antivibration pour microscope à force atomique.” <http://www.msnoise.com/fr/TAVB-AFM-table-antivibration-mesure-microscope-atomique.html>, 2015. Cited on page 180.
- [209] Barry Controls, *Brochure: the world’s most advanced active vibration isolation solution.* Newport, California, USA, 1995. Cited on page 180.
- [210] CSA engineering, *Brochure: Hexapods Platforms for Vibration and Motion Control.* MOOG, California, USA, 2020. Cited on page 180.
- [211] Herzan, “AVI-200 Series.” <https://www.herzan.com/products/active-vibration-control/avi-series/avi-200-series.html>, 2019. Cited on page 180.
- [212] IDE, “Active Vibration Isolation: IDE Leads In Vibration Isolation.” https://www.ideworld.com/en/active_vibration_isolation.html, 2020. Cited on page 180.
- [213] STANDA, “1TS-AVI200S/LP - Active Vibration Isolation System.” http://www.standa.lt/products/catalog/optical_tables?item=335, 2020. Cited on page 180.
- [214] The TableStable Ltd., *Instruction Manual: active vibration isolation system TS-150LP / TS-140LP / TS-300LP.* Mettmenstetten, Switzerland, 2015. Cited on page 180.
- [215] Accurion GmbH, *Halcyonics i4: active vibration isolation desktop unit.* Goettingen, Germany, 2016. Cited on page 180.
- [216] M. Defrise and C. De Mol, *Imaging and Inverse Problems.* Presses Universitaires de Bruxelles, 2013. Cited on page 181.
- [217] T. Okoshi, K. Kikuchi, and A. Nakayama, “Novel method for high resolution measurement of laser output spectrum,” *Electronics letters*, vol. 16, no. 16, pp. 630–631, 1980. Cited on page 182.
- [218] T. N. Huynh, L. Nguyen, and L. P. Barry, “Phase noise characterization of sgdb lasers using phase modulation detection method with delayed self-heterodyne measurements,” *Journal of lightwave technology*, vol. 31, no. 8, pp. 1300–1308, 2013. Cited on page 182.
- [219] S. Camatel and V. Ferrero, “Narrow linewidth cw laser phase noise characterization methods for coherent transmission system applications,” *Journal of Lightwave Technology*, vol. 26, no. 17, pp. 3048–3055, 2008. Cited on pages 182, 183, 184, and 185.
- [220] J. Kim and Y. Song, “Ultralow-noise mode-locked fiber lasers and frequency combs: principles, status, and applications,” *Advances in Optics and Photonics*, vol. 8, no. 3, pp. 465–540, 2016. Cited on page 183.
- [221] D. Xu, F. Yang, D. Chen, F. Wei, H. Cai, Z. Fang, and R. Qu, “Laser phase and frequency noise measurement by michelson interferometer composed of a 3×3 optical fiber coupler,” *Optics express*, vol. 23, no. 17, pp. 22386–22393, 2015. Cited on page 185.
- [222] X. Xie, R. Bouchand, D. Nicolodi, M. Lours, C. Alexandre, and Y. Le Coq, “Phase noise characterization of sub-hertz linewidth lasers via digital cross correlation,” *Optics letters*, vol. 42, no. 7, pp. 1217–1220, 2017. Cited on page 185.

List of publications

Papers

- B. Ding, G. Zhao, **J. Watchi**, A. Sider, C. Collette, An interferometric inertial sensor for low-frequency seismic isolation (2022), *Sensors and Actuators A: Physical*, 335: 113398.
- M. Verma, A. Pece, S. Hellegouarch, **J. Watchi**, G. Durand, S. Chesne, C. Collette, Dynamic stabilization of thin aperture light collector space telescope using active rods (2020), *Journal of Astronomical Telescopes, Instruments, and Systems*, 6(1), 014002.
- G. Zhao, B. Ding, **J. Watchi**, C. Collette, Experimental study on active seismic isolation using interferometric inertial sensors (2020), *Mechanical systems and signal processing*, 145, 106959.
- M. Verma, T. Dehaeze, G. Zhao, **J. Watchi**, C. Collette, Virtual sensor fusion for high precision control (2020), *Mechanical Systems and Signal Processing*, 150, 107241.
- **J. Watchi**, S. Cooper, B. Ding, C. Mow-Lowry, C. Collette, Contributed review: A Review of Compact Interferometers (2018), *Review of Scientific Instruments*, 89(12): 121501.
- **J. Watchi**, B. Ding, D. Thilumba, K.Artoos, C. Collette, Coil-free active stabilisation of extended payloads with optical inertial sensors (2018), *Measurement and Technology*, 29(5): 054005.

Conference proceedings

- **J. Watchi**, B. Ding, G. Zhao, C. Collette, Study of MIMO Control Laws for Seismic Isolation of Flexible Payload, ICCMA (6-8 November 2019: Delft, Netherlands).
- C. Collette, B. Ding, G. Zhao, **J. Watchi**, Towards broadband seismic isolation system, 7WCSCM (22-25 July 2018: Qingdao, China).
- B. Ding, **J. Watchi**, C. Collette, Development of a high resolution optical inertial sensor, 7WCSCM (22-25 July 2018: Qingdao, China).
- **J. Watchi**, B. Ding, F. Matichard, C. Collette, Development of a high-resolution optical inertial sensor for sub-Hz seismic isolation, ISMA conference (September 2016 Leuven: Belgium).

REFERENCES

- **J. Watchi**, K. Artoos, C. Collette, F. Matichard, Interferometric active isolation for extended structures, ASPE conference (November 2015: Austin, USA).

Appendices

Appendix A

Frequency content of stationary random processes

A.1 Power Spectral Density

The frequency information of a time-varying, deterministic signal, such a pure sinusoidal signal, can be obtained by taking the Fourier transform of this signal. Reciprocally, the time domain information of a deterministic signal can be fully recovered from the frequency domain data using the inverse Fourier transform. In fact, the phase and amplitude information of the frequency signal are sufficient to recover the time domain signal.

In the case of a stationary random process, each realization of the Fourier transform and its inverse leads to a different result. Therefore, instead of evaluating the Fourier transform of the signal, the power spectral density (PSD) is calculated. The PSD is the Fourier transform of the auto-correlation function. The auto-correlation function $C(t, \tau)$ is defined by [181]:

$$C(t, \tau) = \langle p(t)p^*(t + \tau) \rangle , \quad (\text{A.1})$$

where $p(t)$ is the stationary random signal.

Hence, knowing the correlation function, the PSD $S_{pp}(\omega)$ is

$$S_{pp}(\omega) = \lim_{T \rightarrow \infty} \frac{1}{2T} \int_{-T}^T \left[\int_{-\infty}^{\infty} \langle p(t)p^*(t+\tau) \rangle d\tau \right] e^{-i\omega t} dt = \lim_{T \rightarrow \infty} \frac{1}{2T} \int_{-T}^T p^2(t) e^{-i\omega t} dt . \quad (\text{A.2})$$

When analyzing the terms, we can see that the PSD $S_{pp}(\omega)$ represents the portion of power fluctuating at ω per unit bandwidth [182], hence the density term in PSD. A direct consequence of the definition of the power spectral density is that the phase information is lost. Therefore, the time domain signal can not be recovered from the PSD.

Other useful quantities are derived from the correlation function and are often used to characterize systems including random processes: the amplitude spectral density, the root mean square, the transfer function and the coherence.

A.1. Power Spectral Density

A.1.1 The amplitude spectral density

In order to represent the frequency content of a stationary random process in term of amplitude instead of power, the amplitude spectral density (ASD) is introduced. It is defined as the square root of the PSD [183].

This quantity is often preferred to the PSD to characterize a signal as it refers to the amplitude of the signal and not its power. Therefore, in this thesis, the ASD is used to represent the frequency content of a signal.

A.1.2 The integrated root mean square

To ease the interpretation, one can prefer to use a quantity that has the units of the amplitude of the signal. By integrating the PSD, the cumulative power spectrum (CPS) [85] is obtained

$$C_p(f) = \int_f^\infty S_{pp}(f)df \quad (\text{A.3})$$

which has the units of power. The CPS calculated for the frequency f_0 allows to know the total power carried by frequencies larger and equal to f_0 .

The square root of the CPS is defined as the integrated root mean square (RMS) (or cumulative RMS). Similarly to the CPS, the integrated RMS gives the total amplitude of the signal carried by frequencies larger and equal to the frequency for which it is evaluated. If not specified, this frequency is 1 Hz. This quantity is commonly used to evaluate the performance of an isolation platform as it permits to evaluate with a single value the global amplitude reduction of the motion in a large frequency range.

A.1.3 The transfer function

In a linear system, the transfer function (TF) indicates, for each forcing frequency f , the ratio between a harmonic input x and the output y at that same frequency. This transfer function can be approximated by [184]

$$TF(f) = \frac{S_{xy}(f)}{S_x(f)}, \quad (\text{A.4})$$

where $S_x(f)$ is the PSD of the input x ;

S_{xy} is the cross spectral density between x and the output y , i.e. the Fourier transform of the cross-correlation function defined by

$$C_{xy}(t, \tau) = \langle x(t)y^*(t + \tau) \rangle . \quad (\text{A.5})$$

Therefore, the cross spectral density of two variables x and y , assuming that their respective Fourier transform is $X(f)$ and $Y(f)$, is

$$S_{xy}(f) = \langle X(f)Y^*(f) \rangle . \quad (\text{A.6})$$

Unlike the PSD, the transfer function has a phase and an amplitude. Therefore, if at a certain frequency, the amplitude of the TF between the signal x and the signal y is one and its phase is zero, it means that the two signals x and y are moving exactly the same way at

this frequency.

In addition, the phase of the TF allows to see if the two signals are moving in-phase or out-of-phase. A phase drop corresponds to the presence of a resonance frequency between the two systems where the signals are measured.

A.1.4 The coherence

In addition to the TF, the relationship between two variables can also be evaluated by the coherence. The coherence between two random variables x and y is defined by [185]

$$Co(f) = \frac{|S_{xy}^2(f)|}{S_x(f)S_y(f)}. \quad (\text{A.7})$$

The coherence is a frequency-dependent variable whose value vary between 0 and 1. When the coherence is close to one, the two signals' amplitude is due to the same source. Similarly, when the coherence is near zero, the two signals are due to different sources. Finally, when the coherence is in between, it means that there is a common source to these two variables but that it is not the only source contributing to the amplitude of the signals.

During experiments, the coherence is measured and plot together with the TF in order to confirm that the transfer function between the two signals is valid. If the coherence is close to one in a certain frequency region, the validity bandwidth of the transfer function can be identified, i.e. we know the frequency range where the TF is valid.

Appendix B

Sensor readout

The working principle of the readouts commonly used to sense motion is presented in this section. They are sorted depending on the physical principle used: optics, electromagnetism and stress-strain relationship.

B.1 Optical readout

Many readouts rely on an optical method. The most common techniques are briefly described here.

These readouts methods are often contactless but they require either to have a flag attached to the moving body or a reflecting surface. However, if the body itself is reflecting, there is no need to add a mirror. Generally, the surface quality is often not good enough to reflect properly the beam and, for example, a reflecting tape can be placed on the surface.

Regarding the resolution and bandwidth of these readouts, they are mainly depending on the properties of the photodetectors used.

B.1.1 Shadow sensor

Its working principle relies on an object attached to the moving body, called a flag, whose position blocks more or less the light emitted by a laser and measured by a photodiode [186], see Fig. B.1.a. It's working range is limited by the width of the laser beam.

B.1.2 Triangular sensor

A beam is reflected on the body and its intensity is measured by an array of photodetectors, see Fig. B.1.b. Depending on the distance between the sensor and the body, the position of the spot on the array moves. The range of the sensor is limited by the dimension of the array of photodetectors.

B.1.3 Optical encoder

A plate with a grating, called a scale [50], is placed on the moving object. The intensity of the laser beam reflected by the grating on the plate varies depending on the reflection spot

on the grating [187]. Therefore, the reflected beam becomes a train of pulses, see Fig. B.1.c. Knowing the dimensions of the pattern, by counting the number of pulses, the distance traveled is identified. To know the direction of motion, two shifted gratings in quadrature are placed next to each other as shown in Fig. B.1.c.

The scale can also be made of a glass with periodic transparent and opaque lines forming the repetitive pattern or it can be made of some transmissive, conductive or magnetic material [50].

The resolution of the encoder is limited by the density of lines of the pattern and its working range is limited by the size of the scale.

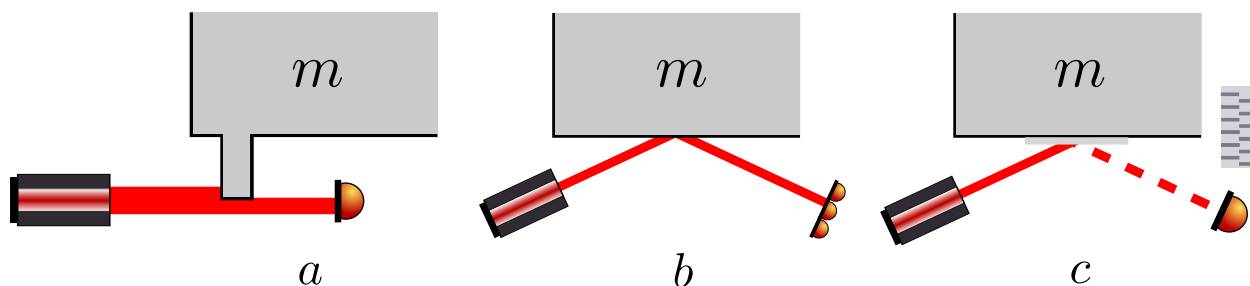


Figure B.1: Representation of (a) shadow sensor, (b) triangular sensor and (c) optical encoder when measuring the vertical motion of a body of mass m . The laser is on the left and the photodetector on the right of each sketch. The sketch on the right of Fig.(c) illustrates the grating of the optical encoder.

B.1.4 Interferometer

The most frequent interferometers used are Michelson interferometers, see Fig. 4, and Fabry-Pérot [30]. In a Michelson interferometer, two beams are interfering with each other, one beam reflected by a fixed mirror and one reflected by a mirror attached to the moving body. The phase of the resulting beam contains the displacement information.

A Fabry-Pérot is made of two parallel mirrors, one fixed and one attached to the moving body. Together, these mirrors form a so-called cavity. The laser enters the cavity and circulates inside of it, making several turns before exiting the cavity. As the mirror moves, the size of the cavity varies and this information is carried by the phase of the exiting beam.

B.2 Electrostatic and electromagnetism readout

The readouts methods described here are based on a probe generating a current or a voltage and interacting with the electromagnetic properties of the moving body or of a body with good electromagnetic properties attached to the moving one.

The range of the sensors presented here is on the order of a few millimeters.

B.2.1 Capacitive sensor

If a probe generating a voltage approaches a conductive plate, the positive and negative charges of the conducting plate are separated and a plane capacitor is formed by the space between the surface of the probe and the plate, see Fig. B.2.a.

B.2. Electrostatic and electromagnetism readout

The capacitance of a plane capacitor is defined by [188]

$$C = \frac{\epsilon S}{e}, \quad (\text{B.1})$$

where ϵ is the permittivity of the material between the two plates;
 S is the surface of the plate and e is the space between the two plates.

If the conductive plate is attached to the moving body, any motion makes vary the distance between the probe and the plate and hence, the capacitance changes. This capacitance is measured with a Wheatstone bridge [85].

B.2.2 Eddy current sensor

A magnetic field is generated by feeding an AC current source to a coil, see Fig. B.2.b. The magnetic field creates a non-constant Eddy current at the surface of the moving body if it is made of a conductive material. The Eddy current then produces an opposed induced electromagnetic field that interacts and modifies the inductance of the sensing coil. The impedance of the sensing coil is then evaluated using a Wheatstone bridge.

The inductance varies depending on the distance between the sensing coil and the conducting plate. The surface of the conducting material has to be of good quality, without cracks or defects in the material.

B.2.3 Linear Variable Differential Transformer (LVDT)

A ferromagnetic material is connected to the moving body. This part is inside a series of three coils [50], see Fig. B.2.c; the middle one, called the primary coil is driven by an AC current. When the ferromagnetic core is in the middle, the voltage induced in the secondary coils, the two external coils, is the same. When the part is moving, the voltage measured at the closest coil increases. As the voltage is proportional to the position of the core, the displacement can be evaluated.

B.2.4 Geophone readout

A moving magnet is surrounded by a coil shunted with a resistor. When the magnet moves, the induced current in the coil can be measured. There exist other configuration where the coil is moving and the magnet is fixed [93]. This system is mostly used in geophones.

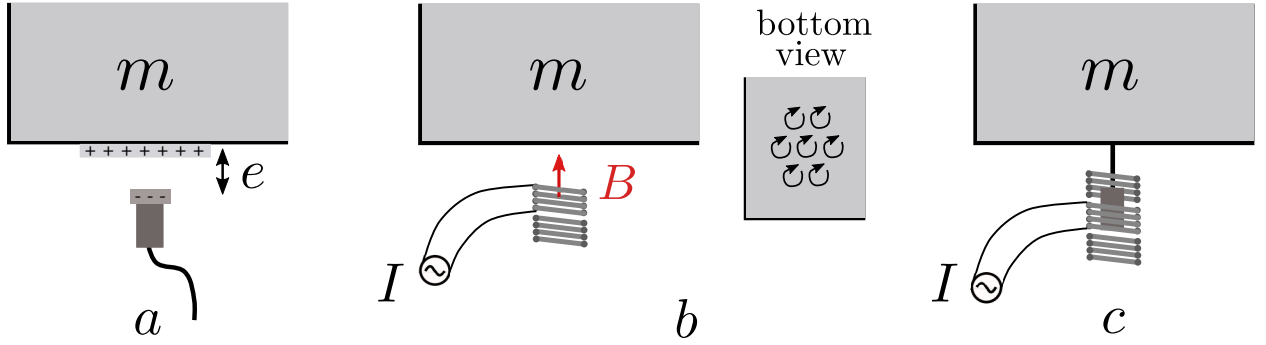


Figure B.2: (a) *Capacitive sensor:* a probe fed by a voltage approaches a conductive plate which accumulates charges. The capacity of the resulting system is measured. The thickness e of the capacitor varies when the body is moving. (b) *Eddy current sensor:* a coil is fed by an AC current I and the resulting magnetic field B creates an induced Eddy current at the surface of the moving body as represented by the small current turns on the bottom view. These turns emitted a counter-propagating magnetic field which alters the magnetic field captured by the secondary coil. (c) *LVDT:* A primary coil is fed by an AC current I . A ferromagnetic core is attached to the moving body and its location alters the intensity of the current at the two secondary coils located on both sides of the primary coil.

B.3 Strain readout

When some materials are subjected to stresses, their deformation can be used to sense the motion of the body. Sensors using this property are sensitive to the strain of the material and hence, their bandwidth starts around 10 Hz [46] and they are suited to measure acceleration when combined with a mechanical system like in Ref. [189]. The strain can be measured in different ways.

B.3.1 Piezoelectric materials

When subjected to stress, some material emits some physical quantity such as a charge or an increase or decrease in temperature [46]. The coupling between these changes and the strain can be described in the constitutive equations of these materials, called smart materials. The smart material the most employed is the piezoelectric transducer (PZT) material where a charge is induced when an external force stresses the material. The resulting charge is responsible for a voltage difference between both ends of the PZT patch that can be measured. The constitutive coupled equations of a PZT material can be found in [93].

The PZT can be used as a patch glued to the system, see Fig B.3.a, or put in stack and combined with a mechanical system whose deformation is measured [190]. In that case, the stack is preloaded with a high stiffness spring to measure positive and negative strains [47].

B.3.2 Strain gauge

The resistor R of an electric conductor is defined by [188]

$$R = \frac{L}{\sigma_e S}, \quad (\text{B.2})$$

B.3. Strain readout

where L is the length of the conductive material, S its transverse section and σ_e its electrical conductivity [$\Omega^{-1}\text{m}^{-1}$].

If the conductive material is stretched, its length is increased and its section decreased, hence, the resistor increases. This principle is used to measure motion by using a foil resistor and measuring its value with a Wheatstone bridge. The gauge is attached similarly to a PZT patch. With a calibration procedure, it is possible to define the force as a function of the resistance of the gauge [191].

B.3.3 Fiber Bragg grating

Equidistant lines are engraved in an optical fiber forming a fiber Bragg grating (FBG). A FBG is equivalent to a series of Fabry-Pérot and hence, the wavelength reflected by the grating depends on the size of the cavities. Therefore, if the optical fiber is connected to the moving body, its deformation induces strains in the fiber that change the length of the cavities and hence, the wavelength reflected, see Fig. B.3.b. An interrogation unit measures the wavelength reflected by the system and the strain can be deduced from this information. The measuring system and the laser used are contained in the interrogation unit. There exist several types of interrogators. In a first system, the laser used is a broadband light [192]. Depending on the wavelength reflected a pixel of the photodetector is enhanced. Another type of interrogator contains a laser with a tunable wavelength and the interrogator emits a light whose wavelength travels periodically the available spectrum during the measurement. When the right wavelength is emitted, it is reflected and measured by the photodetector. Most of the FBG use infrared light. The range of the FBG depends on the wavelength band and is usually on the order of 100 nm.

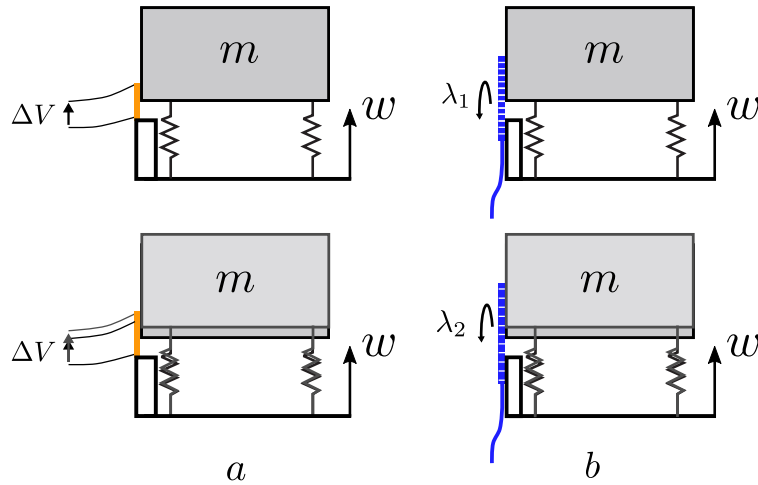


Figure B.3: Strains readout before (top) and after (bottom) deformation. (a) PZT readout using a PZT patch: the voltage difference ΔV at the two extremities of the patch due to the strain is measured. (b) FBG: the fiber length is increased due to the deformation of the body. The reflected wavelength λ_2 is different from the one reflected at rest λ_1 .

Appendix C

MIMO active isolation tables from the literature and commercial products

In table C.1 and table C.2, active isolation tables from the literature using voice coils are listed. Table C.1 contains chronologically all the isolation stages found that use geophones to sense the motion of the system. Table C.2 presents the platforms that use other types of sensors.

The commercial products are listed in table C.3.

The tables give details on the architecture and performance of the platforms: resonance frequency, type of suspension, type of controller and reduction of the motion at 1 Hz when specified.

Table C.1: Properties of active isolation tables with voice coils actuators and geophones found in the literature. They are sorted chronologically. Note: all these systems are combined with passive suspensions.

Product name	Ref.	Sensor	ω_0	Performance at 1 Hz	Type of controller	Passive system
Atomic gravimeter	[22]	Geophones	2 Hz	Vertical: 1/100 Horizontal: -	PI	Springs
Single freq. excit. isolation system	[193]	Geophones	4 Hz	-	PID Centralized	Neoprene isolators
AVIS	[84]	Geophones	vert.: 3 Hz hor.: 1.5 Hz	No isolation at 1 Hz	PID Centralized	Springs
Philips AIMS 2 nd iteration	[85]	Capacitive sensor and Geophone (for the proof mass controlled with PI)	1 Hz	1 dof experiment Vertical: <1/10	PI + PD for the voice coils PI + PID for the pneumatic act.	Pneumatic Springs
Mecal Hummingbird	[83]	Geophones	3 Hz	Vertical: 1/100 Horizontal: 1/30	-	Polymer dampers + negative stiff. springs
MI Partners AVI	[82, 194]	Geophone	3 Hz	Vertical: [1/10;1/100] Horizontal: -	Decentralized + Stretcher	Springs
Mobile gravimeter	[18]	Geophones	1 Hz	Vertical: 1/100 Horizontal: -	-	Minus K
AVI	[73]	Geophones (isolation) Eddy current (monitor)	vert.: 2 Hz hor.: 2 Hz	1/10 (H and V)	decentr.: velocity FB (air springs act.) centralized: sky hook damping	H: IP V: air spring
LIGO	[3, 48]	Low freq.: relative sensor High freq.: inertial sensor	1 Hz	Vertical: 1/1000 Horizontal: 1/1000	Feedback + Feedforward	Springs
World record gravimeter	[2]	Geophones	0.8 Hz	Vertical: 1/100 Horizontal: 1/10	Feedback: lead and lag	Minus K
VIBISO	[1]	Geophone	1 Hz	Vertical: 1/100 Horizontal: -	Feedback: PID + Feedforward: PI	Minus K
AEI-SAS	[195]	LVDT ($f < 0.1$ Hz) Geophones ($f > 0.1$ Hz)	vert.: 0.3 Hz hor.: 0.3 Hz	Vertical: 1/100 Horizontal: 1/100	Damping + PID + sensor correction	hor.: inverted pendulum vert.: GAS filter

APPENDIX C. MIMO ACTIVE ISOLATION TABLES FROM THE LITERATURE AND COMMERCIAL PRODUCTS

Table C.2: Properties of active isolation tables with voice coils actuators found in the literature. The platforms are sorted depending on the sensor used and chronologically. Note: all these systems are combined with passive suspensions.

Product name	Ref.	Sensor	ω_0	Performance at 1 Hz	Type of controller	Passive system
Helicopter Gearbox	[196]	Accelerometer	10 Hz	No isolation at 1 Hz	Damping	Soft rubber
VISS	[197]	Accelerometers	3 Hz	2/5 in strut's direction	Decentralized LMS filter	Viscous fluid
Hexapod	[80]	Accelerometers	2-3 Hz	No isolation at 1 Hz	Lead + Lag + HP + LP + notch	Coil springs
VIRGO	[198]	Accelerometers and linear variable differential transformer (LVDT)	0.04-2 Hz	+/- 1/100 and also @ 0.1 Hz	MIMO -> 3 SISO LF (<2 Hz): inertial control HF (>2 Hz): damping + sensor fusion (10 mHz)	VIRGO super attenuator
Tokkyokiki	[199]	Displacement sensors Accelerometers	vert.: 3 Hz hor.: 2.5 Hz	No isolation at 1 Hz	Feedback with the accelerometers +BP filter	Air springs
SEMIS	[69]	Optical pos. sens. Accelerometers	+/- 1 Hz	No isolation at 1 Hz	acceleration FB (sliding surface opt. ctrl)	EM springs
AVIS	[200]	Accelerometers	3 Hz 20 kg payload	1/10 (unknown) direction)	PID in modal coordinates	Steel springs
JILA 3 stages	[36]	Seismometer and interferometer	vert.: 1 Hz hor.: 0.79 Hz	Vertical: 1/100 Horizontal: 1/60	Lead + Lag + HP + LP	Springs
VVIS	[10]	Inertial sensors	0.7 Hz	Vertical: 1/10 Horizontal: 1/10	Feedback: PD + Feedforward: PD	Springs
Drone camera	[8]	IMU	vert.: 30 Hz X: 20 Hz Y: 40 Hz	No isolation at 1 Hz	Centralized IFF (weak)	Vert. springs
Thier	[201]	4 Capacitive sensors 2 Heterodyne interf.	around 10 Hz	$\geq 1/10$	PID	Magnetic springs
Newell	[202]	Relative displacement sensors	vert.: 1Hz hor.: 0.7 Hz	Vertical: 1/50 Horizontal: 1/20	Centralized Lead and Lag	Coil springs
HDVA (Hybrid DVA)	[203]	Force tsd., mic. or acc. array	30 Hz	No isolation at 1 Hz	Feedforward	Rubber pad

Table C.3: *Properties of commercial active isolation stages with pneumatic actuators, PZT and motors.*

Company	Table	Sensor	Actuator	Dimensions	Payload	Transmissibility at 1 Hz	Comments
TMC [204]	MICRO-G LAB cleanbench	-	Gimball Piston air Isolator	h : 73 cm [62.5x90,90x150]cm ²	max 160 kg	2	$\omega_{0,vert} = 1.2$ Hz $\omega_{0,hor} = 1$ Hz 6 d.o.f.
Newport [205]	Guardian Workstation	Gravim.	Springs + Pneumatic act.	75 x 90 cm ²	[50-190,5] kg	0.2	6 d.o.f.
Thorlabs [206]	PTS series	Accelerom.	Pneumatic act.	h : [45,70]cm r < 30 cm	max 2500 kg	2	-
Kinetics S. [207]	9100 series		Valve adjustm. active	h : 73 cm	290 kg	1.5	$\omega_{0,vert} = 1.9$ Hz $\omega_{0,hor} = 2.2$ Hz
Harvard Apparatus	Vibraplane Workstation		air-susp.	75 x 90 cm ²			
MS NOISE [208]	TAVB		Pneumatic act.	h: 9 cm 40 x 50 cm ²	max 120 kg	1	6 d.o.f. BW [0.6, 200] Hz
Newport [209]	STACIS	xyz velocity sensors	PZT	h : 27.5 cm 30 x 32 cm ²	[182,2045] kg	0.6	6 d.o.f.
CSA [210]	HX-V100 Stuart platform	resolution 0.1 μ m	PZT	h: 20 cm diam.: 21.5 cm	[2,20] kg	-	6 d.o.f. BW < 250 Hz
Herzan [211]	AVI	PZT	PZT	h : 11 cm 13 x 60 cm ²	max 450 kg	1.5	6 d.o.f. BW [0.5,200] Hz
IDE [212]	PAD 600	Velocity sensor	Voice coil	h : 20 cm 80 x 80 cm ²	600 kg	0.2	6 d.o.f. soft & hard mounts
STANDA [213]	ITS AVI200LP		Force transd.	h : 9.2 cm 11 x 36 cm ²	max 200 kg	3	6 d.o.f. BW [1,200] Hz
Tablestable [214]	TS 300	PZT	Force transd.	h : 12 cm 60 x 80 cm ²	max 300 kg	1	6 d.o.f. BW [0.7,200] Hz
Accurion [215]	Halcyonics	PZT	Force transd.	h : 9 cm 40 x 50 cm ²	max 120 kg	1	6 d.o.f. BW [0.6,200] Hz
CSA [210] engineering	HX-P300		Motor driven screw	h : 63.5 cm r = 46 cm	max 225 kg	-	6 d.o.f. Stewart platform

Appendix D

Singular value decomposition

Consider a non-square system G ($m \times n$), where $m \neq n$. It is not possible to evaluate the eigenvalues of this system as eigenvalues can only be evaluated for square systems. However, a similar method can be applied, the singular value decomposition (SVD) [216].

The symmetric system $G^T G$ has n orthonormal eigenvectors v_k , $k = 1, \dots, n$ and n corresponding eigenvalues σ_k^2 , i.e. $\forall k$ we have

$$G^T G v_k = \sigma_k^2 v_k \quad (\text{D.1})$$

with non-negative eigenvalues ranked in a decreasing order $\sigma_1^2 \geq \sigma_2^2 \geq \dots \geq \sigma_r^2 > \sigma_{r+1}^2 = \sigma_{r+2}^2 = \dots = \sigma_n^2 = 0$. The number r of positive non-zero values is the rank of the system G .

We can define r vectors $u_k = \frac{1}{\sigma_k} G v_k \in \mathbb{R}^m$ with $\sigma_k = +\sqrt{\sigma_k^2}$. These vectors are also orthonormal and satisfies

$$G^T u_k = \frac{1}{\sigma_k} G^T G v_k = \sigma_k v_k . \quad (\text{D.2})$$

As the vectors v_k forms an orthonormal basis of \mathbb{R}^n , any $x \in \mathbb{R}^n$ can be decomposed as

$$x = \sum_{k=1}^n \langle x, v_k \rangle v_k . \quad (\text{D.3})$$

Multiplying by the system G yields

$$Gx = \sum_{k=1}^r \langle x, v_k \rangle \sigma_k u_k . \quad (\text{D.4})$$

From the previous assumption, we can say that the system G has the representation

$$G = \sum_{k=1}^r u_k \sigma_k v_k^T = U \Sigma V^T , \quad (\text{D.5})$$

where U is a $m \times r$ matrix with r columns containing the u_k vectors, V is a $n \times r$ matrix with r columns containing the v_k vectors and Σ is a $r \times r$ diagonal matrix with the elements σ_k on the diagonal $\forall k \in [1, r]$.

Σ contains the singular values and U and V are respectively the pre and post compensator to project the system G in this space.

Appendix E

Phase noise measurement methods

In chapter 2, measurements of the phase noise $\phi(t)$ of the Koheras Adjustik laser have been presented. The methods used to measure this phase noise and their limitations are described here.

The three methods impose the beam to interfere either with itself or with another laser with a frequency close to that of the laser characterized. The signal measured contains the difference of phase noise $\Delta\phi$ between the two signals that interfere and the phase noise of the laser is deduced from this difference $\Delta\phi$.

E.1 Delayed self-heterodyne measurement

One beam is split in two and the frequency of one part is offset with respect to the other by a value $\delta\nu$ [217,218], as shown in fig. E.1. The second part travels a long distance but shorter than the coherence length of the laser.

The intensity resulting from the interaction between the two beams is [219]:

$$I(t) = I(1 + \cos(2\pi\delta\nu t + 2\pi(f + \delta\nu)\tau + \Delta\phi(t, \tau))) , \quad (\text{E.1})$$

where τ is the additional time traveled by the beam that propagates in the longer arm and $\Delta\phi(t, \tau) = \phi(t + \tau) - \phi(t)$. The signal measured by a signal source analyzer measures only the radio-frequency (RF) signal, removing the DC part. In the frequency domain, the signal measured is thus

$$\Delta\phi(f) = \phi(f)(1 - e^{-i2\pi f\tau}) . \quad (\text{E.2})$$

Therefore, the PSD of the phase noise S_ϕ can be deduced from the PSD of the phase noise difference $S_{\Delta\phi}$ measured

$$S_\phi = \frac{S_{\Delta\phi}}{|1 - e^{-i2\pi f\tau}|^2} . \quad (\text{E.3})$$

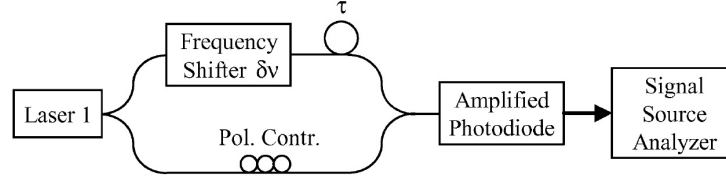


Figure E.1: *Self-heterodyne measurement method [219].*

E.2 Delayed self-homodyne measurement

The laser beam enters a Michelson interferometer and one part of the beam propagates in an arm with a distance larger than the coherence time of the laser (can be several km) [161, 219], as shown in fig. E.2. Therefore the laser interferes with a beam that is not-coherent with itself. The resulting signal measured is

$$I(t) = I_0 + \Delta I \cos(2\pi ft + \Delta\phi(t, \tau)) , \quad (\text{E.4})$$

where ΔI is the maximum amplitude fluctuation due to interference.

The arm lengths of the interferometer are adjusted in order to be in quadrature, i.e. $2\pi f\tau = (n + \frac{1}{2})\pi$ and assuming that the phase noise is small,

$$I = I_0 + \Delta I(-1)^n \Delta\phi(t, \tau) . \quad (\text{E.5})$$

Therefore, the phase noise PSD can be extracted from the PSD of the intensity measured $S_{\Delta\phi}(f) = S_i(f)/\Delta I$. Then Eq. (E.3) is used to extract $S_\phi(f)$ from $S_{\Delta\phi}(f)$.

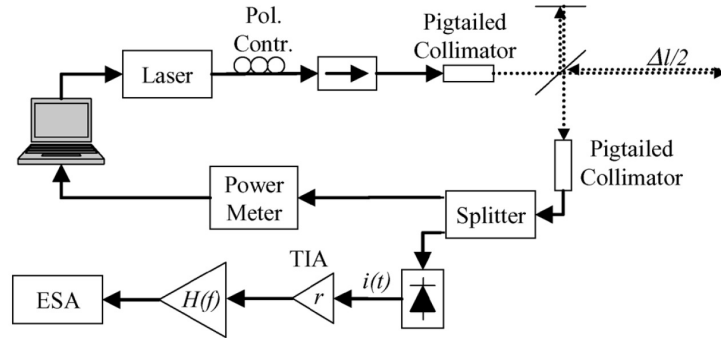


Figure E.2: *Self-homodyne measurement method [219].*

E.3 Beat-note method

Two lasers, with frequency f_1 and f_2 close to each other are coupled together [220], see fig. E.3. The difference $f_1 - f_2$ has to be in the frequency bandwidth of the photodiode, usually in the MHz. The beat-note signal between the two lasers of intensity $I_1 \sin(2\pi f_1 t + \phi_1(t))$ and $I_2 \sin(2\pi f_2 t + \phi_2(t))$ is recorded by a RF photodiode

$$I(t) = \sqrt{I_1 I_2} \cos(2\pi(f_1 - f_2)t + \Delta\phi(t)) , \quad (\text{E.6})$$

E.4. Comparison between the measurements methods

where $\Delta\phi(t) = \phi_1(t) - \phi_2(t)$ and I_1 and I_2 are the intensity of the two lasers.

The signal is recorded using a spectrum analyzer and the OSA (optical spectrum analyzer) is used to check the beat-note frequency.

Here, either two identical lasers are used, or one low-phase noise laser is used as the reference to identify the phase noise of a laser ($\phi_2 \ll \phi_1$), hence, $\Delta\phi(t) \approx \phi_1(t)$

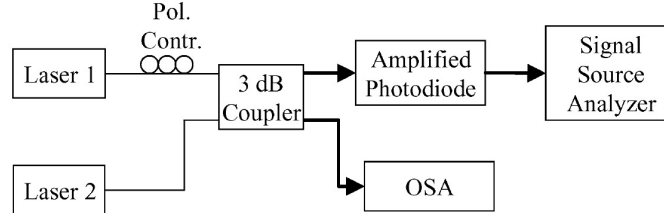


Figure E.3: Beat-note measurement method [219].

E.4 Comparison between the measurements methods

Self-homodyne and self-heterodyne methods overestimate the phase noise due to the low speed measurement [219]. In fact, if, at time t , the carrier frequency is ν_1 and at time $t + \tau$, the carrier frequency is ν_2 , then the resulting phase noise measured is the envelope of the two lorentzian distribution around the two carrier frequencies. This is even worse for the self-heterodyne method as the carrier frequency of the two lasers fluctuates. For example, the FWHM estimated with the delayed self-heterodyne for the laser Anritsu MG9638A is 600 kHz while it is evaluated to be 4.7 kHz when using the delayed self-homodyne method [219].

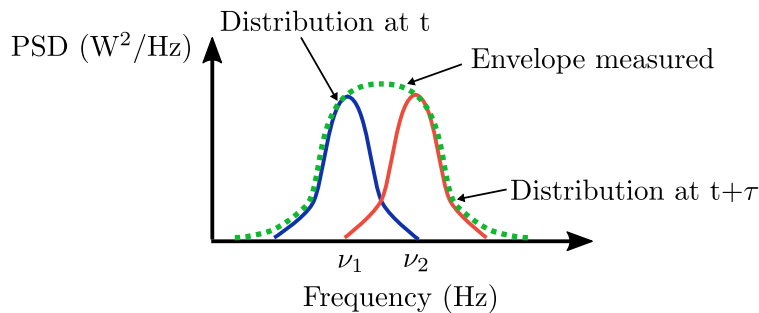


Figure E.4: Illustration of the overestimation of the phase noise using self-heterodyne and self-homodyne methods. As the carrier frequency fluctuates with time, the signal measured by these two methods measures actually the envelope.

The beat-note method is more accurate but requires a very good knowledge of the beat-note value. Again if the beat frequency is too unstable, it can be out of the bandwidth range of the RF detector [219].

Sometimes, the phase noise is extracted from in-phase and quadrature signals, therefore, the intensity noise is subtracted from the signal.

Phase noise is usually measured around the carrier frequency as most application such as telecommunications are interested in characterizing the lorentzian profile of the laser around

APPENDIX E. PHASE NOISE MEASUREMENT METHODS

the carrier frequency. It is therefore not surprising that it was not possible to find the phase noise information for the bandwidth of interest here, between 0.01 Hz and 100 Hz.

Note that there exist several other methods developed [162, 219, 221, 222] but the ones mentioned above are the most commonly used in the literature.

Appendix F

Plant identification of the platform: the diagonal elements

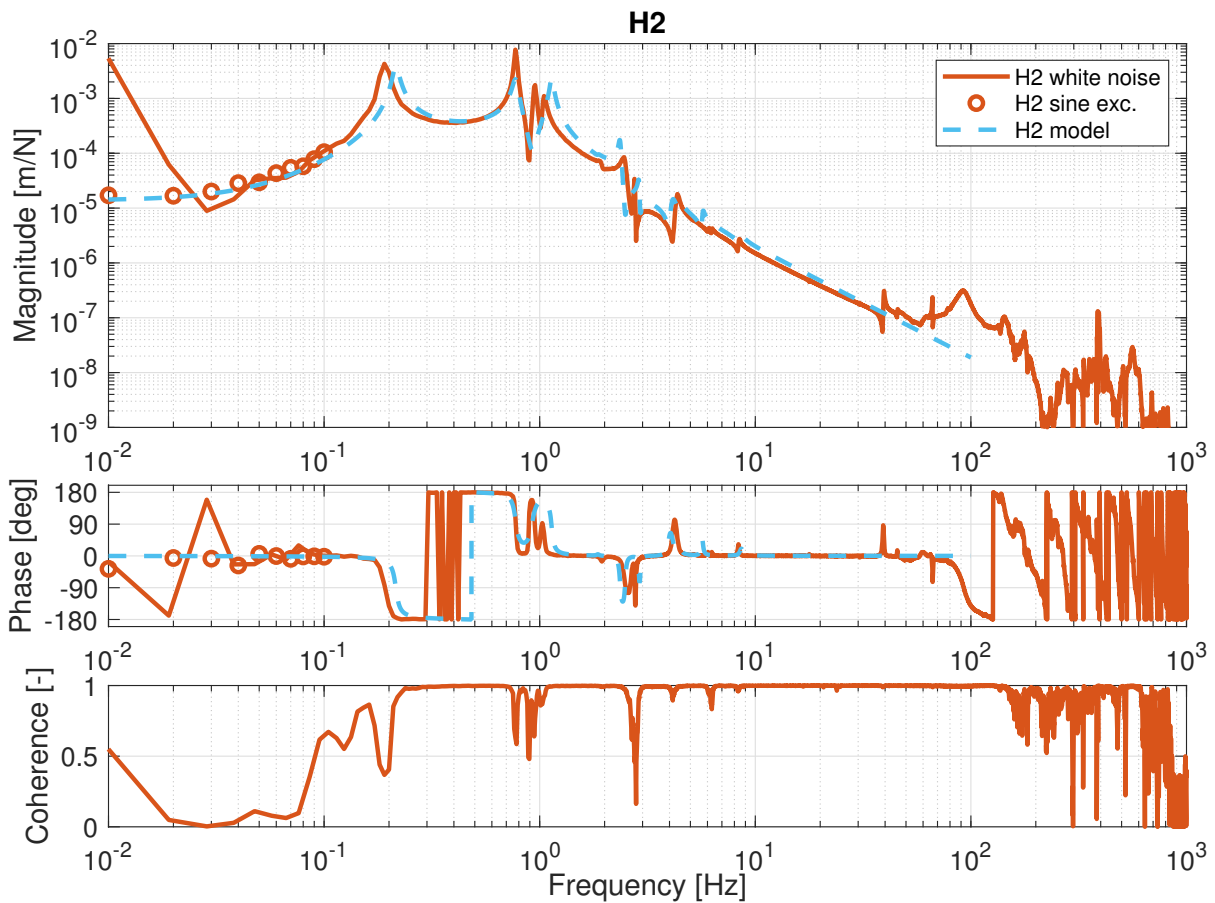


Figure F.1: Transfer function and coherence between the signal injected in the horizontal actuator H2 and the aligned HINS 2. The identification is performed using a sine excitation (dots) at low frequency (below 0.1 Hz) and a white noise at higher frequencies (solid line). The same transfer functions extracted from the simscape model is shown (dashed light blue).

APPENDIX F. PLANT IDENTIFICATION OF THE PLATFORM: THE
DIAGONAL ELEMENTS

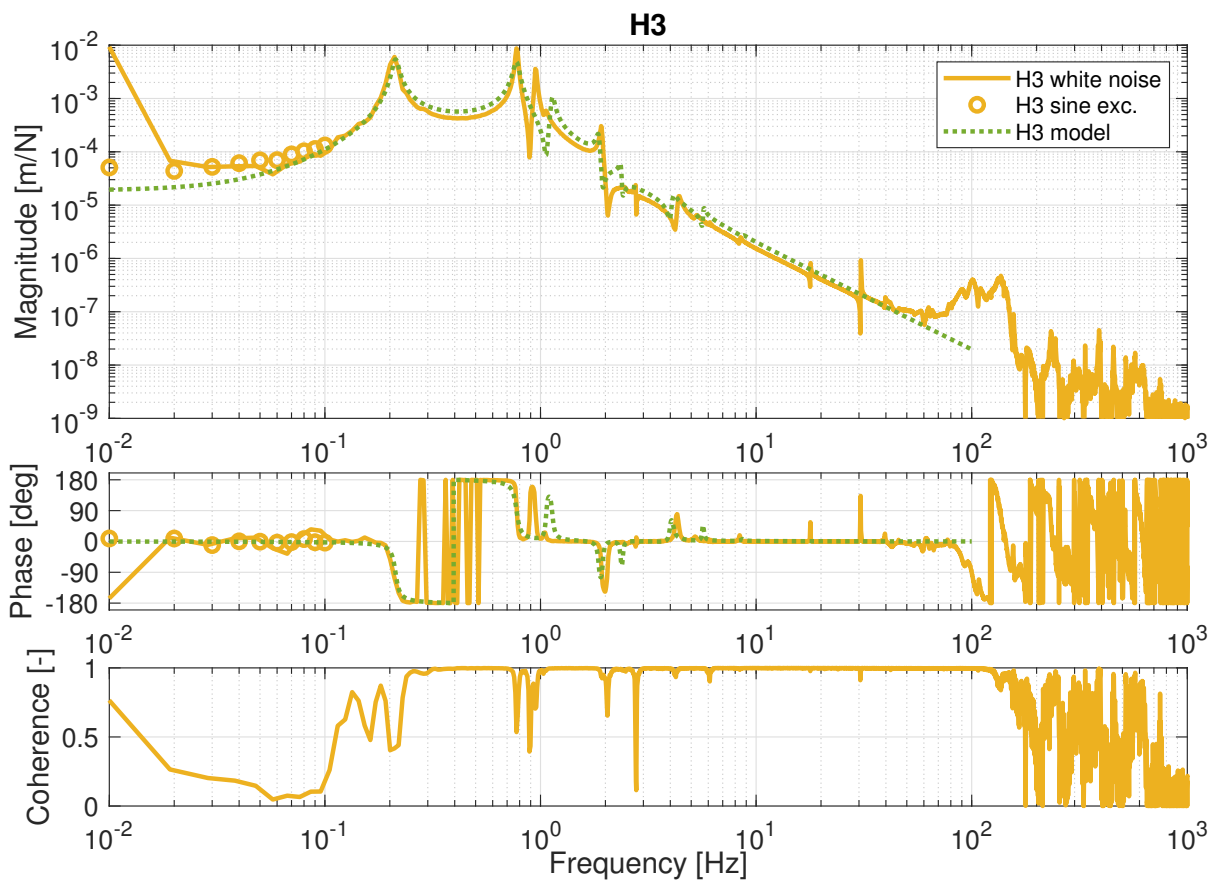


Figure F.2: Transfer function and coherence between the signal injected in the horizontal actuator *H3* and the aligned *HINS 3*. The identification is performed using a sine excitation (dots) at low frequency (below 0.1 Hz) and a white noise at higher frequencies (solid line). The same transfer functions extracted from the *simscape* model is shown (dotted green).

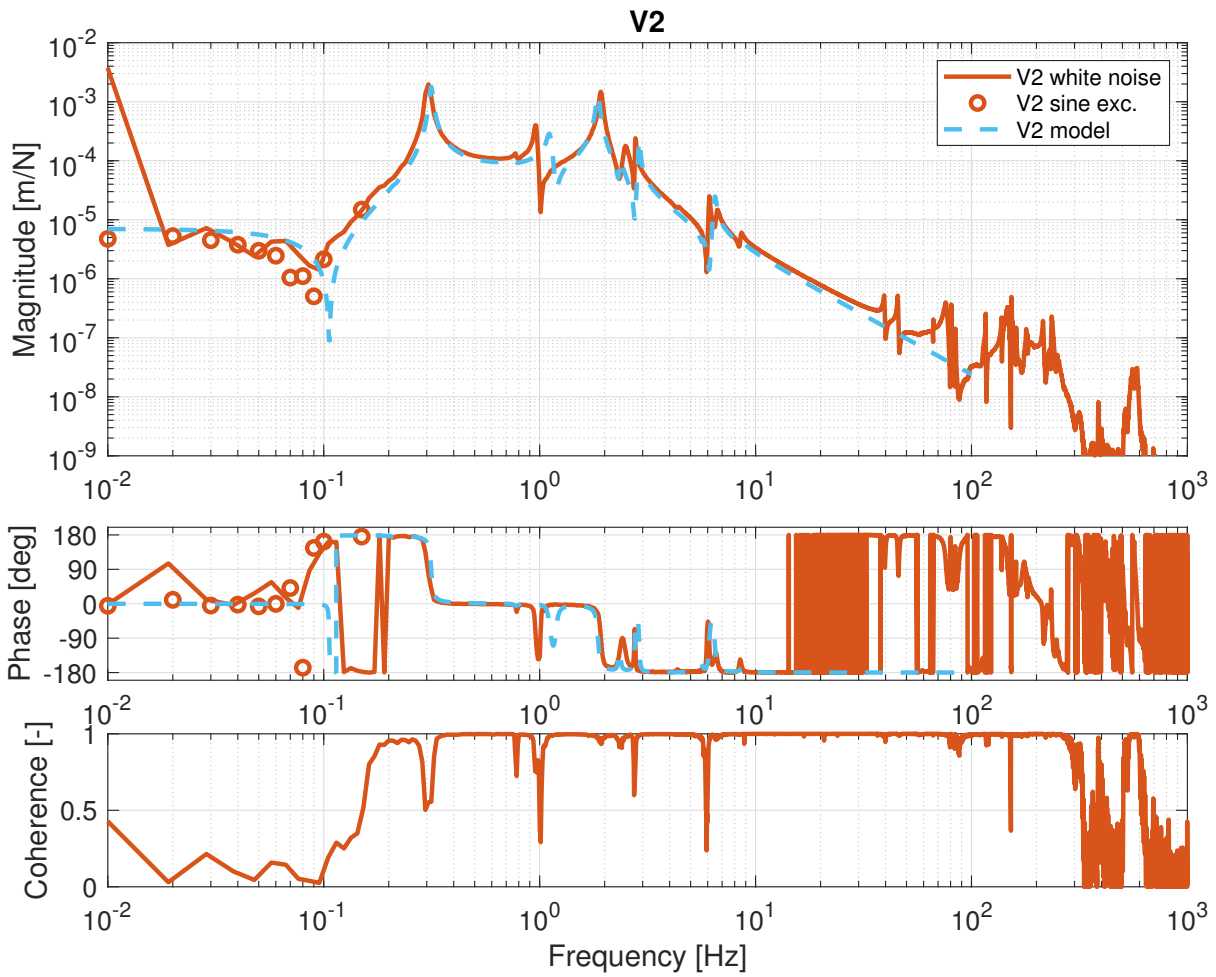


Figure F.3: Transfer function and coherence between the signal injected in the vertical actuator V2 and the aligned VINS 2. The identification is performed using a sine excitation (dots) at low frequency (below 0.1 Hz) and a white noise at higher frequencies (solid line). The same transfer functions extracted from the simscape model also shown V2 (dashed light blue).

APPENDIX F. PLANT IDENTIFICATION OF THE PLATFORM: THE
DIAGONAL ELEMENTS

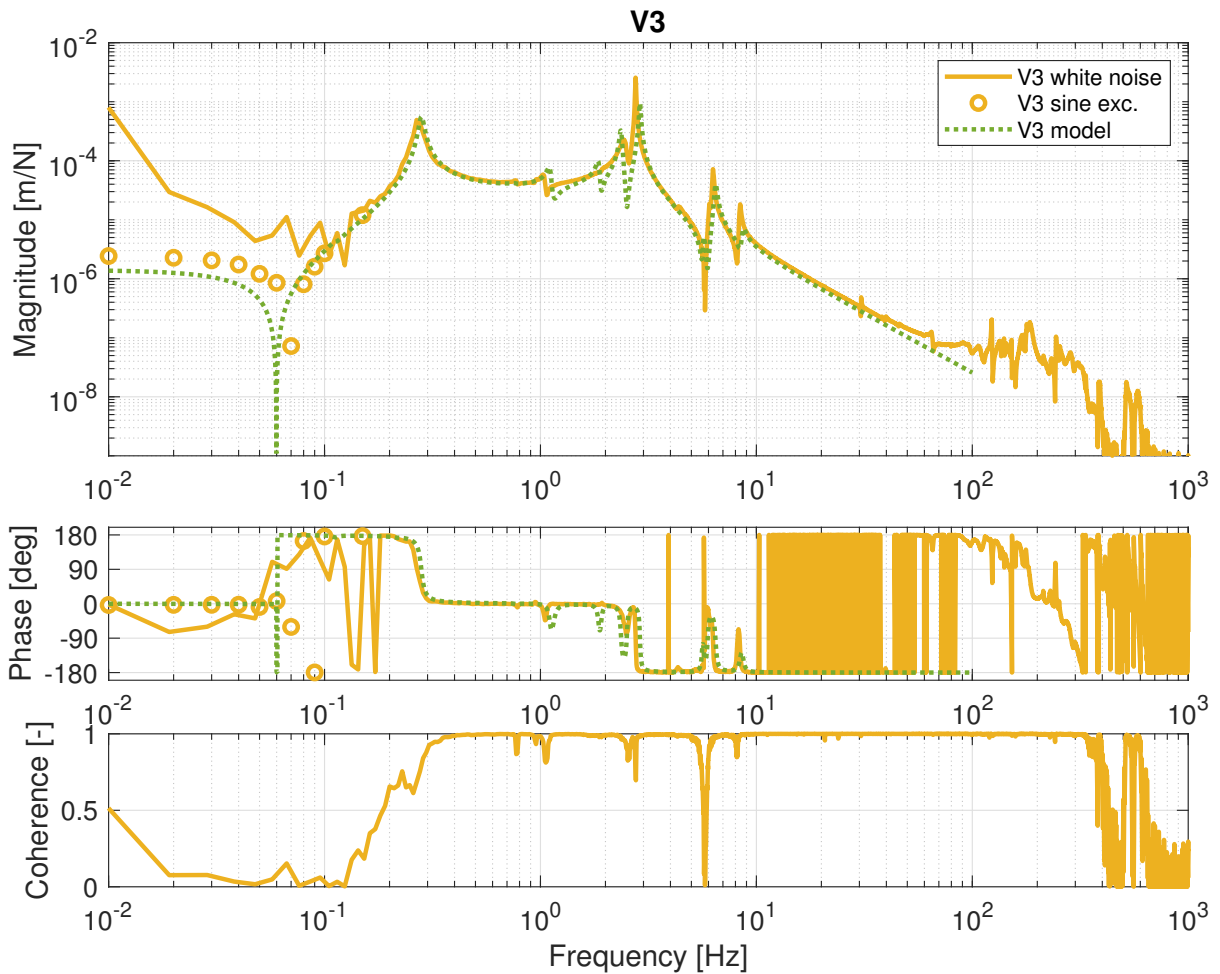


Figure F.4: Transfer function and coherence between the signal injected in the vertical actuator V3 and the aligned VINS 3. The identification is performed using a sine excitation (dots) at low frequency (below 0.1 Hz) and a white noise at higher frequencies (solid line). The same transfer functions extracted from the simscape model also shown (dotted green).